From theoretical stellar spectra to realistic models of the Milky Way:

a never ending Odyssey

Inaugural Thesis

for the Laureateship
of Doctor of Philosophy
presented to the Faculty of Sciences
of the University of Basel

presented by

Karin Ammon
from Herzogenbuchsee (BE)

Basel
February 13, 2007

Approved by the Faculty of Sciences
on request of:

Prof. Dr. R. Buser (Supervisor) and Prof. Dr. F. Cuisinier
(Members of the Dissertationcommission)

Basel
February 13, 2007
(Date of the meeting of the Faculty)

Prof. Dr. Hans-Peter Hauri
(Head of the Faculty)

Für Luis Isaak

Abstract

The main goal of this work is to find the best-fitting galaxy model for the Milky Way by comparing 10 different models with observed star counts and colour distributions. The observational data are taken from the Basel High-Latitude (Basel)- and the Sloan Digital Sky (SDSS) photometric field star Surveys, respectively.
We develop a code to derive synthetic spectra, absolute and apparent magnitudes and colours for stars given by a galactic evolutionary model (3D chemo- dynamical code for the Milky Way by Samland & Gerhard (2003)). The model galaxies provide stellar masses, ages, chemical abundances, velocities and positions at an evolutionary time of 13.5 Gyr. By means of the spectrophotometric data (given in the libraries of stellar evolutionary tracks (Padova 1994) and synthetic stellar spectra (BaSeL 3.2)), we build synthetic colour-magnitude diagrams, star counts, and age- and metallicity distributions for a number of viewing directions and field sizes.

Our intention is to first compare the differences between our suite of models and observations, so as to identify the correlations between the observed data and the input parameters of our models. In a next step we want to fine-tune the model parameters to fit the Basel and/or SDSS survey data and thereby to find the best-fitting galaxy model for our Milky Way.
Unfortunately, the fine-tuning of the model galaxy parameters has not been possible [a] – which forced us to limit our analysis to only 10 models without any further adjustments. We find the best-fitting model galaxy to be the spiral model galaxy S10, described in detail in Subsection 3.2.2.
During our work of comparison we gain deeper insights into all the ingredients that are involved in the conversion of the model data into observables, such as stellar surveys, synthetic photometry or stellar spectral libraries. We track down several inconsistences in the above-mentioned ingredients, and suggest that appropriate corrections need to be applied, before making further *and* unbiased comparisons. Below we enlist the major inconsistencies between the surveys, spectral libraries and between synthetic and observed SDSS colours.

The comparison of the Basel survey with our model galaxies reveals large inadjustable inconsistencies in star counts in all the avaliable viewing directions.

[a] Regrettably, the model-galaxy creator, Markus Samland, had to resign his position at the institute – owing to the lack of funds and the imminent closure of the institute.

We therefore include checks on SDSS data and compare the apparent magnitude histograms of stars in common fields.
A comparison of the Basel- with the Sloan Digital Sky Survey uncovers unexpected large systematic deviations between the apparent magnitude histograms in the magnitude range that is common to both surveys. These differences can only be partly explained by the different resolutions:
a significant number of binary stars and/or galaxies can only be recognised as such in the SDSS survey, whereas the Basel survey defines them as single stars (Jordi, Grebel & Ammon 2005). But this is not a final explanation, why these two surveys end up with different star numbers.
Of course, such mismatches between the two surveys do not allow a definite validation of the model. Therefore, we propose to investigate further the different definitions of single stellar objects by the two surveys, and thus to verify the cause of these striking differences.

The comparison of the SDSS survey- with the model star counts reveals a satisfying agreement in the $u-g$-colour. Unfortunately, other colours do not show the same result, and therefore lead us to analyse the SDSS colours more deeply.
The comparison of theoretical and observed stellar distributions in the $i-z$ versus $r-i$ plane shows (in contrast to the $g-r$ versus $u-g$ distribution) that the observed two-colour distribution can not be reproduced by synthetic colours of any theoretical stars. Only synthetic colours transformed from the Johnson-Cousins system (Jordi, Grebel & Ammon 2005) follow the colour relation of the observed stars correctly. The conclusion appears inevitable that three published SDSS filter functions (r, i and z) do not match the observational system, and are therefore responsible for this deviation.
In future work, the SDSS-filter functions of the r-, i- and z-bands have to be tested by means of synthetic photometry (e.g., Buser (1978)), employing theoretical (e.g., BaSeL 3.2 and PHOENIX) and/or observational stellar spectral libraries (e.g., STELIB (Le Borgne et al. 2003)).

In addition, we have shown that the two theoretical stellar spectral libraries, BaSeL 3.2 and PHOENIX, do not provide matching synthetic colours throughout the full parameter ranges. The largest differences show up in almost all colours at lower effective temperatures (3' 500 $\geq T_{\rm eff}$) and higher surface gravities (2.5 $\leq logg$).
Recent deep surveys allow to aquire spectra and/or colours of faint stellar objects that could be used to test the theoretical libraries in similar low-temperature – high surface gravity ranges (e.g., Westera (2001)).

Due to all these still considerable uncertainties going along with the major ingredients (stellar evolutionary models of Padova, stellar atmosphere models of the BaSeL 3.2 and the PHOENIX library, photometric system parameters, such as the SDSS filter functions, and last but not least: the chemo-dynamical model galaxies) mentioned above, we are unable to draw final conclusions about the validity of the Samland models, or to find a unique best-fitting solution for the Milky Way (if the Milky Way should be reproducible by a unique model at all).

Contents

Abstract **v**

List of Figures **xi**

List of Tables **xxi**

1. Introduction **1**
1.1. Astronomy and earlier work on the determination of the Galactic structure 1
1.2. Motivation for a new phase in the Basel Halo Program 12
1.3. Outline of the Thesis 14

2. Observational data **15**
2.1. New Basel High-Latitude Survey (Basel survey) 15
2.1.1. RGU photometric system 16
2.2. Sloan Digital Sky Survey (SDSS survey) 17
2.2.1. SDSS photometric system 18
2.3. Common fi elds 19
2.3.1. Common stars 20
2.4. Determination of the limiting apparent magnitudes 21

3. Basic theory and theoretical data **25**
3.1. A schematic illustration of the Modus Operandi 25
3.2. Chemo-dynamical galaxy model 28
3.2.1. Code 28
3.2.2. The special model S10 34
3.3. Stellar evolutionary tracks: Padova94 43
3.4. Stellar spectral libraries 49
3.4.1. BaSeL 3.1 49
3.4.2. White dwarfs 53
3.4.3. Planetary nebulae 54
3.4.4. Resulting parameter range of BaSeL 3.2 57
3.4.5. PHOENIX 58

4. Derived theoretical data **61**
4.1. Simulations of theoretical stellar populations and surveys 61
4.1.1. Drawing the stars 61
4.1.2. Atmospheric parameters 64

4.1.3. Synthetic spectra, magnitudes and colours . . . 69
4.1.4. Catalogue of resulting intrinsic parameters . . . 70
4.2. Theoretical stellar populations . . . 71
4.2.1. Single populations with a Salpeter-IMF . . . 71
4.3. Theoretical stellar sample: Gaia . . . 84
4.3.1. Description of the theoretical stellar sample . . . 84
4.3.2. Short excursus: Dependency of the detectability . . . 84
4.3.3. Detectability of the Gaiasphere . . . 86
4.3.4. Stellar fractions depending on limiting apparent magnitudes . . . 89
4.3.5. The three major components of the Gaiasphere . . . 90
4.4. Theoretical stellar surveys . . . 97
4.4.1. Galactic anticentre (SA94) and Galactic centre (SA107) fields . . . 97
4.4.2. Stellar distribution using appropriate isochrones . . . 98
4.4.3. Stellar distributions resulting from different IMFs . . . 102

5. Comparisons of theory and observations 113
5.1. Basel survey fields . . . 113
5.1.1. The effects of extracting a certain number of stars . . . 113
5.1.2. Comparison of only a small part of the $G-R$ colour distribution . . . 116
5.1.3. Comparison of two colours in the same viewing direction (SA94) . . . 117
5.1.4. Comparison of the $U-G$ colour distributions in different viewing directions . 117
5.1.5. Comparison of the BaSeL 3.2− and the PHOENIX stellar spectral libraries . . 119
5.2. SDSS survey fields . . . 120

6. Summary and Conclusions 135
6.1. Success . . . 135
6.2. Problems and uncertainties . . . 136
6.2.1. Chemo-dynamical galaxy model . . . 136
6.2.2. Stellar evolutionary tracks and synthetic photometry . . . 137
6.2.3. Observational data . . . 137
6.3. Future work . . . 138
6.4. Final thoughts . . . 139

Bibliography 141

Acknowledgements 147

Declaration 149

Curriculum vitae 151

A. Appendix: Comparisons 153
A.1. Comparison: BaSeL 3.2 - PHOENIX . . . 153
A.2. Comparison: NLTE and LTE structure of PHOENIX . . . 157

B. Appendix: Publications **159**
B.1. Public outreach 159
B.2. Scientifi c publications 162

C. Appendix: My life at the Astronomical Institute of Basel **187**

List of Figures

1.1. The Nebra sky disk is dated to 1600 BC. Its golden symbols are interpreted as a Sun or full moon, stars (including even a cluster interpreted as the Pleiades) and a crescent moon, as well as the Sun boat with many oars. 1
1.2. Latitude distribution of the Basel Halo Program fields, projected onto the meridional plane through the Sun and the Galactic centre (Becker 1965). 3
1.3. Two-colour diagrams of the Selected Area 51 for two G apparent magnitude ranges, viz. $G \in$ (15.0,16.0) and $G \in$ (18,18.5). The halo stars (open circles) and disk stars (black dots) show quite different behaviour and can therefore be separated (Becker 1972). 4
1.4. Lines of equal space density for halo stars in a plane perpendicular to the Galactic plane. All data are based on three-colour photometry using plates taken with the 48-inch Palomar Schmidt telescope (Becker 1972). 4
1.5. Mean isodensity pattern and z-scale heights for halo main sequence stars with apparent magnitudes of $4.0 < m_G < 5.0$. 5
1.6. Eleven fields of the Basel Halo Program with the lines of equal mean metal abundances of F– and G-type stars (Trefzger 1981). 6
1.7. $G-R$ colour distribution for the New Basel halo field M101. The curves 1 and 2 stand for Galactic models including, respectively, not including a thick disk (Buser, Rong & Karaali 1998). 9
1.8. The shapes of the appropriate luminosity functions of each stellar component (Buser, Rong & Karaali 1998). 10
1.9. Our work is considered a further branch (in green) of the big Basel Halo Program-taxonomy. 11

2.1. Viewing directions of all fourteen fields of the new Basel High-Latitude Survey, mapping (approximately) a meridional cross-section of the Milky Way. 15
2.2. Filter functions of the photometric RGU system (in blue) plotted over two spectra that differ only in metallicity. The metal-richer star (green spectrum) has colours of $U-G$ = 2.10 and $G-R$ = 1.36, whereas the metal-poorer star (red spectrum) has colours of $U-G$ = 1.47 and $G-R$ = 1.31. 16
2.3. Sky coverage of the SDSS Data Release 3 in equatorial coordinates (Abazajian et al. 2005). (Note that it wraps at α = 300° = 20^h.) 17
2.4. Filter functions of the Sloan Digital Sky Survey (Jordi, Grebel & Ammon 2005). . . . 18
2.5. Common fields of the two surveys: SA94, M101, SA107. 19

2.6. The generalised histogram of the apparent G-magnitudes of all Basel stars (green) together with the generalised histogram of the transformed apparent G-magnitudes of all SDSS stars (red) in field M101. The blue line indicates the limiting apparent G-magnitude of the Basel survey. 20
2.7. Apparent U, G and R distributions of all the stars in the Basel survey field SA107. The green lines indicate the limiting apparent magnitudes. 21
2.8. Apparent magnitude distributions: generalised histograms of the U, G and R apparent magnitudes of all the stars in the Basel survey field M101. The blue lines indicate the limiting apparent magnitudes. 22
2.9. Apparent magnitude distributions: generalised histograms of the U, G and R apparent magnitudes of all the stars in the Basel survey field SA94.The magenta lines indicate the limiting apparent magnitudes. 22

3.1. Modus Operandi: the main ingredients and their outputs in their respective order of application (from top to bottom). 26
3.2. A cut through a 100 Mpc x 100 Mpc section of a ΛCDM universe. Bright regions mark the high density halos in which the galaxies form (Immeli 2003). 28
3.3. Components and interaction network of the chemo-dynamical model (Immeli 2003) (modified by K. Ammon). 29
3.4. V-band evolution of a collapse− and an accretion model, face-on and edge-on (Westera et al. 2002). From top to bottom, the images show a time sequence starting at an age of 2.5 Gyr after the Big Bang and ending at the present epoch, i.e. 13.5 Gyr. The most prominent features of these two galaxy types do not appear at the same point in time: for instance, the bar develops much earlier in the collapse model than in the accretion model, at z = 1.07, as opposed to z = 0.49. 31
3.5. The position of the observer (the Sun) and the different viewing directions in the galaxy model. In the upper panel, the galaxy is seen at an inclination of 30 degrees, whereas the lower panel shows the galaxy edge-on. 33
3.6. Morphology of the theoretical model galaxy S10, observed in the V-band in the upper− and in the I-band in the middle panels, respectively. In the lower panels the (not observable) stellar mass surface density distribution is plotted. First column face-on, second edge-on. 34
3.7. Rotation curve of S10. The black curve represents the orbital speed of the disk stars as a function of the distance to the centre of the galaxy, the orange line represents the rotation curve of the galactic disk (HII gas). 36
3.8. Rotation curve of the Milky Way. Filled squares represent the observed large-scale interstellar HI gas rotation curve (Vallee 1994). 37
3.9. Theoretical surface density profiles of the baryonic matter in orange and the dark matter in green. The sum of the two is plotted in black. 37
3.10. Star formation rate of S10 (left) and of the Milky Way (right). The Milky Way SFR is derived from age distributions given by Twarog (1980, filled circles) and Barry (1988, histogram), Figure taken from Noh & Scalo (1990). 38
3.11. Stellar mean age at redshift z = 0 of disk stars (blue), halo stars (magenta) and all stars (black). 40

3.12. Overview of the age-metallicity distribution in our Galaxy. For each Galactic component the bulk properties and approximate ranges are plotted (Buser 2000). 40
3.13. The age-metallicity distribution and the average metallicity of the stellar particles in an accretion model galaxy. 41
3.14. Metallicity distribution of the stars (black), gas (red) and clouds (blue) of S10. 42
3.15. Hertzsprung-Russell diagrams. Left panel: the evolutonary tracks of a 3 $M_{\odot}-$ and a 60 $M_{\odot}$ star are plotted and labeled with all important evolutionary phases that these stars go through during their lifetimes. Right panel: same as in the left panel, but for stars with lower metallicities. The "blue loops" are indicated. 44
3.16. A set of stellar evolutionary tracks for all masses avaliable at the subsolar metallicity $[\mathrm{Fe/H}]$ = -1.646 in Padova94. 44
3.17. A set of stellar evolutionary tracks for all masses avaliable at solar-like metallicity ($[\mathrm{Fe/H}] \sim 0.0$) in Padova94. 46
3.18. A set of stellar evolutionary tracks for all masses avaliable at the supersolar metallicity $[\mathrm{Fe/H}]$ = 1.01 in Padova94. 46
3.19. Two sets of stellar evolutionary tracks at different metallicities ($[\mathrm{Fe/H}]$ = -1.646 in the upper– and $[\mathrm{Fe/H}]$ = 0.0 in the lower panel, respectively), enhanced by Bruzual & Charlot (2003). 47
3.20. Parameter coverage of the BaSeL 2.2 library (Lejeune, Cuisinier & Buser 1998). . . . 50
3.21. Illustration of the calibration algorithm: The algorithm developed by LCB97 changes the shapes of the model spectra to reproduce empirical colours (Westera 2001). 51
3.22. BaSeL 3.1 spectra of our Sun and Vega. 52
3.23. White dwarf stars in the globular cluster M4 as seen from a ground-based telescope (left) and by the Hubble Space Telescope (right). 53
3.24. Theoretical stellar spectra of a white dwarf with T_{eff} = 85'000 K and $\log g$ = 8.0 in two different units. Left panel: [erg/s/cm^2/cm], right panel: [erg/s/cm^2/Hz/sr]. 54
3.25. A composite colour Hubble image of NGC 6751. 55
3.26. Original (black) – and rebinned (red) Rauch (2003) spectrum of a central star of a planetary nebula with T_{eff} = 140'000 K (see NGC 6751) and $\log g$ = 8.0. 56
3.27. Central star spectrum of a planetary nebula with T_{eff} = 140'000 K (see NGC 6751) and $\log g$ = 8.0 including the extension in the optical and near-IR. 56
3.28. Parameter coverage of the final combined BaSeL 3.2 library. Produced by D. Cerrito. . 57
3.29. The variation of the stellar energy distribution of a 3'000 K model star with decreasing α-element abundance (compared to the solar value: $[\alpha/\alpha_{sun}]$ = -0.2). The difference spectra are shown in the lower part of the panel, illustrating the effects of α-element abundances (Brott & Hauschildt 2005). 59
3.30. Variation of the effective temperature in a model with constant metallicity and surface gravity. 60

4.1. From the position of the Sun, we observe the model sky in a certain viewing direction and field size (cyan cone). In this viewing cone, we choose some of the included stellar particles (coloured circles) and dissolve them into individual stars (green triangle). According to the applied IMF individual stars are selected with mass-dependent probabilities. 61

4.2. Left panels: Two pairs of tracks corresponding to neighbouring masses in the age versus luminosity plane: two low-mass stars ($M_* = 0.9\ M_\odot$ and $M_* = 0.8\ M_\odot$) in the upper panel and two higher mass stars ($M_* = 40.0\ M_\odot$ and $M_* = 30.0\ M_\odot$) in the lower panel. Right panels: H-R diagrams for a 0.8 $M_\odot$ (upper panel) and a 40.0 $M_\odot$ (lower panel) star. 65
4.3. The three main steps of the interpolation routine applied to low-mass stars. In red the three parameters provided by the Samland code are given. In black, those of the Padova94 library. Highlighted in blue and green are the resulting interpolated parameters. 66
4.4. Interpolation by inverse distance weighting in $T_{\rm eff}$ (upper panel) and $\log g$ (lower panel) for a stellar mass of 1.18 $M_\odot$. 67
4.5. Luminosity evolutions of four different high-mass stars (a 20 $M_\odot-$ (in blue), a 40 $M_\odot-$ (in red), a 60 $M_\odot-$ (in green), and a 100 $M_\odot$ star (in black)), all with $[\mathrm{Fe/H}] = 0.0$. See also Figure 4.2 (lower panel). 68
4.6. Filter functions of the Sloan Digital Sky Survey (left) and of the New Basel high-latitude field star survey plotted (right) (Jordi, Grebel & Ammon 2005). 69
4.7. Stellar initial mass distribution of the theoretical populations. The blue line indicates the Salpeter-IMF, $\log(\xi) \propto \log(\mathcal{M}^{-1.35})$. 71
4.8. Mass-colour relations of the Population P_{008} at an age of 5 Gyr. The blue lines indicate the upper and lower limits of a colour bin of width given in Tab. 4.7. 73
4.8. Mass-colour relations of the Population P_{008} at an age of 5 Gyr. The blue lines indicate the upper and lower limits of a colour bin of width given in Tab. 4.7 (continued). . . . 74
4.9. Evolution of the $u-g$ colour distribution of the population P_{008}. 75
4.10. Evolution of the $g-z$ colour distribution of the population P_{008}. 76
4.11. Left panel: M_g, $u-g$ colour-magnitude diagram of the population P_{008} at the age of 0.1 Gyr. Shown in colour are the two bins, where the peaks in the star counts appear ($0.8 \leq u-g < 1.0$ in yellow $1.0 \leq u-g < 1.2$ in orange). The line represents main sequence stars exclusively. Right panel: M_g, $g-z$ colour-magnitude diagram of the population P_{008} at the age of 0.1 Gyr. 77
4.12. Positions of DA white dwarfs (hatched area) in a two-colour diagram, which clearly deviate from the black-body line (bb line, Weidemann (1971). Lower right: H^- absorption, strongest in red, shifts the flux to the blue and the ultraviolet (dashed arrow). . 78
4.13. The same colour-magnitude diagram as in the left panel of Figure 4.11, but additionally the positions of the three examined stars are marked in black. 78
4.14. Spectral energy distributions of the three examined stars. The response filter functions of the $u-$ and $g-$ bands are added in blue. 79
4.15. Absorption coefficients per unit electron pressure compared at unit optical depth in a solar model photosphere (Gray 1992). The whole absorption is dominated by the H^- ion. 80
4.16. $u-g$ colour distributions of the Population P_{004} (left plots) and P_{008} (right plots) at an age of 10, resp. 12 Gyr. 80
4.17. Colour distributions of different populations at the age of 0.1 Gyr. The bins crosshatched in blue are populated by young stars with low metallicities ($Z < 0.004$) only. 82
4.18. Colour distributions of the populations P_{05} (upper panels), P_{008} (middle panels) and P_{0001} (lower panels) at ages 0.1 and 12 Gyr, respectively. The coloured bin contains only metal-rich ($Z = 0.05$) stars. 83

4.19. Main sequence stars brighter than the apparent V-magnitude of 20.0 (crosses: $[\mathrm{Fe/H}] = 0.09$; black dots: $[\mathrm{Fe/H}] = -0.33$; open circles: $[\mathrm{Fe/H}] = -1.65$). 84
4.20. Spectra of two stars of the same initial mass ($M_* = 1 M_\odot$) and age (3 Gyr), but different metallicities ([Fe/H] = -1.65 in black, [Fe/H] = -0.33 in blue, respectively. In green: The filter response function of the Johnson V-band. 85
4.21. Spectra of two stars of the same T_{eff} and $\log g$, but different metallicities ($[\mathrm{Fe/H}] = -1.65$ in black, $[\mathrm{Fe/H}] = 0.0$ in blue, respectively. In green: The response filter function of the Johnson V-band. 86
4.22. Star counts of the Gaiasphere depending on limiting apparent magnitudes. Left: Mass distributions. Right: Corresponding HR-diagrams. Top row: Full sample; second row: $m_v \leq 22.0$; third row: $m_v \leq 19.0$; fourth row: $m_v \leq 16.0$. 87
4.23. Star counts of the Gaiasphere depending on limiting apparent magnitudes. Left: Age distribution. Right: [Fe/H] distribution. Top: Full sample; second row: $m_v \leq 22.0$; third row: $m_v \leq 19.0$; fourth row: $m_v \leq 16.0$. 88
4.24. Age-metallicity diagram of a simulated field of the Gaiasphere in the viewing direction towards the Anticentre. Left panel: all stars in this direction, right panel: only stars with a V-magnitude ≤ 18.0. 88
4.25. Star fractions as functions of metallicity and distance (panels a, b), and limiting magnitudes (dotted, dashed, and full line). The dotted line stands for $m_v \leq 22.0$, the dashed line for $m_v \leq 19.0$ and the full line for $m_v \leq 16.0$. 89
4.26. Star fractions with a limiting apparent magnitude of $m_v \leq 18.0$ as functions of age and in different viewing directions (left panel towards the galactic centre, middle towards the halo and right panel towards the galactic anticentre. 90
4.27. Left: Colour-magnitude diagram of the Gaiasphere stellar distribution for different metallicities (green stars: $[\mathrm{Fe/H}] \leq -1.19$ (halo stars), red dots: $[\mathrm{Fe/H}] \geq -0.46$ (thin disk stars), black dots: thick disk stars with $-1.19 < [\mathrm{Fe/H}] < -0.46$). Right: Corresponding star counts, in green the halo stars, in black the thick disk−, and in red the thin disk stars. 91
4.28. Stellar metallicity as a function of the distance from the Sun of the 'Gaiasphere population stars': in green halo−, in black thick disk−, and in red thin disk stars. 92
4.29. Stellar ages as functions of the radial distances to the galactic centre. Plotted in green are the halo-, in black the thick disk- and in red thin disk stars. 92
4.30. Radial distances from the galactic centre as functions of the z-distances of stars of the three components, highlighted in different colors (thin disk stars: red dots, thick disk stars: black dots and halo stars: green stars). 93
4.31. Closeup view of the Galactic disk and halo structure perpendicular to the Galactic plane (Buser 2000). Note that the colours do not correspond to the code of the earlier Figures 4.27 - 4.30. 94
4.32. Upper two panels: rotational velocities (left panel) and vertical velocities (right panel) as functions of vertical distances of the three stellar components, highlighted in different colours (thin disk stars: red dots, thick disk stars: black dots, and halo stars: green stars). Lower Panel: the radial velocities versus vertical velocities of all three components. 95

4.33. Positions of the bulge-sphere halo stars (upper left panel) and the halo stars outside the sphere (lower left panel) in the z-distance - radial distance plane, marked in green. The two right panels show the positions of the bulge-sphere halo stars (upper panel) and the halo stars outside the sphere (lower panel) in the v_z - v_{rot} plane, marked in green. . . . 96
4.34. H-R diagrams and the corresponding stellar distributions for two different viewing directions (left: SA94, right: SA107). . . . 97
4.35. Colour-magnitude diagram of the globular cluster NGC 288 (black dots) with a fitting theoretical isochrone (red line) produced by J. Clem. . . . 98
4.36. Left panel: Colour-magnitude diagram of the stars in the halo field SA94. Right panel: Isochrones of single stellar populations of the same age (4.5 Gyr), but different metallicities. . . . 99
4.37. Isochrones and the halo population in a colour-magnitude diagram. . . . 99
4.38. Isochrones of 20 single stellar populations of different ages (0.5, 1.5, 4.5 and 6.5 Gyr) and metallicities ($[\mathrm{Fe/H}]$ = -2.0, -1.0, -0.5, 0.0 and +0.5). . . . 100
4.39. Left panel: The age-metallicity degeneracy as visualised by Worthey (1999). Right panel: The age-metallicity degeneracy visualised by Wenger (2005). . . . 101
4.40. The Abstract of Salpeter's famous paper "Luminosity Function and Stellar Evolution" (Salpeter 1955). . . . 102
4.41. The Salpeter-IMF, normalized to a total mass of 1 $M_{\odot}$. . . . 102
4.42. The logarithm of the stellar luminosity function ϕ as a function of the visual magnitude, M_v (*total* = all stars, *m.s.* = main-sequence stars only) (Salpeter 1955)). . . . 103
4.43. Various IMFs, all normalized to a total mass of 1 $M_{\odot}$ (Wenger 2005). . . . 104
4.44. The two stellar Initial Mass Functions used to generate the two different model galaxies: the Kroupa-IMF in blue and the Salpeter-IMF in red. In the upper panel the Initial Mass Functions (ξ) are plotted on a linear scale, whereas $\mathcal{M}_{tot} = \int_{\mathcal{M}_{0.1}}^{\mathcal{M}_{50.0}} \cdot c \cdot \mathcal{M}^{-x} \cdot d\mathcal{M} = 1 M_{\odot}$. In the lower panel both IMFs are shown on a logarithmic scale. Figure produced by P. Westera. . . . 106
4.45. Stellar U-G distributions (field SA94) of a galaxy with a Kroupa-IMF (left panel) and a Salpeter-IMF (right panel). . . . 107
4.46. The positions of **main sequence**−, giant−, and white dwarf stars in the Hertzsprung-Russell diagrams of the three viewing directions are plotted. In the left panels, the stellar distributions of the Salpeter-galaxy are shown and in the right panels those of the Kroupa-galaxy. . . . 109
4.47. The positions of **main sequence**−, giant−, and white dwarf stars in the two-colour diagrams of the three viewing directions are plotted. In the left panels, the stellar distributions of the Salpeter-galaxy are shown and in the right panels those of the Kroupa-galaxy. 110
4.48. Colour-magnitude diagrams of two different viewing directions in the Kroupa-galaxy. . 111

5.1. The stellar initial mass distributions of the 100' 000 stars sample (left panel) and the 10' 000 stars sample (right panel), respectively. The blue curve marks the Salpeter(1955)-IMF. . . . 113

5.2. HR-diagrams (upper panels) and $G-R$ colour distributions (lower panels) of two theoretical stellar samples towards the anticentre (SA94), both with applied limiting apparent $G-$ and $R-$ magnitude, plotted in red. The two left plots are produced with a sample of 100'000 stars, whereas the right panels show the HR-diagram and star count of a sample of only 10'000 stars in red (normalised to the total number of stars in the corresponding field of the survey). The observed $G-R$ colour distribution towards the Galactic anticentre is plotted in black in the lower two panels. 114
5.3. CMDs (upper panels) and $G-R$ colour distributions (lower panels) of the same theoretical stellar sample towards the anticentre (SA94) plotted in red. In the left panels all 100'000 theoretical stars are plotted, whereas in the right panels only theoretical stars in a certain colour range ($1.0 \leq G-R \leq 2.0$) are taken into account. The observed $G-R$ colour distribution towards the Galactic anticentre is plotted in black in the lower two panels. 116
5.4. $U-G$ (left panel) and $G-R$ (right panel) colour distributions towards the Galactic anticentre (field SA94). In black the colour distributions of the Basel survey data are shown and in red the ones of the model galaxy. 117
5.5. Stellar $U-G$ colour distributions towards the Galactic anticentre (SA94). In black the colour star counts of the Basel survey data are shown, and in red the corresponding colour distributions of the model galaxy. 118
5.6. As in Figure 5.5, but towards the inner Galaxy (SA107, upper panel) and the outer Galactic halo (M101, lower panel). 118
5.7. Stellar $G-R$ colour distributions towards the outer Galactic halo (M101). The left panel shows the distribution obtained with the BaSeL 3.2 stellar spectral library (in red) and the right panel the one using the PHOENIX stellar spectral library (in blue), respectively. In black the colour star count of the Basel survey data is shown. 119
5.8. Mass distributions of all stars of the theoretical data set (in black) towards SA94. Shown in colours are the distributions of the stars resulting from the cuts at the limiting apparent magnitudes (with the limiting magnitudes of the SDSS in the left$-$ and of the Basel survey in the right panel). 120
5.9. $u-g$ colour distribution of the theoretical stellar sample towards the anticentre (SA94) in red, and of the observed SDSS data in black. Both after applying the limiting apparent $g-$ and $u-$ magnitudes. The hatched bins (in colour) are the two most populated colour bins. 121
5.10. Distribution of the theoretical stellar sample towards the Galactic anticentre in five different diagrams: a) mass – metallicity-, b) mass – age-, c) mass – distance-, d) mass – surface gravity - and e) mass – effective temperature. In green, all stars with $u-g$ colours between 0.8 and 1.0 are highlighted, and in orange, all stars with any colours between 1.0 and 1.2. The rest of the stars are shown as black dots. 122
5.11. Stellar colour distributions in all SDSS colours towards the Galactic anticentre. In each panel, the observed distribution is shown in black, and in red the theoretical one. 123
5.12. Left panel: $T_{\rm eff}$ versus $\log g$ of all the stars that populate the most overcrowded bins in each colour. Right panel: $stellar\ mass$ versus age of the same stars as in the left panel. 124
5.13. Stellar mass - distance diagrams of the sample as limited in all four SDSS colours. The black dots show the full theoretical stellar sample towards the galactic anticentre (field SA94), the coloured stars the limited ones. 125

5.14. A two-colour diagram ($g-r$ versus $u-g$) of the observed SDSS stars (plotted in black), of the limited theoretical model stars (red) towards the Galactic anticentre, and of all the stars that are included in the entire Basel 3.2 stellar spectral library (orange). . 126
5.15. A two-colour diagram ($g-r$ versus $u-g$) of the objects classified as quasars (in green) and the residual SDSS objects (in black) of the observed stellar sample towards the Galactic anticentre. 126
5.16. Two-colour diagram of all SDSS objects towards the Galactic anticentre. The objects classified as quasars by Richards et al. (2002) are plotted in magenta. In orange the appropriately limited BaSeL 3.2 spectral library and in blue the quasars of the second edition of the Sloan Digital Sky Survey Quasar Catalog are plotted. In black the observed SDSS stars in the field SA94 are shown. 127
5.17. The red lines highlight the region in the two-colour diagram within we define all stars as quasars. 128
5.18. In the left panel, the objects classified by us as uncertain are shown. In the right panel, the reduced SDSS sample, that is the sample of all objects classified as real stars, towards the Galactic anticentre is plotted. 128
5.19. Magnitude errors for all stars (in black) and for the ones with restricted magnitude limits (in orange). 129
5.20. Star counts in the $u-g$-colour towards the Galactic anticentre: the observed distribution is shown in black, and in red the theoretical one. In the left panel the "raw" theoretical distribution is shown, whereas in the right panel the one without the "assumed model quasars" and added observational errors is plotted. 130
5.21. Star counts in the $g-r$-colour towards the Galactic anticentre: the observed distribution is shown in black, and in red the theoretical star count. In the left panel the "raw" theoretical distribution is shown, whereas in the right panel the one without quasars and added observational errors is plotted. 130
5.22. A two-colour ($i-z$ versus $r-i$) diagram of the observed SDSS stars (in black) and the limited theoretical stellar sample (red) towards the Galactic anticentre, and of the entire Basel 3.2 stellar spectral library (orange). 131
5.23. As in Figure 5.22, but with the BaSeL 3.2 colours transformed from the Johnson-Cousins– to the SDSS system, added in blue. 131
5.24. As in Figure 5.23, but for the $g-r$ versus $u-g$. 132
5.25. As in Figure 5.23, the two-colour ($i-z$ versus $r-i$) diagram of the observed SDSS stars (in black) and the limited theoretical stellar sample (red) towards the Galactic anticentre, and two times of the entire Basel 3.2 stellar spectral library, once of the original one (orange) and once of the transformed one (blue). In green the transformed model stars are shown. 132
5.26. As in Figure 5.25, but additionally fiducial relations (black lines) are added. 133
5.27. Left panel: As in Figure 5.25. Right panel: The transformed BaSeL 3.2 colours (in blue) together with the synthetic photometry of the entire BaSeL 3.2 library using three different zeropoints: $zp_{(i-z)}$ = 0.17 (orange), $zp_{(i-z)}$ = 0.07 (green) and $zp_{(i-z)}$ = 0.27 (cyan). 134
5.28. As in Figure 5.25, but additionally the outer limits of the error ranges (cyan) are drawn in. 134

A.1. Comparison of BaSeL 3.2– and PHOENIX $U-B$ colours in the $T_{\rm eff}$ – $logg$ plane. The colour code of the differences works as follows: red = 1.0 mag, orange = 0.6 mag, green = 0.2 mag, and blue = -0.2 mag difference. 154
A.2. Comparison of BaSeL 3.2– and PHOENIX $B-V$ colours in the $T_{\rm eff}$ – $logg$ plane. . . 155
A.3. Comparison of BaSeL 3.2– and PHOENIX $V-R$ colours (left panel) and $V-I$ colours (right panel), respectively, in the $T_{\rm eff}$ – $logg$ plane. 155
A.4. Comparison of BaSeL 3.2– and PHOENIX $V-K$ colours (left panel) and $R-I$ colours (right panel), respectively, in the $T_{\rm eff}$ – $logg$ plane. 156
A.5. Comparison of BaSeL 3.2– and PHOENIX $I-K$ colours (left panel) and $J-H$ colours (right panel), respectively, in the $T_{\rm eff}$ – $logg$ plane. 156
A.6. Comparison between NLTE and LTE structure of PHOENIX solar NLTE models. τ_{std} is the optical depth in the continuum at 1.2 μ. 157
A.7. Comparison between NLTE and LTE structure of PHOENIX Vega NLTE models. τ_{std} is the optical depth in the continuum at 1.2 μ. 157

C.1. All members of the Astronomical Institute in front of the Dome in March 2006. 187
C.2. The Buser group (from the left to the right): Erich Wenger, Thibault Lejeune, Roland Buser, Pieter Westera and my humble self. 187
C.3. Being astronomer, a job for women (included here are our two secretaries). 188
C.4. Excursion by institute members to the Papiliorama in Kerzers in June 2006 (only few are visible here). 188
C.5. Demonstrations against the closing of the Institute in March 2004. 189
C.6. Old Emma, the 20 cm refractor telesope of the Astronomical Institute of Basel. 190

List of Tables

1.1. Resulting model parameters of the first three comparisons 8

2.1. Properties of the RGU-passbands 17
2.2. SDSS filter parameters 18
2.3. Common fields: Galactic coordinates and field sizes 19
2.4. The limiting apparent magnitudes of all three Basel survey fields in both filter systems. 23
2.5. Number of all stars measured in the two surveys. 23

3.1. Stellar properties provided by Padova94 43
3.2. Metal abundance in *Z* and [Fe/H] 45

4.1. Main parameters delivered by the Samland model. 62
4.2. Dynamical parameters delivered by the Samland model. 63
4.3. Chemical parameters delivered by the Samland model. 63
4.4. Dynamical parameters at the date of birth delivered by the Samland model. 63
4.5. The first four columns of a Padova1994 track directory 64
4.6. Masses $M_{\odot}$ of the track directory with Z = 0.020 (i. e., $[\mathrm{Fe/H}] = 0.0$) 64
4.7. Bin widths depending on colours 72
4.8. Parameters of the three stars 77
4.9. Number of main sequence stars ($> 0.6 M_{\odot}$) during the evolution of the SSPs 81
4.10. Mean metallicities of the Galactic components 91
4.11. The Salpeter (1955) IMF 105
4.12. The Kroupa (2001) Universal IMF 105
4.13. Mass ratios 107
4.14. Stellar distributions towards the inner Galaxy (SA107), the outer Galaxy (M101) and the Galactic anticentre (SA94). 107
4.15. Stellar distributions towards the inner Galaxy (SA107), the outer Galaxy (M101) and the Galactic anticentre (SA94). 108

5.1. Star counts and applied factors 115

A.1. Comparison of the main characteristics of the two synthetic libraries 153

1. Introduction

1.1. Astronomy and earlier work on the determination of the Galactic structure

Human curiosity and passion forced human beings from the dawn of mankind to observe the regular patterns of the motions of visible objects in the sky.
A proof of this ancient tradition can be found in the Nebra sky disk, probably the oldest illustration of the cosmos (Figure 1.1). It is a metal plate of around 30 cm diameter that has even been associated with the Bronze Age. Our ancestors working in astronomy as probably the oldest natural science on earth have sought for an order in the Universe and tried to grasp the essence of the rules underlying that order and thereby to find answers to the great questions of existence.

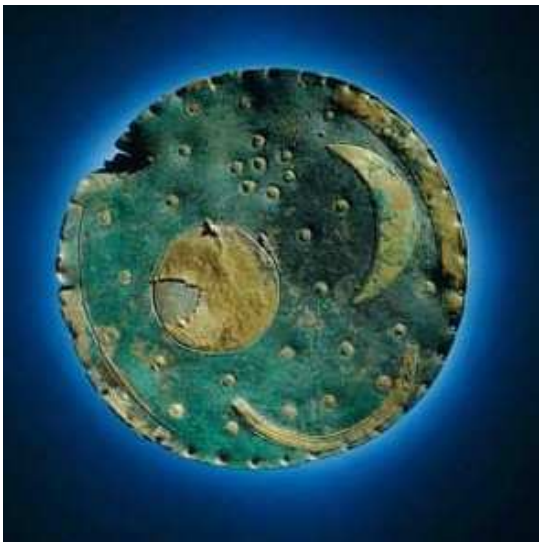

FIGURE 1.1.: The Nebra sky disk is dated to 1600 BC. Its golden symbols are interpreted as a Sun or full moon, stars (including even a cluster interpreted as the Pleiades) and a crescent moon, as well as the Sun boat with many oars.

After thousands of years of cultivated astronomy, the used technology has evolved like the wind, but curiosity, passion, and the basic way of working in this discipline are still the same: working in a framework of understanding, extending and refining that framework through analysis of observations

with state-of-the-art instruments and testing the framework's boundaries, still with the goal of achieving a more consolidated knowledge about the rules of nature and our existence.

The framework outlining this study is based on knowledge and ideas from previous studies and recent observations.
The latter indicate that the main body of our luminous Galaxy consists of at least five major components: an essentially rotationless spheroidal halo, three coplanar disks (a thick, a thin, and an extreme disk), and a bar-like bulge – the central concentration of luminous matter. All of these elements differ in density, flattening and rotation speed (Buser 2000).
This current understanding of the large-scale space and luminosity distributions of the stars in the Milky Way is based on investigations and experiences that started here in Basel already forty years ago.
In this subsection, we show how the picture of the Galactic structure has evolved since the pioneering work of Becker (1965), and how our work can be deemed a logical continuation of this scientific heritage.
For a historical overview, we have a look at Becker's and succeeding studies, all of which were related to the Basel Halo Program. In this brief scientific outline, the most important links to this work are embedded.

With the photometric analysis of faint stars and stellar populations in Kapteyn's Selected Area No. 51 in the mid-sixties, **Becker (1965)** set the stage for the Basel Halo Program, a long-term project with the objective of mapping the density structure in the halo of the Milky Way.
In those days, the Milky Way system was believed to consist of mainly two distinct stellar types belonging to two different components of the Galaxy: the young and metal-rich population I located in a disk-like neighbourhood embedding Galactic equator plane, and the old and metal-poor population II, distributed with much lower space densities within a halo-like, slightly flattened sphere around the Galactic centre. The dominant features of the disk (spiral arms and their fragments) and some quantitative indications of its scale-height and scale-length of its density distribution were already known.
By contrast, the knowledge about the density structure of the halo was poorer at that time and based on the assumption that the density was roughly symmetrical with respect to the Galactic polar axis (stellar distribution in concentric surfaces of equal density, possibly ellipsoids with the Galactic nucleus as the centre (Becker 1972)), without showing any dominant features. To get more information about the stellar density distribution of the Galactic halo, Becker initiated

the Basel Halo Program.

The Basel Halo Program mapped the density structure in the halo of our Galaxy by observing in the RGU filter system fifteen small intermediate-to-high latitude (halo) fields distributed systematically near a meridional plane of the Galaxy (Becker 1946, 1965). The galactic latitudes of the selected fields are displayed in Figure 1.2.

Given the way these fields are distributed over the sky (in a plane perpendicular to the Galactic disk, containing the Galactic centre and the Sun, see Figure 1.2), the analysis of the photometric data in these test-directions should reveal some of the large-scale properties of a representative cross section of the halo. The derived density gradients along the directions to the stellar fields should allow the determination of halo-isodensity lines in the meridian, engendering the corresponding halo-isodensity surfaces by rotation around the Galactic polar axis, should the rotational symmetry be confirmed.

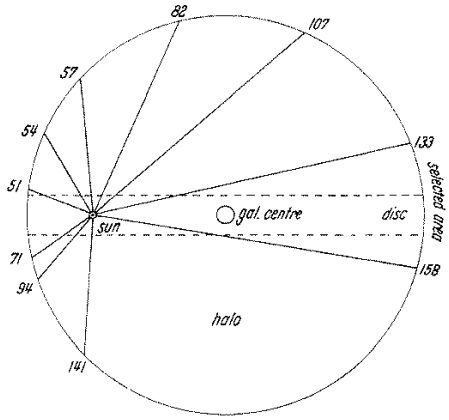

FIGURE 1.2.: Latitude distribution of the Basel Halo Program fields, projected onto the meridional plane through the Sun and the Galactic centre (Becker 1965).

According to this rough picture of the Galactic structure (population I in the disk, population II in the halo), all halo fields should consist of both populations (even though the disk-fraction in the corresponding lines of sight is small). Before investigating all stars, a separation into halo and disk stars was necessary. In addition to that, a procedure for assigning absolute magnitudes and distance moduli to the halo stars had to be developped.
For both tasks, Becker (1965) established methodical solutions that were applied homogeneously to all fifteen fields. He based the segregation into halo and disk stars on a purely photometric classification of stellar populations: The pronounced metallicity sensitivity of the $U-G$ colour allows a statistical separation of the metal-poor(er) halo stars from the metal-richer Galactic disk stars through analysis of the stellar distributions in the $U-G$ vs. $G-R$ two-colour plane (see Figure 1.3). The deficiency of metals in the atmospheres of the halo stars leads to a deblanketing that lifts the metal-poor(er) halo stars above and to the right of the late branch of the (metal-rich) disk main sequence in the two-colour diagram, along their deblanketing vectors (UV-excess) [1]. Those effects in the intensity distributions of halo stars were kept in mind, when the RGU system was defined, even though this particular UV-excess was not yet known at that time (Becker 1946). Calculations of the blanketing effects in the RGU photometric system by Smith & Steinlin (1964) confirmed many years later the ability of the RGU system to separate halo from disk stars.

The absolute magnitudes of the halo stars were found by shifting the stars in the two-colour diagram back to the main sequence along the direction of its (de-)blanketing vector. Each intersection point provided the appropriate value for the absolute magnitude (Becker 1972). The medium– and late-type giants were recognised as giants from their positions in the two-colour diagram, where they form a separate group. Becker (1972) assumed a common mean absolute magnitude of about 1.0 in the G-band. By means of the distance modulus each star was then given its appropriate distance.
After applying these two methods, Becker (1972) established the density functions for given intervals of absolute magnitude in different viewing directions [2].

[1] For more details about this method see Fenkart et al. (1987).
[2] With a limiting apparent G-magnitude of 19.5, the survey extended to distances up to 14.0 kpc for the intrinsically brightest halo stars (Becker 1972).

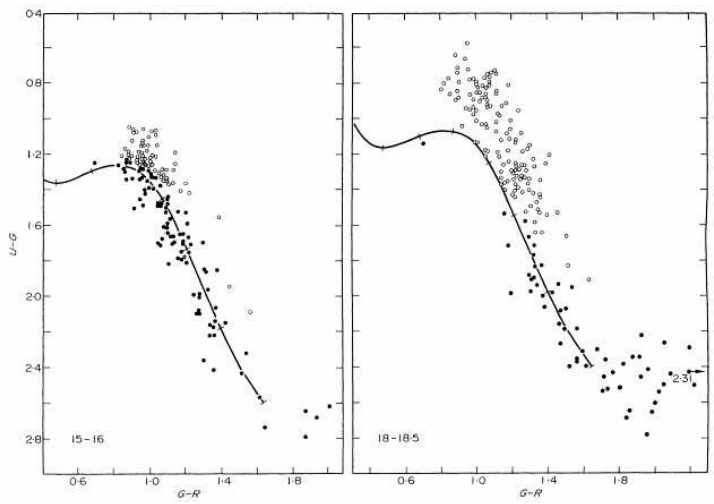

FIGURE 1.3.: Two-colour diagrams of the Selected Area 51 for two G apparent magnitude ranges, viz. $G \in$ (15.0,16.0) and $G \in$ (18,18.5). The halo stars (open circles) and disk stars (black dots) show quite different behaviour and can therefore be separated (Becker 1972).

Assuming that the halo space density distribution is symmetric with respect to the Galactic equator and to the Galactic rotation axis, the stellar density distribution along the directions projected onto the meridional plane through the Sun and the Galactic centre should allow the determination of halo-isodensity lines in the meridian.
Becker (1980) published his results in form of a first comprehensive halo-isodensity profile in the Galactic meridian, reduced from the Sun to the Galactic centre.

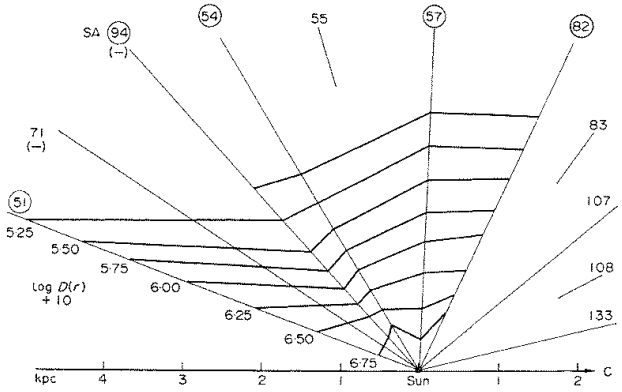

FIGURE 1.4.: Lines of equal space density for halo stars in a plane perpendicular to the Galactic plane. All data are based on three-colour photometry using plates taken with the 48-inch Palomar Schmidt telescope (Becker 1972).

The isodensity-lines (Figure 1.4) reveal a considerable flattening of the Galactic $halo$ [3] ($b/a = 0.5$, Fenkart (1980)), visible in the outmost line (Figure 1.4, $log\, D(r) + 10 = 5.25$), which corresponds to a density about 30 times lower than the one near the Sun (Becker 1972).

[3] $Halo$ here means the three-colour photometrically defined halo population.

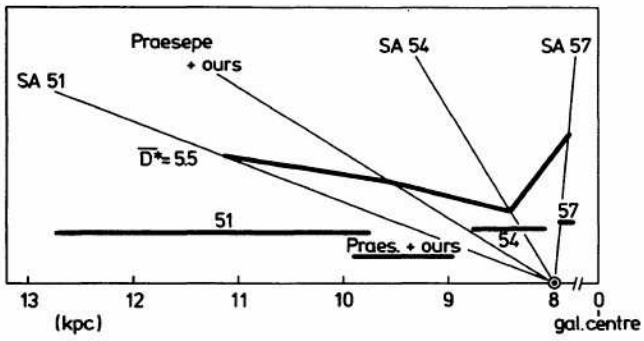

FIGURE 1.5.: Mean isodensity pattern and z-scale heights for halo main sequence stars with apparent magnitudes of $4.0 < m_G < 5.0$.

Becker (1972) discovered a significant discontinuity at about b = +60°, the direction to SA54, which led to further investigations by **Fenkart & Karaali (1984)**. They analysed the isodensity pattern in the anticentre-northern quarter of the Galactic meridian (in the directions to Praesepe and M67) in more detail and confirmed and extended this discontinuity to about b = +30° (see Figure 1.5).

After all this work on determining the isodensity profile of the Galactic halo, they ended up with quite a detailed knowledge about the distribution and some dicontinuities of the halo stars along the meridian.
To check if this overall density-picture was not falsified by the use of the RGU-photometry, a further, very important step in the Basel Halo Program followed:
To derive independent density results, the RGU-based method was applied analogously directly upon four fields measured in another photometric system, the Johnson-UBV system.
Fenkart & Esin-Yilmaz (1983, 1984, 1985) and **Fenkart et al. (1986)** studied four fields (SA54, SA82, SA57 and SA133) that were observed in two different photometric systems (RGU and UBV). The comparison between the density distributions derived from the different photometric systems showed a satisfactory agreement and confirmed the halo-isodensity lines of the simple two-component model.

Further investigations of the three-colour photometric results of eleven Basel Halo Program fields, combined together to a photometrically defined mean local halo luminosity function, led to an estimate of the halo-to-disk mass ratio as well as to the overall mass distribution in the Galactic halo (Fenkart 1977, 1980).

In 1981, **Buser & Chiu (1981)** presented their comparison of two different ways of defining the stellar populations in high-latitude fields: either by three-colour photometry (Becker 1965) (population II stars), or reduced proper motion (halo stars). This distinction had a great impact on the derived density profile of our Galaxy.
They concluded that the three-colour photometrically determined Population II was not identical to the population of genuine halo stars, which were counted among the halo by their larger velocity dispersion relative to disk stars. According to their study, Becker's method overestimated the number of halo

stars, because the photometrically determined stellar classification did not account for the rather large metallicity dispersion and radial metallicity gradients among the disk stars.
Some stellar fields revealed the presence of a non-negligible fraction of evolved disk stars that could not be separated from the unevolved halo stars using only their colours. On the basis of these new insights, Becker's (1965) isodensity profile had to be updated.

Beside the profound knowledge of the density and mass distributions of the halo stars, the knowledge about stellar metallicities was still too poor to analyse the metal abundance gradient in the halo at the time of Becker's investigations.
This work was done later by **Trefzger (1981)**, who used photoelectric data of stars selected from the photographic survey to calibrate the complete photographic survey of the mean metallicities of F– and G-type dwarfs and subgiants derived in different parts of the spheroid.
The estimation of the metallicities was based on the photometrically measured UV-excess (line blocking effect) as it was measured in the RGU system. Trefzger (1981) established an $[\mathrm{Fe/H}]$ versus δ(U-G) relation for stars more metal-rich than about $[\mathrm{Fe/H}]$ = -2.0:

$$[\mathrm{Fe/H}] \approx -6.5 * \delta(U-G) + 0.15. \tag{1.1}$$

The distribution of δ(U-G) was calculated for all eleven published halo fields (Becker & Steppe 1977) as functions of the apparent G-magnitude. Applying estimated mean absolute magnitudes to all stars, Trefzger (1981) found the metallicities to vary with z-distance above the plane in different halo directions. Figure 1.6 shows the resulting lines of equal mean metallicities of the selected stars.
Near the Sun the metal-rich stars ($[\mathrm{Fe/H}]$ = 0.0) dominate the sample. In all fields, it was clearly visible that the mean metallicity decreased with increasing distance from the Sun. The existence of an abundance gradient in the inner halo is confirmed by this study. Furthermore, these lines of equal mean metallicity have a flattened shape with respect to the disk.
The lines of equal stellar halo space density (Figure 1.4, Becker (1972)) and the iso-abundance contours (Figure 1.6) are very similar: both turn out to have the same shape and a similar degree of flattening. Out of this they drew the conclusion, that in the halo a close correlation between stellar density and heavy element enrichment exists.

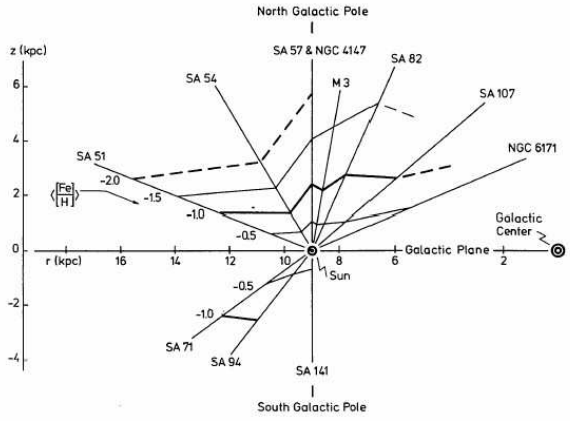

FIGURE 1.6.: Eleven fields of the Basel Halo Program with the lines of equal mean metal abundances of F– and G-type stars (Trefzger 1981).

This rapidly grown knowledge about the luminosity density and metallicity distribution of the local region of the Milky Way, and the deeper insight into the large-scale structure of external galaxies (such as luminosity profiles as functions of radial distance from the Galactic centre or of vertical height above its plane of rotation), led Bahcall & Soneira (1980) and Gilmore & Reid (1983) (amongst others) in the early Eighties to propose various quantitative, multi-parametric models describing the stellar distribution in our Galaxy.
The availability of models that allowed for a rather straight-forward direct comparison between predicted and observed photometric data (star counts and colours) in a certain viewing direction and of a certain field size heralded a new phase in the Basel Halo Program:

the model−comparison phase.

The agreement or disagreement between the theoretically predicted and observed stellar distributions was used to constrain the acceptable ranges of parameters (such as density normalisations, scale lengths and heights) and therefore broadened our understanding of the large-scale structure of our Galaxy, that hitherto was limited due to the lack of observations of faint stars.
The first model that was used in connection with the Basel Halo Program was the standard Bahcall-Soneira Galaxy model **(Bahcall & Soneira 1980, 1984)**. In Bahcall & Soneira (1980), the model is presented in all details and the general comparison procedure extensively discussed. Here, we just give a brief description of it, put more emphasis on the results.
The standard Bahcall-Soneira code is a descriptive two-component model that embodies two major populations: exponential disk Population I− and de Vaucouleurs spheroid Population II stars, each of them consisting of an evolved and an unevolved component [4]. The luminosity functions and scale heights were assumed to be constant throughout the Galaxy as determined from observations in the solar neighbourhood. The assumed global forms of the density laws were derived from observed light distributions in external galaxies. Furthermore, the spheroid stars in the field were considered to be similar to stars in globular clusters. By varying the model parameters (scale heights and lengths, spheroid normalisation) around certain mean values taken from observations, they looked for the parameter value combination that was most successful in reproducing the observed star colours and number counts in different viewing directions.
The best fitting parameter combinations of the three first studies, which compared the observed star counts of different Basel survey fields with the Bahcall-Soneira model are summerised in the Table 1.1 below:

Buser & Kaeser (1985) showed the "halo" component to be highly flattened ($b/a \sim 0.6$) − a result that led to the later identification of this component as *thick disk* (rather than halo).

The collaboration of the Princeton and Basel groups resulted in a joint paper **(Bahcall et al. 1985)**. Comparisons of twelve observed stellar fields of the Basel survey with the standard Bahcall-Soneira Galaxy model (the parameter values were taken from Bahcall & Soneira (1984), Table 1.1, right column) showed good agreement between the two, and furthermore uncovered the possible existence of a third intermediate stellar component beside the thin disk and the spheroid:

[4] Bahcall & Soneira (1980) reserved the term $halo$ for a third stellar distribution of high mass-to-light ratio.
[5] $\varrho_{H,0}/\varrho_{D,0}$ stands for local halo-to-disk ratio.

a thick disk with a spheroid-like luminosity function!

They demonstrated that some of the spheroid stars can be assigned to this thick disk population without disturbing the agreement with observations. These results confirmed the suggestion of Gilmore (1984), who had presented a three-component Galaxy model already one year before.

In a series of four papers (Fenkart 1989a,b,c,d), **Fenkart** extended the model comparison phase by re-examining the comparisons of all 15 halo fields of the Basel Halo Program with five standard multi-component models (three versions of the Bahcall et al. (1985) two-component model and the three– and four-component versions of the Gilmore & Wyse (1985) model) with the purpose of coming to a synoptical picture of the density structure of the Galaxy.
For each field, he determined the best fitting model, comparing the observed three-colour total (Populations I and II together) space densities with the predicted gradients of the five models by varying the parameters of their population components, each calculated for a specific viewing direction and field size (Fenkart 1989a). (For further information about the method applied in all four papers and/or the definitions of the Galaxy models involved, please have a look at the Appendix of Fenkart (1989a).)
After having analysed all 15 halo fields Fenkart (1989d) concluded, that all observations were best described by the Gilmore & Wyse (1985) four-component model that consists of a young and an old thin disk, a moderately flattened de Vaucouleurs spheroid and a double exponential thick disk. Like earlier investigations (described above), these studies confirmed the existence of an intermediate thick-disk population with a local density of 2% and a scale height of the order of 1.0 kpc.

In the meantime, detailed investigations of the Basel high-latitude field star survey data revealed the existence of inhomogeneities and systematic calibration errors that led Buser & Fenkart (1990) to establish the required standard and calibrations using synthetic photometry techniques, and then construct a new homogeneous data set from the original plate material, from the very beginning:

TABLE 1.1.: Resulting model parameters of the first three comparisons

Component/ Parameter	Bahcall & Soneira (1980)	Bahcall & Soneira (1984)	Buser & Kaeser (1985)
Disk scale length	3.5 ± 0.5 kpc	≥ 2.5 kpc	3.5 kpc
Disk dwarfs scale height ($M_v \geq 5.0$)	325 pc	325 ± 50 pc	~ 360 pc
Disk giants scale height	~ 250 pc	250 ± 100 pc	150 - 250 pc
Halo density normalisation (stars pc^{-3}, $M_v \geq 16.5$)	0.00125	0.002	$0.002 \leq \varrho_{H,0}/\varrho_{D,0}{}^5 \leq 0.005$
Halo axis ration	0.85	$0.80^{+20.0}_{-0.05}$	< 0.8
Halo giants	exist: consistent with globular CMDs	exist: consistent with globular CMDs	exist: consistent with globular cluster LF

the New Basel high-latitude field star survey of the Galaxy.

To improve the picture of the large-scale structural parameters of the density, luminosity, and metallicity distributions of the Galactic thick disk stars, **Buser & Rong (1995)** investigated seven stellar fields of the New Basel high-latitude field star survey.
In their theoretical approach, the various stellar populations were represented by a four-component parameterised Galaxy model (a young and an old exponential thin disk, an exponential thick disk, and an oblate spheroidal halo component) of the density distributions, luminosity functions, and colour-magnitude relations. For the statistical analysis theoretical and observed star counts and colour distributions were compared by means of a least-squares algorithm, systematically varying the parameter values of the model **(Buser, Rong & Karaali 1998)**.
Their best fitting model suggested a thick disk component with a local density of 5.4 ± 1.5 % relative to the thin disk, an exponential scale height of 1.15 ± 0.15 kpc, and a mean metallicity $\langle$[M/H]$\rangle$ of around -0.6 dex with a dispersion $\sigma_{\langle [M/H] \rangle} of \sim 0.4$ dex. In contrast to this, the halo turned out to be relatively weak with a local density of only 0.0005 ± 0.0003 relative to the thin disk.
Their results showed on the one hand that the observed data are highly homogeneous, therefore our Galaxy can be described by a global model, and on the other hand that an intermediate population, the thick disk, exists, much more prominent than originally suggested by Fenkart (1989a,b,c,d).
Further investigations (Buser, Rong & Karaali 1999) aimed at determining the large-scale metallicity distribution of the Galactic thick disk using the metallicity-sensitive $U-G$ data. For this more detailed analysis, the preliminary model (Buser & Rong 1995; Buser, Rong & Karaali 1998) was reexamined and improved by extending the structural parameter ranges, thereby introducing more realistic luminosity functions and colour transformations.

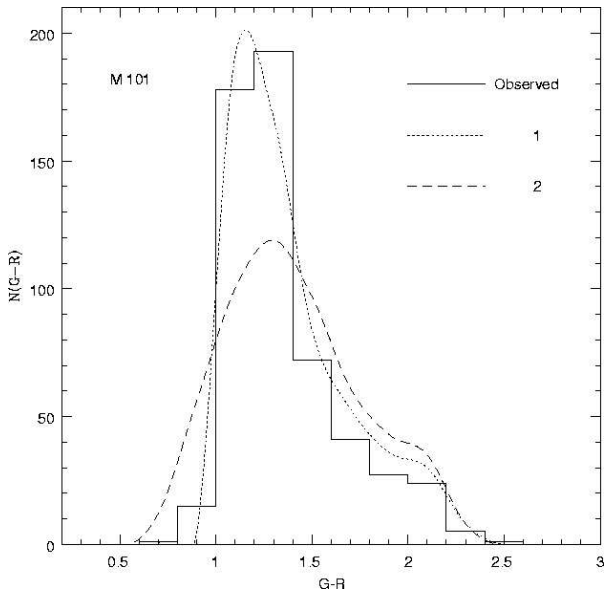

FIGURE 1.7.: $G-R$ colour distribution for the New Basel halo field M101. The curves 1 and 2 stand for Galactic models including, respectively, not including a thick disk (Buser, Rong & Karaali 1998).

Figure 1.7 shows one of the main results of this study, that models including only a weak or even no thick disk component (Figure 1.7, curve 2) could plainly be ruled out. As well as in Buser, Rong & Karaali (1998), the existence of a substantial thick disk component was evident [6].
Beside this more or less expected result, Buser, Rong & Karaali (1998) provided more and new insight into the characteristics of the different stellar components of our Galaxy concerning their local luminosity functions (see Figure 1.8): they demonstrated that the data of the New Basel survey strongly favour

an appropriate luminosity function defined by a
distinctly specific shape and metallicity for each component.

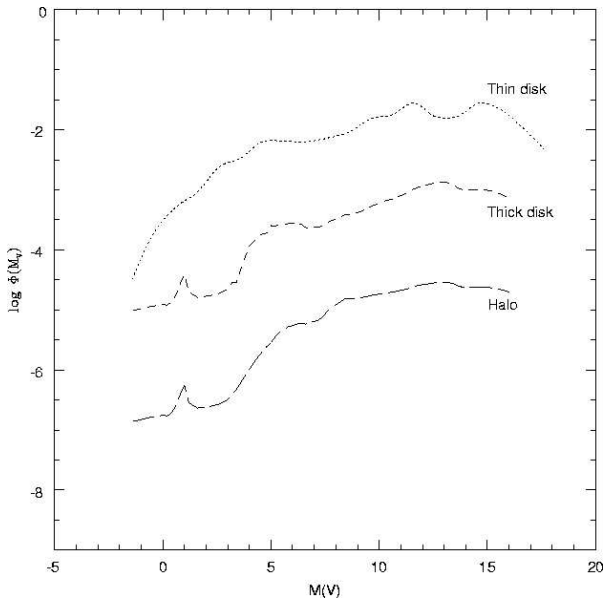

FIGURE 1.8.: The shapes of the appropriate luminosity functions of each stellar component (Buser, Rong & Karaali 1998).

A further step towards a more comprehensive picture of the large-scale density and metallicity structures of our Galaxy was done by analysing (using the same tools as in Buser, Rong & Karaali (1998, 1999)) two more New Basel halo fields (SA107 and NGC6171) that lie in the *inner region* of the Galaxy: one at intermediate latitude, and the other one near the transition from high to low latitudes, approaching the Galactic bulge, therefore demanding the inclusion of interstellar reddening and extinction **(Rong, Buser & Karaali 2001)**.
Beside the confirmation of the optimised parameter values from the earlier studies (Buser, Rong & Karaali 1999), the investigation of these two inner Galaxy fields led Rong, Buser & Karaali (2001) to the conclusion that the scale height of the thin disk could even be divided into a smaller scale height for young dwarf stars and a larger one for older dwarfs.

[6] The best fitting parameter values for the thick disk are the following: A local density of 5.9 ± 3.0 % (Buser, Rong & Karaali (1998) had obtained 5.4 ± 1.5 %) relative to the thin disk, an exponential scale length of 3.0 ± 1.5 kpc, and an exponential scale height of 0.91 ± 0.3 kpc. The mean metallicity result confirmed the one of the former investigation, $\langle$[M/H]$\rangle \sim -0.63$ dex with a dispersion of $\sigma_{\langle [M/H] \rangle} \sim 0.4$ dex.

The former corresponded very well to the observed OB star formation in the inner disk, whereas the latter supported the theory of an earlier and perhaps even more efficient star formation phase in the thin disk, dynamically heating it of over a longer period. These new results had a broad impact on the general understanding of the large-scale star formation history of the Milky Way and modified our picture of the formation and evolution of the disk components.
Concerning the shape of the thick disk, Rong, Buser & Karaali (2001) attributed the large differences between the best fitting mean thick disk parameter values in the two fields to a possible nonuniformity in the density and metallicity structure of the Galaxy rather than to random fluctuations.
Furthermore, they found a vertical metallicity gradient for this intermediate population, but no (or only a small) radial gradient for the thick disk, in contrast to the thin disk.

Keeping the profound knowledge of all results summarised in the previous paragraphs in our minds, with this study, we want to make a contribution to the overall picture of the formation and evolution of our Galaxy by ringing in another phase of the Basel Halo Program:

the chemo-dynamical model−comparison phase.

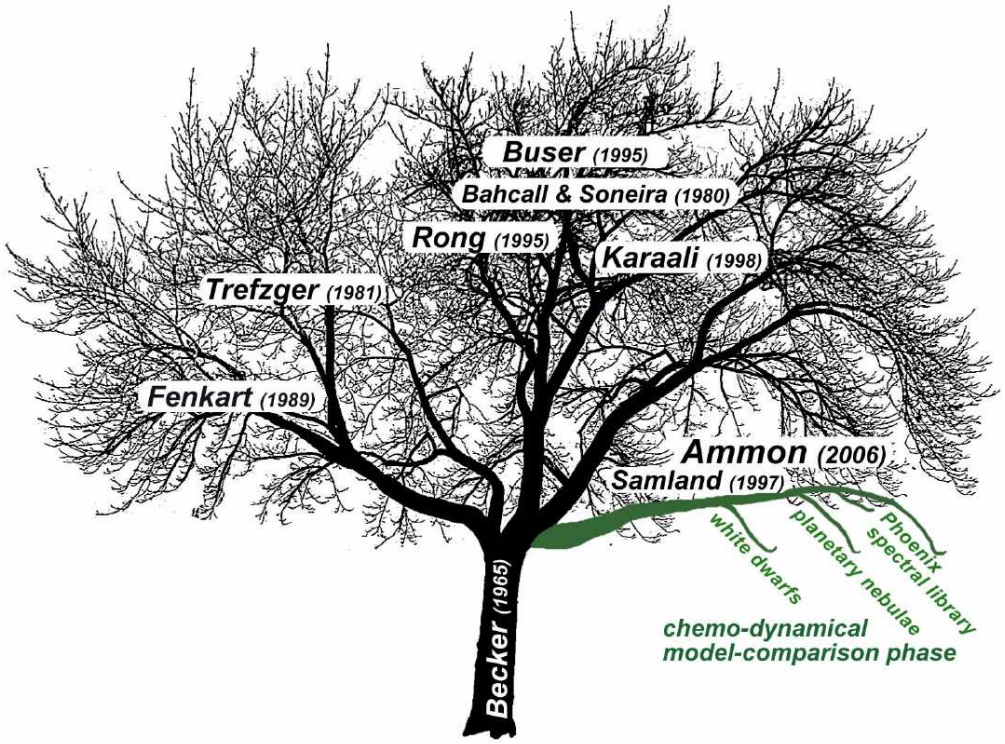

FIGURE 1.9.: Our work is considered a further branch (in green) of the big Basel Halo Program-taxonomy.

As one can see in Figure 1.9, we regard our work as a further branch (in green) of a large taxonomy-tree, which has grown over the years due to all the systematic investigations of the Basel (New) high-latitude survey data carried out by different scientists.
In the next Subsection, we demonstrate why this new branch is just a logical consequence of the knowledge-tree achieved to date.

1.2. Motivation for a new phase in the Basel Halo Program

Before we started our study, *descriptive models* (Bahcall & Soneira 1980; Buser & Rong 1995) were used to produce theoretical colours and star counts, in order to be compared with the observed data of the (New) Basel high-latitude survey.
During the last decade, signifi cant progress has been made in understanding cosmic structure formation and galactic evolution. High-resolution cosmological simulations provided constraints on the large-scale mass distribution, the halo merging histories, the structural parameters of the dark halos and the formation of galaxies inside these dark halos.
The body of newly acquired knowledge has forced and still forces theoreticians, supported by increasing computational power, to program simulations of the formation and evolution of single galaxies or even galaxy groups in three-dimensional numerical models, taking into account all important physical processes and implementing the latest calculated cosmological initial conditions.
These models have to reproduce galaxy formation, a very complex network of physical processes reigned by the total mass and angular momentum, the halo formation history, and the environment. The shape and interior structure of a galaxy is determined by different processes, such as star formation, the interactions between stars and gas, or the interplay between the different phases of the interstellar medium (Samland 2003).

Samland, Hensler & Theis (1997) and Samland & Gerhard (2003) used the latest results from cosmological structure formation simulations to defi ne slowly growing dark matter halos, in which massive disk galaxies form and evolve. By means of a three-dimensional chemo-dynamical code that includes dark matter, stars and a multi-phase interstellar medium, the formation and all the evolutionary phases for a disk galaxy like our Milky Way, were computed.

Due to our fortunate situation of having obtained ten different detailed Galaxy models by Dr. Samland with – at the project's start – even the opportunity of adjusting them, we go a step further with the Basel Halo Program by comparing the observed stellar distributions with the ones derived from these *chemo-dynamical evolutionary models* of the Galaxy.
The chemo-dynamical models are a powerful tool to investigate galaxy formation and evolution on different scales: For a better understanding of the evolution and formation of galaxies since the Big Bang, they can be used to compare young galaxies with galaxies at high redshift through direct determination of the model colours and morphology (Westera et al. 2002). For a more profound knowledge about our own Galaxy, chemo-dynamical models are able to provide the detailed kinematical structure and metallicity distribution of model stars that can be compared with observed stellar surveys of the Milky Way. This is the aim of this work.

The challenge of our work lies in the transformation from physical quantities (Samland models) to observables (BaSeL, SDSS survey). The Samland models provide the initial masses, current ages, metallicities, positions and velocities for all stars present in a certain viewing direction and field size, as well as the distribution of gas and dust in the same volume, which have to be converted into observables like colours and magnitudes.
In order to generate colours and magnitudes comparable with the observed data, we have to bring all the up-to-date knowledge of different astronomical fields of work together: first of all chemo-dynamical modelling (Samland models), secondly stellar evolution (in form of the stellar evolutionary track library (Padova 1994)), thirdly synthetic stellar spectral modelling (the BaSeL 3.2 library), and last synthetic photometry in various filter systems.
In particular, we develop a code – described in more detail in Chapter 3 – for calculating spectra, colours and luminosities for stars of different masses, ages and metallicities, and for deriving synthetic star counts in various colour bands and colour- magnitude diagrams as functions of limiting apparent magnitudes for different viewing directions and field sizes.
These theoretical results are compared with the observed star counts and colour-magnitude diagrams of the New Basel high-latitude and SDSS surveys, with the goal to find the best-fitting model of our own Galaxy, and therefore to investigate the complex interplay of the various physical processes involved in the formation and evolution of the different components of our Galaxy.

Unfortunately, the available model selection turned out too small for finding a unique best fitting model. Furthermore, a major drawback of our project was the cancellation of Dr. Samland's contract, who had to quit his research position here at the institute in Basel and accept a job in the banking sector. His withdrawal got in the way of adjusting the different parameter values of his model to the Milky Way.

But even without having found the best fitting model or having adjusted it to our Milky Way, having gone a sometimes stony but most of the time fascinating way, we still end up with interesting and complementing new insights which we are going to present here. Admittedly, we could not build up as big a new branch as we hoped for at the beginning of our analysis, but the Basel Halo Program-tree still gained several new smaller branches as a direct result of our work.

1.3. Outline of the Thesis

My thesis is structured in the following way:

In Chapter 1, I first provide a brief scientific outline with the most important links to our work and then reflect our motivation to build up a theoretical stellar census in the context of this scientific framework. Additionally, our code is introduced.

The observational data included in our work are addressed in Chapter 2: the two different stellar surveys, the Basel High-Latitude Field Star Survey (Section 2.1), and the Sloan Digital Sky Survey (Section 2.2), and their photometric systems .

Chapter 3 contains a detailed description of our code and its ingredients. In Section 3.2, the 3D chemo-dynamical calculations based on Samland & Gerhard (2003) for the formation and evolution of a massive disk galaxy are presented. Section 3.3 provides an overview of the stellar evolutionary Padova94 tracks which are implemented in our code. In Section 3.4, the two synthetic stellar spectral libraries used in the study, BaSeL 3.2 and PHOENIX, are briefly described.

The derived theoretical data are presented in Chapter 4. In Section 4.1, we explain how stars are drawn out of the theoretical model galaxy and how their theoretical parameters are transformed to observable magnitudes and colours. In the last three Sections of Chapter 4, several different applications of such theoretical stellar census are illustrated and discussed.

The validity of the theoretical model galaxy based on comparisons of its stellar distributions in different viewing directions and field sizes with the photometric field star observations from both the Basel High-Latitude Field Star Survey (Section 5.1) and the Sloan Digital Sky Survey (Section 5.2) is given in Chapter 5.

The results and conclusions are combined in Chapter 6, where also an outlook of possible future scientific projects is given.

2. Observational data

Every galaxy model is worthless without being tested with – and at best adjusted to – real data. After the transformation from the physical parameters given by the galaxy model to observable magnitudes and colours (described in Chapter 3), we are ready to compare our theoretical stellar samples with observed ones.
In our analysis, the observational data are taken from the New Basel High-Latitude Field Star Survey and from the Sloan Digital Sky Survey. They are described in the following Subsections 2.1 and 2.2, respectively.

2.1. New Basel High-Latitude Survey (Basel survey)

For our comparisons we use the Galactic coordinates and solid angles of the fourteen fi elds defi ned by the New Basel High-Latitude Field Star Survey taken by Buser, Rong & Karaali (1998, 1999) to detect stellar distributions in different viewing directions.

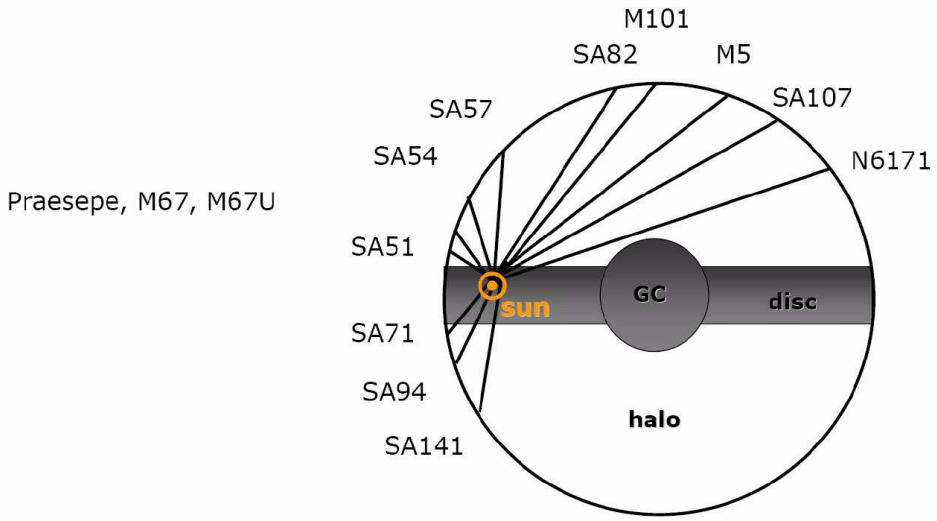

FIGURE 2.1.: Viewing directions of all fourteen fi elds of the new Basel High-Latitude Survey, mapping (approximately) a meridional cross-section of the Milky Way.

As mentioned in Section 1.1, the New Basel High-Latitude Field Star Survey is the successor of the Basel High-Latitude Field Star Survey. All stars that were detected with the Palomar 48 inch Schmidt camera during the precedent survey in the years 1961, 1962 and 1964, were remeasured with the Iris

photometer, re-reduced in a homogeneous way, and put together to make up a new database, the New Basel High-Latitude Field Star Survey (later just called Basel survey) (Buser, Rong & Karaali 1998).

The Basel survey aims at mapping the Galactic density structure and the metallicity distribution of the major stellar components of our Milky Way. For this purpose, fourteen intermediate and high-latitude fields were observed down to faint magnitudes to build a catalogue of new photographic three-colour data for more than 18'000 stars.
Its predecessor, the Basel High-Latitude Survey (Buser & Kaeser 1985), was started in 1960 assuming central symmetry of the large scale stellar distribution. Therefore, all fields were chosen near the meridional plane, which includes the Sun and the Galactic centre, as displayed in Figure 2.1.
A great advantage of the Basel survey lies in the fact, that it gives stellar magnitudes and colours also of stars with distances relatively close to the Sun. These stars are not included in the Sloan Digital Sky survey catalogue due to the magnitude saturation limit at $r \sim 14.0$.

2.1.1. RGU photometric system

A photometric system should be able to single out characteristic features in stellar spectra to identify the atmospheric parameters of different stellar types. As mentioned earlier in Subsection 1.1, Becker (1946, 1965) invented the RGU filter system to fulfill the need for a reform of the astronomical integral photometry, which had at that time only grown historically: The yellow range in visual photometry was used to reproduce the spectral range of the human eye and the blue range in photographic photometry to account for the sensitivity of the photographic plate. Becker's RGU [1] photometric system consists of three colour bands in new spectral ranges, centred at dominant intrinsic stellar features in order to reflect in their brightness the flux distribution of the stellar spectra as well as possible. The response functions and positions of the RGU-filters can be seen in Figure 2.2, marked in blue, and the main properties of the RGU-filter curves are summarised in Table 2.1.

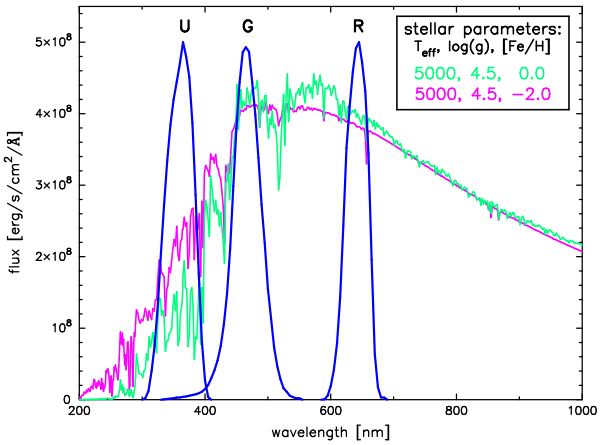

FIGURE 2.2.: Filter functions of the photometric RGU system (in blue) plotted over two spectra that differ only in metallicity. The metal-richer star (green spectrum) has colours of $U-G$ = 2.10 and $G-R$ = 1.36, whereas the metal-poorer star (red spectrum) has colours of $U-G$ = 1.47 and $G-R$ = 1.31.

[1] We use the RGU(73) photometric system, that differs slightly from the RGU(64) system. For further details see Buser (1978).

TABLE 2.1.: Properties of the RGU-passbands

passband	mean wavelength (λ_o)	full-width at half-maximum ($\Delta\lambda$)
R(73)	6407 Å	430 Å
G(73)	4658 Å	495 Å
U(73)	3593 Å	530 Å

One characteristic stellar feature, the metal abundance, can be measured with the RGU system: The U-passband is very sensitive to metallicity. This can be seen in Figure 2.2, where two spectra (green and magenta curves) that differ only in metallicity, differ most of all in the U-band. Due to the position of the U-passband, a separation of stars with different metal content is easier in RGU than in e.g. UBV.

2.2. Sloan Digital Sky Survey (SDSS survey)

The Sloan Digital Sky Survey (SDSS; York et al (2000)) is the largest optical photometric and spectroscopic survey existing today. When completed, the SDSS will provide high-resolution CCD-images of one quarter of the sky around the North Galactic Pole and three stripes in the southern Galactic Hemisphere. Analysis will then also provide a 3-dimensional map of about a million galaxies and quasars. The SDSS collects information about the stellar distribution in our own Galaxy as well. For our project the positions and photometric data of Milky Way stars are of interest.
The DR3 [2] imaging data cover 5282 square degrees and include information on roughly 141 million objects. Figure 2.3 shows the sky coverage of the third data release (marked in black) in equatorial coordinates, containing data taken until June 2003 (Abazajian et al. 2005).

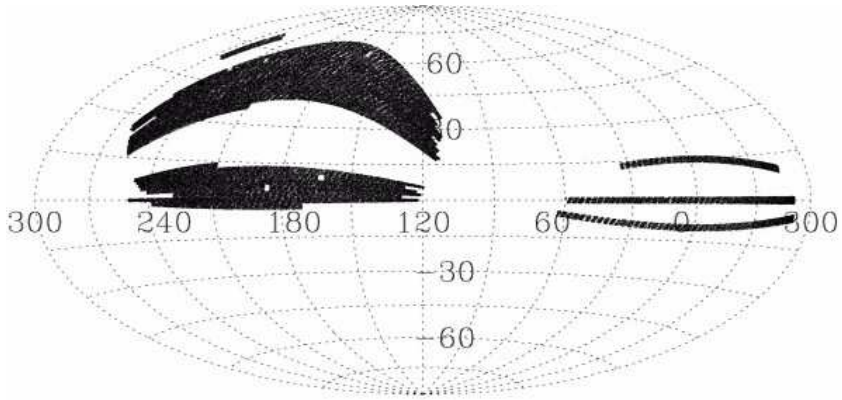

FIGURE 2.3.: Sky coverage of the SDSS Data Release 3 in equatorial coordinates (Abazajian et al. 2005). (Note that it wraps at $\alpha = 300° = 20^h$.)

[2] D(ata) R(elease) 3 means the third data release of observational data into the public domain.

Clearly visible in Figure 2.3 are the three stripes in the southern Galactic cap ($60° > \alpha > 300°$) covered by the observations. In the northern Galactic cap already a larger area is observed. Here, the SDSS is working north from the celestial equator and south from a region centred at $\delta \approx +45°$.

2.2.1. SDSS photometric system

The SDSS photometric system consists of five slightly overlapping passbands ($ugriz$) in the spectral region ranging from the near-UV (3500 Å) to the far-red (9000 Å) (Stoughton et al. 2002). Figure 2.4 shows the filter response functions, and Table 2.2 gives their main properties: the mean wavelength ($\lambda_\circ$) and the full-width at half-maximum ($\Delta\lambda$) of each filter.
These relatively wide filter bands ensure a high efficiency for faint-object detections on Earth's surface.

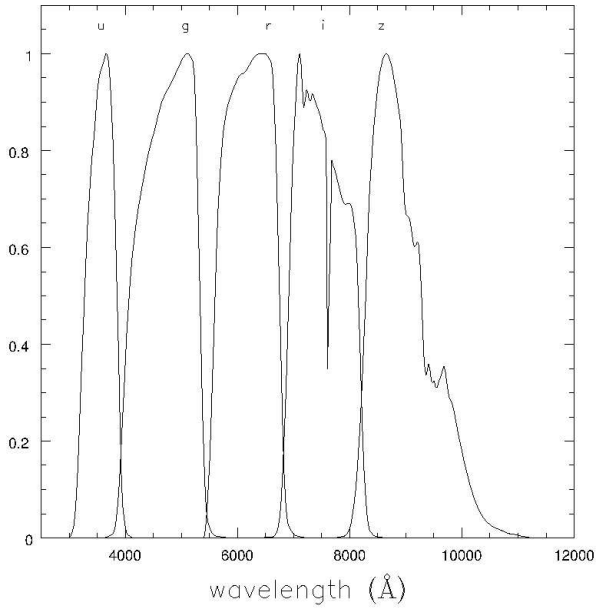

FIGURE 2.4.: Filter functions of the Sloan Digital Sky Survey (Jordi, Grebel & Ammon 2005).

TABLE 2.2.: SDSS filter parameters

passband	mean wavelength ($\lambda_\circ$)	full-width at half-maximum ($\Delta\lambda$)
u	3351	581
g	4686	1262
r	6166	1149
i	7480	1237
z	8932	994

The wide-field camera at Apache Point Observatory, New Mexico, consists of six identical CCD rows aligned in the scanning direction (i.e. six parallel scan lines on the sky). Each row contains five CCDs, one for each passband (Gunn et al. 1998). The camera collects the data in drift-scan mode. This means that the telescope is parked in a certain position, and as the earth rotates, the sky moves over the camera, from top to bottom. Due to the alignment of the CCDs an object observed on the sky drifts almost simultaneously through the five filters.
The data reduction can not be done at the site of measurement. Therefore, the data are sent on tape to Fermi National Accelerator Laboratory near Chicago, where the reduction and photometric calibration to a set of standard stars is done automatically [3].
For every star, the SDSS image-processing software sets 59 object flags, indicating the status of the object and possible problems. A certain flag combination ensures the quality of the photometric data. It excludes stars of which the photometry is questionable for a number of reasons, e. g., saturation, overlap with other objects (blends), location at the edge of a frame, ect.

2.3. Common fields

Having available the data from two different surveys, we also investigate if the model data reproduce one survey better than the other. To do this, we first sort out which fields both surveys have in common.
The positions of all fourteen Basel survey fields are given by a pair of Galactic coordinates, which we transform by means of the IRAF task $galactic$ into equatorial coordinates for comparison with the SDSS database, where all positions are given in equatorial coordinates. The coordinate pairs given by the Basel survey do not always represent the centre of the observed fields: the given coordinate pairs of field M101, for example, mark the lower left corner.

TABLE 2.3.: Common fields: Galactic coordinates and field sizes

field	l	b	size ($\square^\circ$)
SA107	5.7	$+41.3$	0.95
M101	101.0	$+60.0$	2.0
SA94	175.3	-49.2	2.03

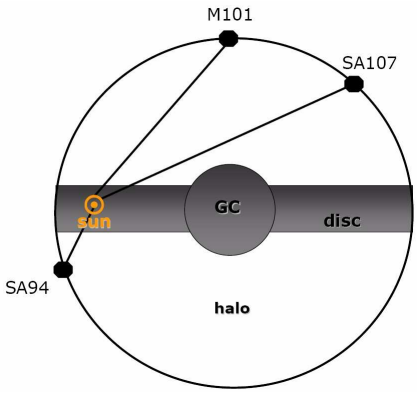

FIGURE 2.5.: Common fields of the two surveys: SA94, M101, SA107.

[3] All the available data are published on the internet. For the Data Release 3 visit http://cas.sdss.org/astrodr3/en/.

A comparison of these two stellar surveys (Basel survey and SDSS survey) shows that only three fields are completely covered by both (in terms used in the Basel survey): SA94, M101 and SA107. Table 2.3 displays their Galactic coordinates (longitudes (l), latutides (b)) and field sizes. For our comparisons with the Galactic model and between the two stellar surveys themselves, we mainly use these three common fields.
As can be seen in Figure 2.5, these three fields stand for three different viewing directions: SA94 is taken towards the outer Galaxy, M101 represents an observation field towards the Galactic halo, and SA107 one towards the inner Galaxy.
Two of them do not suffer from any interstellar reddening (SA94, M101). SA107 exhibits a rather uniform interstellar reddening. Most of its stars are affected by a colour excess, E_{G-R}, of the order of $\sim$ 0.15 mag (Rong, Buser & Karaali 2001).

2.3.1. Common stars

As mentioned in the previous subsection, we always take into account all the stars within the three common fields for our analyses and especially for the comparison with the theoretical model data. For completeness, we mention here another effort of a direct comparison of the two stellar surveys that was done, considering only the stars in common in both of them (Jordi, Grebel & Ammon 2005).
The search for common stars turned out to be more difficult than initially thought, because the Basel survey does not provide the coordinates of its stars. Therefore, Jordi, Grebel & Ammon (2005) searched for common stars on the photo- (Basel survey) and CCD plates (SDSS survey), by looking for distinct star groups with the naked eye. Jordi, Grebel & Ammon (2005) could not find matching partners for all Basel survey stars in the SDSS survey catalogue. Due to the higher resolution of the SDSS CCD plates, this survey sometimes recognised an object as a galaxy or close binaries, whereas in the Basel survey they were treated as single stars. In all those cases, these objects were removed from the sample in order to ensure reliable photographic photometry.
The final list consists only of SDSS stars that are matched with Basel stars, and fulfill the criteria for clean photometry in the SDSS.

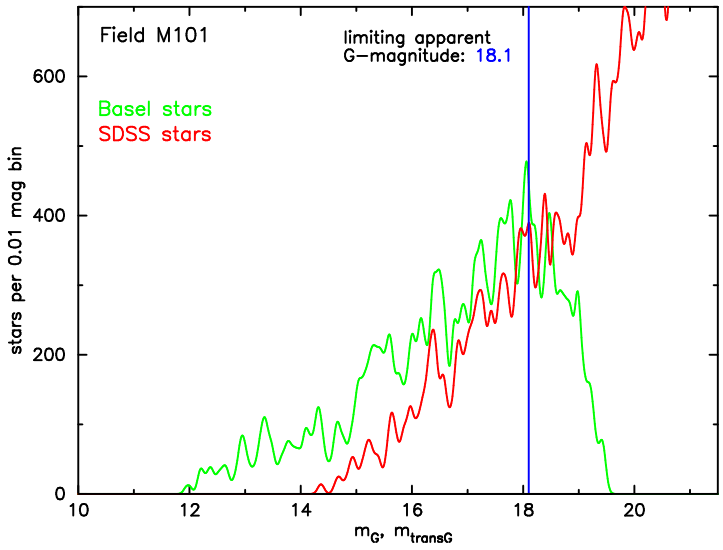

FIGURE 2.6.: The generalised histogram of the apparent G-magnitudes of all Basel stars (green) together with the generalised histogram of the transformed apparent G-magnitudes of all SDSS stars (red) in field M101. The blue line indicates the limiting apparent G-magnitude of the Basel survey.

In order to illustrate how these two surveys differ, Figure 2.6 displays the generalised histograms of the apparent G-magnitudes of all Basel (green) – and the transformed apparent G-magnitudes of all SDSS (red)

stars in the Basel field M101[4].
Due to the saturation limit at r = 14.0, the SDSS collects only those stars that are fainter than this apparent magnitude. However, since the limiting apparent g-magnitude of the SDSS is 22.2 mag, this survey catalogues much deeper than the Basel survey. Puzzling to see is the discrepancy between these two surveys in the magnitude range of $14.0 \leq G \leq 18.1$. The reasons for this discrepancy in absolute star numbers is still an open question that has to be investigated in future projects.

2.4. Determination of the limiting apparent magnitudes

The photometry of faint stars is highly incomplete. Therefore, we omit these faint stars from the photographic samples of all analysed fields by applying a limiting apparent magnitude to each filterband (the R, G and U band for the Basel survey, and the u, g, r, i and z band for the SDSS), and consider the remaining samples as $complete$.
In order to determine the cuttoff magnitudes in the RGU-photometry, we first produce a generalised histogram for each passband, considering that every data point has a certain error: We smear out the magnitude value of each star by placing a Gaussian Function with a half width of σ = 0.08 mag (Bahcall et al. 1985) in the abscissa and then sum up all the contributions from all Gaussians together. From these generalised histograms, apparent magnitudes lying close to the peaks of the observed apparent magnitude distributions were determined and chosen to be the magnitude cutoffs in each field sample and filterband of the Basel survey.
Figures 2.7, 2.8 and 2.9 show the generalised magnitude-histograms. The selected limits of the Basel survey fields (SA107, M101 and SA94) are indicated by the vertical lines in these Figures and separate the complete from the incomplete samplings at fainter magnitudes.

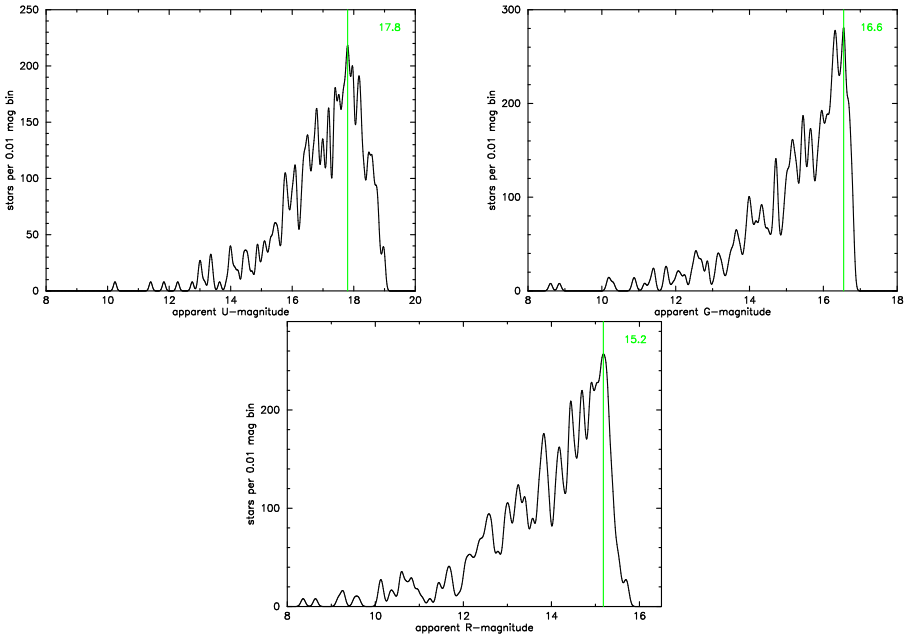

FIGURE 2.7.: Apparent U, G and R distributions of all the stars in the Basel survey field SA107. The green lines indicate the limiting apparent magnitudes.

[4]The transformation of the apparent g-magnitude of the SDSS photometric system into the apparent G-magnitude of the Basel survey has been done by using the transformation equation established by Jordi, Grebel & Ammon (2005).

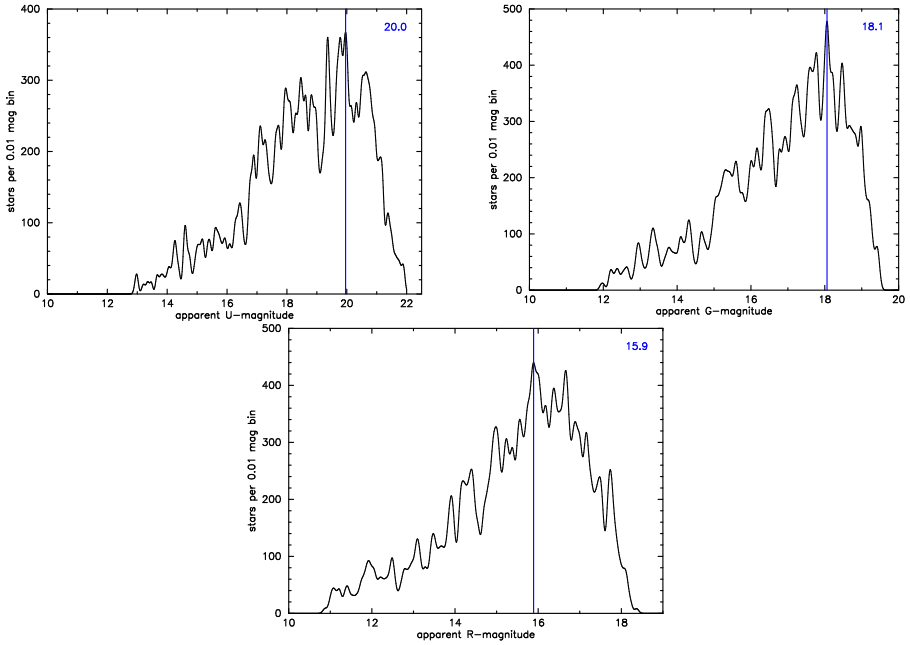

FIGURE 2.8.: Apparent magnitude distributions: generalised histograms of the U, G and R apparent magnitudes of all the stars in the Basel survey field M101. The blue lines indicate the limiting apparent magnitudes.

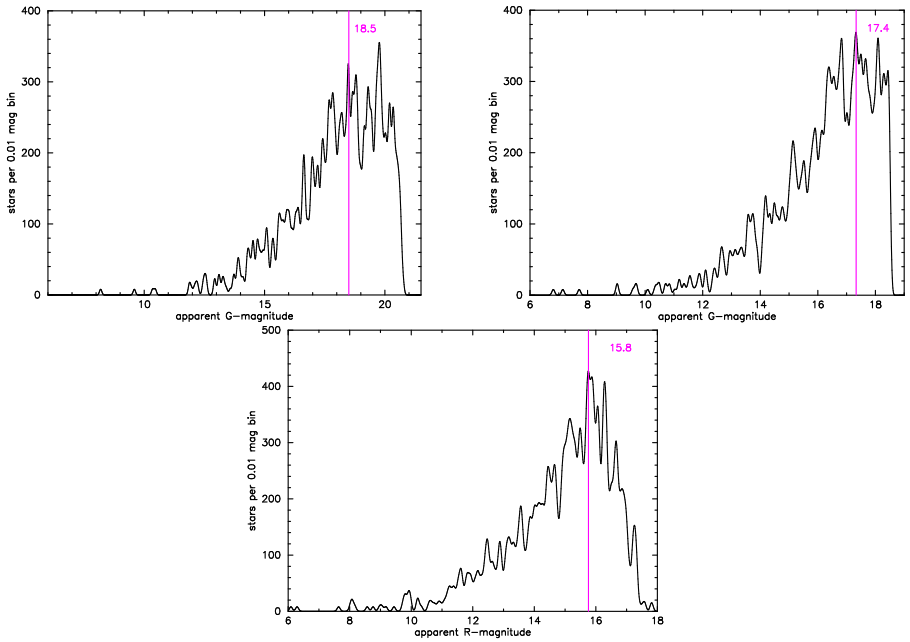

FIGURE 2.9.: Apparent magnitude distributions: generalised histograms of the U, G and R apparent magnitudes of all the stars in the Basel survey field SA94.The magenta lines indicate the limiting apparent magnitudes.

Table 2.4 lists all the limiting apparent magnitudes in both filter systems for the three analysed Basel survey fields. The apparent magnitude limits of the SDSS survey are defined by a specific magnitude value for each passband, independent of the viewing direction (see Table 2.4, columns 5 - 9).

Stellar samples consisting only of stars with apparent magnitudes brighter than these listed limits are assumed to be complete.

TABLE 2.4.: The limiting apparent magnitudes of all three Basel survey fields in both filter systems.

field	$m_{U,lim}$	$m_{G,lim}$	$m_{R,lim}$	$m_{u,lim}$	$m_{g,lim}$	$m_{r,lim}$	$m_{i,lim}$	$m_{z,lim}$
SA107	17.8	16.6	15.2	22.0	22.2	22.2	21.3	20.5
M101	20.0	18.1	15.9	22.0	22.2	22.2	21.3	20.5
SA94	18.5	17.4	15.8	22.0	22.2	22.2	21.3	20.5

These detected limits are used in both the model and the observed star samples. Table 2.5 lists the numbers of all stars measured in the Basel and SDSS survey, respectively.

TABLE 2.5.: Number of all stars measured in the two surveys.

field	No. stars in Basel	No. "clean" stars in SDSS
SA107	532	11857
M101	1388	10407
SA94	1187	10093

3. Basic theory and theoretical data

As contribution to the aforementioned Basel Halo Program-taxonomy (see Subsection 1.1), we checked the validity of Galactic chemo-dynamical models of Samland (Samland, Hensler & Theis 1997; Samland & Gerhard 2003) by comparing their theoretically predicted data transformed into observable magnitudes and colours with the observed data from the New Basel high-latitude field star survey and the Sloan Digital Sky Survey.

In the following, we first give a brief overview of the way we proceed in our analyses, before we then give in the course of the following Sections detailed descriptions of all ingredients and their extensions needed to produce our simulated observations.

Our project gives us a unique opportunity and a great challenge to poke our nose into the state of the art of different astronomical fields of work, bringing all their current knowledge together: next to the galactic modelling, we access the stellar evolutionary track library (Padova94) as well as the theoretical stellar spectral library (Basel 3.2), the latter in connection with synthetic photometry, to constrain a theoretical model of our Milky Way with a full catalogue of physical and observable parameters.

3.1. A schematic illustration of the Modus Operandi

In particular, we develop a code - in connection with galactic models as mentioned above - for calculating spectra, colours and luminosities for different stellar masses, ages and metallicities and for deriving synthetic star counts and H-R-diagrams as functions of apparent magnitudes and colours for different viewing directions and field sizes in the theoretical model.
Figure 3.1 should introduce the reader into the code procedure we apply for the analyses in hand. On the left hand side, the main ingredients (galactic modelling, stellar track− as well as spectral libraries and synthetic photometry, respectively) in their respective order of application are listed, and in the middle and on the right hand side the resulting parameters are displayed in orange.

We start our work by converting the aggregated stellar particles (coloured circles) of the model into single stars as a function of angle of view and field size (indicated by the light blue cone).
Each model star is described by its initial mass (our example star has a mass of 1.0 $M_{\odot}$), current age (10.0 Gyr), time-independent metallicity ($[\mathrm{Fe}/\mathrm{H}]$ = 0.0), position and velocity. In addition to the stellar properties, the Samland model provides us also with the distribution of gas and dust in the selected model volume.

For each star defined by its physical triplet: initial mass, current age and constant metallicity, the Padova94 library of stellar evolutionary tracks provides the appropriate physical parameters, i.e., effective temperature and surface gravity (in our example: $\log g$ = 4.15 and T_{eff} = 5754 K).

The next ingredient we access is the BaSeL 3.2 synthetic stellar spectral library, that includes theoretical model atmospheres (theoretical spectra) for a wide range of effective temperatures, surface gravities and metallicities. For the constant metallicity (given by the galaxy code), effective temperature and surface gravity (extracted

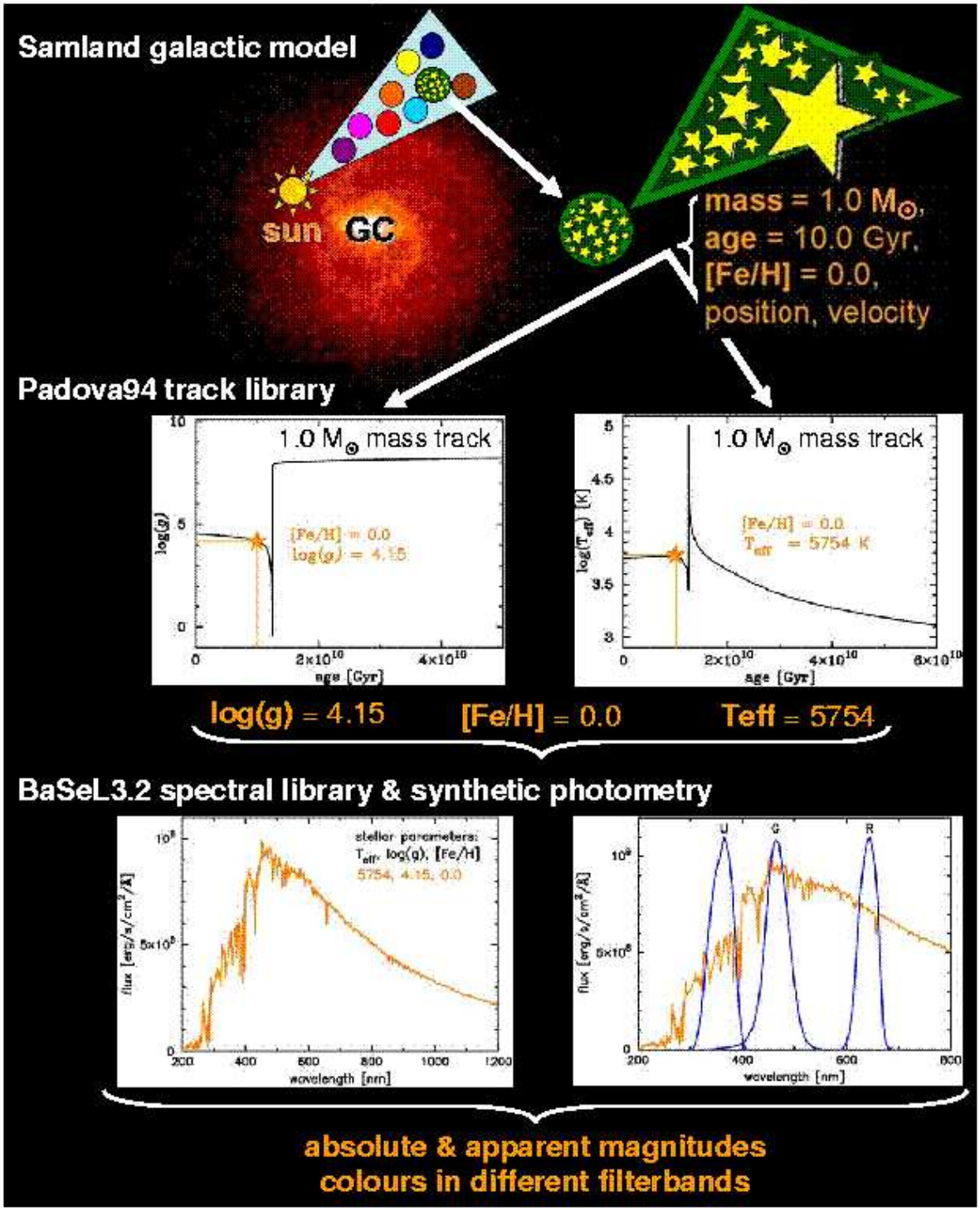

FIGURE 3.1.: Modus Operandi: the main ingredients and their outputs in their respective order of application (from top to bottom).

by means of the evolutionary track library), we find only one corresponding spectrum in the whole BaseL 3.2 library.

Using synthetic photometry, i.e., applying filter functions of a selected photometric system, we then calculate colours and absolute magnitudes of our example star.

Based on the position of the star and the interstellar reddening conditions given by the galactic evolution model, we finally compute the star's apparent magnitudes and colours.

3.2. Chemo-dynamical galaxy model

3.2.1. Code

The chemo-dynamical model of Samland, Hensler & Theis (1997) and Samland & Gerhard (2003) describes the formation and evolution of a massive disk galaxy within a slowly growing dark halo in a Λ cold dark matter universe (ΛCDM: H_0 = 70 km s^{-1}/Mpc, Ω_0 = 0.3, Ω_Λ = 0.7, and $M_{baryon}/M_{darkmatter}$ = 1/5) from redshift $z = 10$ until the present epoch.
Forty years ago, Penzias & Wilson (1965) discovered the cosmic microwave background (CMB). Further observations revealed that the CMB is surprisingly isotropic (T_{CMB} = 2.728 $\pm$ 0.004 K), but still shows some temperature fluctuations of the order of 10 $^{-5}$ K. These tiny fluctuations reflect the density fluctuations in the early universe (Hu & Dodelson 2002) and build the point of origin of structure formation (see Figure 3.2, in which the densest structures appear in yellow).
The ΛCDM paradigm is based on the knowledge of the CMB and states that these regions of enhanced density started to contract due to self-gravity and decoupled later from the expanding universe. These low-mass objects built up the first dark halos and later formed higher masses through hierarchical merging with other low mass objects.

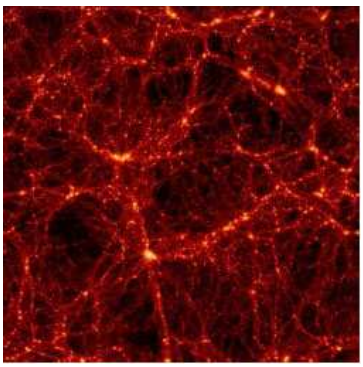

FIGURE 3.2.: A cut through a 100 Mpc x 100 Mpc section of a ΛCDM universe. Bright regions mark the high density halos in which the galaxies form (Immeli 2003).

The halo of a Samland galaxy grows by accreting dark and baryonic matter in spherical shells with an accretion rate that is derived from cosmological simulations. Within such a dark halo, the model galaxies form when the baryonic matter condenses, cools and forms stars at the bottom of the potential wells. This three-dimensional numerical code combines a hydrodynamical grid code for the phases of the interstellar medium (ISM) with a particle-mesh code for the stars, stellar remnants, and dark matter (Samland, Hensler & Theis 1997). The baryonic components (stars and ISM) are connected through an interaction network that describes star formation, stellar evolution, star death, heating and cooling of the ISM, dissipation, and ISM mixing processes. However, dark and baryonic matter are coupled only by gravity. Mass infall at the volume boundaries and the angular momentum distribution are taken from cosmological simulations. Finally, dark and baryonic matter together have a mass of around 1.8 $\times$ 10^{12} $M_\odot$ for a galaxy model that is meant to simulate our Milky Way.

Figure 3.3 gives an overview of all the involved components and their interactions among each other during the galaxy evolution.
Within this model, it is possible to follow in detail the evolution of the stellar components - halo, bulge, and disk - and their kinematical and chemical signatures.

The formation of a massive disk galaxy consists of different evolutionary phases: in short, the star formation from the dissipating cloud proceeds vertically from halo to disk and radially from the inside outwards.

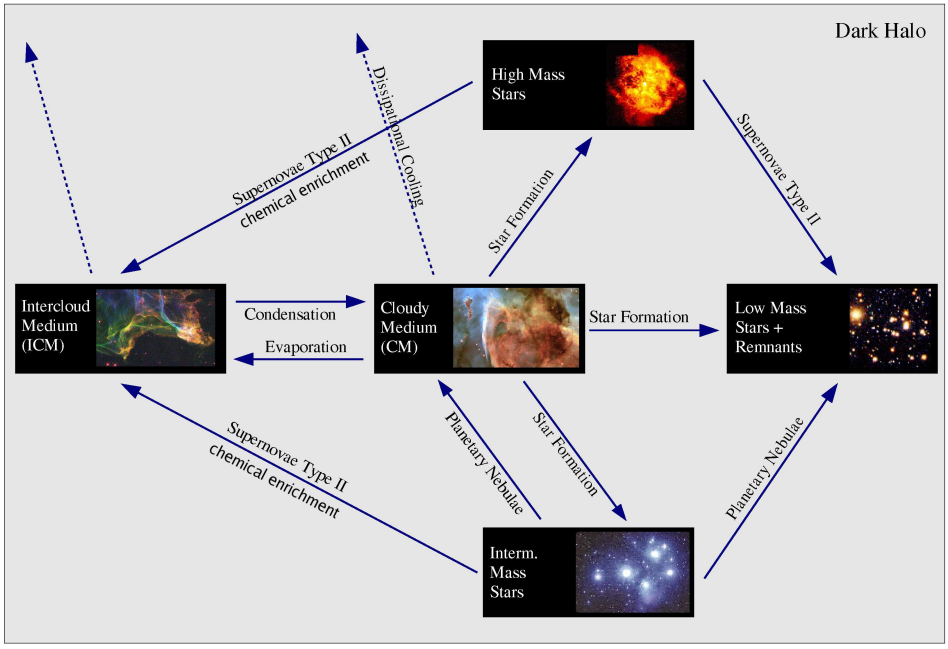

FIGURE 3.3.: Components and interaction network of the chemo-dynamical model (Immeli 2003) (modified by K. Ammon).

Here, we just give a brief outline of the formation and evolution processes as found by the chemo-dynamical evolution model, referring to Samland & Gerhard (2003) and Samland (2004). On some of these processes, we dwell in Subsection 3.2.2 by describing one galaxy model (S10) in great length.

- From redshift $z = 10$ to redshift $z = 2$
  At such high redshifts, the mass of the dark halo increases dramatically, and due to the accretion of baryonic (together with dark) matter a massive protogalactic cloud begins to form.
  This cloud is not stable. The accreted primordial baryonic matter dissipates its kinetic energy, cools efficiently and therefore reduces the internal pressure. As a result the protogalactic cloud starts to collapse inside the dark halo.
  During this collapse, the inner stellar halo and a protobulge form. Thus the earliest stars at redshift $z \geq 2$ form in separated clumps (see Immeli (2003)) over the whole volume (halo formation) with a concentration to the central bulge region (protobulge formation).

- From redshift $z = 2$ to redshift $z = 1$
  In this redshift interval, the collapse is still going on. Due to the increasing density, the dissipation rate increases and hence the collapse becomes stronger. During this collapse, the star formation rate increases and in consequence the stellar feedback becomes more efficient. At a redshift of $z = 2$, the collapse turns into a quasi-static contraction. Until redshift $z = 1$, the flow of cold and warm (i. e., atomic and molecular) gas into the inner galaxy decreases and leads the star formation rate to slow down.
  At around $z = 1.3$ (4.7 Gyr) a (thick) disk component first appears.
  At a redshift of $z = 1.2$, the gas consumption by the star formation in the inner disk can no longer be compensated by the gas infall from the halo. The reason lies in the higher specific angular momentum of the infalling molecular cloud medium, so that its infall timescale becomes longer than the central star formation timescale (Samland & Gerhard 2003). As a result, the region of the highest star formation density moves radially outwards from the centre and form a ring. This ring grows to a radius of ~ 4 kpc, at redshift $z = 0.85$ (6.4 Gyr), the disk becomes unstable. Within 150 Myr the ring then fragments, and

for a short time a very elongated bar appears. By the end of this evolutionary phase, a bar, which later develops into a bar-bulge, and most of the thick disk have formed.

- From redshift z = 1 to redshift z = 0.5
  In this galactic evolutionary phase, in which the bar forms, the star formation moves more and more away from the inner galaxy into the equatorial plane, where the gas is already pre-enriched. A thin stellar disk appears. The most metal-rich stars are born in the bulge and in the inner disk. Later, the infall of low-metallicity gas from the halo and, more importantly, the stellar mass return from old and hence metal-poor stars reduce the metallicity in the disk a little.
  The disk grows from the inside outwards, because the early accreted mass has a low specific angular momentum. At the same time, the vertical scale-height in a fixed radial range decreases. The reasons why the cloudy medium settling is more pronounced to the equatorial plane at late times can be found on the one hand in the more efficient cooling because of higher metallicity, and on the other hand in higher gas density and, thus, also higher dissipation rate for the gas near the angular momentum barrier in a deeper potential well.
  After the bar-bulge has formed (including the old bulge component formed in the early collapse), two trailing spiral arms, which are connected to the bar-bulge, appear in the disk. The bar induces large-scale gas motions in the interstellar medium and the gas from the inner galaxy mixes with the disk interstellar medium.
- From redshift z = 0.5 to redshift z = 0.2
  At redshift z = 0.5 the galaxy has reached its final shape and its evolution proceeds more quietly. The disk still grows radially, however very slowly, and the star formation levels off, concentrated in the galactic plane.
- From redshift z = 0.2 to redshift z = 0.0
  This phase is characterised by the mass return from low-mass stars and the infall of pre-enriched inter-galactic gas. As the dark halo grows, it can capture gas expelled at earlier stages and enriched up to one fourth of the solar metallicity. By falling back into the galactic disk and mixing with the gas returned from older stellar populations, this gas can trigger new star formation events.

As visual examples of galaxy formation and evolution, two different kinds of galaxy models - built up through collapse or accretion, respectively - are shown in the V-band in Figure 3.4.

Each row corresponds to a different epoch: starting 2.5 Gyr after the Big Bang and ending with the image of the galaxy at the present epoch (exact ages of the Universe: 2.5, 3.5, 5.5, 8.5, and 13.5 Gyr, which correspond to z = 2.57, 1.84, 1.07, 0.49, and 0.0, respectivelly). The totally different formation and evolution of these two galaxy types are clearly reflected in these images.
The $collapse\ model$ starts with an extended halo of 250 kpc radius and a total mass of $10^{12}\ M_{\odot}$ (Westera et al. 2002). The dissipation and feedback processes between stars (only the baryonic matter is assumed to be able to collapse) and interstellar medium are the only factors that determine the infall of baryonic matter into the innermost 20 kpc of the dark halo.
Due to the fact, that most of the star formation takes place in this innermost region, the total star formation rate is stronlgy correlated with the collapse time. The early mass infall of the collapse model ends more or less at z = 1.0, and therefore the star formation rate peaks very early at $z \backsimeq 2$ (Westera et al. 2002). This can be seen by the fact that its most interesting features appear at the beginning of the evolution of the collapse model, when its star formation is strongest, at z = 1.84 (Universe age of 3.5 Gyr). The core is already burnt out and a ring-shaped star formation region catches the eye (Figure 3.4, first column, second row). 1 Gyr later, at z = 1.07, this star forming region collapses to a bar and two spiral arms form (Figure 3.4, first column, third row). The bar is still visible at z = 0.49 (Figure 3.4, first column, fourth row), but has disappeared at z = 0.0 (fifth row), when the morphology of the collapsing galaxy appears as that of an early-type disk galaxy.

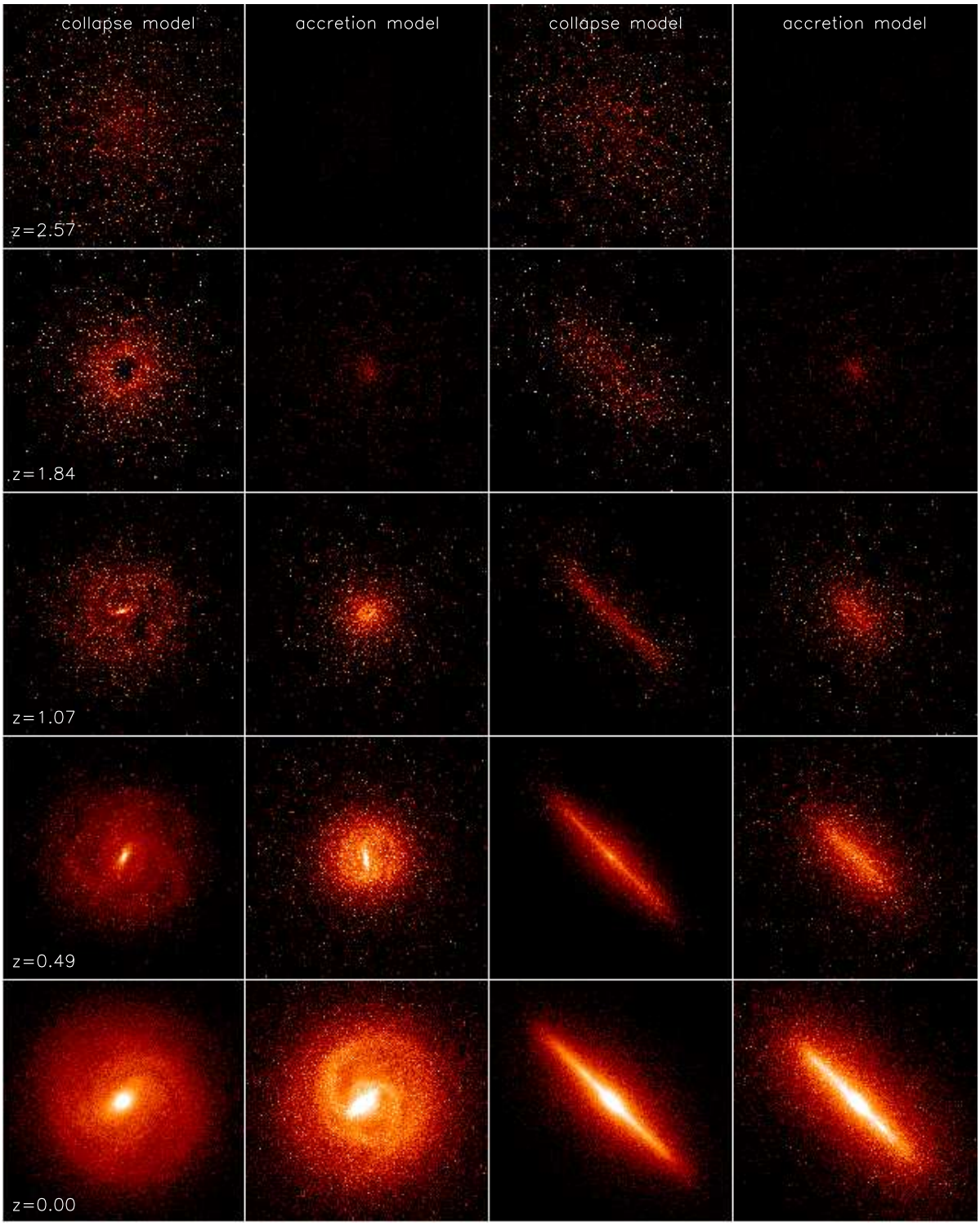

FIGURE 3.4.: V-band evolution of a collapse– and an accretion model, face-on and edge-on (Westera et al. 2002). From top to bottom, the images show a time sequence starting at an age of 2.5 Gyr after the Big Bang and ending at the present epoch, i.e. 13.5 Gyr. The most prominent features of these two galaxy types do not appear at the same point in time: for instance, the bar develops much earlier in the collapse model than in the accretion model, at z = 1.07, as opposed to z = 0.49.

The formation of the $accretion\,model$ takes place in a much smoother way compared to the collapse model. The most prominent features here show up only at low redshifts (Figure 3.4, second column, fourth and fifth row). A slowly growing dark halo (from a radius of 15 kpc at z = 4.85 to 250 kpc at z = 0.0) with continuous gas and dark matter infall characterises this model galaxy. The accreted gas cools, forms clouds, dissipates kinetic energy and finally collapses inside the dark halo. This collapse is delayed by feedback processes, which leads to a galaxy with an extended disk (Figure 3.4, second column, fourth row). The mass flow of the accrection model into the inner 20 kpc has a maximum at z = 1.1, but in contrast to the collapse model, it stays high until around z = 0 (Westera et al. 2002). In Figure 3.4, second column and fourth row (z = 0.49), a bar is visible next to the disk. The spiral arms are slowly nascent in this evolutionary stadium and become better observable at z = 0.0. Both features (bar and spiral arms) survive till the present epoch (z = 0.0, fifth row).

Even though the galaxy models used in this project are neither pure collapse nor pure accretion models (for further information see Section 3.2.2), Figure 3.4 shows the precious jewels that lie in the code of Samland: we are not only able to analyse the inner structure of a galaxy at the present epoch, but also to freeze successive moments of its evolution. The comparison of these stages leads us to a better understanding of the changing importance of the involved processes during a galaxy's life.

In this work, we investigate to what extent the Samland model galaxies are able to reproduce our Milky Way by comparing the model data with real observed star counts. For this purpose, the Samland code allows us to occupy the position of our Sun in a model galaxy and theoretically observe the model sky from there. The theoretical observer's position, the viewing direction and field size are all model input parameters that allow us to simulate any possible stellar survey.

Figure 3.5 gives an impression of all the "observation" possibilities of the galaxy model. As can be seen, the galactic code allows us to look in every desired direction with variable field sizes. The position of the Sun (and therefore the position of the theoretical observer as well) is marked by the solar symbol in yellow and lies 8 kpc away from the galactic centre and 200 pc above the galactic disk (Samland, Hensler & Theis 1997).
After having fed the viewing direction and field size of a desired stellar survey field into the code, we extract the stellar parameters of all model stars in the cone defined by these quantities. The parameters provided by the Samland models are the initial mass, current age, time-independent, i.e. constant metallicity, position and velocity for every star.

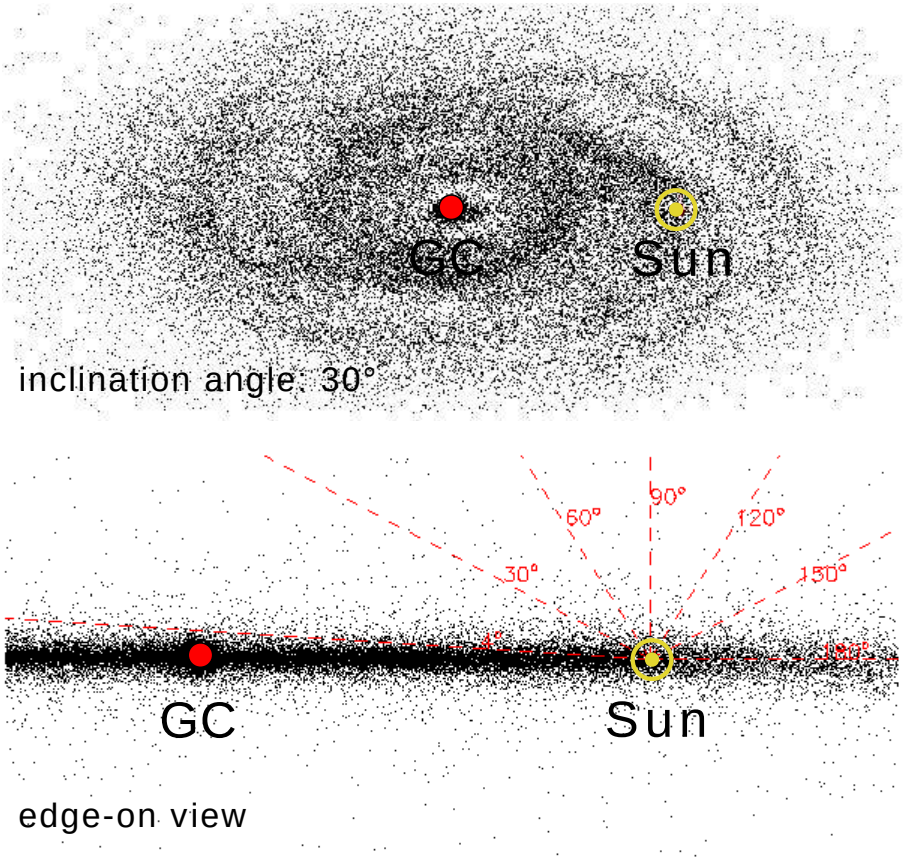

FIGURE 3.5.: The position of the observer (the Sun) and the different viewing directions in the galaxy model. In the upper panel, the galaxy is seen at an inclination of 30 degrees, whereas the lower panel shows the galaxy edge-on.

3.2.2. The special model S10

After a general introduction into the characteristics of the chemo-dynamical galaxy simulations of Samland, Hensler & Theis (1997) and Samland & Gerhard (2003) in the previous subsection, we would like to give a more detailed description of the model galaxy S10, which looks very similar to the Milky Way and is therefore most often used for our comparisons with the New Basel high-latitude fi eld star and the Sloan Digital Sky survey.

As mentioned in Subsection 3.2.1, the formation and evolution of a galaxy depends on the one hand on the initial cosmological and environmental conditions (here: a ΛCDM universe with $\Lambda = 0.7$, $\Omega = 0.3$, a Hubble constant of $h_0 = 0.7$ and a baryonic-to-dark matter ratio of 1:5), and on the other hand on internal processes, such as mass return and chemical enrichment by different stellar types, heating by massive stars and supernovae, dissipation and radiative cooling of the interstellar medium and internal galactic gas fbws.

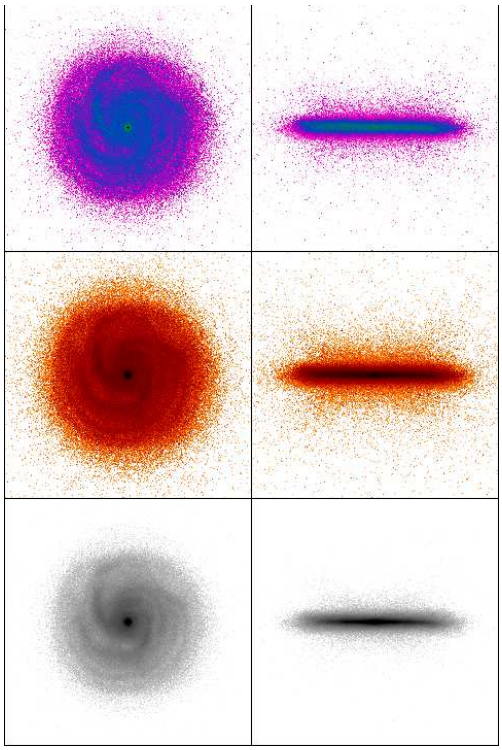

FIGURE 3.6.: Morphology of the theoretical model galaxy S10, observed in the V-band in the upper– and in the I-band in the middle panels, respectively. In the lower panels the (not observable) stellar mass surface density distribution is plotted. First column face-on, second edge-on.

The S10 galaxy develops in a hybrid scenario: The inner galactic halo forms early during a dissipation process, whereas the outer part is build up later by merging and accretion of sub-galactic objects. This is very similar to hierarchical formation models in which the galaxies form from a few large fragments with additional slow accretion of mass (e.g., Navarro, Frenk & White (1995); Navarro & Steinmetz (2000)).
Samland, Hensler & Theis (1997) and Samland & Gerhard (2003) use $1.5 \times 10^{12}\ M_\odot$ for the total dark matter mass, $0.3 \times 10^{12}\ M_\odot$ for the total baryonic mass, a spin parameter of $\lambda = 0.05$ and an angular momentum profi le similar to the universal profi le found by Bullock et al. (2001).

We start our examination of the S10 model galaxy with the analysis of its morphology. In Figure 3.6 three different views of S10 are given: The upper panels show the model galaxy in the $V_{555}-$ and the middle panels in the I_{884}-band, respectively (calculated using the method of Westera et al. (2002), first column face-on, second edge-on). The lower plots show the stellar mass surface density distribution (first column face-on, second edge-on), which is not observable, but provided by the model.
As one can see, the morphology resembles the one of our Galaxy quite well: the halo and disk with spiral arms and the central bulge resemble the ones found in the Milky Way.
The first column in detail: Clearly visible are three continuous closely wrapped trailing arms and several short arm-segments. The arms of spiral galaxies are permanently subject to variations and live only for around 250 up to 500 Myr, while new arms form. Depending on the moment of observation, spirals show a different number of arms. Most frequently two or four are observable.
Furthermore, a luminous bulge is visible in the centre. Most of the recent star formation takes place in the thin (extreme) disk. Young, massive stars that only live about 10.0 Myr and strongly illuminate this region of a galaxy. HII regions and molecular clouds are also associated with the thin disk.
Furthermore, the spiral arms in the V-band are more pronounced than in the I-band, since young stars are brighter in this bluer region of the stellar spectrum.

The formation of spiral structure still has its puzzling aspects, which – unfortunately – cannot be explained by simple theoretical models.
The S10 model galaxy consists of 614' 500 stellar particles interacting with more than 2 million gas cells. The very complex interplay between the multiphase interstellar medium and the stars, both coupled through various mass, momentum and energy exchange processes with each other, inhibits an easy deduction, where and, particularly, when spiral arms form. The formation and dissolution of the spiral pattern are dependent on interwoven dynamical processes, that cannot be decomposed into well-defined single processes.

The edge-on views in the upper two panels of the second column show that the young stars are concentrated in the thin (extreme) disk of the galaxy, which ends quite abruptly in the outer part of the galaxy.

Another aspect worth mentioning is found when comparing the spatial distribution of light and mass (upper four panels with the two lower ones). The theoretical model allows us to plot the stellar mass surface density distribution, even though this quantity is not directly observable.
It is striking that the luminosity distribution is not congruent with the one of the mass. The mass density distribution of the stellar disk is much more concentrated than the luminosity distribution. The reason for this is, that the stellar disk evolves inside out. Therefore, the star formation is higher in the outer part of the galactic disk and this region is brighter than expected from looking only at the mass distribution. It is important to be aware of the fact that the luminosity– and the mass distributions are not the same.
The mass density distribution of a galaxy cannot be derived simply from observations in some filter bands. Westera et al. (2002) investigated the relation between magnitudes and mass of a galaxy and concluded that the Johnson K-band centered at 2.22 μm (Johnson & Morgan 1953) can be used as a reliable (stellar) mass tracer.

To get an idea of the composition and dynamics of the model galaxy S10, Figure 3.7 shows the calculated overall rotation curve (circular velocity) of the galactic disk as deduced from the gravitational potential in orange, and the rotational velocity of the disk stars in black.
Looking at the entire disk rotation curve, the very rapid increase in rotation speed over the inner few parsecs to a maximum of about 280.0 km/s at $\sim$ 1.0 kpc from the galactic centre, followed by a decrease to about 200.0 km/s at about 3.0 kpc is worth mentioning. From here on, the curve rises slightly and generally flattens out around 220.0 km/s.
This flattening with radial distance surprised astronomers in the last century. In 1970, Rubin & Ford (1970) published the groundbreaking paper on the dynamics of M31, where they determined the gravitational potential as a function of radius from spectroscopic observations of ionised HII regions within M31. Their measurements

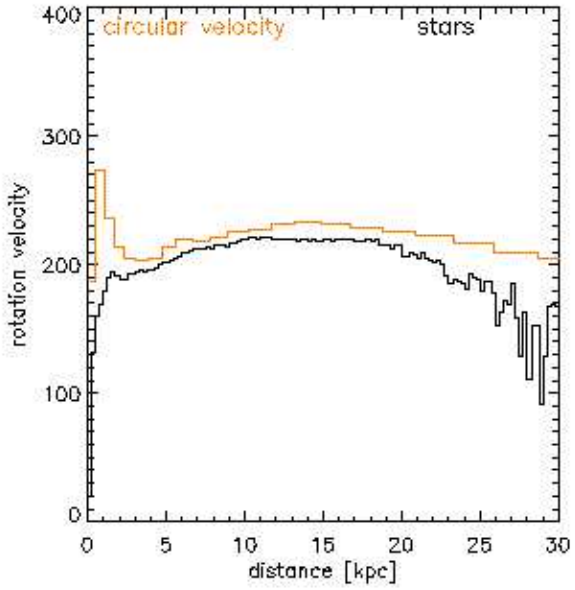

FIGURE 3.7.: Rotation curve of S10. The black curve represents the orbital speed of the disk stars as a function of the distance to the centre of the galaxy, the orange line represents the rotation curve of the galactic disk (HII gas).

were in strong disagreement with the predictions of a Keplerian system with the mass concentrated in the central bulge.
Like in our Figure 3.7, the mass did not follow the light, respectively the circular velocity (here: full disk rotation curve) did not correspond to the one calculated from the light profile assuming a constant mass to light ratio: While the radial light profile decreases with radius, the calculated mass profile is still increasing (out to 24.0 kpc). Using the rotation curve of a galaxy is still the most common tool to determine its mass: By applying Kepler's law, Rubin & Ford (1970) proposed a mass-to-light ratio at 24.0 kpc of ~ 10. This discovery overthrew the long-held ideas about the distribution of mass in galaxies!
Today we know that, in order to provide the needed gravitational potential, dark matter must be present in galaxies. In Figure 3.7, the stars move on almost circular orbits out to 10.0 kpc, which can be seen in the similarities of the total– and the stellar rotation curves. Within this radius, the baryonic mass dominates. It resides in the inner 2.0 kpc, whereas dark matter covers the whole galaxy.
Further out, the stars move more slowly, even though the total rotation velocity remains about the same. In this outermost part of the galaxy (the halo), the mass is completely dominated by dark matter, which causes a flat rotation curve, and the stellar velocity cannot be taken as an indication for the galaxy's baryonic mass anymore.
Note: Near the galactic centre (within 1.5 kpc) the stellar circular velocities are not well defined, because of highly non-circular motions there. The small bar in the centre of S10 disturbs the spherical symmetry, causing the stars to move on elliptical orbits. Depending on their positions, they have different rotational velocities (the closer to the centre the slower).

Comparing the Galactic rotation curve of Vallee (1994) (see Figure 3.8) with the rotation curve of our model galaxy S10, one finds good agreement in the range between 2.0 kpc and 14.0 kpc from the centre. Further out than 14.0 kpc, the measured HI rotation speed rises very steeply, whereas the theoretical rotation curve remains flat. An explanation for this divergence can be found either in our model galaxy (too little mass in the outer part compared to the Milky Way) or in the observations (relatively large errors in that region).

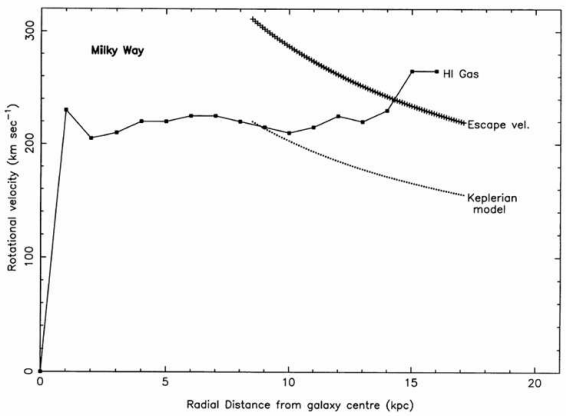

FIGURE 3.8.: Rotation curve of the Milky Way. Filled squares represent the observed large-scale interstellar HI gas rotation curve (Vallee 1994).

As mentioned above, the circular velocity distribution was calculated from the gravitational potential of the galactic disk only. Another possibility to get more information about the properties of S10, is to have a look at the summed up spatial density distribution. Figure 3.9 displays the surface density profiles of the baryonic– (orange curve), the dark matter (green curve) and the sum of the two (black curve).

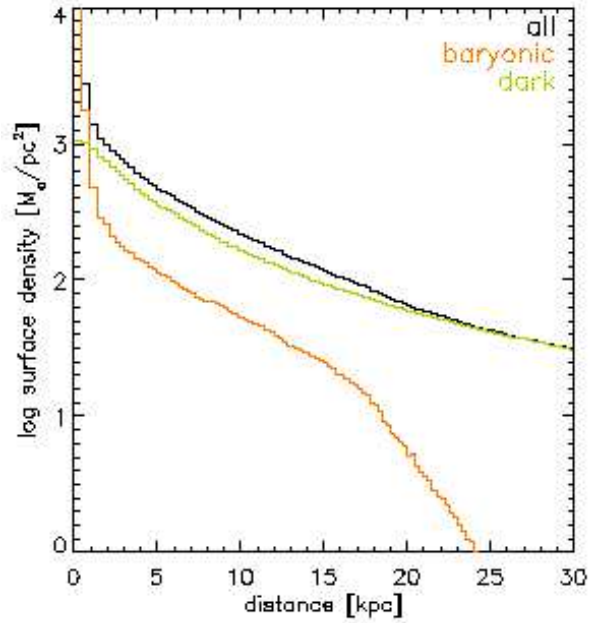

FIGURE 3.9.: Theoretical surface density profiles of the baryonic matter in orange and the dark matter in green. The sum of the two is plotted in black.

This Figure allows a different view on the two components of S10 (dark matter and stars) than Figure 3.7: Within a radius of 2.0 kpc from the galactic centre, the summed up surface density of the baryonic matter seen face-on (Figure 3.9, orange curve) is higher than the one of the dark matter (Figure 3.9, green curve). Even though we sum up over the whole spatial extent of the galaxy, in the inner galactic region there is more baryonic

mass than dark matter. In other words: the closer to the centre of S10, the higher the stellar density.
In the early stages of the galaxy' s evolution, its dark halo was fed by the dark halos of smaller infalling objects that have a dark matter-to-baryonic ratio of 5:1. The exchange of angular momentum between the baryonic– and the dark matter causes the baryonic matter to dissipate into the centre of the galaxy.
Another consequence of the dissipation process can be seen at $\sim$ 17.5 kpc, where the baryonic matter density drops rather abruptly. The luminous part of S10 stretches over 34.0 kpc. In contrast, the dark matter halo has an extent of 300.0 kpc! This means that the baryonic matter collapsed to a tenth of its volume and its density grew by a factor of 1' 000 on average in the central region of the galaxy!

The star formation rates [1] of our theoretical galaxies are not an input parameter, but a result of the galactic evolution, especially the duration of infall and dissipation processes.
In Figure 3.10, the SFR of the S10 model galaxy (left plot) is compared to the "observed" SFR of the Milky Way (right plot).

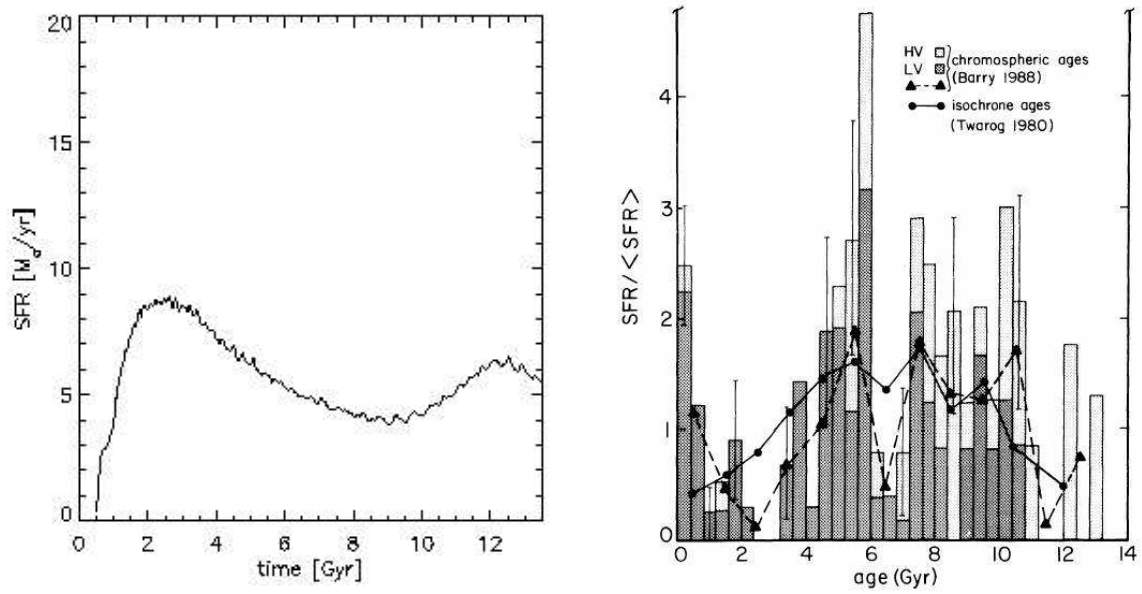

FIGURE 3.10.: Star formation rate of S10 (left) and of the Milky Way (right). The Milky Way SFR is derived from age distributions given by Twarog (1980, filled circles) and Barry (1988, histogram), Figure taken from Noh & Scalo (1990).

This "observed" SFR of Barry (1988) and Twarog (1980) is based on disk stars in the $solar\ neighbourhood$ only, whereas our model provides a $global$ SFR of the whole galaxy. A quantitative comparison between the theoretical SFR and the SFRs deduced from observations is therefore not possible. Here, we just have a look at the overall shapes of the two.
Barry (1988) (Figure 3.10, right plot: histogram) derived the ages of late F and G dwarfs from their chromospherical activities, and Twarog (1980) (Figure 3.10, right plot: filled circles) age-dated southern hemisphere F dwarfs from their $uvby\beta$ - photometry using theoretical isochrones. The filled triangles connected by the dashed line represent the SFR of Barry' s low-velocity stars after smoothing to the same time resolution as Twarog' s isochrone ages (1.0 Gyr).

[1] The star formation rate (SFR) of a composite stellar population provides the number of stars per time unit that are born, as a function of time.

Apart from a few short episodes, both SFRs are more or less constant. The SFR of S10 is on average 6.0 $M_{\odot}$ per year, and the three main episodes of SF in the solar neighbourhood (right panel, at around 5.5, 7.5 and 9.5 Gyr) are only $\sim 3-5$ times higher than the average observed SFR,<SFR>.

The SFR of S10 shows one main period of star formation taking place at an age of around 2.5 Gyr after the Big Bang. Here, the SFR is only a factor of 1.5 higher than the average star formation rate.
This agrees well with the data of Barry (1988) that show another peak at this Galactic age of 11.0 Gyr. Clearly visible is the divergence between the global model star formation episode and the star formation of Twarog (1980)' s data; where at a Galactic age of 11.0 Gyr, the SF is low.

The first peak in the theoretical SFR can be explained by the fact that, at the beginning of the galactic formation, the baryonic matter dissipates, due to gravity, into the central region, where the density increases and stars are formed.
The high mass stars explode as supernovae (SN) after a relatively short lifetime (3.0 − 30.0 Myr). High amounts of energy (of the order of 10^{51} erg per SN) are released and heat up and ionize the gas in the interstellar space. As a result of these ejections, fast expanding bubbles and shells of hot gas form in the interstellar medium (ISM), which leads to a decrease of the gas density in the immediate surroundings, but can trigger SF in other regions. Bubbles and shells and the now heated ISM slow down the infall of further baryonic matter. After the supernovae explosions the infall of baryonic mass still continues, but at a lower level. The same can be said for the SFR: slightly less stars are produced $\geq$ 3.5 Gyr after the Big Bang (left plot of Figure 3.10).

The second, much smaller peak at 12.0 Gyr after the Big Bang is mainly due to mass return from intermediate mass stars (0.8 $M_{\odot} \leq M_{*} \leq 10.0 M_{\odot}$). These stars act as a mass reservoir for the ISM. Their mass loss only plays a role at the end of their stellar lives, when they enter the AGB and planetary nebulae phases. They end up as white dwarfs with masses between 0.5 and 1.0 $M_{\odot}$ and, in total, return twice as much mass to the ISM as the massive stars (Samland & Gerhard 2003). With this additional mass return, the gas pool of the ISM is refilled and more star formation takes place.
Apart from the mass return from local stars, gas falling in from the outer reaches of the galaxy is responsible for the second peak as well, but to a much smaller extent. The dark halo of the young galaxy is relatively small. Because of the low gravitational potential at that time, galactic winds, produced by supernova explosions, are able to transport mass to the outer regions of the galaxy. This gas starts to orbit the galactic centre at large distances or escapes. (Its cooling rate is very low due to the low density.) During the evolution of the galaxy, more material is accreted and a deeper gravitational potential well is built up. The deeper galactic potential at that time pulls the gas back to the central plane and new stars form in the disk of the galaxy.

After discussing the global SFR, we take a closer look at the radial stellar age profile of the model galaxy at z = 0. Figure 3.11 shows the mean ages of the disk (blue −), the halo (magenta −) and all stars (black curve).

In principle, large fluctuations in the age profile indicate statistical errors. For example, the accuracy in the outer part of the galaxy ($\geq$ 25.0 kpc) is quite low, because of the small number of stellar particles. The same is true for the inner-most region, where small radii and, therefore, small volumes are not populated with a high number of stellar particles. Therefore, only the data points between 2.0 and 20.0 kpc are reliable.

Two overall trends are visible in Figure 3.11:
First, the disk stars (here: the combined thin− and thick disk stars) are on average 2.0 Gyr younger than the halo stars (which show larger fluctuations in the age profile due to the smaller number of particles in the halo).
Second, the mean ages of both components decrease from the centre of the galaxy out to $\sim$ 17.0 kpc, and then increase again.

For comparison with observed data, Figure 3.12 shows an overview of the ages and metallicities of different

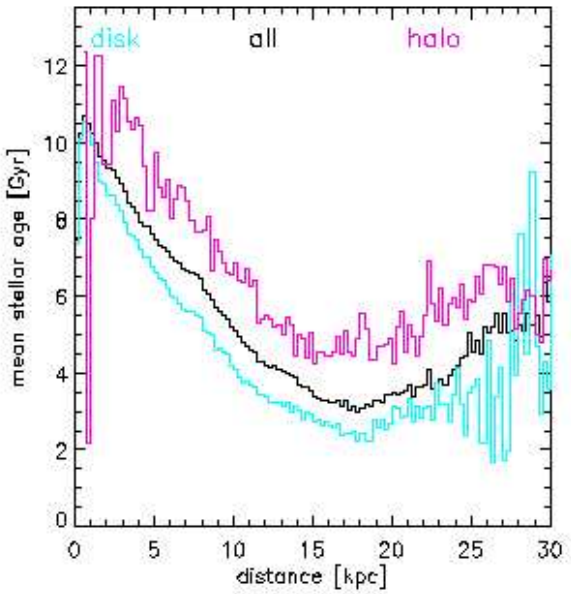

FIGURE 3.11.: Stellar mean age at redshift z = 0 of disk stars (blue), halo stars (magenta) and all stars (black).

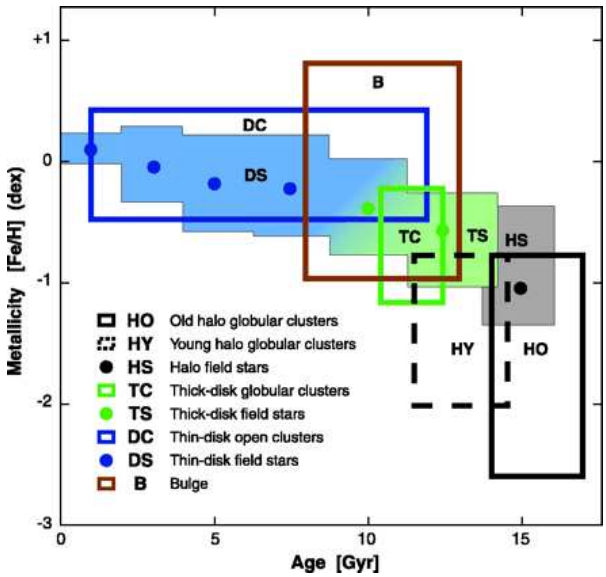

FIGURE 3.12.: Overview of the age-metallicity distribution in our Galaxy. For each Galactic component the bulk properties and approximate ranges are plotted (Buser 2000).

components of the Milky Way (Buser 2000). It is obvious, that the halo stars are very old (on average older than 12.0 Gyr) and metal-poor (see the black rectangles in Figure 3.12). The thick disk stars have almost the same ages as the Galactic halo stars, but intermediate metallicities (rectangles in green). Much younger are the stars that belong to the thin and especially to the extreme disk (blue rectangles). Their ages vary from 10.0 to 1.0 Gyr. As a rule of thumb, the mean stellar ages of the Galactic thin− and thick disks together are on average 1.0−2.0 Gyr lower than the ones of the Galactic halo stars. This agrees well with the age distribution of our model. (For completion: Thin disk stars are mostly metal-rich.)

Since the chemo-dynamical code causes the galaxy to evolve from the inside outwards, the second trend, the decrease of mean ages from the inside out, is just a syllogism (see Section 3.2.1).

Looking at the mean age distribution of the model halo stars, one can divide them into two distinct subpopulations: an older halo in the inner part of the galaxy ($\leq$ 4.0 kpc) and a younger one that dominates the outer part of the halo ($>$ 4.0 kpc).
Several kinds of evidence suggest that the halo of the Milky Way has two distinct components (see Norris (1996)). Within the solar circle, RR Lyrae stars, which are like globular clusters typical members of the halo populations, have a somewhat flattened spatial distribution, while further out they scatter spherically.
Horizontal-branch morphology divides metal-poor globular clusters into a young and an old group. The group of old clusters has a flattened shape, a clearly defined radial metallicity gradient, and a weak prograde rotation, while the young clusters are spherically distributed, without metallicity gradient, and – like halo stars at large distances from the plane – a net retrograde rotation of about 60.0 km/s.

Just like observed for the Milky Way, one process is taking place since the early formation of the model galaxy: accretion of satellites and fragments into the halo. Evidence of such accretion events in the past in the outer, spherical halo stems from observations of ' moving groups' (Eggen 1987). For example, multi-colour photometry and radial velocity measurements show a dwarf galaxy just 16.0 kpc from the Galactic centre in the direction of Sagittarius (Ibata, Gilmore & Irwin 1994). This galaxy is evidently being torn apart by tidal forces as it falls into the Milky Way (Irwin et al. 1996). The accretion of this galaxy will add four globular clusters, including the luminous cluster M54, as well as perhaps 10^8 $M_\odot$ of old and intermediate-age stars to the halo of the Milky Way.
The same process is taking place in the model galaxy: gas that falls into the halo of the galaxy causes new stars to form. No density threshold for star formation is applied in the code (perhaps unrealistically), so that even the slightest gas infall can lead to low star formation. Because of the low density of the halo, these new stars have a high impact on the mean age distribution (see Subsection 5.1.2).

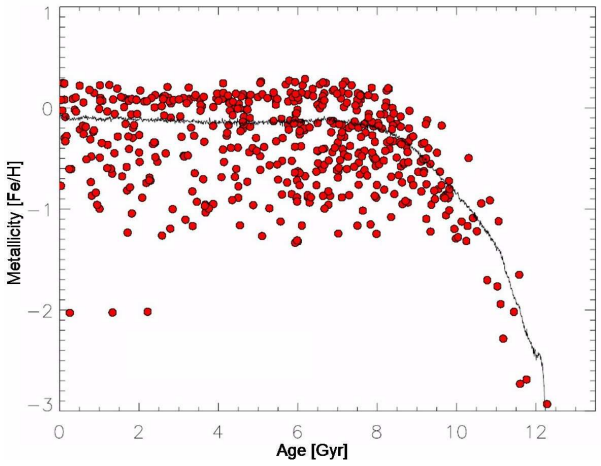

FIGURE 3.13.: The age-metallicity distribution and the average metallicity of the stellar particles in an accretion model galaxy.

Another way of presenting the chemical enrichment of a galaxy with time is shown in Figure 3.13. Unfortunately no such figure exists for the galaxy S10. However in order to highlight the similarities between model galaxies and Milky Way (Figure 3.12), we show the age-metallicity distribution and average metallicity of the stellar particles as a function of time of a model galaxy similar to S10. The average stellar particle metallicity

[Fe/H] of this accretion model starts at [Fe/H] ∼ -3.0, and reaches its present value of ∼ -0.1 dex at around 5.5 Gyrs after the Big Bang. The overall shape and the relatively broad dispersion of the metallicity agrees well with the observed age-metallicity relation of the Milky Way (Figure 3.12).

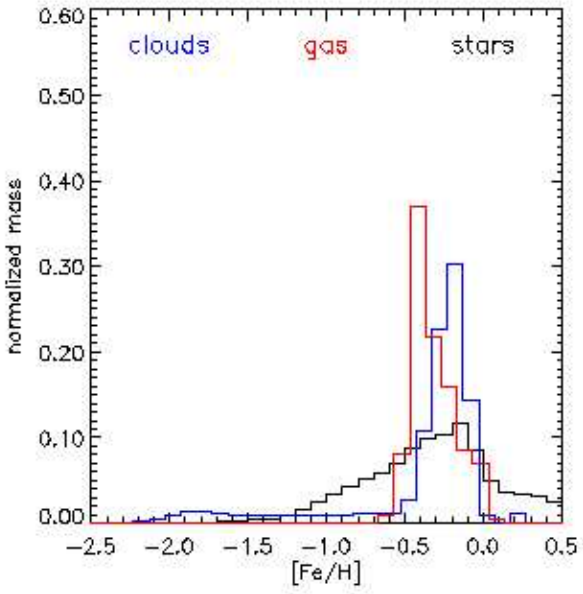

FIGURE 3.14.: Metallicity distribution of the stars (black), gas (red) and clouds (blue) of S10.

Finally, we look at the metallicity distribution of the molecular clouds and gas, the hot gas and the stars, shown in Figure 3.14.
The stars cover a broad metallicity range of $-1.7 \leq [\mathrm{Fe/H}] > 0.5$. The molecular clouds' metallicities lie between around one third of the solar metallicity and very low metallicities (down to -2.2 dex). The metallicity distribution of the hot gas peaks at lower metallicities than the ones of the molecular clouds and the stars.
This figure reveals two astonishing phenomena: First, the molecular clouds are on average less metal-rich than the stars, even though the stars are made out of them. Second, the hot gas that is ejected by supernovae is less metal-rich than the stars.

This can be explained as follows:
Stars are born mainly in the thin (extreme) disk, where the gas is enriched by supernovae and is therefore metal-rich. Looking only at the metallicity distribution of stars and molecular gas from the disk, the cold gas is more metal-rich than the stars, and the hot gas is even more metal-rich, because it is directly enriched by the new and therefore metal-rich supernovae.
In Figure 3.14, however, we see the present total metallicity distribution not only of the disk, but of all the components together. Gas clouds that fall into the halo are very metal-poor, because they were never involved in star formation. In Figure 3.14 this part of the clouds is represented by the low metallicity tail at $-2.25 \leq [\mathrm{Fe/H}] \leq -0.5$. Most of the hot gas with metallicities around -0.5 dex located in the outer halo is enriched by outfbws from the bulge and the disks.

3.3. Stellar evolutionary tracks: Padova94

The stellar parameters provided by the galactic model (initial mass, current age, constant metallicity) are used to select the corresponding evolutionary track from the library computed by Bressan et al. (1993), Fagotto et al. (1994a, 1994b, 1994c) and Girardi et al. (1996), to derive the appropriate stellar atmospheric parameters (i.e., $\log g$ and $T_{\rm eff}$). [2]

TABLE 3.1.: Stellar properties provided by Padova94

symbol	explanation
AGE	age of models in years
log(L/LO)	logarithm (base 10) of the total luminosity in solar units
$T_{\rm eff}$	logarithm (base 10) of the effective temperature
$\log g$	logarithm (base 10) of the surface gravity
Tc	logarithm (base 10) of the central temperature
rho$_c$	logarithm (base 10) of the central density
COMP	central abundance (by mass) of hydrogen or helium
X$_C$	central abundance of 12 C
X$_O$	central abundance of 16 O
Conv	fractionary mass of the convective core (inclusive of overshoot)
Q$_{disc}$	fractionary mass of the first mesh point where the chemical composition differs from the surface value
L$_H$	logarithm (base 10) of the hydrogen luminosity in solar units
Q1$_H$	fractionary mass of the inner border of the hydrogen rich region
Q2$_H$	fractionary mass of the outer border of the H-burning region. The boundary is taken where the nuclear energy generation rate becomes greater than a suitable value
L$_{He}$	logarithm (base 10) of the helium luminosity in solar units
Q1$_{He}$	fractionary mass of the inner border of the He-burning region (when greater than zero He-burning is in a shell). The boundary is taken where the nuclear energy generation rate becomes greater than a suitable value
Q2$_{He}$	fractionary mass of the upper border of the He-burning region. The boundary is taken as above.
L$_C$	logarithm (base 10) of the carbon luminosity in solar units
L$_{nu}$	logarithm (base 10) of the neutrinos luminosity (absolute value) in solar units
Q$_{Tmax}$	fractionary mass of the point where the temperature attains the maximum value

Stellar evolutionary tracks describe the evolutionary paths of stars in a Hertzsprung-Russell or a colour-magnitude diagram with all the different stellar phases during their lifetimes.

[2] We refer to this library as the ' Padova94' library.

In the following paragraphs, we discuss those stellar evolutionary phases that are included in the Padova94 track library. As a help for the reader, we plot four different stellar evolutionary tracks in Figure 3.15. In the left panel of Figure 3.15, we show a Hertzsprung-Russell diagram (HRD) with the evolution of two stars with masses of 3 $M_{\odot}$ and 60 $M_{\odot}$, assigned all the important stellar evolutionary phases. In the right panel, the evolution of two stars with the same masses but lower metallicities is displayed. Additionally, the positions of the – so called – "blue loops" that are part of the metal-poorer stellar tracks, are indicated.

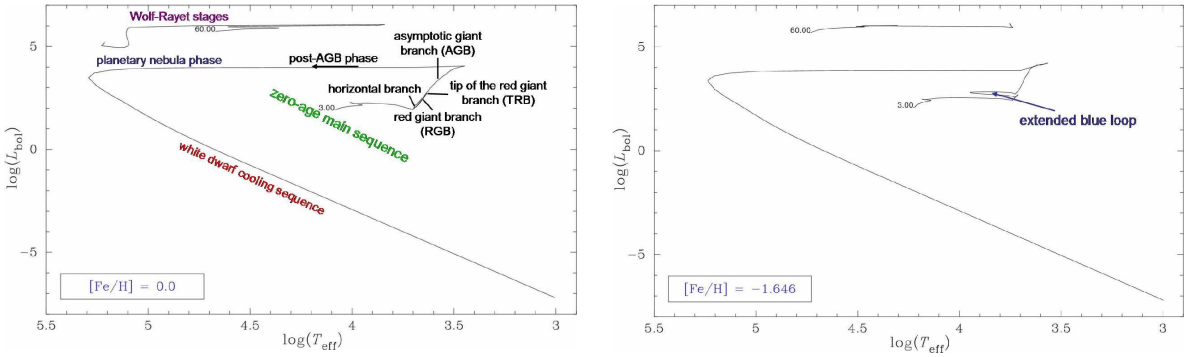

FIGURE 3.15.: Hertzsprung-Russell diagrams. Left panel: the evolutonary tracks of a 3 $M_{\odot}$ – and a 60 $M_{\odot}$ star are plotted and labeled with all important evolutionary phases that these stars go through during their lifetimes. Right panel: same as in the left panel, but for stars with lower metallicities. The "blue loops" are indicated.

For each star and every age step in the theoretical Hertzsprung-Russell-Diagram that is taken into account by the library, a full set of stellar properties (listed in Table 3.1) is given by the Padova94 tracks.

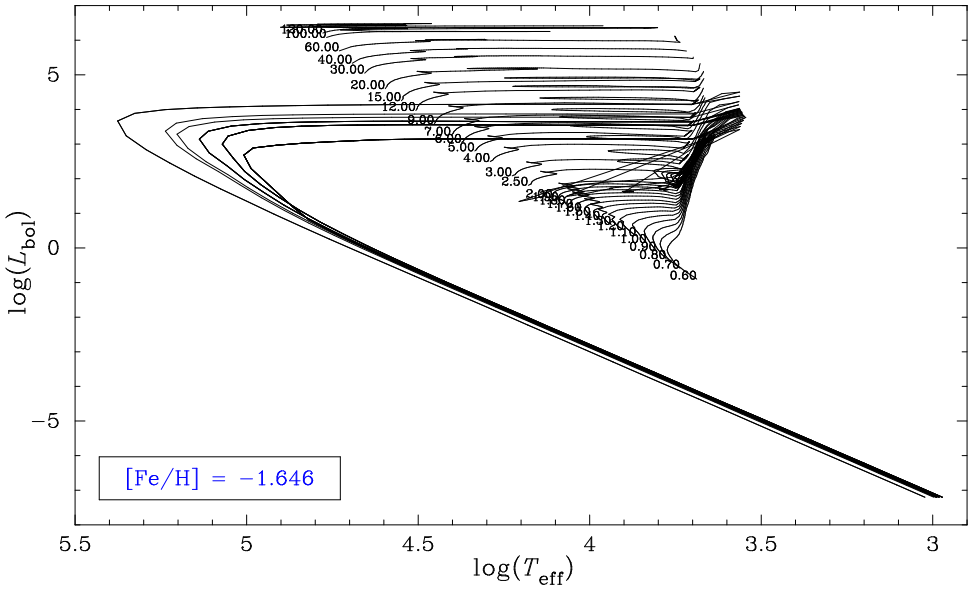

FIGURE 3.16.: A set of stellar evolutionary tracks for all masses avaliable at the subsolar metallicity [Fe/H] = -1.646 in Padova94.

Each of the three Figures 3.16, 3.17 and 3.18 shows a set of stellar evolutionary tracks for all masses included in Padova94 library. Every set, shown here, represents a different metallicity: [Fe/H] = -1.646 (Figure 3.16), [Fe/H] = 0.0 (Figure 3.17), and [Fe/H] = 1.01 (Figure 3.18), respectively.

By comparing the three Figures 3.16, 3.17 and 3.18 with each other, the small mass range covered for the highest metallicity, $[\mathrm{Fe/H}] = 1.01$, catches the eye at first. Padova94 only provides evolutionary paths of stars with masses between 0.6 and 9 $M_{\odot}$ for this metallicity (Figure 3.18), whereas for all the other metallicities, tracks are provided for stars with masses up to 120 $M_{\odot}$ (Figures 3.16 and 3.17).
Furthermore, the different behaviour of the solar metallicity high-mass stars (Figure 3.17) compared to high-mass stars of a subsolar metallicity (Figure 3.16) attracts attention as well. The stellar paths of high-mass stars (> 12 $M_{\odot}$) are calculated in both track sets from the zero age main sequence up to the core C-ignition phase. Solar metallicity stars with masses of 100 and 120 $M_{\odot}$ reach the central C-ignition at a much higher temperature than metal-poorer stars. As one can see, the metal-poorer models of any stellar initial mass never enter the Wolf-Rayet stages in contrast to the metal-richer models (Fagotto et al. 1994a).
Another difference between the metal-poor and metal-richer tracks are the different morphologies of the He-burning sequences: the metal-poor tracks (Figure 3.16) exhibit extended loops in the Herztsprung-Russell diagram, whereas the metal-rich ones (Figure 3.17 and 3.18) do not show blue loops at all.

The Padova94 track library encompasses a wide range of initial metallicities (Z = 0.0001, 0.0004, 0.004, 0.008, 0.02, 0.05, and 0.1, assuming $Y = 2.5Z + 0.23$; where $Z_{\odot} = 0.02$ and$Y_{\odot} = 0.28$). They are based on the radiative opacities of Iglesias, Rogers & Wilson (1992).
Since the metallicities of stellar evolutionary tracks are given in Z, and the metal abundance in spectral libraries (BaSeL 3.1/3.2 and Phoenix) are indicated in [Fe/H], Table 3.2 displays these values in both metallicity units.

TABLE 3.2.: Metal abundance in Z and [Fe/H]

Name	Z	[Fe/H]
Padova 1994	0.0001	-2.2490
	0.0004	-1.6464
	0.004	-0.6329
	0.008	-0.3300
	0.02	0.0923
	0.05	0.5595
	0.1	1.0090

Stellar initial masses range from 0.6 to 120 $M_{\odot}$ for all metallicities, except for the lowest and the highest, where masses are taken into account only from 0.6 to 100 $M_{\odot}$, respectively from 0.6 to 9 $M_{\odot}$ (see Figure 3.18).

Depending on the initial stellar mass, a different number of age steps is given: high-mass stars (≥ 4 $M_{\odot}$) are represented by 261 evolutionary phases, whereas the lives of low-mass stars ($0.6 \leq M_{*} < 4$ $M_{\odot}$) are divided into 312 stages.

All phases of stellar evolution from the zero-age main sequence to the onset of the thermally pulsing regime of the asymptotic giant branch (TP-AGB) for low ($0.6 \leq$ $M_{\odot}$) - and intermediate-mass stars, and on to core-carbon ignition for massive stars are covered by the tracks. Mild overshooting in the convective cores is included in all of them (for stars with masses between 1.0 and 1.5 $M_{\odot}$, core overshooting is included with a reduced efficiency). Overshooting in the convective envelopes of low− and intermediate-mass stars is also included.
As we will describe in the next paragraph, Bruzual & Charlot (2003) complete the tracks of low- and intermediate-mass stars by including TP-AGB and post-AGB evolutionary tracks beyond the early-AGB.

All evolutionary tracks for solar composition are normalised to the T_{eff}, bolometric luminosity and the radius

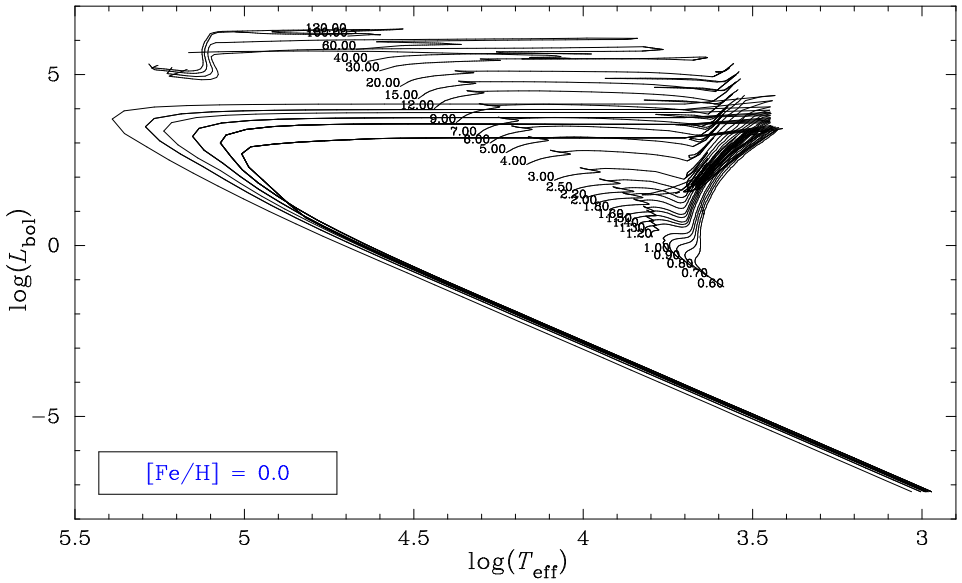

FIGURE 3.17.: A set of stellar evolutionary tracks for all masses avaliable at solar-like metallicity ([Fe/H] ∼ 0.0) in Padova94.

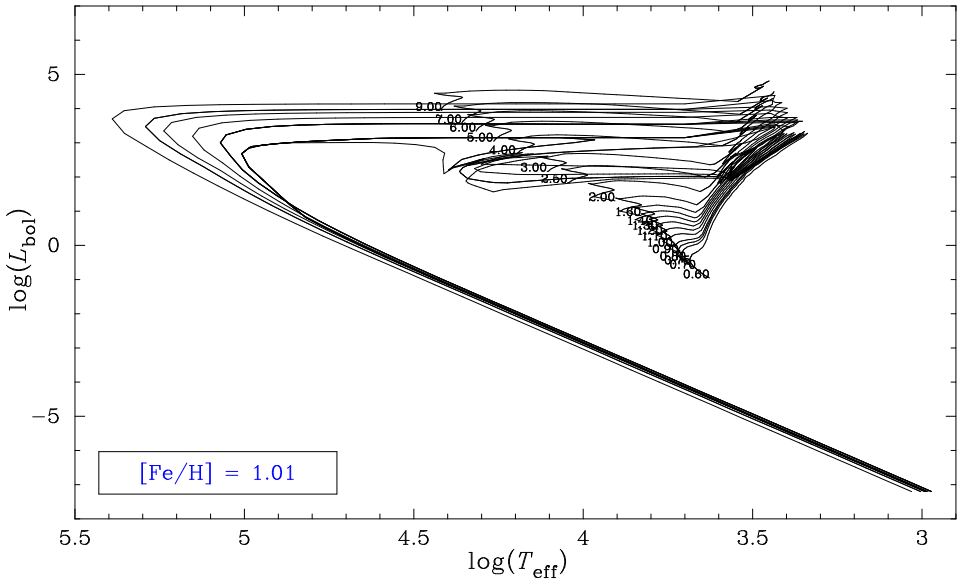

FIGURE 3.18.: A set of stellar evolutionary tracks for all masses avaliable at the supersolar metallicity [Fe/H] = 1.01 in Padova94. .

of the Sun at an age of 4.6 Gyr (Bressan et al. 1993).

Enhancement by G. Bruzual & S. Charlot

Lower-mass stars ($< 0.6\ M_{\odot}$) are not included in Padova94. Therefore, we use the supplement added to this library by Bruzual & Charlot (2003), who incorporated multi-metallicity models of unevolved main sequence stars with masses from 0.09 to 0.6 $M_{\odot}$. Low-mass stars have a main sequence lifetime from 20 Gyr up to 80 Gyr

and can be therefore treated as unevolved main sequence stars.
The now extended Padova94 library covers all phases of stellar evolution from the zero-age main sequence to the stellar remnant stage for all stars with masses between 0.09 and 120 $M_{\odot}$, and provides the physical parameters effective temperature, surface gravity, and (time-independent, i.e., constant) metallicity for each star in every evolutionary phase.

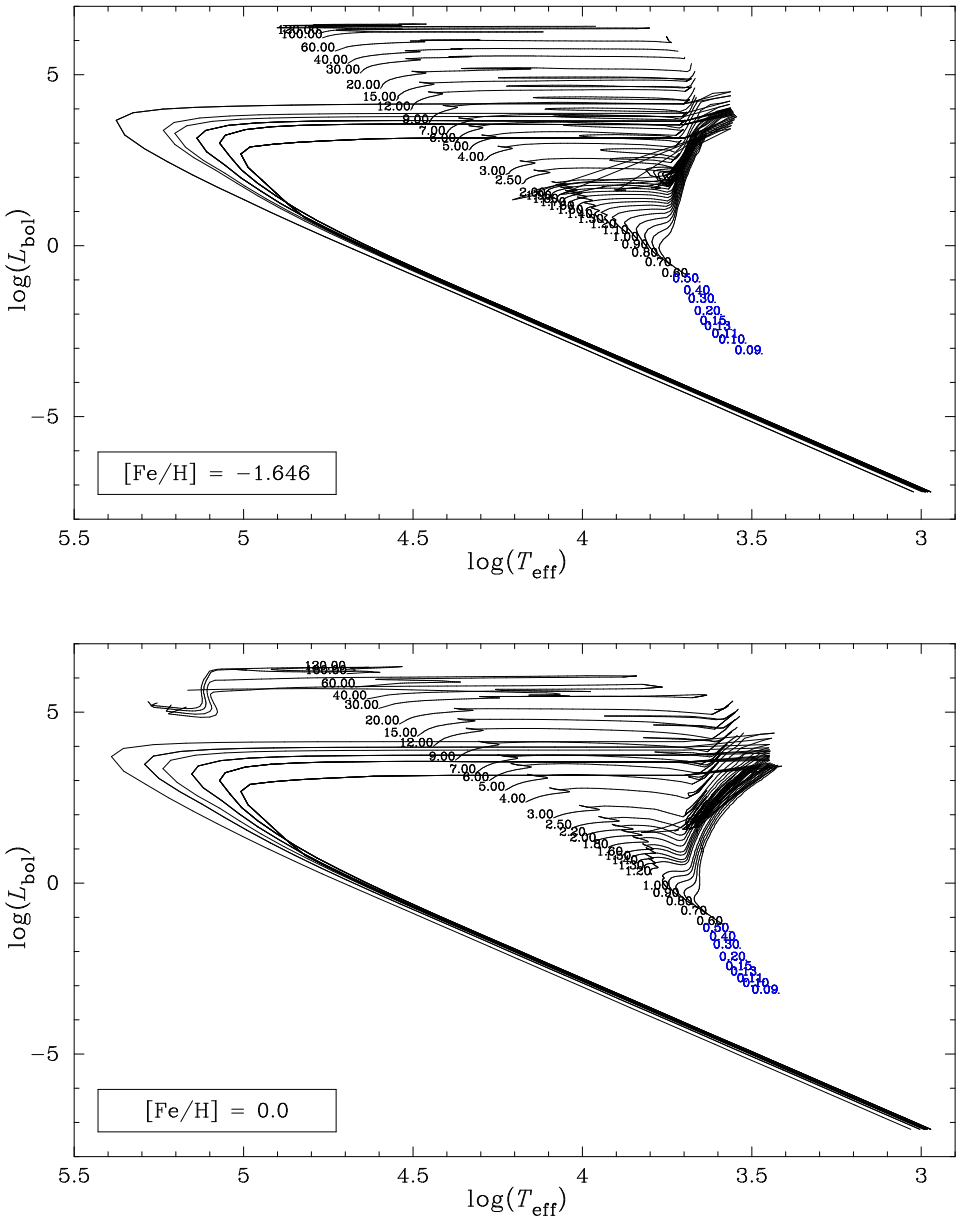

FIGURE 3.19.: Two sets of stellar evolutionary tracks at different metallicities ([Fe/H] = -1.646 in the upper– and [Fe/H] = 0.0 in the lower panel, respectively), enhanced by Bruzual & Charlot (2003).

Figure 3.19 shows the enhanced versions of the Padova94 tracks (for the original ones, see Figures 3.16 and 3.17) with metallicities of [Fe/H] = -1.646 in the upper– and [Fe/H] = 0.0 in the lower panel. In blue all low

mass stars added by Bruzual & Charlot (2003) are indicated. As mentioned above, low-mass stars spend such a long time of their lives on the main sequence, that no other phase for these models is of importance for our project.

3.4. Stellar spectral libraries

So far, each star is characterised by its initial mass, current age and constant metallicity provided by the galactic model (Section 3.2), and by its effective temperature and surface gravity derived from the Padova94 tracks (Section 3.3). In a next step, considering its metallicity, effective temperature and surface gravity we look for an appropriate spectral energy distribution.
Synthetic stellar spectral libraries contain theoretical spectra for stars of a wide range of effective temperatures $T_{\rm eff}$, (logarithm of the) gravitational accelerations at the stellar surfaces $\log g$, and metallicities $[{\rm Fe/H}]$. To obtain observable magnitudes and colours from these physical parameters, we use the BaSeL 3.1 stellar spectral library produced by Westera (2001) and Westera et al. (2002), or, as an interesting alternative due to its higher resolution (typically 50' 000 wavelength points), the PHOENIX model atmospheres, computed by Hauschildt, Lowenthal & Baron (2001). Both libraries cover the same metallicity range as Padova1994.

Kučinskas et al. (2005) investigated the influence of model parameters on a grid of synthetic broad-band photometric colours for late-type giants with solar abundances, based on the PHOENIX library. Their grid for late-type giants covered effective temperatures = $T_{\rm eff}$ 3000 ... 5000 K, gravities $\log g$ = -0.5... +3.5, and metallicities $[{\rm Fe/H}]$ = +0.5 ... -4.0.
In one part of their study, they compared these broad-band colours with theoretical $T_{\rm eff}$-colour and colour-colour relations from the BaSeL 2.2 library.
They found out that, for a broad range of temperatures, surface gravities and metallicities, these two synthetic stellar spectral libraries yield in general well matching colours, and only slightly different colours for late-type giants. A larger colour discrepancy appeared for cool stars ($<$ 4000 K), where a significant disagreement between theoretical models and observations still exists (Kučinskas et al. 2005).
In Appendix A.1, we compare $UBVRIJHK$ colours synthesised with the libraries BaSeL 3.2 and PHOENIX in the whole parameter range ($[{\rm Fe/H}] = 0.0$) covered by both synthetic spectral libraries.

3.4.1. BaSeL 3.1

BaSeL (Basel Stellar Library) 3.1 (Westera 2001; Westera et al. 2002), is an improved version of the Basel stellar spectral library BaSeL 2.2, constructed by Lejeune (1997), and Lejeune, Cuisinier & Buser (1997, 1998).

The BaSeL 2.2 spectral library combines three different theoretical spectral grids (see Figure 3.20):

- the Kurucz (1995) models:
  3' 500K $\leq T_{\rm eff} \leq$ 50' 000K, -5.0 $\leq [{\rm Fe/H}] \leq$ +0.5, 0.0 $\leq \log g \leq$ 5.0
- the Fluks et al. (1994), Bessell et al. (1989) and Bessell et al. (1991) models:
  2' 500K $\leq T_{\rm eff} \leq$ 3' 500K, -2.0 $\leq [{\rm Fe/H}] \leq$ +0.5, -1.02 $\leq \log g \leq$ 2.0
- the Allard & Hauschildt (1995) models:
  2' 000K $\leq T_{\rm eff} \leq$ 3' 500K, -4.5 $\leq [{\rm Fe/H}] \leq$ +0.5, 3.5 $\leq \log g \leq$ 5.5

Note: Later, Lejeune, Cuisinier & Buser (1997) replaced the Fluks et al. (1994), Bessell et al. (1989) and Bessell et al. (1991) models with the newer models calculated by Scholz (1997).
It provides synthetic stellar spectra of a useful resolution (20Å) on a homogeneous wavelength grid from 9.1 nm to 160 μm.

Lejeune (1997) compared the $UBVRIJHKL$ colour-temperature relations from these theoretical models as originally published by their builders to empirically derived relations and discovered that theory and observation deviated systematically.

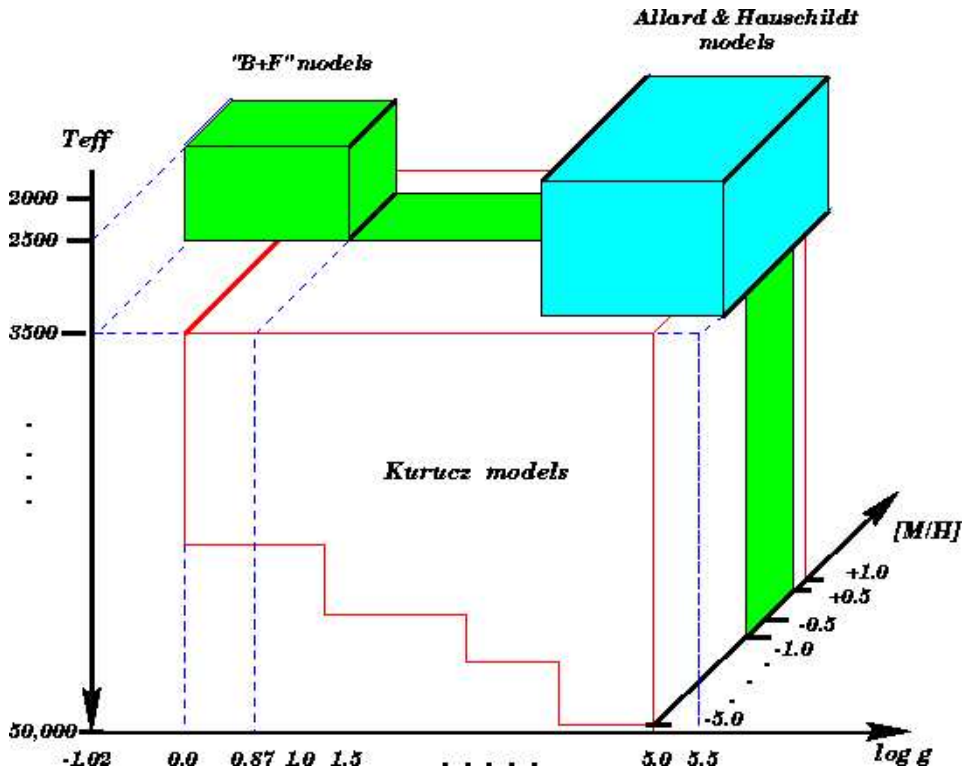

FIGURE 3.20.: Parameter coverage of the BaSeL 2.2 library (Lejeune, Cuisinier & Buser 1998).

In order to adjust the theoretical spectra, Lejeune, Cuisinier & Buser (1997) (later called *LCB97*) calibrated the model atmospheres using the empirical $T_{\rm eff}$-$\log g$-($UBVRIJHKL$) colour relations from solar neighbourhood giants and dwarfs which all have solar abundances.
These calibrations were used to colour-calibrate and hence to correct the original model spectra, using a method developed by LCB97.
Their algorithm calculates for each temperature a correction function, Φ_λ, which is then multiplied with the theoretical spectrum corresponding to the stellar parameters given in the above-mentioned calibration relation for that temperature, such that the model spectrum reproduces the colours as given in the calibration relation. In the end, the spectrum is rescaled, such that the bolometric flux matches the temperature.
The correction functions only adjust the continuum, whereas the line strength indices are left untouched (for this reason the BaSeL 2.2 library is called a $semi-empirical$ library). The whole adjustment procedure is illustrated in Figure 3.21.
All spectra of a given temperature are then corrected using the same correction function derived for this specific temperature. More precisely, for each temperature between 2' 500 to 6' 000 K, two correction functions are calculated, one for giants and one for dwarfs, also taking the possible effects due to surface gravity into account. In this temperature range, the correction functions for giants are used to calibrate the models with $\log g < 3.5$, and for the whole rest of the grid, the correction functions for dwarfs are applied.
A physically fully consistent library demands correction functions that take into account any possible metallicity effect. This means that LCB97 would have had to determine correction functions for every combination of the three atmospheric parameters: $T_{\rm eff}$, $\log g$ and [Fe/H].

Due to the lack of calibration standards at non-solar metallicities, LCB97 applied the correction functions derived for solar metallicity to models of all metallicities. Thereby it was ensured that the differentiation of stellar properties with respect to metallicity was the same as in the original data set.

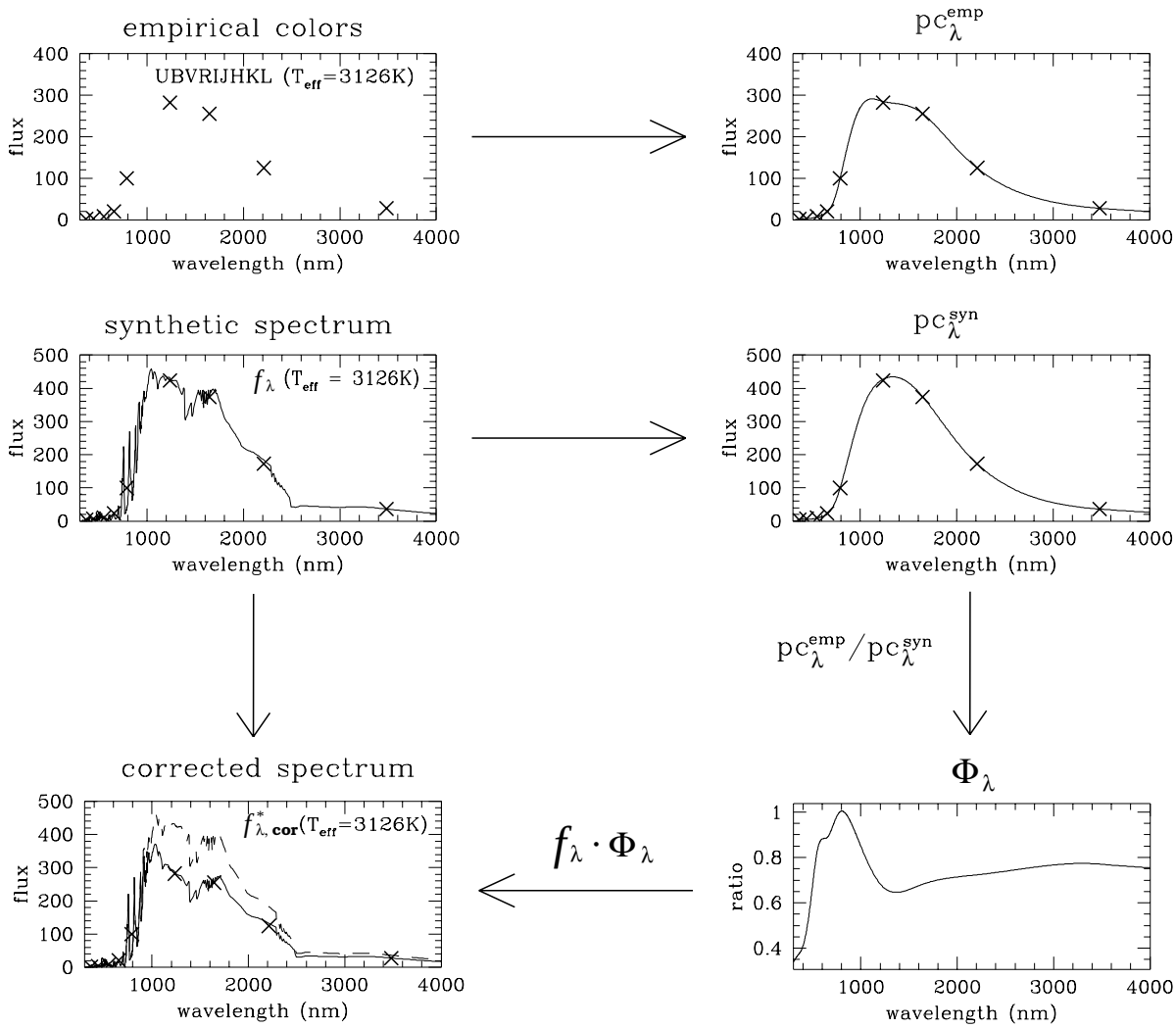

FIGURE 3.21.: Illustration of the calibration algorithm: The algorithm developed by LCB97 changes the shapes of the model spectra to reproduce empirical colours (Westera 2001).

BaSeL 3.1 removes these weaknesses at low metallicities by calculating correction functions for all metallicities from $[\mathrm{Fe/H}] = 0.0$ to -2.0.
As basis for the calibration, Westera (2001) used $UBVRIJHKL$ photometry of five well-known Galactic globular clusters with metallicities of $[\mathrm{Fe/H}]$ = -0.7, -1.11, -1.34, -1.82 and -2.16, combined with empirical $(V-K)$ - temperature - and - T_{eff} - $\log g$ - relations.
He collected all available data (colours) of these clusters from different sources (di Benedetto 1998; von Braun et al. 1998; Ridgway et al. 1980), and linked them to T_{eff}. For all metallicities, Westera (2001) used the Ridgway relation, which was already used to define the temperature scale for the BaSeL 2.2, and which covers the entire temperature range. For dwarfs, the colour - temperature relation of Sekiguchi & Fukugita (2000) was applied.
Afterwards, he supplemented the now metallicity-dependent $UBVRIJHKL$ - T_{eff} relations with appropriate $\log g$ values using fiducial relations in the T_{eff} - $\log g$ plane of the globular cluster giant stars.
As demonstrated in Westera (2001), the resulting library BaSeL 3.1 reproduces the empirical colour - temperature relations very well and is therefore a useful tool for studies of individual stars like the present one. The

spectra of the Sun and of Vega from the BaSeL 3.1 library are displayed in Figure 3.22.

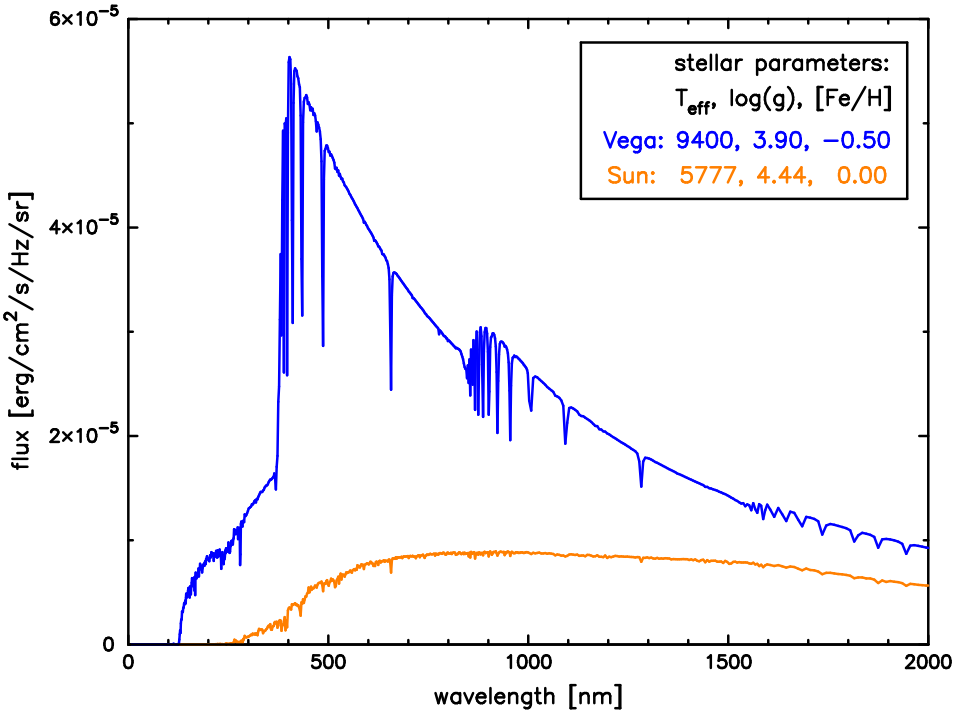

FIGURE 3.22.: BaSeL 3.1 spectra of our Sun and Vega.

3.4.2. White dwarfs

Stars with high surface gravities ($\log g > 5.0$) and high effective temperatures ($T_{\rm eff} > 50'000$ K) were not originally included in the BaSeL 3.1 library. This gap is filled here by implementing a grid of theoretical white dwarf spectra calculated by Koester (2004) for stars with temperatures up to 100'000 K.

The Hubble Space Telescope (HST) image shown in Figure 3.23 (right panel) covers a small region near the centre of the globular cluster M4 (Figure 3.23, left panel). Peering deep into this globular cluster, HST detected tiny spots, called white dwarfs (highlighted with circles). In Figure 3.23 (right panel) eight white dwarf stars can be seen among the cluster's much brighter population of yellow, solar-like stars and cooler red dwarf stars. White dwarfs have faint absolute magnitudes, and hence are difficult to observe. Due to its bright apparent magnitude limits, the Basel survey does not contain any white dwarfs, and the SDSS survey only a small number. Therefore, white dwarfs are not of great importance for our comparison with observations. They are more relevant for the determination of the Galactic initial mass function or the refinement of the Galactic age estimate.

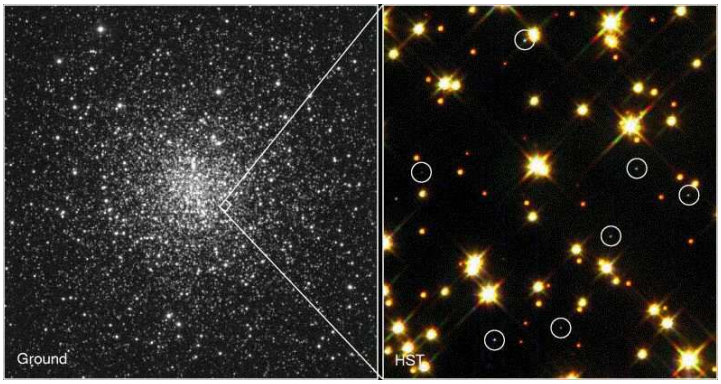

FIGURE 3.23.: White dwarf stars in the globular cluster M4 as seen from a ground-based telescope (left) and by the Hubble Space Telescope (right).

About 80% of the white dwarfs in our Galaxy have hydrogen atmospheres, exhibiting the Balmer lines of hydrogen in their optical spectra (Kawaler & Winget 1987). On this account, we take only DA white dwarfs with hydrogen atmospheres into consideration. Details of the calculations and input physics of the Koester models are described in Finley, Koester & Basri (1997), Koester & Wolff (2000) and Homeier et al. (1998). Please note: Compared to the spectra described in Finley, Koester & Basri (1997), the updated grid of the current models uses the now-standard ML2/α = 0.6 convection model (Kleinmann et al. 2004).

The used white dwarf stellar spectra models encompass a temperature range of $6'000 \leq T_{\rm eff} \leq 100'000$ K and have a surface gravity of $\log g = 8.0$ (which is equivalent to stars of $0.6 M_{\odot}$). They cover a wavelength range between 100 and 30'000Å at resolution 1.0 Å.

The astrophysical fluxes (F = 4H) are given in [erg/s/cm ^{2}/cm], different from the unit used in the BaSeL 3.1 library, where the energy distributions are given in [erg/s/cm^2/Hz/sr]. To transform the fluxes of the white dwarfs into the same units as in the BaSeL 3.1 spectra, we first convert them into flux per Å:

$$flux_{\lambda} = flux \cdot \pi \cdot 10^8, \tag{3.1}$$

then into flux per Hertz and Steradian:

$$flux_{/Hr/sr} = flux_{\lambda} \cdot (\lambda^2/0.4 \cdot c_0), \tag{3.2}$$

where c_0 is the speed of light = $2.9979 \cdot 10^{17}$ [nm/s].

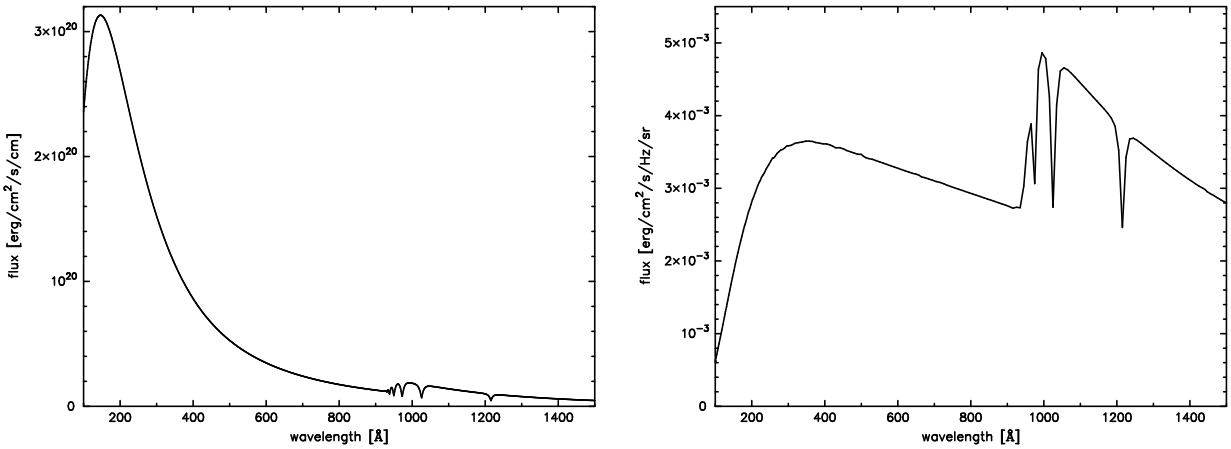

FIGURE 3.24.: Theoretical stellar spectra of a white dwarf with $T_{\rm eff}$ = 85' 000 K and $\log g$ = 8.0 in two different units. Left panel: [erg/s/cm^2/cm], right panel: [erg/s/cm^2/Hz/sr].

Figure 3.24 shows the different shapes of the energy distribution of a white dwarf depending on its flux units. The left panel provides the spectrum in the units of [erg/s/cm^2/cm], whereas the right panel displays the BaSeL 3.1 library units [erg/s/cm^2/Hz/sr].
For their implementation into the BaSeL 3.2 library, these spectra are degraded to the lower resolution of that library of 20 Å.

3.4.3. Planetary nebulae

To cover stars with even higher temperatures and surface gravities than the DA white dwarf spectra in our enhanced version of the BaSeL 3.1 library, we also include hot central star (CSPN) spectra of planetary nebulae (PN) computed by Rauch (2003).
In Figure 3.25 a very well-known planetary nebula is shown, NGC 6751. It is an example of a classic planetary nebula with complex features (the different colours represent different gas temperatures, decreasing from blue through orange to red). The streamer-like features are created by strong winds and radiation from the hot central star ($T_{\rm eff}$ = 140' 273 K). The diameter of NGC 6751 amounts to 600 times the size of our solar system (i.e., 0.8 light-years); NGC 6751 lies 6' 500 light-years away in the constellation Aquila.

Rauch' s (2003) spectra cover a temperature range of 100' 000 $\leq T_{\rm eff} \leq$ 1' 000' 000 K and surface gravities of $5.0 \leq \log g \leq 9.0$ [3]. He calculated fully metal-line blanketed NLTE model atmosphere fluxes, taking into account all elements from hydrogen up to the iron group for metallicities of $Z = Z_\odot$ and $Z = 0.1 Z_\odot$ at wavelengths between 5 and 2000 Å. It is important to know, that signifi cant flux output from such stars occurs only in the UV spectral range. But for our study, we extend the PN spectra by adding black tails (see Figure 3.27).

Just like the white dwarf spectra, the fluxes are given in astrophysical fluxes [erg/s/cm ^{2}/cm] and were transformed in the same way as the white dwarf spectra into the BaSeL 3.1 units of [erg/s/cm^2/Hz/sr].
All CSPN spectra are given with a very high resolution of 0.1 Å. We degrade them to the Basel 3.1 wavelength scale of 20 Å by rebinning (see Figure 3.26).

Since most of the commonly used fi lter systems (UBVRI, RGU, *ugriz*, ect.) cover the optical spectral region, we extend the CSPN spectra by appropriately fi tting blackbody tails (with the same $T_{\rm eff}$ as given by Rauch (2003)) at wavelengths $\lambda > 2000$ Å (see Figure 3.27).

[3] The stellar model atmosphere fluxes (H - Ca) of hot central stars of planetary nebulae are available at: http://astro.uni-tuebingen.de/ rauch.

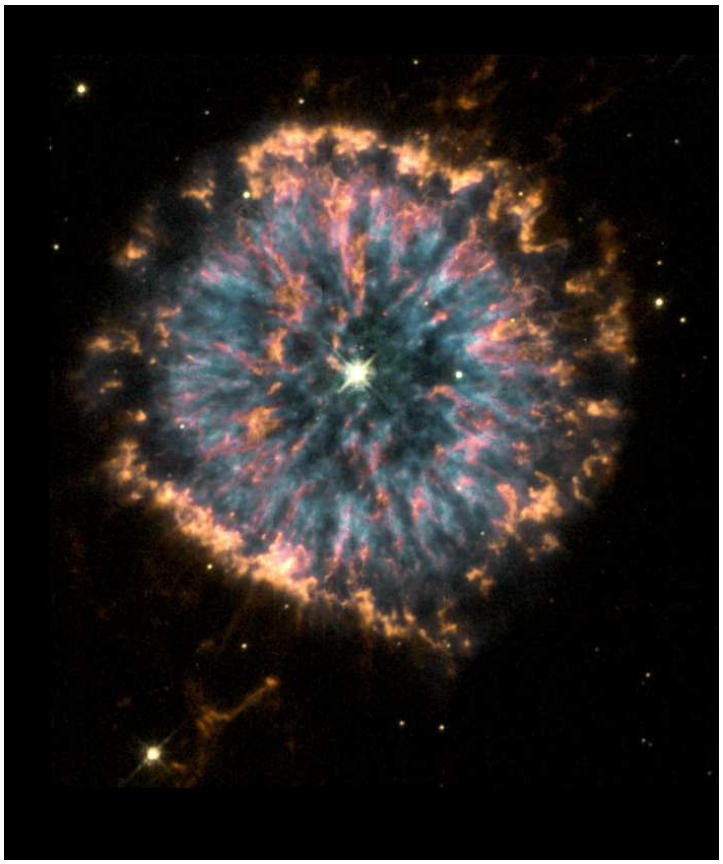

FIGURE 3.25.: A composite colour Hubble image of NGC 6751.

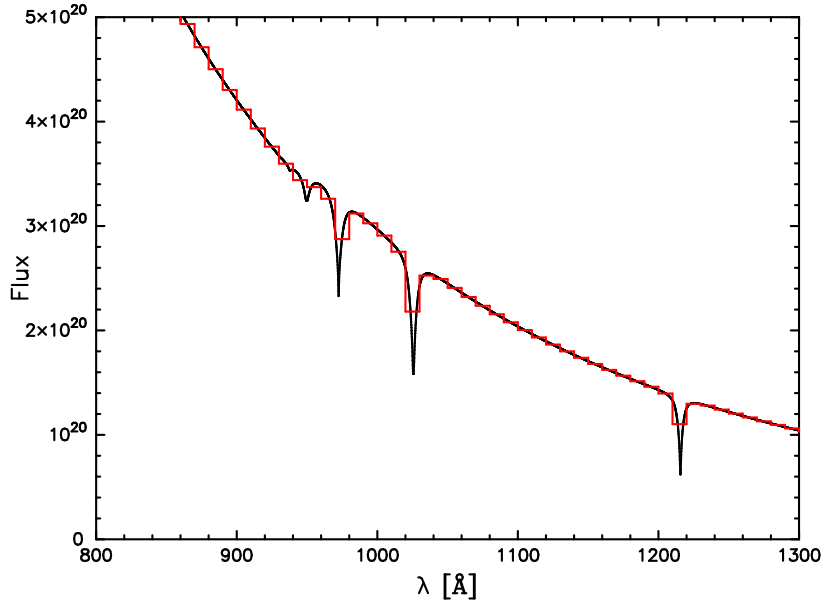

FIGURE 3.26.: Original (black) – and rebinned (red) Rauch (2003) spectrum of a central star of a planetary nebula with $T_{\rm eff}$ = 140' 000 K (see NGC 6751) and $\log g$ = 8.0.

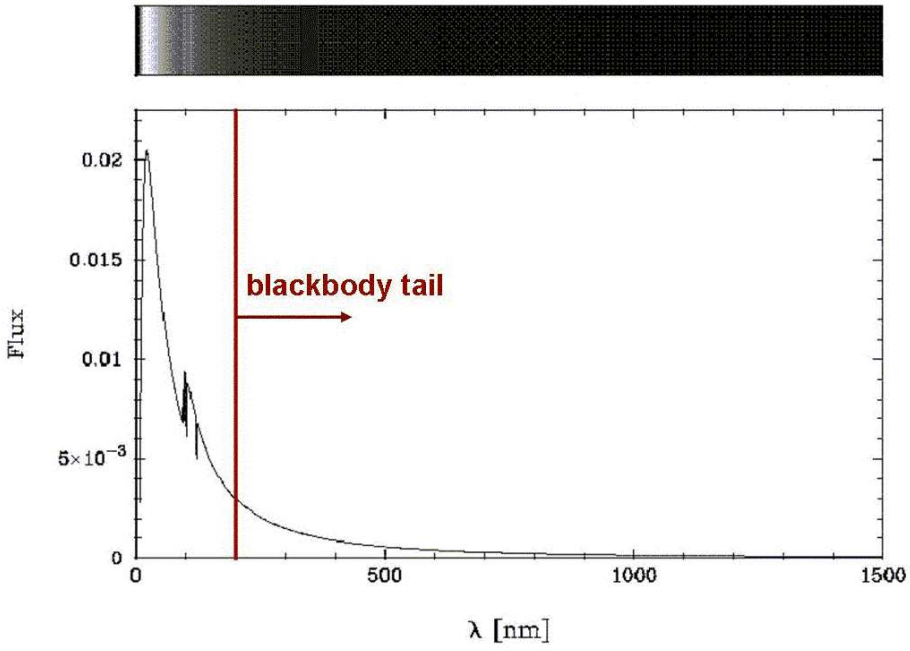

FIGURE 3.27.: Central star spectrum of a planetary nebula with $T_{\rm eff}$ = 140' 000 K (see NGC 6751) and $\log g$ = 8.0 including the extension in the optical and near-IR.

3.4.4. Resulting parameter range of BaSeL 3.2

The enhancement of the BaSeL 3.1 library (with spectra of white dwarfs and hot central star spectra of planetary nebulae) led to the new library: BaSeL 3.2. This theoretical spectral library encompasses the parameter ranges illustrated in Figure 3.28.

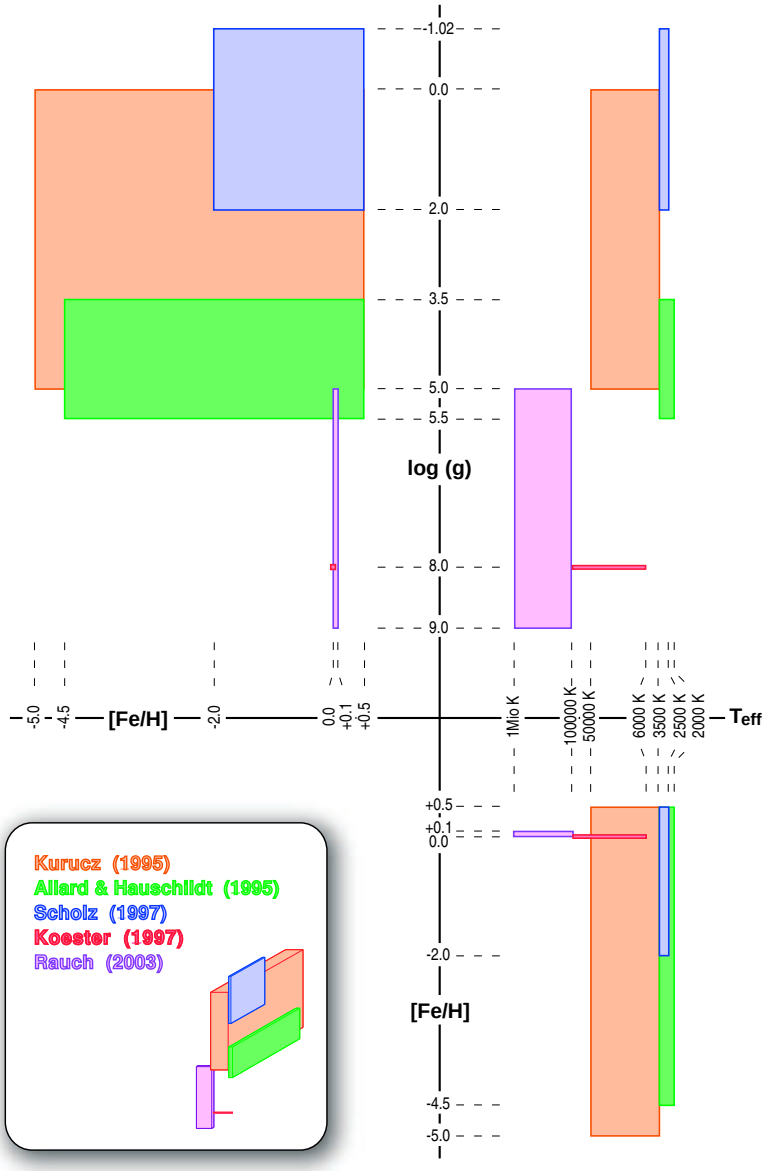

FIGURE 3.28.: Parameter coverage of the final combined BaSeL 3.2 library. Produced by D. Cerrito.

The final stellar spectral BaSeL 3.2 library covers all evolutionary phases that are important for this project, and contains a total of 2961 spectra. Each spectrum covers a wavelength range from 9.1 nm to 160 μm, with a mean resolution of 10 Å in the ultraviolet and 20 Å in the visible. In total, each spectrum consists of 1221 wavelength points.

3.4.5. PHOENIX

A very general NLTE stellar atmosphere software package - the PHOENIX code - was used to compute a large variety of stellar spectra: it can calculate models of static stellar atmospheres, i.e., regular main sequence stars, giants, white dwarfs, irradiated planets (Barman, Hauschildt & Allard 2000), and of expanding stellar atmospheres such as nova and supernova shells (Hauschildt & Baron 1999, 2004).

The code is able to deal with extremely complex atomic models as well as line blanketing by hundreds of millions of atomic and molecular lines. The model atmospheres can be calculated in non-local thermodynamic equilibrium, NLTE (for further information about the differences between NLTE and LTE see Appendix A.2), for as many atoms and energy levels as the computational power allows.
Opacities for a given atmosphere structure are directly calculated for as many spectral lines as possible (even blended ones). Atomic and molecular line opacities are selected dynamically for the appropriate LTE background lines and the contribution of all lines are summed up to compute the total line opacity at arbitrary wavelength points. No pre-computed opacity tables but individual line profiles are used. This approach allows to use detailed and depth-dependent line profiles during the iteration process. In this way millions of molecular and dust lines [4], both of which are crucial for the model structure and synthetic spectrum, can be taken into account for cool stellar atmospheres.
Furthermore, a large number of NLTE and LTE background lines are included. The code solves the radiative transfer equation for each of these lines without using a simplifying approximation. Therefore, high resolution is needed. The Phoenix code resolves the line profiles into typically 50' 000 wavelength points! (In contrast, the BaSeL 3.2 theoretical spectra have only 1' 221 wavelength points.) Details about the numerical methods of the code can be found in Hauschildt, Lowenthal & Baron (2001).
The atmospheres are divided into multiple layers at different optical depths. For each of them a set of physical variables (i.e., temperature, density, velocity field, population number of each atomic level, and the radiation field) are calculated (Petz 2005). All required equations have to be simultaneously solved for each layer. In each iteration step, the code calculates the temperature structure, the opacities, and the NLTE departure coefficients for each layer from a previous iteration. (The departure coefficients describe the relative fractions of level population numbers calculated in NLTE to LTE. For further information see Petz (2005)).
The radius from the centre of the star to each layer is also calculated. To each radial point the code assigns a set of physical variables like temperature, gas pressure and level populations. As a next step, the radiation transport equation is solved for all wavelength points. The radiation field for all wavelength points is then obtained for each layer. In addition, the flux at each wavelength, a synthetic spectrum, can be calculated.

The radiative transfer in this code is treated with special relativity, one-dimensional spherical geometry in the models and a fixed stellar mass of $1 M_{\odot}$ (Brott & Hauschildt 2005). The basic assumptions for the grid are time independence, hydrostatic and thermal equilibrium, and local thermal equilibrium. The mixing length parameter $\alpha_{ML} \equiv l / H_p = 2.0$ (l is the mixing length, H_p the local pressure scale height) defines the convection treatment. All models include a constant statistical velocity field, $\chi = 2$ km^{-1}, which is treated like a microturbulence.

For this study, we are interested in the 44' 000 model atmospheres that were generated for the Gaia mission (the so called "Gaia grid", produced by Brott & Hauschildt (2005)).

The model atmospheres and synthetic spectra of the Gaia grid computed with the PHOENIX v13 code cover the following parameter ranges (Brott & Hauschildt 2005)[5]:

- 2' 700 $\leq T_{\rm eff} \leq$ 5' 000 K in steps of 100 K
  5' 000 $\leq T_{\rm eff} \leq$ 10' 000 K in steps of 200 K

[4] The dust in cooler models forms and immediately rains out completely below the photosphere. For $T_{\rm eff} > 2'$ 700 K, dust formation can be neglected.

[5] All synthetic spectra of the Gaia grid are publicly available via ftp: ftp.hs.uni-hamburg.de/pub/outgoing/phoenix/GAIA.

- $-0.5 \leq \log g \leq 5.5$ in steps of 0.5
- $-3.5 \leq [\mathrm{Fe/H}] \leq +0.5$ in steps of 0.5
- $-0.2 \leq [\alpha/\alpha_{\odot}] \leq +0.8$ in steps of 0.2.

The Gaia grid also includes variations of α-elements, where α denotes elements such as O, Ne, Mg, Si, S, Ar, Ca and Ti, for each set of parameters (T_{eff}, $\log g$ and $[\mathrm{Fe/H}]$). All α-elements are multiples of He, synthesised by alpha capture in Type II supernovae shells.
Today, we know that the solar heavy-element distribution should not be applied to all Galactic populations. Especially, for the stellar components of the Galactic halo (field– and globular cluster stars) that have enhanced α-abundances with respect to iron ($[\alpha/\mathrm{Fe}] > 0.0$), this assumption is wrong (Lambert 1989). Nevertheless, we neglect the α-element enhancements and use only solar element ratios for our analyses. We give our motivation in the following paragraphs.

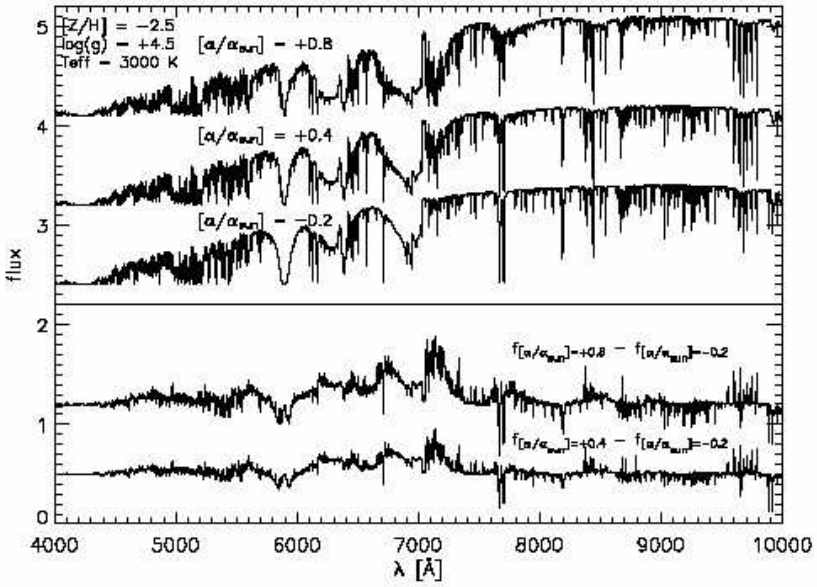

FIGURE 3.29.: The variation of the stellar energy distribution of a 3' 000 K model star with decreasing α-element abundance (compared to the solar value: $[\alpha/\alpha_{sun}]$ = -0.2). The difference spectra are shown in the lower part of the panel, illustrating the effects of α-element abundances (Brott & Hauschildt 2005).

After varying the abundance of the α-elements O, Ne, Mg, Si, S, Ca, Ti in their models (for an example see Figure 3.29), Brott & Hauschildt (2005) pointed out, that the effect of α-element abundances on synthetic spectra is small. It only becomes important at low temperatures ($T_{\mathrm{eff}} \leq$ 3' 000 K) and/or metal rich atmospheres ($[\mathrm{Fe/H}] \geq$ +0.5). The percentage of cool (= faint) stars in our theoretical stellar samples is very low due to the applied limiting apparent magnitude. Similarly, high metallicity stars are considered to be outnumbered by metal-poorer stars.

Another reason why we ignore α-element enhancements in our analyses can be found in King (1997), Carney et al. (1997) or Nissen & Schuster (1997): they all detected halo stars that have significantly lower $[\alpha/\mathrm{Fe}]$ values than disk stars of the same metallicity. Even if it is only a matter of anomalous halo stars that were accreted from dwarf galaxies with a chemical evolution history different from that of the inner halo and disk, it would be inappropriate to use a certain α-enhancement for all halo stars.
For these reasons we only use solar element ratios.

The original PHOENIX models have a resolution of 2 Å (with typically 50' 000 wavelength points, as mentioned above) from the UV (1.0 nm) to the infrared (50 μm), which we convert to the lower BaSeL 3.2 resolution of 10 or 20 Å.
In order to make the BaSeL 3.2 and the Phoenix library congruent, we supplement the Gaia grid for stars with effective temperatures of 10' 000 $< T_{\rm eff} \leq$ 50' 000 K with spectra from the BaSeL 3.2 library. Futhermore, we extend this library in the same manner as the enhanced BaSeL 3.1 library, with spectra of white dwarfs and hot central stars of planetary nebulae. Examples of spectra from the Phoenix library are shown in Figure 3.30.

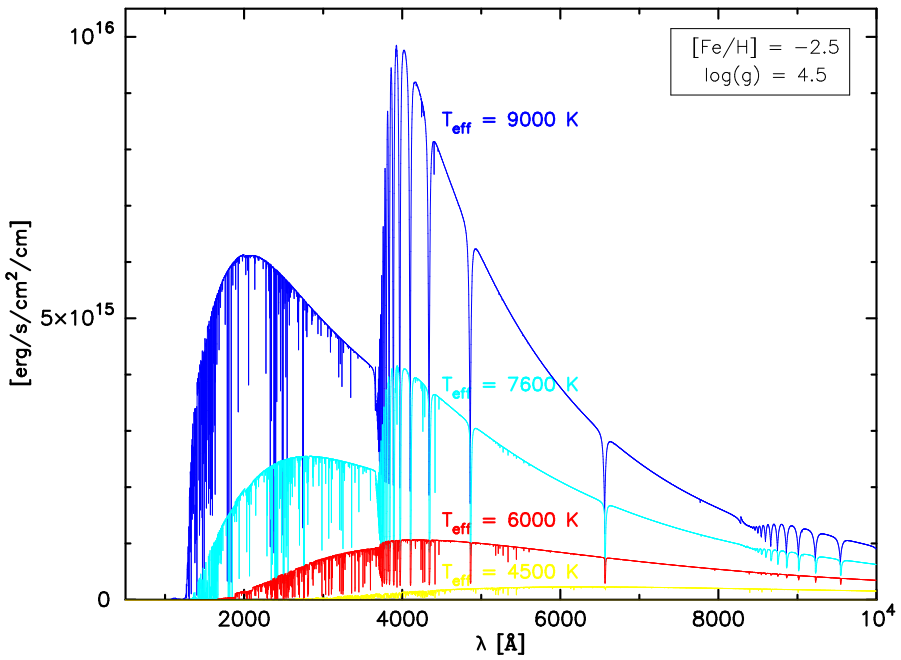

FIGURE 3.30.: Variation of the effective temperature in a model with constant metallicity and surface gravity.

4. Derived theoretical data

4.1. Simulations of theoretical stellar populations and surveys

4.1.1. Drawing the stars

Stars are the fundamental building blocks of galaxies. In this work, we test the realism of the model galaxy by comparing the theoretical stellar distribution with observations. Our real Milky Way galaxy is composed of 200 to 400 billion stars (the exact number is not yet known). Treating stars like point masses allows one to describe their dynamics as classical mechanics. However unfortunately, due to computational limits, it is not possible yet to calculate the orbit of each star individually.

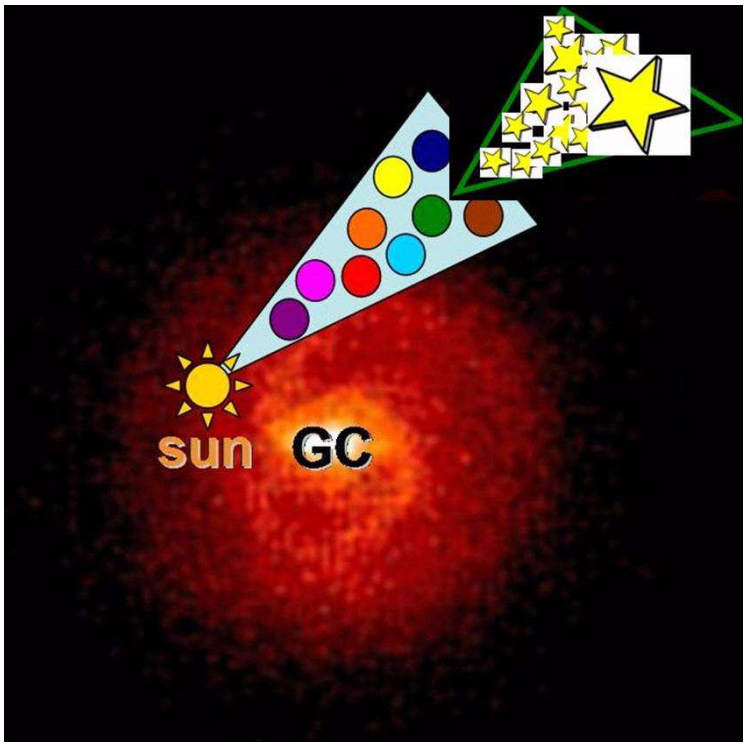

FIGURE 4.1.: From the position of the Sun, we observe the model sky in a certain viewing direction and field size (cyan cone). In this viewing cone, we choose some of the included stellar particles (coloured circles) and dissolve them into individual stars (green triangle). According to the applied IMF individual stars are selected with mass-dependent probabilities.

Samland, Hensler & Theis (1997) and Samland & Gerhard (2003) circumvent this problem by combining a certain number of stars into so-called stellar particles.
These stellar particles represent single stellar populations (SSPs) with typical masses around a few times $10^5\ M_\odot$ and are formed out of a gas cloud in a star forming region. Until this day, the exact mechanisms of the formation of individual stars is not yet completely understood, and therefore, the present substitution of stars by SSPs is justifiable. In that way, 200 billion stars are reduced to 700' 000 stelllar particles.

To be able to compare our models with observational data, we rely on all information concerning individual stars. For this reason, we dissolve the stellar particles into single stars.
The code allows us as observers to take the place of the Sun in the model galaxy (Figure 4.1).
Thence, we "observe" in a certain viewing direction and field size. The particles that belong to this section of the sky have slightly different masses. For these particles, the probability of being "observed" is mass-dependent: The more massive they are, the higher is the probability of being drawn. After the selection of one stellar particle, it is dissolved into individual stars and one of them is drawn mass-weighted according to the applied IMF (Salpeter- or Kroupa-IMF). This procedure of selecting a stellar particle and drawing one star out of that, is repeated until the theoretical stellar sample has the predetermined size.

Each star that has been extracted from the theoretical galaxy as computed by the Samland code has 17 different parameters. The Tables 4.1 – 4.4 list the parameter values of eight stars picked at random from such a model galaxy of a theoretical stellar sample.
For our project the most important parameters are given in Table 4.1: distance to the observer, time-independent, i.e. constant metallicity, current age and initial mass.
The stellar metallicity is provided in different units (Table 4.3): $logZ$ is used to extract $T_{\rm eff}$ together with $\log g$ from the Padova94 stellar evolutionary track library (see Subsection 4.1.2) and $[{\rm Fe/H}]$ to find the appropriate stellar spectrum out of the BaSeL 3.2 library (see Subsection 4.1.3).

TABLE 4.1.: Main parameters delivered by the Samland model.

Star number	dist [kpc]	log Z	age [Gyr]	mass [$M_\odot$]
1	0.193	-1.109	11.17	0.27
2	0.214	-0.061	0.69	0.21
3	0.236	-0.046	2.73	0.29
4	0.306	-0.034	2.45	0.11
5	0.308	-0.269	6.77	0.14
6	0.326	-0.107	2.01	0.23
7	0.342	-0.208	10.64	1.47
8	0.378	-0.171	8.05	0.11

TABLE 4.2.: Dynamical parameters delivered by the Samland model.

Star number	r-dist [kpc]	z-dist [kpc]	vrad [km/s]	vrot [km/s]	vz [km/s]
1	8.183	-0.0575	-9.540	161.903	18.113
2	8.062	-0.1766	21.883	195.062	2.998
3	7.884	-0.0778	11.096	167.020	-9.175
4	7.960	0.0970	50.546	198.568	-7.769
5	7.786	0.0988	-5.071	241.849	13.192
6	8.277	-0.1132	32.759	217.237	-3.867
7	7.933	-0.1808	-17.624	187.225	23.122
8	8.100	-0.0546	-63.869	225.322	-13.434

TABLE 4.3.: Chemical parameters delivered by the Samland model.

Star number	log Z	[Fe/H]	[O/H]	[C/H]
1	-1.109	-1.327	0.348	-1.351
2	-0.061	-0.127	-0.124	-0.251
3	-0.046	-0.082	-0.278	-0.236
4	-0.034	-0.087	-0.485	-0.222
5	-0.268	-0.345	0.272	-0.482
6	-0.107	-0.180	-0.036	-0.303
7	-0.207	-0.410	-0.125	-0.474
8	-0.171	-0.263	-0.077	-0.397

Additionally, the Samland code also delivers the position and velocities of each star at its birth (Table 4.4).

TABLE 4.4.: Dynamical parameters at the date of birth delivered by the Samland model.

Star number	r-dist [kpc]	z-dist [kpc]	vrad [km/s]	vrot [km/s]	vz [km/s]
1	6.167	0.774	-67.594	174.595	-16.571
2	7.915	0.118	0.421	209.889	9.275
3	7.624	0.215	-24.044	208.588	-3.670
4	7.921	-0.070	6.397	202.421	-1.708
5	9.892	0.438	23.730	182.856	17.346
6	10.523	-0.105	-1.016	208.296	1.191
7	4.000	0.148	31.494	143.142	26.447
8	6.564	-0.062	-18.538	170.021	-9.355

4.1.2. Atmospheric parameters

The **chemo-dynamical code** of Samland, Hensler & Theis (1997) and Samland & Gerhard (2003) provides stellar initial mass, current age and metallicity for each star. As mentioned in Subsection 3.3, in order to transform these parameters into observable magnitudes and colours, we take a little detour to the **Padova94** library and assign the corresponding atmospheric parameters (effective temperature ($T_{\rm eff}$) and surface gravity ($\log g$)) to each star from these stellar evolutionary tracks.
The stellar masses, ages and metallicities provided by the Samland code typically lie in between the mass, age and metallicity values covered by the Padova94 library, so we have to interpolate between two neighbouring values. Table 4.5 lists the first four columns of the stellar evolutionary track of a one solar mass star of solar metallicity to show how the Padova94 tracks are structured: for a certain number of initial stellar masses (on average 37 different masses) and metallicities (7, therefore the Padova94 tracks are divided into seven subsamples), the tracks provide for each age step (usually 311 time steps for one track) the values of $T_{\rm eff}$ and $\log g$.

TABLE 4.5.: The first four columns of a Padova1994 track directory

M = 1.00 $M_\odot$: **Z = 0.020**, Y = 0.280 (i. e., $[{\rm Fe/H}]$ = 0.0)

age	$L/L_\odot$	$T_{\rm eff}$	$\log g$
0.00000E+00	-0.181	3.745	4.545
2.00910E+09	-0.100	3.754	4.499
3.68795E+09	-0.046	3.758	4.46
...	...	...	...

As can be seen in Table 4.6, the mass steps for lower mass stars ($< 4.0\ M_\odot$) are much smaller than for higher mass stars ($\geq 4.0\ M_\odot$).

TABLE 4.6.: Masses $M_\odot$ of the track directory with Z = 0.020 (i. e., $[{\rm Fe/H}]$ = 0.0)

120.0000	100.0000	60.00000	40.00000	30.00000
20.00000	15.00000	12.00000	9.000000	7.000000
6.000000	5.000000	4.000000	3.000000	2.500000
2.200000	2.000000	1.800000	1.600000	1.500000
1.400000	1.300000	1.200000	1.000000	0.9000000
0.8000000	0.7000000	0.6000000	0.5000000	0.4000000
0.3000000	0.2000000	0.1500000	0.1300000	0.1100000
0.1000000	9.0000004E-02			

Because of this, our derivation of the physical parameters also follows this mass-dependency. The left panels of Figure 4.2 display the luminosity evolutions of four stars with different initial masses. In the upper left panel, the evolutionary paths of a pair of low-mass stars ($M_* = 0.9\ M_\odot$ and $M_* = 0.8\ M_\odot$, respectively) are shown and

in the lower left panel those of two higher-mass stars ($M_* = 40.0\ M_\odot$ and $M_* = 30.0\ M_\odot$, respectively).
To better understand the shapes of the evolutionary tracks in the left panels, we show the H-R diagrams of a 0.8 $M_\odot$ star and a 40.0 $M_\odot$ star in the upper and lower right panels.

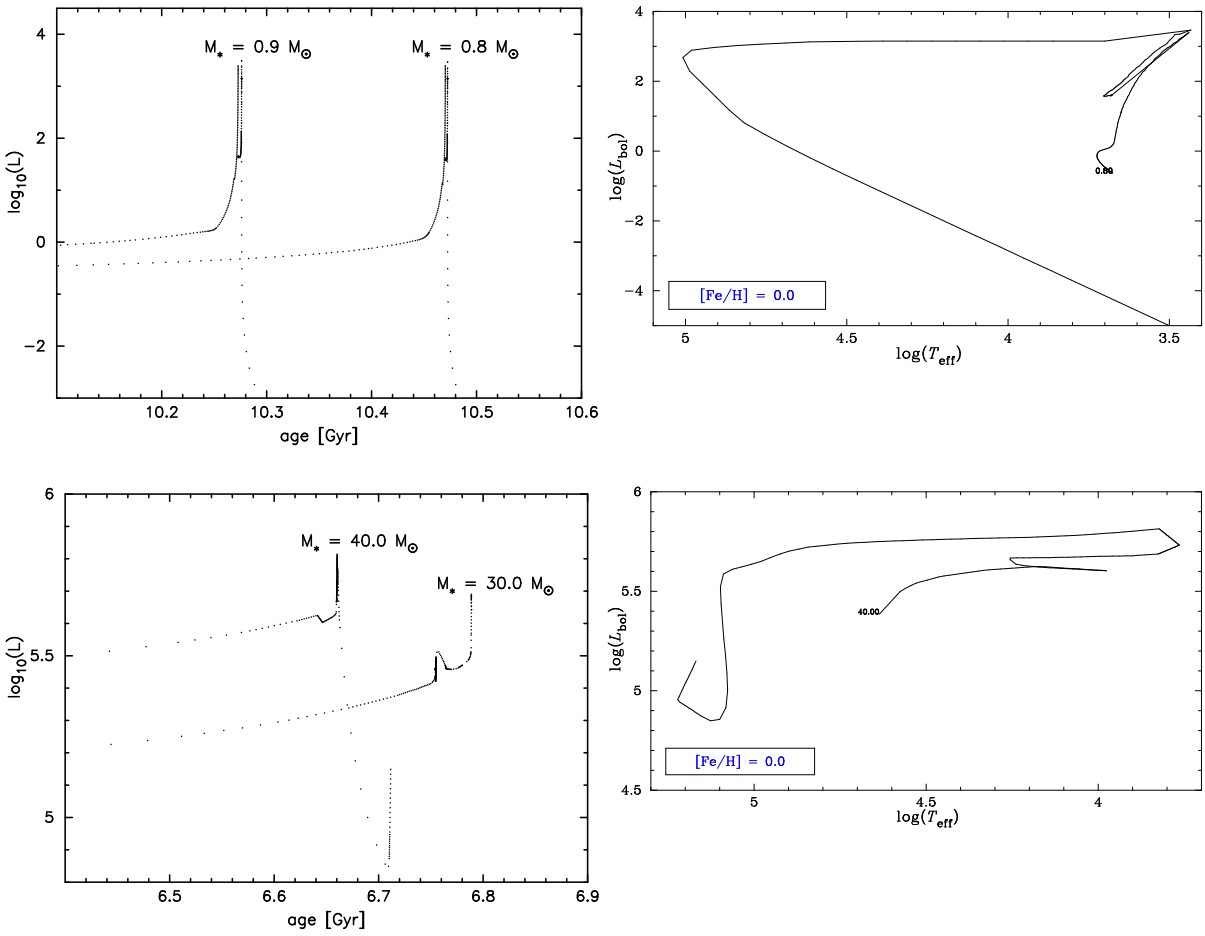

FIGURE 4.2.: Left panels: Two pairs of tracks corresponding to neighbouring masses in the age versus luminosity plane: two low-mass stars ($M_* = 0.9\ M_\odot$ and $M_* = 0.8\ M_\odot$) in the upper panel and two higher mass stars ($M_* = 40.0\ M_\odot$ and $M_* = 30.0\ M_\odot$) in the lower panel. Right panels: H-R diagrams for a 0.8 $M_\odot$ (upper panel) and a 40.0 $M_\odot$ (lower panel) star.

The difference between these two pairs is obvious: The shapes of the paths of the two low-mass stars are much more similar than those of the higher-mass stars. Therefore, we divide the theoretical stars into two subsamples depending on their masses, stars with stellar masses $< 4.0\ M_\odot$ and stars with stellar masses $\geq 4.0\ M_\odot$, and use another method for stars from either subsample to derive atmospherical parameters. In the next two parts the two different ways of extraction are described.

Stars with masses $< 4.0\ M_\odot$

As stated above, the Samland code provides stars of certain initial masses, ages and metallicities, which typically lie between two values provided by Padova94. The quite similar shapes of the luminosity-$T_{\rm eff}-$ and the luminosity-$\log g$ functions of two neighbouring low-mass stars (see Figure 4.2, upper panel) allows us to simply

interpolate between the neighbouring values.
Figure 4.3 gives an overview of the main methodical steps we apply to lower mass stars.

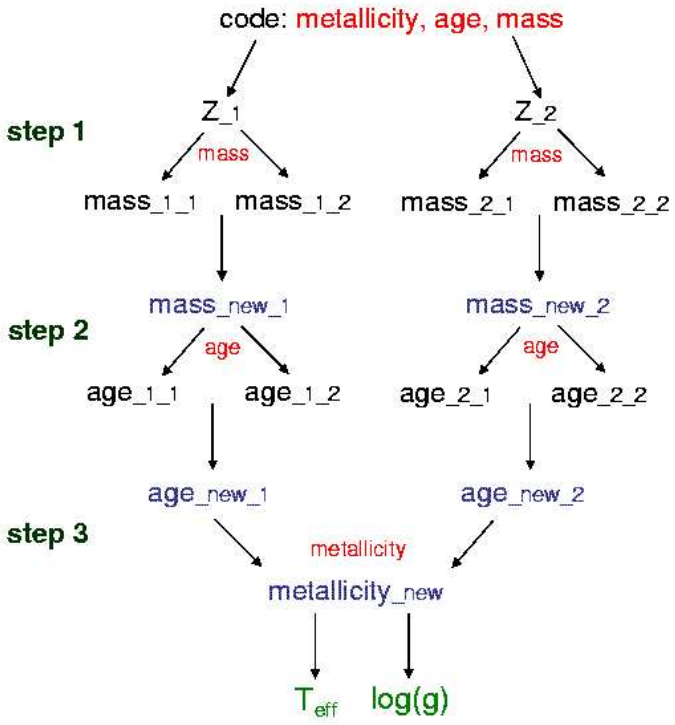

FIGURE 4.3.: The three main steps of the interpolation routine applied to low-mass stars. In red the three parameters provided by the Samland code are given. In black, those of the Padova94 library. Highlighted in blue and green are the resulting interpolated parameters.

First, we choose the two metallicity subsamples (Z_1, Z_2) of the Padova94 library that bracket the metallicity given by the code ($[\mathrm{Fe/H}]_{code}$). For each metallicity pair (Z_1, Z_2), we interpolate between the two masses (between $mass_{1_1}$ and $mass_{1_2}$ and between $mass_{2_1}$ and $mass_{2_2}$, respectively) that lie next to the mass given by the code (M_{*code}) (see step1 in Figure 4.3).

Figure 4.4 shows an example of the inverse distance weighting interpolation between two neighbouring Padova masses (1.0 $M_\odot$ and 1.2 $M_\odot$) to derive new age-$T_{\rm eff}$ – and age-$\log g$ functions, for the star with the initial mass M_{*code} =1.18 $M_\odot$.
For one metallicity (Z_1), the resulting temperature– and surface gravity evolutions can be seen in the upper and lower panel, respectively.
The same procedure is applied to the other neighbouring metallicity (Z_2). By proceeding in this way, we end up here with two new functions in the age-$T_{\rm eff}$ plane and two new functions in the age-$\log g$ plane, in each case one for each metallicity.

As a next step, we interpolate between the new functions in the age-$T_{\rm eff}$ plane of the first bracketing metallicity (Z_1) and the new functions in the age-$T_{\rm eff}$ plane of the second one (Z_2), for the age given by the code (age_{code}) (see step2 in Figure 4.3). The same is done for the new functions in the age-$\log g$ plane. We now have one new function each in the age-$T_{\rm eff}$ – and the age-$\log g$ plane. From these two functions, we read in each case the two ages (age_{1_1} and age_{1_2} and age_{2_1} and age_{2_2}, respectively), from the Padova94 library that are the closest

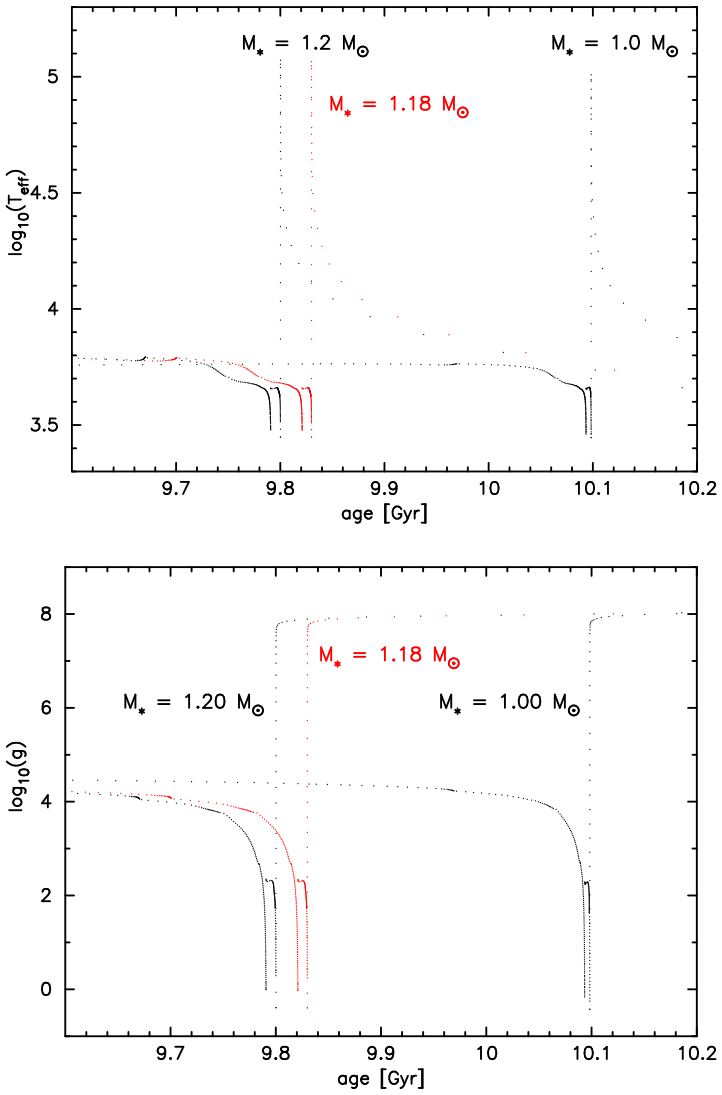

FIGURE 4.4.: Interpolation by inverse distance weighting in $T_{\rm eff}$ (upper panel) and $\log g$ (lower panel) for a stellar mass of 1.18 $M_{\odot}$.

to the age (age_{code}) given by the code.

The next step consists of the interpolation between these bracketing ages (age_{1_1} and age_{1_2}, and age_{2_1} and age_{2_2}, respectively) in both planes (the age-$T_{\rm eff}$ and age-$\log g$) onto the metallicity of the drawn star, $[{\rm Fe/H}]_{code}$ (see step3 in Figure 4.3).

In a final step, we read out the appropriate $T_{\rm eff}$ and $\log g$.

Stars with masses $\geq$ 4.0 $M_{\odot}$

For stars with higher (or equal) masses than 4.0 $M_{\odot}$, linear interpolation is not possible anymore. The mass steps increase strongly with the stellar mass (see Table 4.6), and the shapes of the tracks change drastically in the age-$T_{\rm eff}$ and in the age-$\log g$ planes.

As an example, Figure 4.5 shows the different shapes of four stellar evolutionary tracks of the Padova94 library in the age - log(L) plane. All of them have the same metallicity, $[\mathrm{Fe/H}] = 0.0$. Obviously, linear interpolations between two neighbouring tracks does not make sense. Therefore, we just select the track, whose mass lies closest to the M_{*code}.

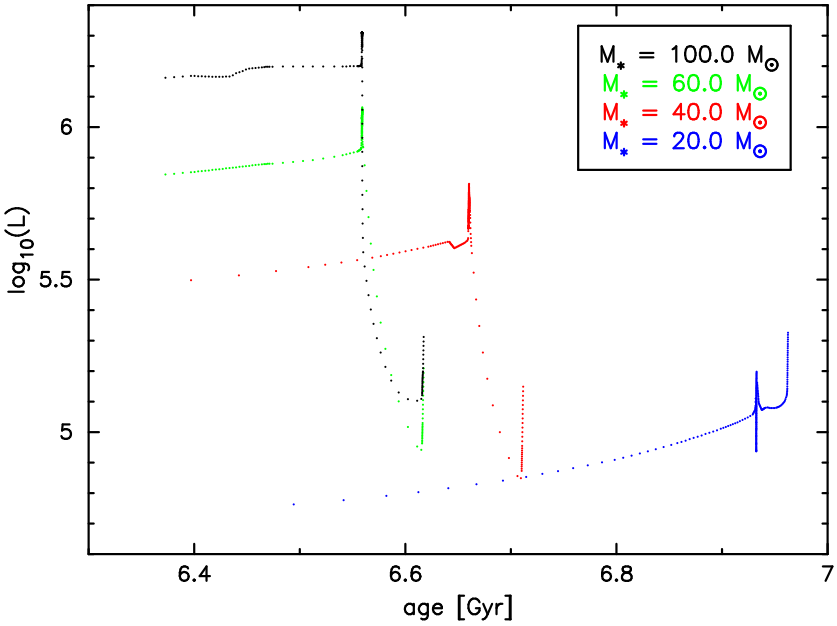

FIGURE 4.5.: Luminosity evolutions of four different high-mass stars (a 20 $M_\odot$ – (in blue), a 40 $M_\odot$ – (in red), a 60 $M_\odot$ – (in green), and a 100 $M_\odot$ star (in black)), all with $[\mathrm{Fe/H}] = 0.0$. See also Figure 4.2 (lower panel).

4.1.3. Synthetic spectra, magnitudes and colours

The stellar evolutionary track library Padova1994 provides a set of fundamental atmospheric parameters ($T_{\rm eff}$, $\log g$ and $[{\rm Fe/H}]$) for every star, which we use to generate synthetic stellar spectra and synthetic photometry from the extended BaSeL 3.1 and PHOENIX libraries.
To extract the appropriate spectrum, we linearly interpolate the spectra of the chosen library grid first in $T_{\rm eff}$ and $\log g$, and finally in $[{\rm Fe/H}]$.

We use the photometric response functions of the Sloan Digital Sky Survey system (Fukugita et al. 1996) (plotted in Figure 4.6: left panel) and those of the New Basel high-latitude field star survey system (Buser & Kaeser 1985; Buser, Rong & Karaali 1998, 1999) (see Figure 4.6: right panel), to obtain absolute magnitudes and colours in the *ugriz*− and RGU photometric passbands, respectively.

The chemo-dynamical galaxy model gives the stellar distance, and by means of the distance modulus

$$m = M + 5 \cdot log(r) - 5 + A(r) \tag{4.1}$$

(r = stellar distance in pc, A(r) = interstellar extinction and absorption),
we calculate the apparent magnitudes and colours for every star. In our study, for comparisons with observational data, we take only those fields into consideration that are known not to suffer from interstellar reddening (SA94, M101). Therefore, A(r) is zero in Equation 4.1 .

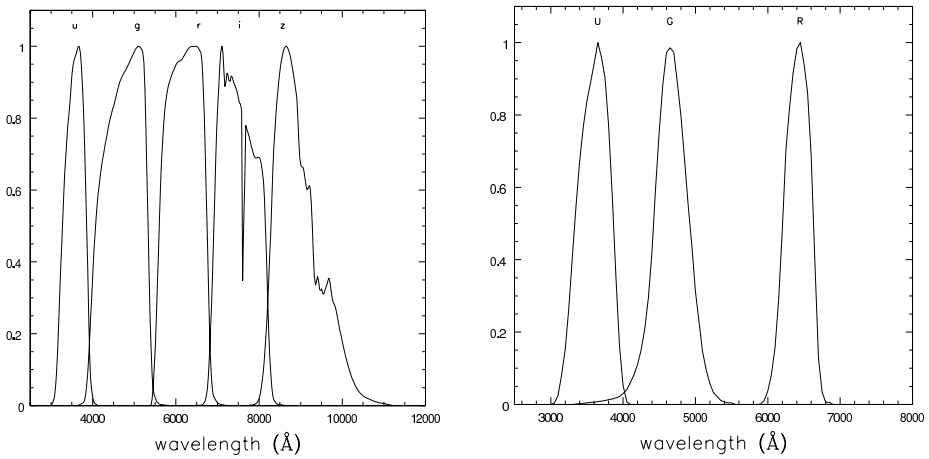

FIGURE 4.6.: Filter functions of the Sloan Digital Sky Survey (left) and of the New Basel high-latitude field star survey plotted (right) (Jordi, Grebel & Ammon 2005).

4.1.4. Catalogue of resulting intrinsic parameters

By merging all these ingredients together we end up with a full set of parameters for every kind of star.

The **Galactic model** provides:

- *mass*
- *age*
- *metallicity*
- *distance and velocity*
- *gas and dust distribution.*

The **stellar evolutionary tracks** deliver:

- *effective temperature*
- *surface gravity.*

The **synthetic spectral libraries** give:

- *spectra.*

From these, in connection with various adopted **filter systems** and **interstellar reddening conditions**, we get:

- *absolute and apparent magnitudes*
- *apparent colours in different filterbands.*

Our code allows us to generate the whole parameter set for every star in a certain viewing direction and of a certain field size within different types of galaxies at different evolutionary stages.

4.2. Theoretical stellar populations

4.2.1. Single populations with a Salpeter-IMF

In this Subsection, we investigate the impact of varying ages and metallicities on the colour distributions of single stellar populations (SSPs). This basic knowledge is of great importance for the interpretation of the differences between observational and theoretical star counts, following in Sections 5.1 and 5.2.
An SSP is defined as a stellar population formed during one single, infinitesimally short burst (a so called δ-burst) with an initial mass function (IMF) that describes the stellar mass distribution of the SSP at its birth.

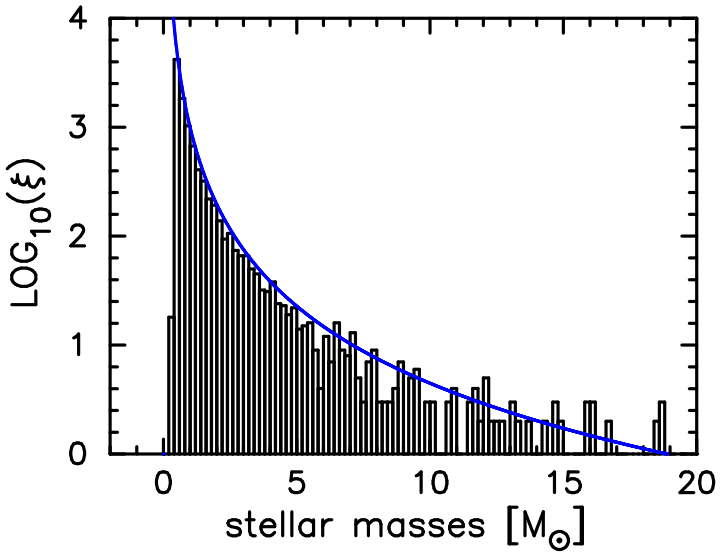

FIGURE 4.7.: Stellar initial mass distribution of the theoretical populations. The blue line indicates the Salpeter-IMF, $\log(\xi) \propto \log(\mathcal{M}^{-1.35})$.

For this analysis we generate 6 test populations, each consisting of 10' 000 randomly drawn stars. Their initial masses follow a Salpeter-IMF (1955) (for further information about the Salpeter-IMF, please look at Section 4.4.3). Figure 4.7 shows the stellar initial mass distribution of these 10' 000 stars. The blue curve shows the Salpeter-IMF, $\xi(\mathcal{M})$. It is described by a power law:

$$\log(\xi) \;=\; \log(c \cdot \mathcal{M}^{-x})$$

where $\xi(\mathcal{M})$: IMF (number of stars per unit mass interval centred on mass $\mathcal{M}$.
c : normalizing factor
x : (negative) exponent

where for the Salpeter-IMF $c = 0.03$ and $x = 1.35$.

The exponent and mass range of the IMF, along with the metallicity characterise a single stellar population (Wenger 2005). These three properties can be used as the elements of a parameter vector that defines an SSP. In this Section, we keep the IMF fixed and just allow the metallicity to vary as follows:

$$\begin{pmatrix}\text{name of the population}\\ \text{IMF slope}\\ \text{IMF mass range}\\ \text{metallicity } Z\end{pmatrix} : \begin{pmatrix}\mathrm{P}_{0001}\\ 1.35\\ 0.4-50.0\\ 0.0001\end{pmatrix} \begin{pmatrix}\mathrm{P}_{0004}\\ 1.35\\ 0.4-50.0\\ 0.0004\end{pmatrix} \begin{pmatrix}\mathrm{P}_{004}\\ 1.35\\ 0.4-50.0\\ 0.004\end{pmatrix}$$

$$\begin{pmatrix}\text{name of the population}\\ \text{IMF slope}\\ \text{IMF mass range}\\ \text{metallicity } Z\end{pmatrix} : \begin{pmatrix}\mathrm{P}_{008}\\ 1.35\\ 0.4-50.0\\ 0.008\end{pmatrix} \begin{pmatrix}\mathrm{P}_{02}\\ 1.35\\ 0.4-50.0\\ 0.02\end{pmatrix} \begin{pmatrix}\mathrm{P}_{05}\\ 1.35\\ 0.4-50.0\\ 0.05\end{pmatrix}$$

Using the synthetic spectra of the stars of these test populations at ages 0.1, 0.3, 1.0, 3.0, 5.0 10.0 and 12.0 Gyr, respectively, we investigate their $ugriz$ colours in the SDSS photometric system.

Analysis of the colour-mass relations of P_{008}

As a first step, we have a look at the colours of the stars of one population as a function of stellar mass. Figure 4.8 shows the mass-colour distributions of the Population P_{008} at an age of 5 Gyr for all possible $ugriz$ colours. In general, the colours in all the plots of Figure 4.8 become bluer (i.e., numerically smaller) with increasing mass. Only for stars with masses $\geq 1.15 M_{\odot}$, this is not the case. At the age of 5 Gyr, these more massive stars are about to leave the main sequence and become subgiants.
The plots produced with the redder colours $r-i$, $r-z$ and $i-z$ show a strange turning-point at a mass of around $0.53 M_{\odot}$. It is not clear yet, whether this is an artefact due to the stellar tracks or due to the BaSeL 3.2 spectral library, which is not sufficiently tested in this low-mass range. For the comparison with observations this feature is not of prime importance, simply because such low-mass stars are not very numerous in the actual observed surveys.
Upon closer inspection, one notices that some curves flatten quite a bit in certain mass ranges. For instance, $u-g$ stays almost constant ($\sim$ 1.0 mag) for all stars with masses between $1.0 M_{\odot}$ and $1.14 M_{\odot}$.

TABLE 4.7.: Bin widths depending on colours

bin width [mag]	colours
0.2	u-g, u-r, u-i, u-z
0.1	g-r, g-i, g-z
0.05	r-i, r-z, i-z

In order to compare observations with our theoretical stellar samples, we first bin the stars in colour bins and then analyse the resulting colour distributions. Because of the large differences in the sizes of the colour ranges, we chose different widths for the bins of different colours, given in Table 4.7.
For illustration, in Figure 4.8 the upper and lower limits of the bluest colour bins are marked (violet-blue horizontal lines), bracketing the flattened parts of the colour curves. As one can easily read out of the $u-g$ - mass relation plot, all stars within the mass range of $0.87 M_{\odot}$ and $1.17 M_{\odot}$ fall into the same colour bin. Considering that the majority of the stars observed nowadays lie in the mass range $0.8 M_{\odot} \leq M_{*} \leq 1.2 M_{\odot}$, the impact of this on the binned colour distribution is not negligible, as we shall see below.
Also note that the flattening gradient is colour-dependent: Colours like $u-g$, $u-r$ and $i-z$ have flatter curves than the other ones.

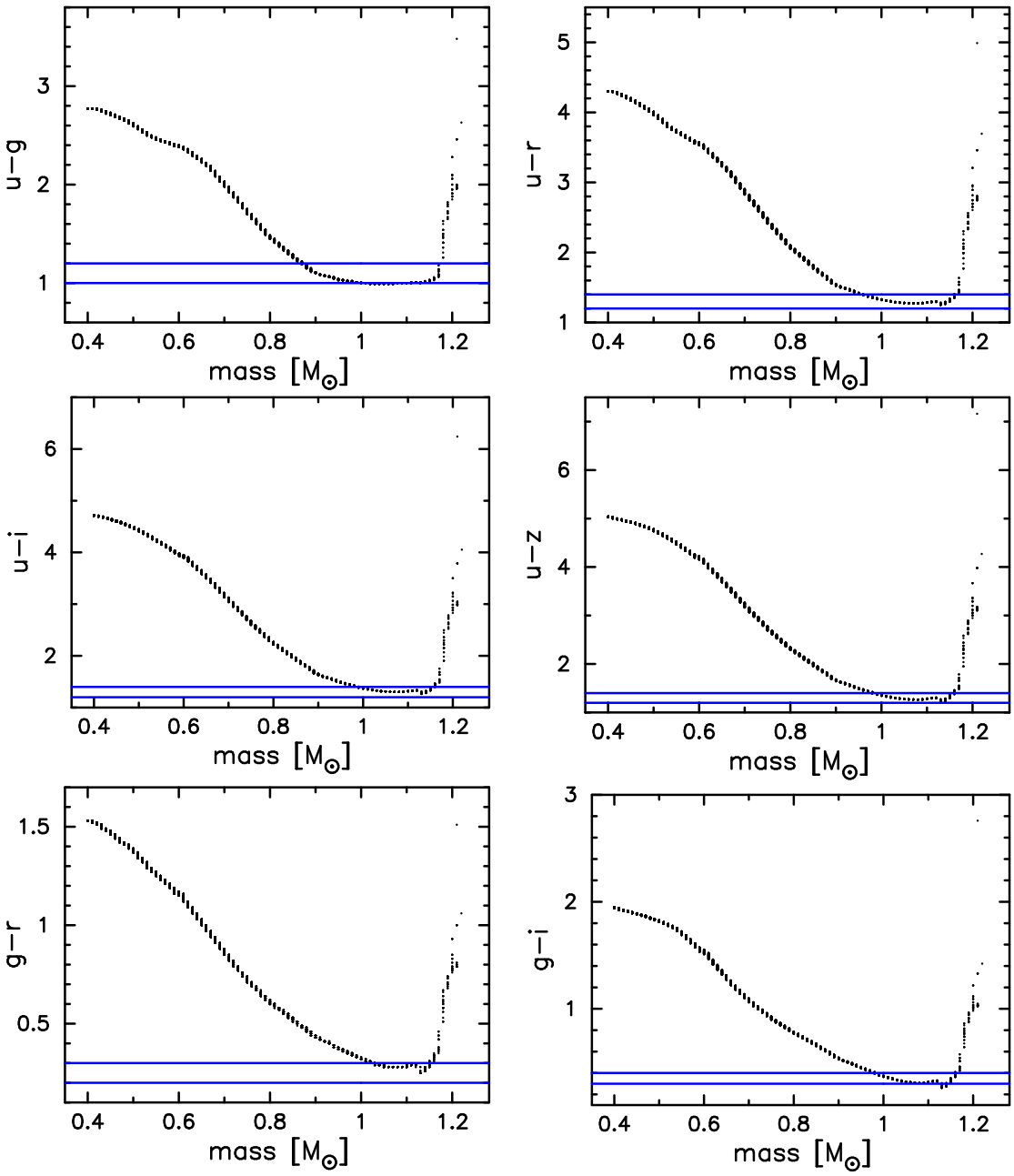

FIGURE 4.8.: Mass-colour relations of the Population P_{008} at an age of 5 Gyr. The blue lines indicate the upper and lower limits of a colour bin of width given in Tab. 4.7.

Analysis of two colours of P_{008} at different ages

In Subsection 4.2.1, we identified the flattening of some colours in certain mass ranges of the population P_{008} at 5 Gyr. In this Subsection we investigate their age-dependence by analysing star counts in two colours ($u-g$ and $g-z$) of the same population (P_{008}), but at different ages.

Figure 4.9 illustrates the evolution of the $u-g$ colour histogram in different time steps, demonstrated in star count diagrams. The Salpeter-IMF makes the histograms peak in the region $u-g > 2.2$ at every age. The flat-

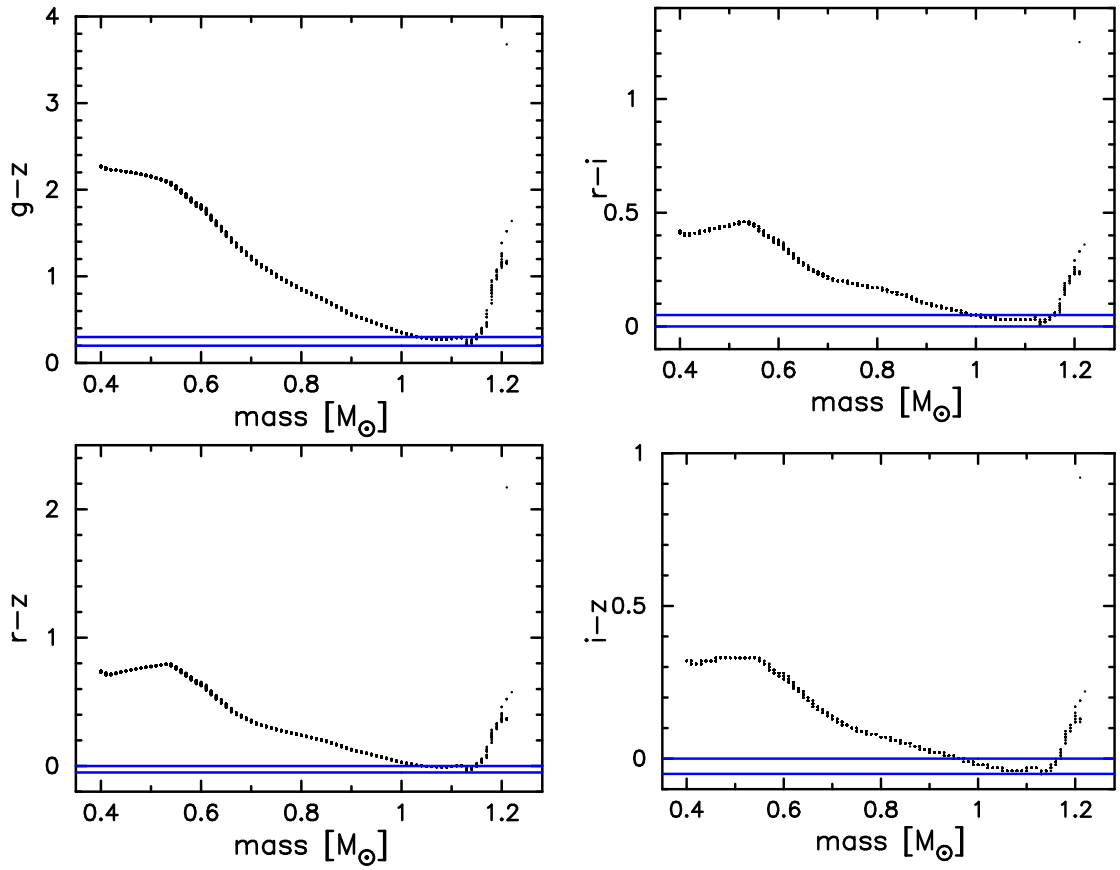

FIGURE 4.8.: Mass-colour relations of the Population P_{008} at an age of 5 Gyr. The blue lines indicate the upper and lower limits of a colour bin of width given in Tab. 4.7 (continued).

tening detected in Subsection 4.2.1, which is visible in the higher colour bins at $0.8 \leq u-g < 1.0$ (painted in yellow) and at $1.0 \leq u-g < 1.2$ (painted in orange), appears at all ages. At ages > 5 Gyr, the massive stars that populated the $0.8 \leq u-g < 1.0$ bin before, have left the main sequence and turned into redder subgiants. This migration empties the $0.8 \leq u-g < 1.0$ bin at that age.
Nevertheless, even at the age of 12 Gyr the peak $1.0 \leq u-g < 1.2$ remains in this theoretical star count.
Figure 4.10 is a counter-example, which shows that many other colours do not produce such peaks. In this colour, the low mass stars become manifest in the bins $g-z > 2.2$. Another small peak is apparent in all plots in the bluest bins. But its height is not much above the average height of the $g-z < 2.2$ bins.

The colour-magnitude diagram should help to understand how the flattenings that we have seen in Subsection 4.2.1 develop.
The left panel of Figure 4.11 shows the relation between the absolute g-Magnitude (M_g) and the $u-g$ colour, and in the right panel of Figure 4.11 the relation between the absolute g-Magnitude (M_g) and the $g-z$ colour is plotted.
The differences in the main sequences catch the eye: the $(g-z) - M_g$ relation can be described as approximately linear, whereas in the $(u-g) - M_g$ plot, only the bluest and the reddest part of the graph are approximately linear. In the colour range $0.8 \leq u-g < 1.2$ an s-shaped region appears. Shown in colour are the two bins (in the same way as in Figure 4.9), where the peaks in the colour star counts and the flattenings in the colour-mass relation were detected. In this region, the same colour can be assigned to a range of magnitude values and, therefore, an unambiguous assignment is not possible here.

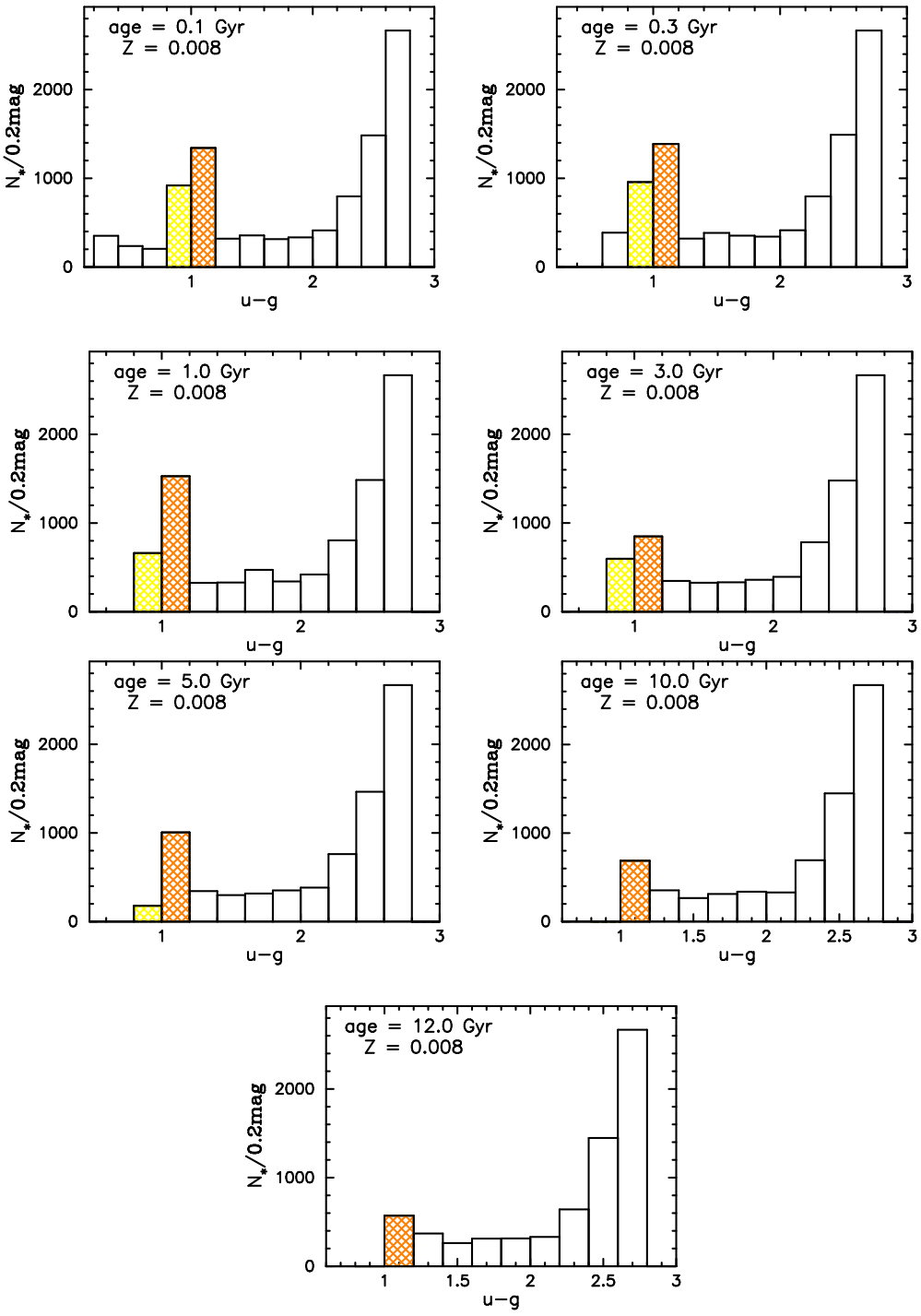

FIGURE 4.9.: Evolution of the $u-g$ colour distribution of the population P_{008}.

It is well known, that the $u-g$ colours of black-body spectra of different temperatures reveal the same trend as the $(g-z)-M_g$ curve.

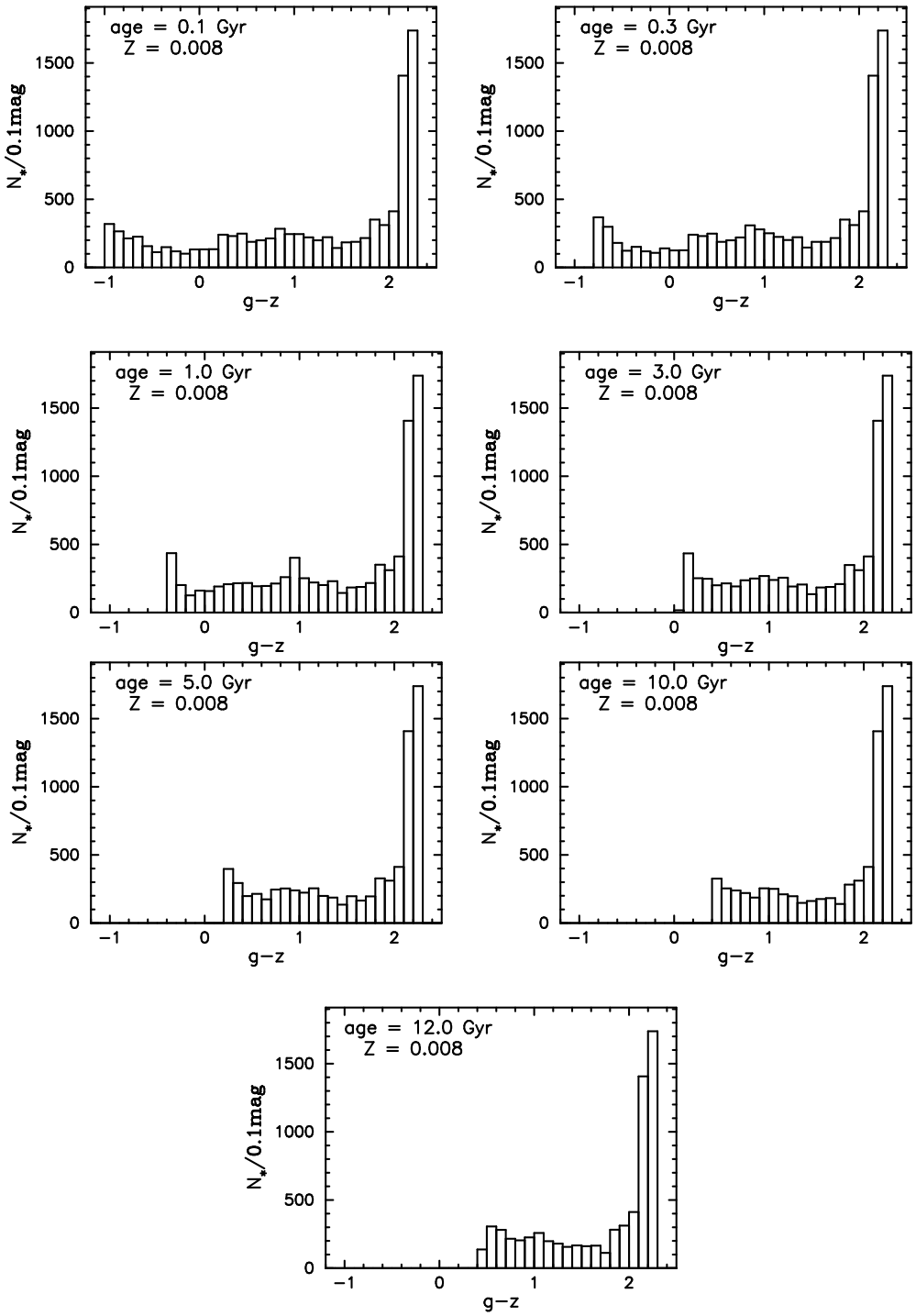

FIGURE 4.10.: Evolution of the $g-z$ colour distribution of the population P_{008}.

As an example for the behaviour of the $U-B$ colours of white dwarfs, Figure 4.12 summarizes all the effects (Balmer jump, Balmer lines, H^- maximum and backwarming (bw)) that displace the UBV positions of DA

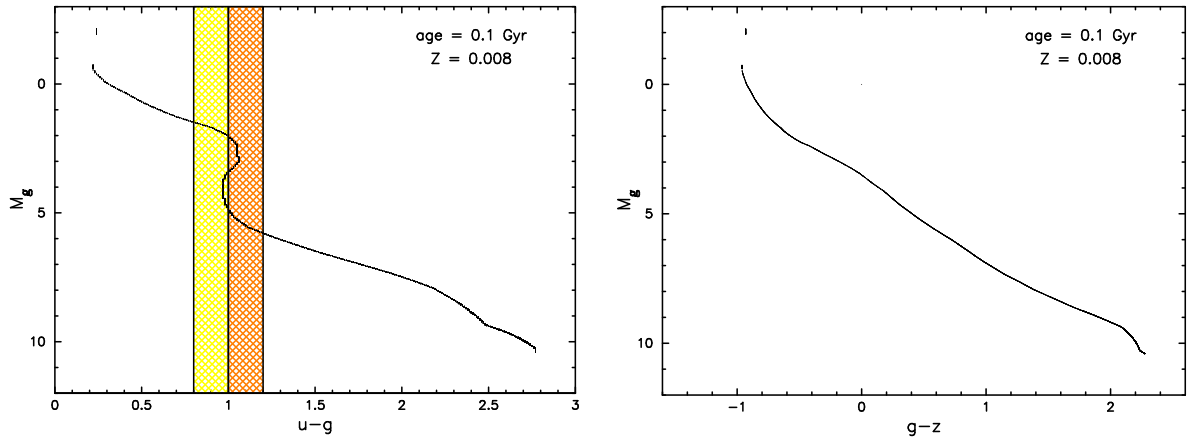

FIGURE 4.11.: Left panel: M_g, $u-g$ colour-magnitude diagram of the population P_{008} at the age of 0.1 Gyr. Shown in colour are the two bins, where the peaks in the star counts appear ($0.8 \leq u-g < 1.0$ in yellow $1.0 \leq u-g < 1.2$ in orange). The line represents main sequence stars exclusively. Right panel: M_g, $g-z$ colour-magnitude diagram of the population P_{008} at the age of 0.1 Gyr.

white dwarfs away from the UBV black-body line.
A similar deviation from the black-body line can be found for main sequence stars in a M_g, $u-g$ colour-magnitude diagram, and is caused by several processes, which are discussed in the following part.

To provide deeper insight into the $u-g$ question, we chose three stars, whose positions mark the most prominent features along the $(u-g) - M_g$ graph in the colour-magnitude diagram. In Figure 4.13, the exact locations of these three stars are shown in black.

From star1 to star3 (earlier- to later-type star) the effective temperatures and masses decrease, whereas the surface gravities increase. Table 4.8 lists the main properties of the three stars: M_u, M_g, u-g, $T_{\rm eff}$, $logg$, and mass.
As one can see, the differences in $u-g$ are not that large, only a few hundredths of a magnitude. But these small colour differences are enough to produce noticable turning points in the colour-magnitude diagram.
From the comparison of the two colour-magnitude diagrams (Figure 4.11, left and right panels), one concludes that the differences in integrated flux in the $u-$band must cause these turning points, since such features are not visible in the $(g-z) - M_g$ plot, where the u-magnitude is not involved.

TABLE 4.8.: Parameters of the three stars

star	M_u	M_g	u-g	$T_{\rm eff}$	$logg$	mass
star1	3.557	2.507	1.05	8267	4.37	1.56
star2	4.971	4.001	0.97	6637	4.41	1.22
star3	6.605	5.505	1.10	5778	4.58	0.95

The three different energy distributions are compared in Figure 4.14. The photometric response functions of the $u-$ and the $g-$ band , respectively, are indicated in blue.
For star1, the (bound-free) Balmer absorption strongly dominates the whole spectrum at wavelengths $\lambda < 370$ nm[1]. The $u-$band covers one section of the Balmer lines ($\lambda > 300$ nm), including the Balmer jump at $\lambda = 365$

[1]The effective temperature of 8267 K is high enough to produce a high Balmer jump, which has its maximum in A0 stellar

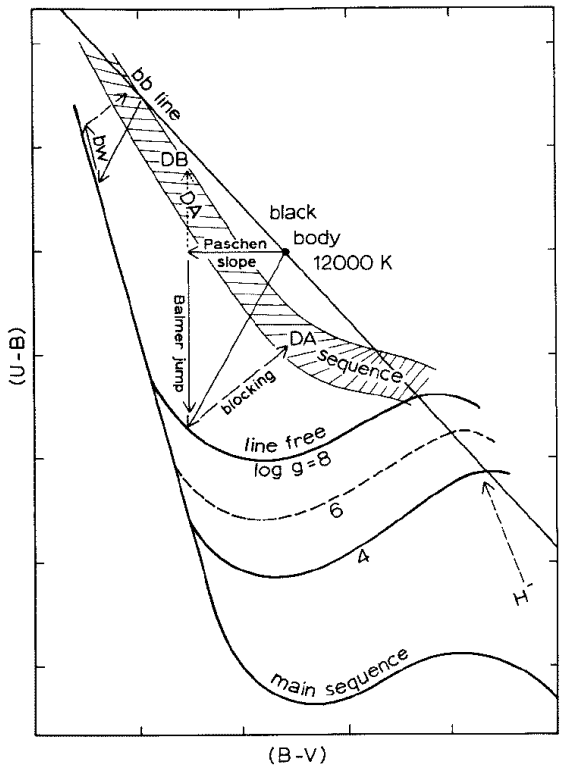

FIGURE 4.12.: Positions of DA white dwarfs (hatched area) in a two-colour diagram, which clearly deviate from the black-body line (bb line, Weidemann (1971). Lower right: H^- absorption, strongest in red, shifts the flux to the blue and the ultraviolet (dashed arrow).

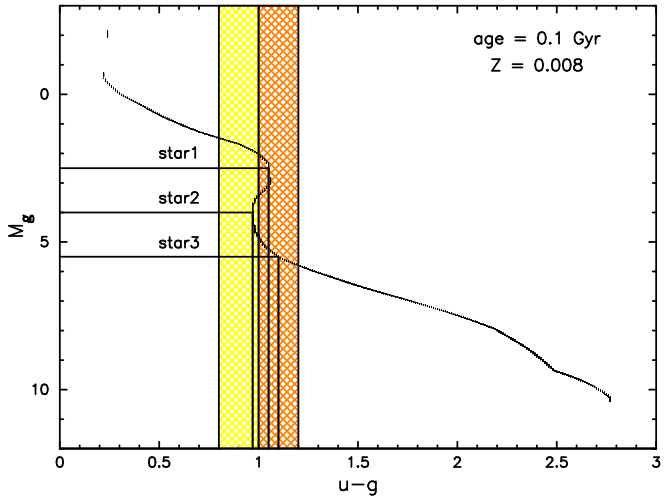

FIGURE 4.13.: The same colour-magnitude diagram as in the left panel of Figure 4.11, but additionally the positions of the three examined stars are marked in black.

nm. This means that this colour band is very sensitive to the effective temperature. It is sensitive to the surface

spectra, i.e., at temperature $T_{\rm eff} \approx 10'\ 000$ K.

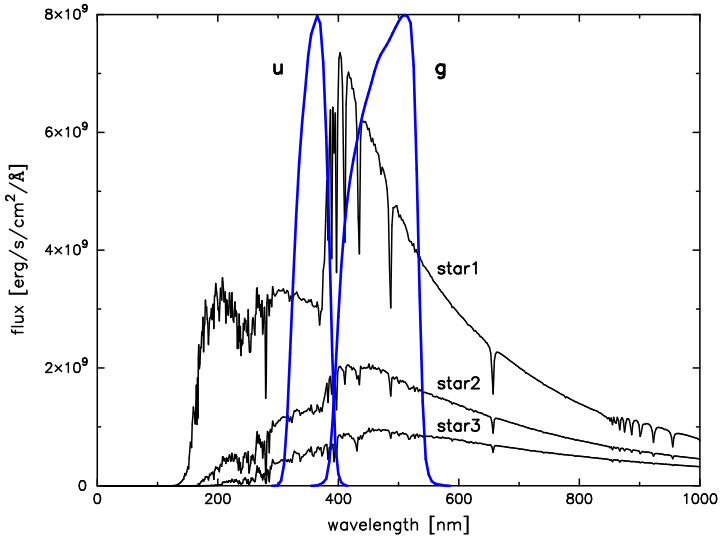

FIGURE 4.14.: Spectral energy distributions of the three examined stars. The response filter functions of the $u-$ and $g-$ bands are added in blue.

gravity as well: lower gravity (star1) causes a bigger Balmer jump.
Because of the cooler temperatures of star2 and star3, very little Balmer absorption takes place. Even though these stars also have a lot of hydrogen in their atmospheres, most of their electrons are in the ground state and therefore the Balmer lines are very weak.
Beside the increase of metal lines and the decrease of the Balmer series and -jump, the opacity due to the negative hydrogen ions plays an important role in cooler stellar atmospheres (star2 and star3) (Wildt 1939). The H atom is able to hold a second electron in a bound state (binding energy 0.754eV). All photons with $\lambda < 1.655\,\mu$m have sufficient energy to ionize this ion back to neutral hydrogen and a free electron (for a recent discussion, see, e.g., Unsöld & Baschek (2002)). Equally, a free-free absorption can also occur, when a free electron flies by too close to a neutral hydrogen atom.

In Figure 4.15 the bound-free (H^-_{bf}) and the free-free (H^-_{ff}) absorption coefficients are plotted. The bound-free H^- absorption peaks around 8500 Å and reaches its minimum just above 16' 000Å. The free-free H^- absorption is proportional to $\sim \lambda^3$.
For solar-like stars (star3), the negative hydrogen ion seems to be the dominant continuum opacity source at optical wavelengths (Wildt 1939). Therefore, the $u-$band is also affected by the negative hydrogen ion at this temperature.
The different values of the Balmer jump, the Balmer lines, and the H^- maximum cause a divergence of the $(u-g) - M_g$ graph from the black-body line, due to the strongly affected $u-$band.

Analysis of $u-g$ colour distributions of a theoretical thick disk

Most of the stars observed in the Basel survey belong to the thick disk of our Galaxy. This is the reason, why in this part we want to turn our attention especially to these stars.
The star counts of two populations, shown in Figure 4.16, illustrate the colour distribution of this Galactic component.
The average metallicity of the thick disk stars lies in the vicinity of ~ -0.7 dex. This is situated between the metallicities of the populations P_{004} ($[\mathrm{Fe/H}] = -1.0$; left panels) and P_{008} ($[\mathrm{Fe/H}] = -0.56$; right panels).
Thick disk stars are assumed to have an average age of $\sim$ 11 Gyr. Harris (1998) determined the mean age of the thick disk as $\sim 11.4 \pm 0.8$ Gyr. For a rough approximation, we calculated the colours of these two populations at the ages of 10 - (upper panels) and 12 Gyr (lower panels).

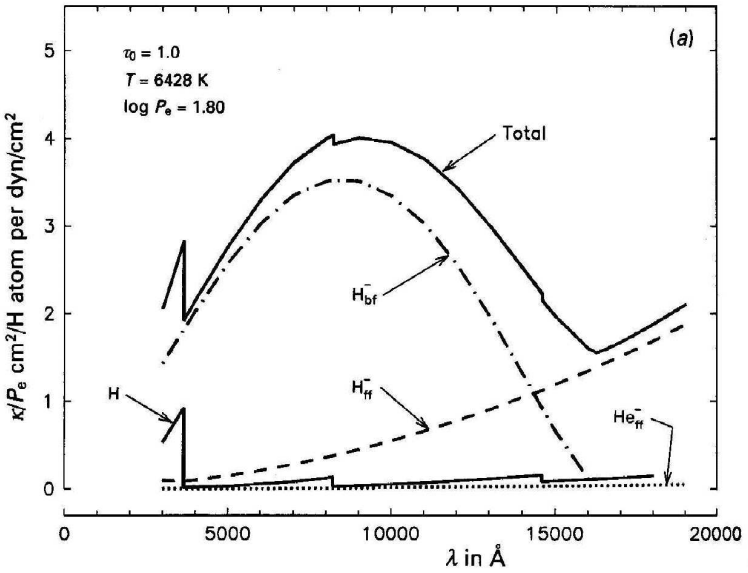

FIGURE 4.15.: Absorption coeffi cients per unit electron pressure compared at unit optical depth in a solar model photosphere (Gray 1992). The whole absorption is dominated by the H^- ion.

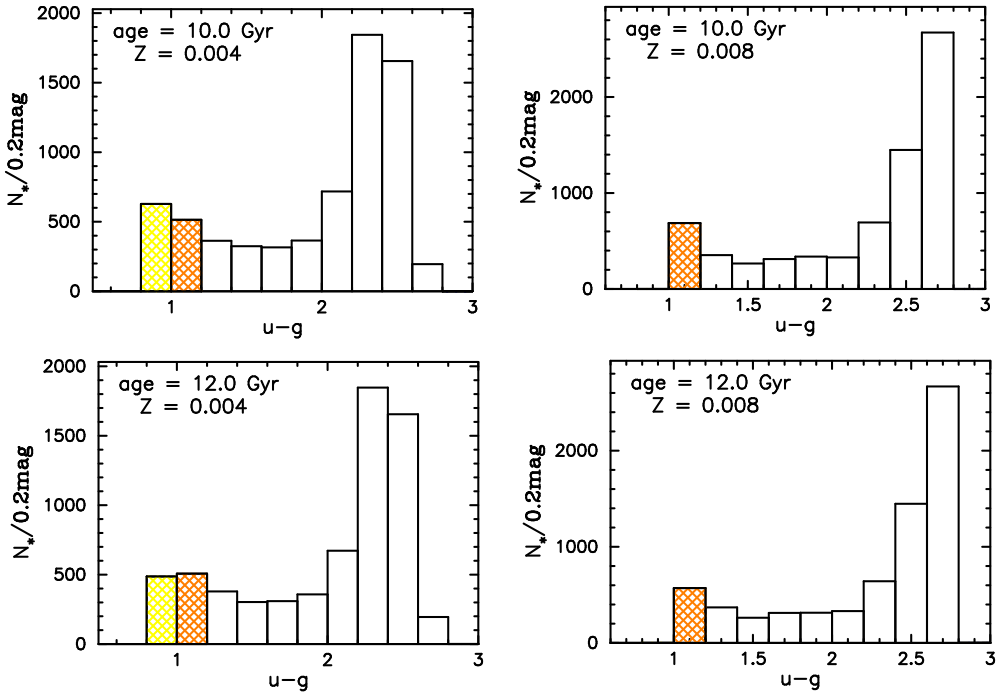

FIGURE 4.16.: $u-g$ colour distributions of the Population P_{004} (left plots) and P_{008} (right plots) at an age of 10, resp. 12 Gyr.

Beside the numerous low-mass stars with colours $u-g \geq 2.5$, the colour distributions of both populations peak at colours of $1.0 \leq u-g < 1.2$ for the Population P_{008} respectively, at $0.8 \leq u-g < 1.2$ for the P_{004} population. Regardless of how these two populations are mixed together in the thick disk, one peak should still remain.

This should be seen in the observed star counts as well. If this is not the case, it probably indicates that the stellar evolutionary tracks are not yet very well known, assuming that the spectra for solar mass stars are well reproduced. If the colour distribution is just shifted to redder or bluer colours, probably the zero points of the filter functions are not well set.

Well-defined assignments from colours

To know more about the behaviour of colour distributions, we examine the star counts for all populations at ages of 0.1, 0.3, 1.0, 3.0, 5.0, 10.0 and 12.0 Gyr.
Table 4.9 shows the evolution of the $u-g$ colour distribution of the main sequence stars (ms-stars) more massive than M and K dwarfs ($M_* > 0.6 M_\odot$) at the seven different ages.
At an age of 0.1 Gyr, all populations contain the same number of ms-stars more massive than M, K dwarfs: 5534 stars. During the evolution of these SSPs, the stars of the metal-poorer populations (P_{0001}, P_{0004}) leave the main sequence sooner than the metal-richer stars. The reason why the fusion of hydrogen to helium is more efficient in these populations can be found in the lower opacity. Metals block escaping photons. If the metal content is low, energy can be carried outward more easily from the stellar core. As a result, the star is denser and, therefore, its core is hotter. It produces more energy, and in doing so, it uses up its hydrogen content faster. Accordingly, metal-poor stars leave the main sequence at a younger age than stars of the same mass in metal-richer populations.

TABLE 4.9.: Number of main sequence stars ($> 0.6 M_\odot$) during the evolution of the SSPs

Population	0.1 Gyr	0.3 Gyr	1.0 Gyr	3.0 Gyr	5.0 Gyr	10.0 Gyr	12.0 Gyr
P_{0001}	5534	5130	4513	3619	3131	2317	2082
P_{0004}	5534	5175	4579	3700	3224	2439	2247
P_{004}	5534	5265	4753	3851	3445	2715	2506
P_{008}	5534	5299	4829	3931	3563	2896	2714
P_{02}	5534	5314	4860	4078	3719	3186	2939
P_{05}	5534	5267	4825	4040	3671	3078	2916

Now, let' s turn back to the actual subject, star counts:

By binning the stars into colour bins, some of these bins (mainly at the colour extremes) are populated only by stars with a certain metallicity. This knowledge can be used to assign metallicities to the stars that populate these certain bins.

Figure 4.17 shows the bins, into which only young stars with low metallicities ($Z < 0.004$) fall highlighted in blue. Metal-richer populations like P_{004} and P_{02} (lower two panels) do not have stars with colours $u-g \leq 0.0$. The same phenomenon can be seen at the red edge of the colour distribution in Figure 4.18. The colour bin $2.8 \leq u-g < 3.0$ (crosshatched in red) is filled only with stars of high metallicity ($Z = 0.05$). No stars of the metal-poorer populations (P_{008} and P_{0001}) enter this reddest bin.
Unfortunately, only stars in the outer bins (of all colours) can be identified unambiguously. The stars in the inner bins can not be subdivided into stars with well-defined metallicities and ages. Different stars with different combinations of these two parameters share these bins.

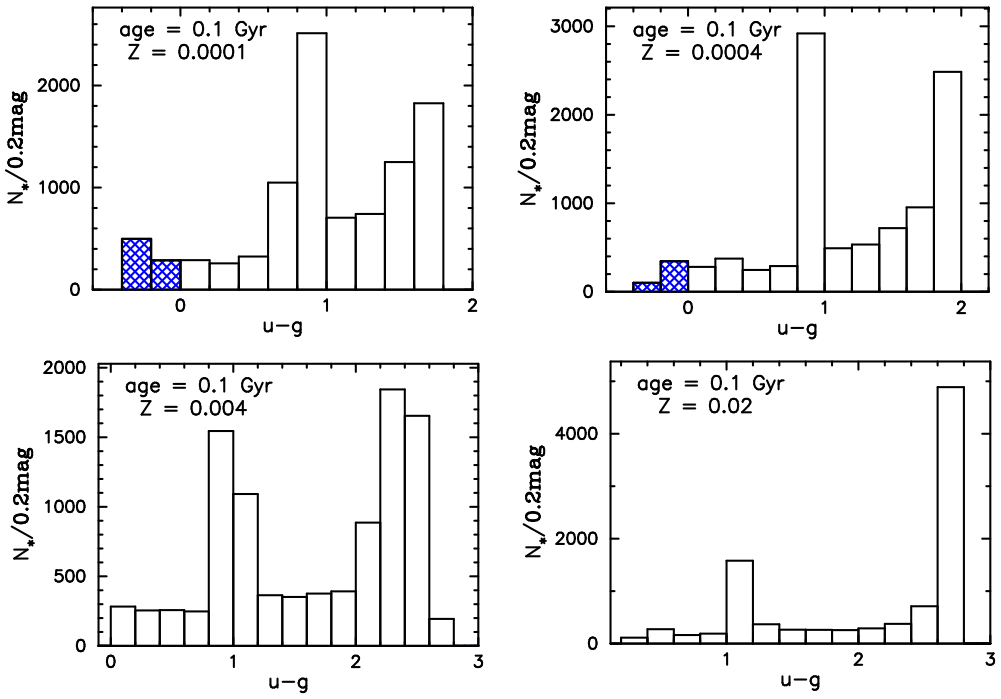

FIGURE 4.17.: Colour distributions of different populations at the age of 0.1 Gyr. The bins crosshatched in blue are populated by young stars with low metallicities ($Z < 0.004$) only.

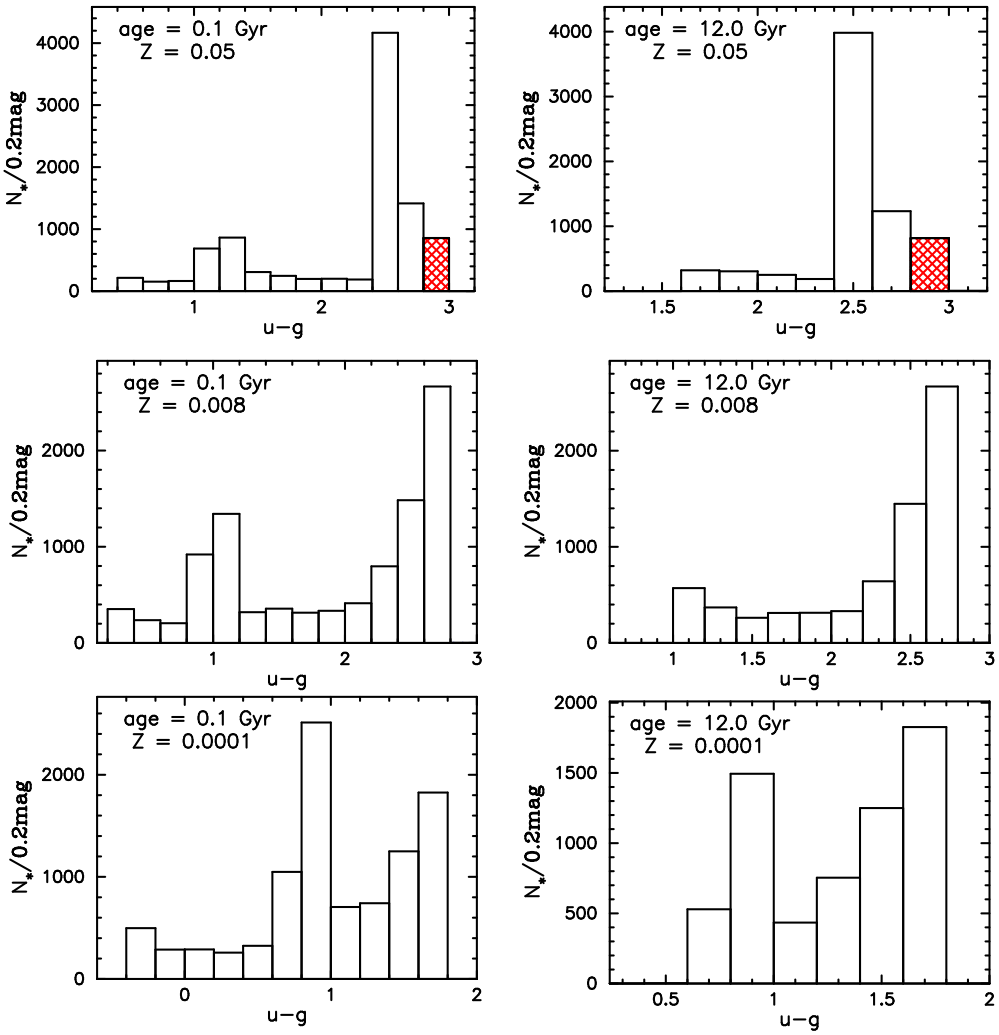

FIGURE 4.18.: Colour distributions of the populations P_{05} (upper panels), P_{008} (middle panels) and P_{0001} (lower panels) at ages 0.1 and 12 Gyr, respectively. The coloured bin contains only metal-rich ($Z = 0.05$) stars.

4.3. Theoretical stellar sample: Gaia

4.3.1. Description of the theoretical stellar sample

In 2011 the European Gaia satellite will be launched for its All-Sky Astrometry Survey mission, hopefully providing accurate data (positions, radial velocities, and low-resolution spectra) of about one billion stars in our Galaxy and throughout the whole Local Group, to address the most important questions concerning the physics of stars and galaxies.
An interesting challenge for theoreticians lies in the prediction of the stellar distribution that will be detected by Gaia. Even though we now (March 2, 2006) know about the replacement of the MBP and BBP filter system by low-dispersion spectra (Bastian 2006), we nevertheless created a theoretical stellar sample to simulate this survey.
We draw 30' 000 stars from the galaxy model within a sphere of 10 kpc (we refer to it as the $Gaiasphere$). The Gaiasphere enables us to visualise different aspects of "observations in theory" (like detectability of stars, distributions in HR-diagrams depending on various stellar parameters, and selection effects).

4.3.2. Short excursus: Dependency of the detectability

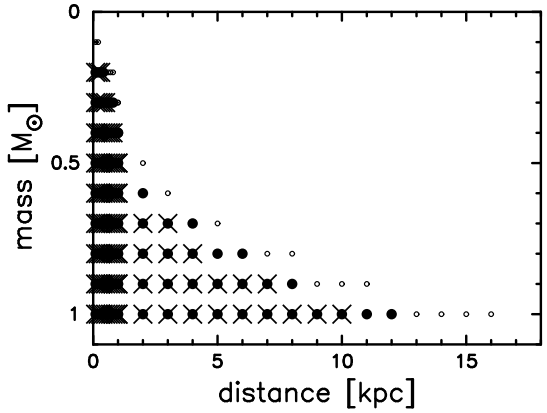

FIGURE 4.19.: Main sequence stars brighter than the apparent V-magnitude of 20.0 (crosses: $[\mathrm{Fe/H}] = 0.09$; black dots: $[\mathrm{Fe/H}] = -0.33$; open circles: $[\mathrm{Fe/H}] = -1.65$).

Already completed or still ongoing stellar surveys provide celestial (sub-)samples, by means of which we try to compile an overall picture of our Galaxy. Depending on the depths of the stellar surveys, different selection effects play an important role and lead to distorted impressions of the Milky Way.
At first, we analysed the detectability of stars, which depends not only on their masses. Figure 4.19 shows 3 Gyr old stars with different initial masses and metallicities, that can be detected using a given limiting apparent V-magnitude of 20.0, ignoring interstellar extinction.
As is already well known, more massive stars are visible at larger distances; but, additionally, the limiting detection distance is also determined by metallicity. Metal-poor stars are detectable out to larger distances than metal-richer stars of the same initial mass. As one can see in Figure 4.19, a $1M_{\odot}$ star with a metallicity of $[\mathrm{Fe/H}] = -1.65$ is visible out to 16 kpc, whereas a star with solar metallicity can be seen only as far out as 10 kpc. Increasing the metallicity leads to a rise in opacity, hence to a lower temperature and - consequently - a lower luminosity.

To illustrate this, we calculated the spectra of two synthetic stars of the same initial mass ($M_* = 1M_{\odot}$) and age (3 Gyr), and almost the same surface gravities ($\log g$ = 4.45 and 4.46, respectively), but different metallicities

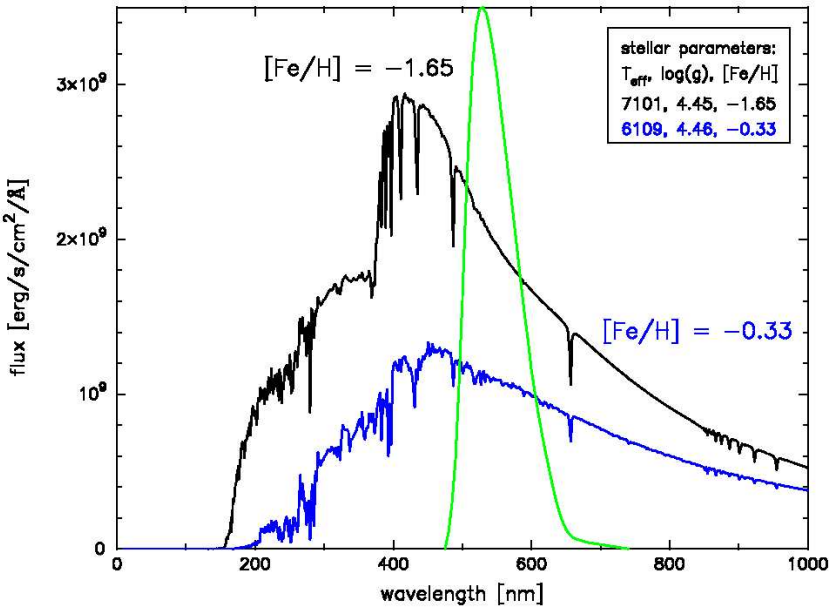

FIGURE 4.20.: Spectra of two stars of the same initial mass ($M_* = 1M_\odot$) and age (3 Gyr), but different metallicities ([Fe/H] = -1.65 in black, [Fe/H] = -0.33 in blue, respectively. In green: The filter response function of the Johnson V-band.

([Fe/H] = -1.65 and [Fe/H] = -0.33)[2]. Their spectra are plotted in Figure 4.20. The green curve represents the filter response function of the Johnson V-band. The V-magnitude is obtained by integrating the flux per unit wavelength ($F(\lambda)$) multiplied by the response function of the V passband ($S_V\ (\lambda)$):

$$m_V = -2.5log \int_0^\infty F(\lambda) S_V(\lambda) d(\lambda). \tag{4.2}$$

Clearly, the flux of the metal-poor star is higher than the flux of the metal-richer star at all wavelengths, including those of the V-band. Due to its higher effective temperature, the metal-poorer star has a brighter absolute V-magnitude, M_v = 3.9 mag. The metal-richer star has an absolute V-magnitude of only M_v = 4.59 mag. Therefore: Of two stars of the same initial mass, surface gravity and age, but different metallicities, the metal-poorer star is detectable out to larger distances.

To illustrate the metallicity effect, Figure 4.21 shows the spectra of two stars of the same effective temperature and surface gravity, but different metallicities ($[\mathrm{Fe/H}] = -1.65$ in black, $[\mathrm{Fe/H}] = 0.0$ in blue, respectively). Because of the identical effective temperatures (and radii, implied by their identical masses and surface gravities) the total fluxes, that is the integrals over the whole spectral range, are also the same for both stars.
The line blanketing is particularly noticeable in the ultraviolet region of the spectrum of the metal-richer star, where line absorption by atoms and molecules is highest. The lower flux in this region is compensated by the reemission of photons in the red and infrared spectral regions. This leads to a slightly brighter absolute V-magnitude for the solar-metallicity star. Thus in this example, of two stars of the same effective temperature and surface gravity, but different metallicities, the metal-richer star is detectable out to slightly larger distances.

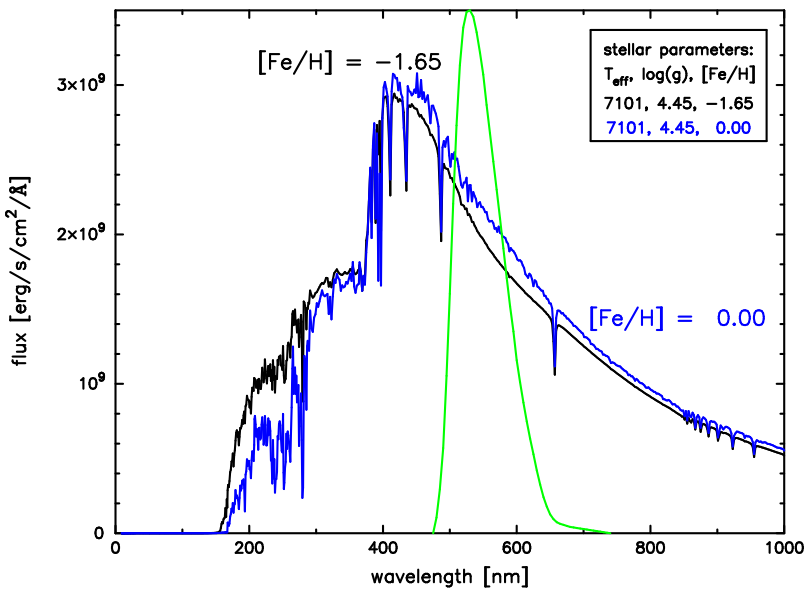

FIGURE 4.21.: Spectra of two stars of the same $T_{\rm eff}$ and $\log g$, but different metallicities ($[{\rm Fe/H}] = -1.65$ in black, $[{\rm Fe/H}] = 0.0$ in blue, respectively. In green: The response filter function of the Johnson V-band.

4.3.3. Detectability of the Gaiasphere

Returning to the Gaiasphere, Figure 4.22 shows, on the left side, the initial mass distributions and on the right the HR-diagrams of the simulated Gaiasphere, cut off at different limiting apparent V-magnitudes.
One can see how the average initial mass of the detected stars increases when the limiting magnitudes become brighter. Taking all stars into consideration, the majority of the stars (88%) have masses between $0.1 M_{\odot}$ and $0.4 M_{\odot}$. When considering only stars with $m_v \leq 19.0$, the masses usually lie between $0.8 M_{\odot}$ and $1.2 M_{\odot}$ (in $\sim$ 75% of these cases). Using the brightest limiting magnitude ($m_v \leq 16.0$) leads to a domination of masses between 1.0 $M_{\odot}$ and $1.4 M_{\odot}$ (38%). The average mass increases with increasing limiting apparent magnitude from 0.3 to 0.8, 1.1 and 1.5 $M_{\odot}$. The number of stars decreases from 30' 000 to 1543, 382 and 60, and the average age of the stars from 7.9 Gyr to 7.1 Gyr, 5.6 Gyr and 4.0 Gyr.

Depending on the limiting apparent magnitude of a stellar survey, selection effects lead to different pictures of our Galaxy. Figure 4.23 displays (in the same manner as in Figure 4.22) Gaiasphere star counts as functions of age on the left and metallicity on the right. In contrast to the overall shape of the age distribution histogram, the shape of the stellar metallicity histogram does not change much with decreasing limiting magnitude. The majority of the stars in each row still lies in the metallicity bin of -0.2 $\leq [{\rm Fe/H}] \leq$ 0.0.
The shape of the age distribution changes with the limiting apparent magnitude of the simulated survey. The brighter the limiting apparent magnitude of a survey (from the second row down to the fourth in Figure 4.23), the fewer older stars are detected in relation to the younger ones. For example, when applying a bright limiting apparent magnitude ($m_v \leq 16.0$, fourth row), stars with ages > 8 Gyr are underrepresented relative to the distribution of the whole sample (first row). From this, it follows that a star's probability of being observed is age-dependent. Generally, observers get a wrong picture of the age distribution of stars in the Galaxy because of this selection effect, which should be corrected for afterwards.

[2] To generate a stellar spectrum we enter stellar initial mass, age and metallicity in our code, which then calculates the corresponding stellar atmospheric parameters $T_{\rm eff}$ and $\log g$. According to the combination of the input data, $T_{\rm eff}$ and $\log g$ vary. The difference in metallicity leads in this example to a difference in temperature.

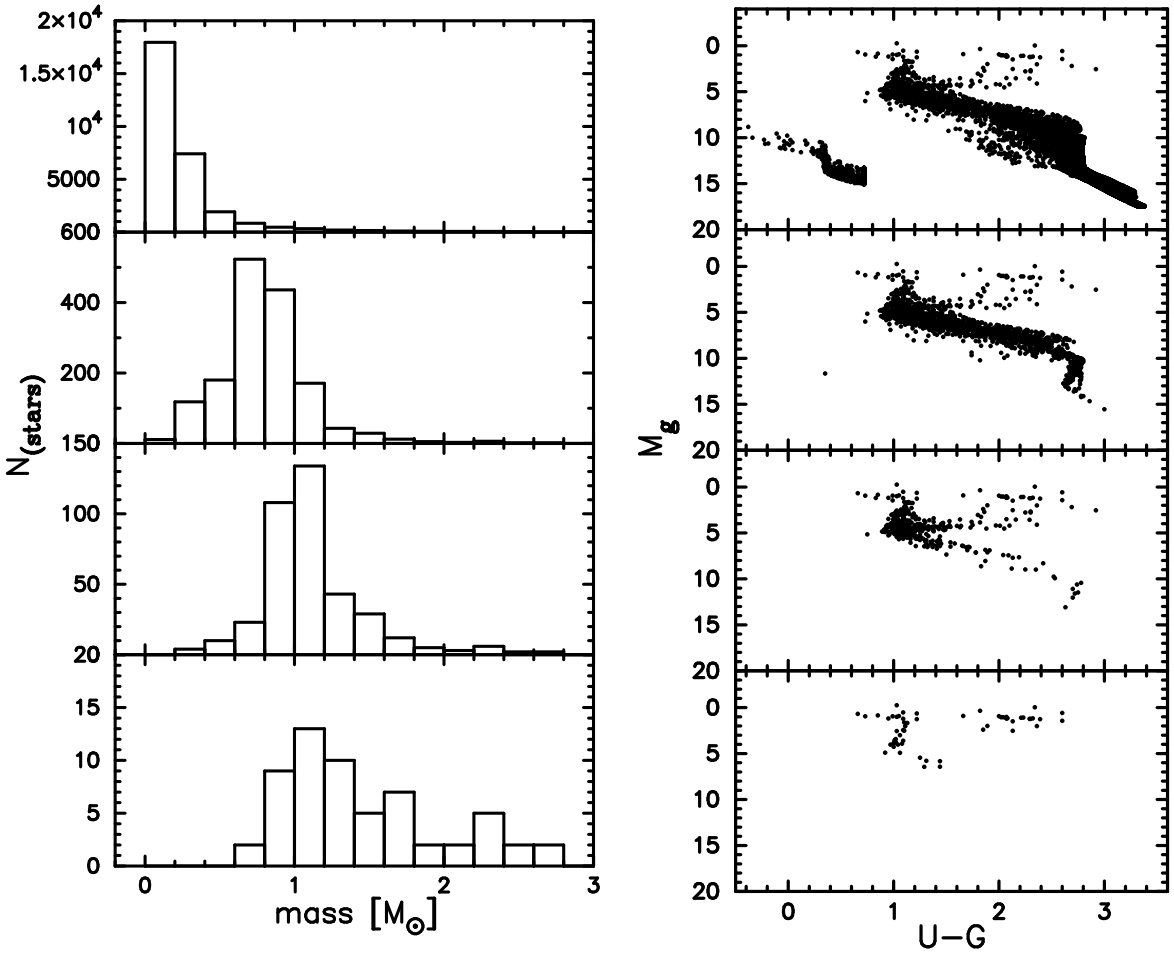

FIGURE 4.22.: Star counts of the Gaiasphere depending on limiting apparent magnitudes. Left: Mass distributions. Right: Corresponding HR-diagrams. Top row: Full sample; second row: $m_v \leq 22.0$; third row: $m_v \leq 19.0$; fourth row: $m_v \leq 16.0$.

By taking all the stars of the Gaiasphere in one viewing direction (i.e., towards the Anticentre) and plotting their stellar metallicities versus the ages, we end up with a stellar distribution as shown in Figure 4.24. In the left panel all stars in this direction are plotted, and in the right one only the stars with a V-magnitude of ≤ 18.0.
These two panels provide an alternative presentation of the selection effect "age-dependent detectability". In the left panel, an accumulation at ages between 8 and 9 Gyr with metallicities of $-0.2 \leq [\mathrm{Fe/H}] \leq -0.5$ is clearly visible. This indicates a relatively high star formation rate with a quite uniform metallicity.
When limiting the sample by applying an apparent magnitude ($m_V \leq 18.0$), the concentration of stars fades away (right panel). Therefore, deriving a star formation rate from a limited sample (right panel) leads to a quite different result than deriving it from the full sample (left panel).
Another striking point due to selection effects is the decrease of the metallicity range. The full sample (left panel) covers metallicities from $-$ 2.0 to + 0.2 dex, whereas the limited sample contains only stars above $[\mathrm{Fe/H}]$ = -1.0. By applying a limiting apparent magnitude, both the metal-poor and the metal-rich stars disappear. But in contrast to the above discussed age distribution, the overall metallicity distribution stays the same.

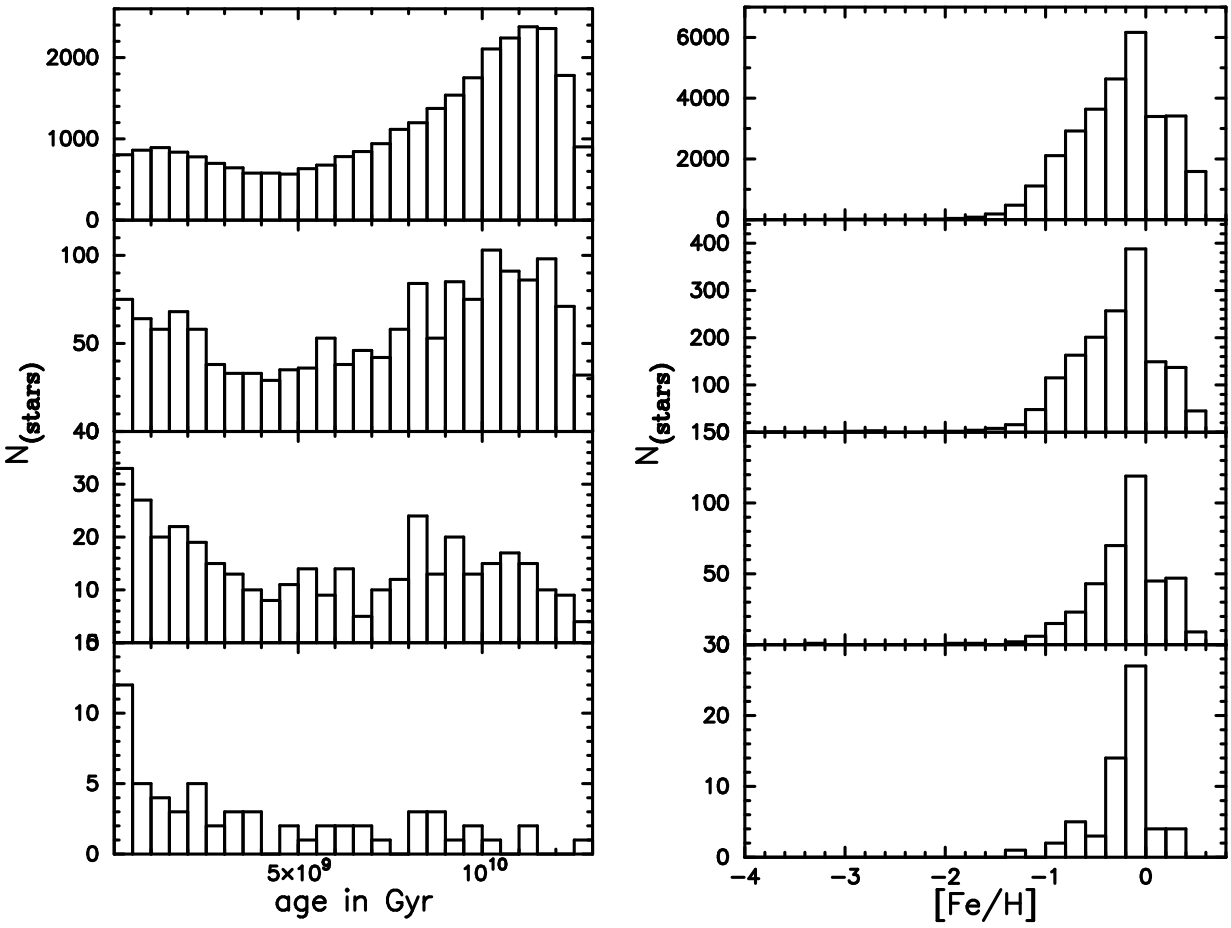

FIGURE 4.23.: Star counts of the Gaiasphere depending on limiting apparent magnitudes. Left: Age distribution. Right: [Fe/H] distribution. Top: Full sample; second row: $m_v \leq 22.0$; third row: $m_v \leq 19.0$; fourth row: $m_v \leq 16.0$.

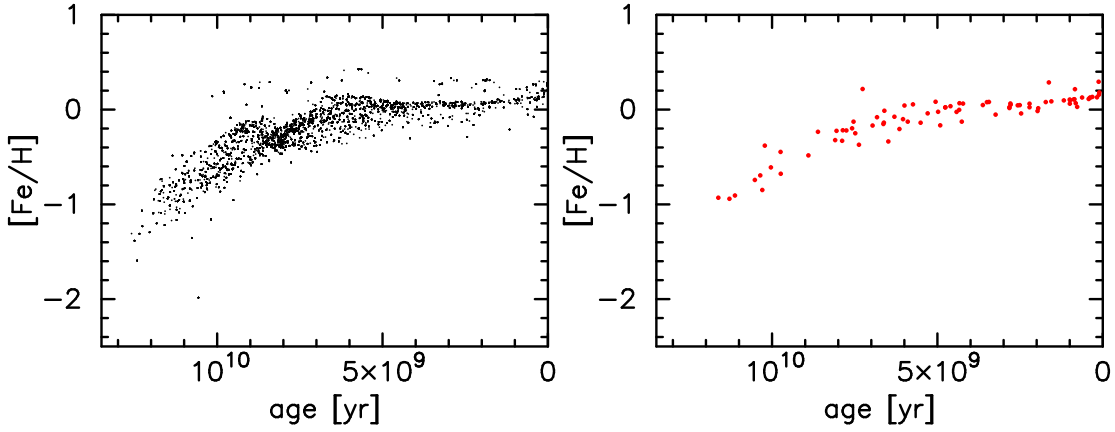

FIGURE 4.24.: Age-metallicity diagram of a simulated field of the Gaiasphere in the viewing direction towards the Anticentre. Left panel: all stars in this direction, right panel: only stars with a V-magnitude ≤ 18.0.

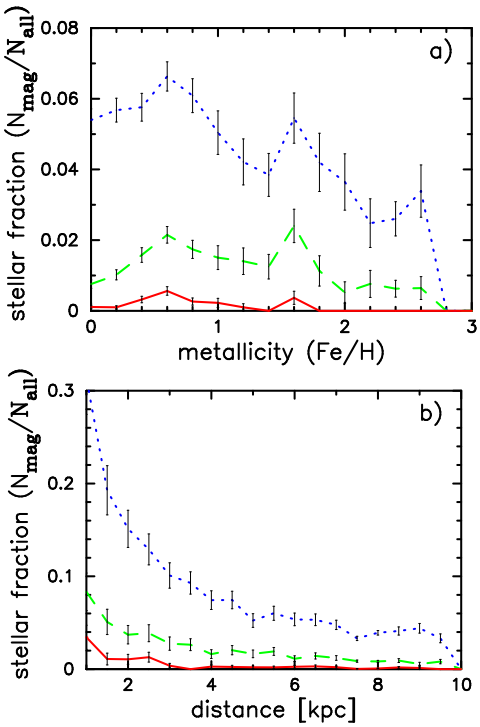

FIGURE 4.25.: Star fractions as functions of metallicity and distance (panels a, b), and limiting magnitudes (dotted, dashed, and full line). The dotted line stands for $m_v \leq 22.0$, the dashed line for $m_v \leq 19.0$ and the full line for $m_v \leq 16.0$.

4.3.4. Stellar fractions depending on limiting apparent magnitudes

Another way of investigating selection effects is the analysis of ratios between the number of stars belonging to a restricted stellar sample (using a limiting apparent magnitude) (in Figure 4.25: N_{mag}) and the number of stars of the full sample (in Figure 4.25: N_{all}). Henceforth, we will call these ratios stellar fractions. Stellar fractions vary with the applied limiting apparent magnitude and, hence, allow drawing conclusions concerning the extent of the selection effects.

The panels in Figure 4.25 give an overview of the fractions of detected stars as functions of metallicity, distance (panels a, b), and limiting apparent magnitudes (dotted, dashed, and full lines). The dotted line stands for $m_v \leq 22.0$, the dashed line for $m_v \leq 19.0$, and the full line for $m_v \leq 16.0$.

At first glance, the graphs corresponding to different limiting magnitudes seem to have the same shapes, just starting at different fractions. At closer inspection, one notices the levelling off at bright magnitudes of some features that are visible at the faintest ones ($m_v \leq 22.0$).

By analysing the trend of the $m_v \leq 22.0$ - curve in Figure 4.25a), a noticeable peak at $(\mathrm{Fe/H}) = 2.6$ ($[\mathrm{Fe/H}] = 0.41$) becomes visible. When decreasing the magnitude threshold, this peak disappears. Other features that vanishs when decreasing the limiting magnitude can be seen in Figure 4.25b) at a distance between 8.5 and 9.5 kpc.

A selection effect is introduced by the fact that observational instruments collect stellar data from only a subset of the target population. Luminous stars can be seen out to much greater distances than fainter stars, hence luminous sources may be grossly over-represented in present-day surveys [3]. The limitations of the data collection process due to the sensitivity of the measuring device affects the inferences one can draw from the data. To get a realistic picture of our Galaxy from the collected data, it is necessary to have a detailed knowledge of the selection process

[3]This particular selection effect is called *Malmquist Bias*, discovered in 1920 by K. G. Malmquist.

and to always be aware of it.
Taking the metallicity distribution as an example (Figure 4.25a)), a reconstruction of the peak at $(\mathrm{Fe/H}) = 2.6$, which is visible at the faintest limiting apparent magnitude, from the data collected using the brightest limiting apparent magnitude (full line) requires *a priory* knowledge of the metallicity distribution in space, which has to be either assumed or derived from the data, before the correction for this bias can be made.
The selection effect is magnitude- and therefore age-dependent. With increasing age, stars become redder and mostly fainter. In comparison to younger stars, old stars are underrepresented in samples with a bright limiting apparent magnitude.

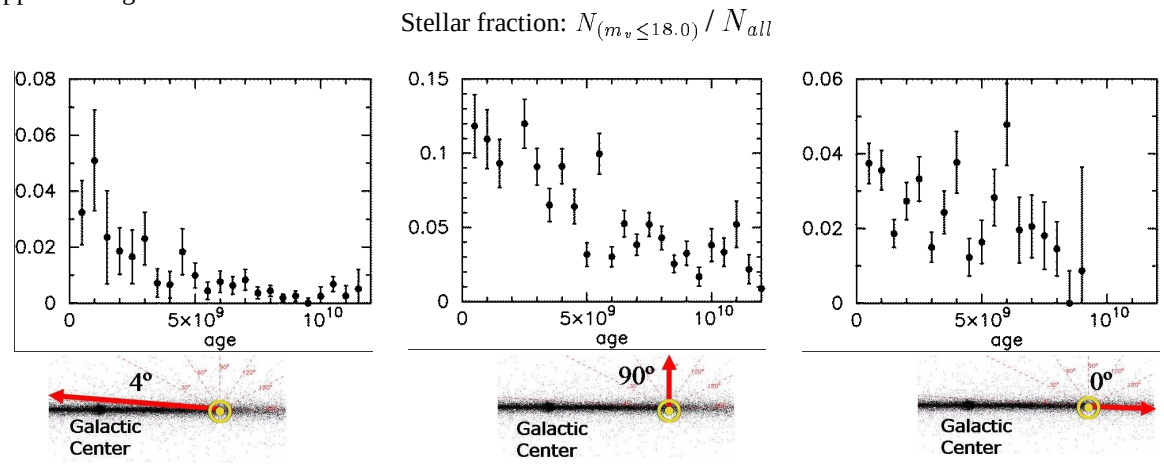

FIGURE 4.26.: Star fractions with a limiting apparent magnitude of $m_v \leq 18.0$ as functions of age and in different viewing directions (left panel towards the galactic centre, middle towards the halo and right panel towards the galactic anticentre.

Plotting the fractions of the visible– (apparent V-magnitudes ≤ 18.0) to all stars in different viewing directions (see Figure 4.26), makes it clear that on average 5% of the young stars are bright enough to appear in the restricted sample, whereas only 0.5% of the very old stars are detectable.
The rate at which stars form in a galaxy is one of the key aspects to any model of galaxy formation and evolution, and therefore of great interest. Stellar ages can only provide a meaningful guide for the understanding of the Milky Way' s star formation rate if all biases can be accounted for from the beginning. One possibility lies in the limitation of the stellar sample to a certain volume, hoping that the remaining sample is *complete*. Star counts from the solar neighbourhood can constrain the SFR of our Galaxy (e.g., Cignoni, Prada Moroni & Degl' Innocenti (2004)).

4.3.5. The three major components of the Gaiasphere

Metallicity can be taken as a criterion for assigning Galactic stars to a certain stellar component (thin disk, thick disk or halo). In this subsection, we focus on the major stellar components of the Galaxy and divide the Gaiasphere into the three main Galactic populations according to the metallicities of the stars. We investigate to which extent other stellar properties like age, rotation velocity or distance perpendicular to the Galactic plane (z-dist) support such a classifi cation of the model stars.
Gaia will detect all stars down to the 20th apparent magnitude in the V-band [4], hence we limit our sample ' Gaiasphere' in the same way before grouping the stars.
Table 4.10 lists the mean metallicities of the three major stellar components of our Galaxy as defi ned by Buser, Rong & Karaali (1999). We chose $[\mathrm{Fe/H}] = -0.46$ dex as a metallicity criterion to distinguish between the thin and the thick disk stars, because this value lies in the middle of the overlap of the two metallicity ranges. For the

[4]The 20th magnitude in the V-band was given as the limiting apparent magnitude before the fi lter replacement.

separation between thick disk and halo stars, a limit of $[\mathrm{Fe/H}] = -1.19$ dex was used, because this marks the centre between the upper limit for halo stars (-1.5 dex) and the lower limit for the thick disk stars (-1.03 dex).

TABLE 4.10.: Mean metallicities of the Galactic components

Galactic component	metallicity [dex]
old thin disk	$[\mathrm{Fe/H}] = -0.13 \pm 0.21$
thick disk	$[\mathrm{Fe/H}] = -0.73 \pm 0.15$
inner halo	$[\mathrm{Fe/H}] = -1.80 \pm 0.30$

Henceforth, we use green to mark halo stars ($[\mathrm{Fe/H}] \leq -1.19$), and red to mark thin disk stars ($[\mathrm{Fe/H}] \geq -0.46$). The stars that lie in between, the thick disk stars, are always plotted in black.

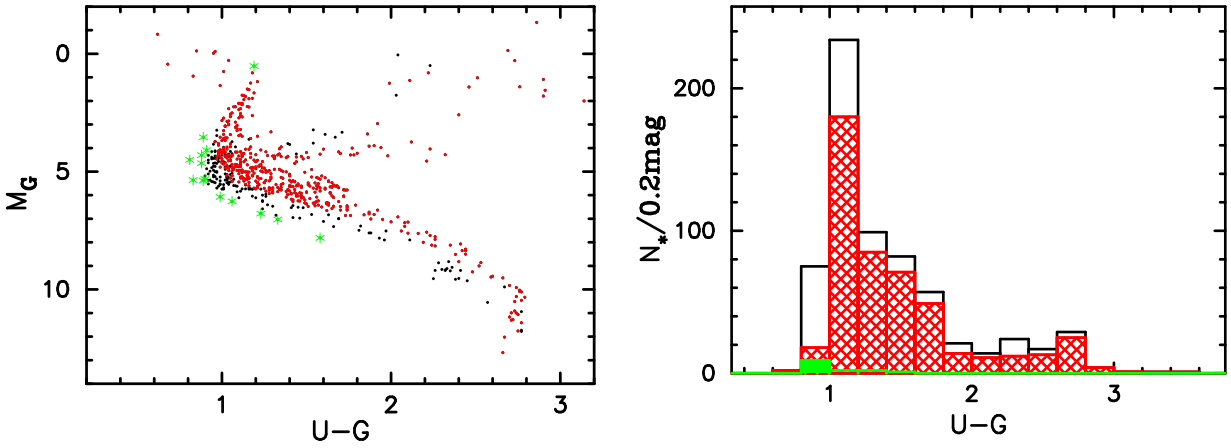

FIGURE 4.27.: Left: Colour-magnitude diagram of the Gaiasphere stellar distribution for different metallicities (green stars: $[\mathrm{Fe/H}] \leq -1.19$ (halo stars), red dots: $[\mathrm{Fe/H}] \geq -0.46$ (thin disk stars), black dots: thick disk stars with $-1.19 < [\mathrm{Fe/H}] < -0.46$). Right: Corresponding star counts, in green the halo stars, in black the thick disk−, and in red the thin disk stars.

The colour-magnitude diagram of the magnitude limited Gaiasphere is plotted in the left panel of Figure 4.27 and its star count in the right panel, devided into the three major galactic components.
Depending on their metallicity, stars lie in different regions in the Hertzsprung-Russell diagram. Metal-poor halo stars lie in the lower part of the main sequence, whereas the most metal-rich ones, the thin disk stars, populate the upper part. A similar distinction is visible in the star count histogram (Figure 4.27, right panel). The metal-poorer halo stars appear mainly in the bluer U-G bins around 0.6 and 1.0 mag (green columns), and the metal-richer stars in the redder U-G bins around 1.0 and 1.8 mag (red columns). Metals block escaping photons and increase the stellar opacity in the blue− and UV-range of a spectrum. Therefore metal-richer (thin disk) stars are redder. Even though the sphere is quite large (radius = 10 kpc) and comprises a huge fraction of the halo, most of the stars belong to the thin disk (73,7%). Thick disk stars are represented by 24,3% and halo stars only by 2% of all stars. Figure 4.28 explains why most of the stars belong to the thin disk:

At the distance of $\sim$ 8 kpc an accumulation of stars, especially thin disk stars, sticks out. The Gaiasphere is centred on the position of the Sun. Seen from the Sun' s position, the bulge is located in 8 kpc distance. Like in our Galaxy, all components of the Gaiasphere have their highest stellar densities in the central bulge. We only

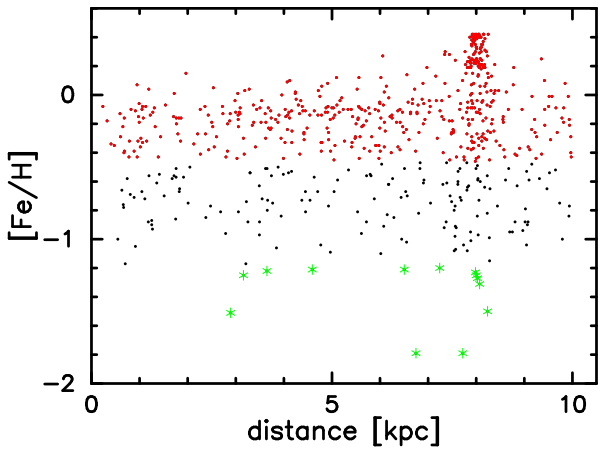

FIGURE 4.28.: Stellar metallicity as a function of the distance from the Sun of the ' Gaiasphere population stars' : in green halo−, in black thick disk−, and in red thin disk stars.

selected 30' 000 stars and they are mainly drawn from the most populated part of the galaxy: from the bulge (the more loosely populated halo is only weakly represented in the sample). As can be seen in Figure 4.28, this bulge mostly consists of metal-rich thin disk-like stars, but stars with lower metallicities also lie in this distance.

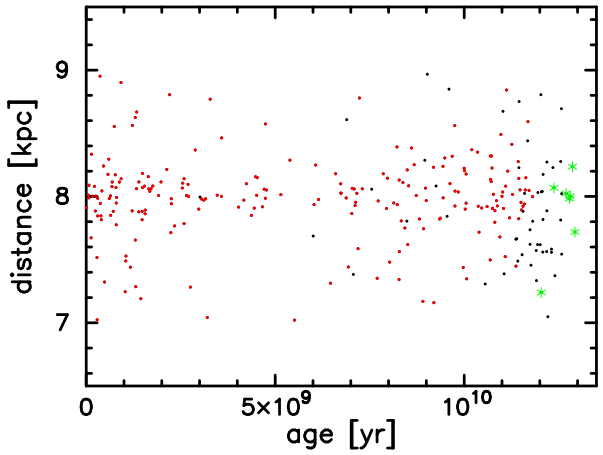

FIGURE 4.29.: Stellar ages as functions of the radial distances to the galactic centre. Plotted in green are the halo-, in black the thick disk- and in red thin disk stars.

For a closer inspection of the stellar ages at the distance of 8 kpc, we plotted in Figure 4.29 the stellar ages versus the distances of all stars that are located in the distance range between 7 kpc and 9 kpc.
As one can see, stars in this distance range cover the whole age range but with clear separations between the mean ages of the different components: The thin disk stars (red dots) are the youngest ones, with ages up to 11.9 Gyr. The thick disk stars (black dots) follow with ages between 6.0 and 12.7 Gyr. The halo stars (green stars) are the oldest, covering ages between 12.0 and 13.0 Gyr.
Our classifi cation of the stars regarding their metallicities is supported by this age distribution: metal-poor halo stars are the oldest ones, whereas the metal-richer thin disk stars are much younger.
The galaxy grows from the inside out. The inner region of the galaxy is older than the one that lies towards the anticentre. In Figure 4.29, it seems, that the bulge consists of at least two distinct subpopulations: the older one is represented by an accumulation of stars at around 11 Gyr, and another accumulation of stars is visible at around

1 Gyr. The younger subpopulation is a consequence of the still ongoing SFR in this region.
One has to consider that, due to the selection effects that influence the number of older stars more than the one of younger stars (as seen in the Subsection 4.3.4), the intrinsic ratio of old− to young stars is in fact much higher. The halo stars are the most affected by this effect: they are on average very old (stellar ages $>$ 12.0 Gyr), and only the lower-mass and, therefore, fainter stars have survived till our days.

For each star the chemo-dynamical code provides, apart from the radial distance from the galactic centre (r-dist), also the distance perpendicular to the galactic plane (z-dist) and different velocities (the rotational velocity, v_{rot}, and the velocity perpendicular to the galactic plane, v_z).
A galaxy is a huge gravitationally bound system of stars, interstellar gas, dust, and dark matter that orbit a common centre of gravity. Given these continuous stellar movements, Figure 4.30 represents only a snapshot of the stellar structure in the model galaxy at a particular time.

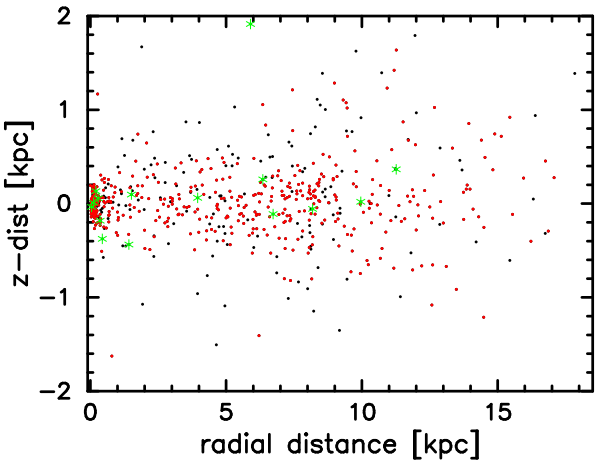

FIGURE 4.30.: Radial distances from the galactic centre as functions of the z-distances of stars of the three components, highlighted in different colors (thin disk stars: red dots, thick disk stars: black dots and halo stars: green stars).

The arbitrary nature of this picture inhibits the use of the distance perpendicular to the galactic plane (v_z) as a criterion to separate the three components. As one can see in Figure 4.30, the three components are not spacially separated but overlap each other, and most of them have z-distances around 0.0 kpc.
Comparing the vertical distribution of the different components of the model galaxy to Figure 4.31, which shows the vertical distribution of the Galaxy' s populations, we obtain good agreement. In the galaxy model, most thin− and thick disk stars lie in the same plane as in the Milky Way. The relatively high amount of halo stars with z-distances around 0.0 kpc, however, attracts attention.
In the solar neighbourhood there is only 1 halo star per 1000 thin disk stars (Buser 2000). In our example (Figure 4.29), there are 28 halo stars per 1000 thin disk stars. We still have to bear in mind that the theoretical stellar sample is restricted to a certain number of stars and to a limiting apparent V-magnitude, and drawn within a quite large radius of 10 kpc. It is puzzling, that a lot of these halo stars, as we classifi ed them according to their low metallicities, lie at a radial distance of around 0.0 $-$ 0.1 kpc, an indication of them being members of the bulge. These stars are too metal-poor to assign them to the bulge. We try to solve this by taking into account the kinematics of the stars.

Beside the metallicity, the kinematics of a star can be taken as a criterion to assign it to a certain Galactic component as well.
Thin disk stars belong to the thin disk because they all have roughly the same high rotational velocities around the Galactic centre ($\sim$220 km s^{-1}, Buser (2000)) and lie nearly in the same plane, orbiting the Galactic centre in

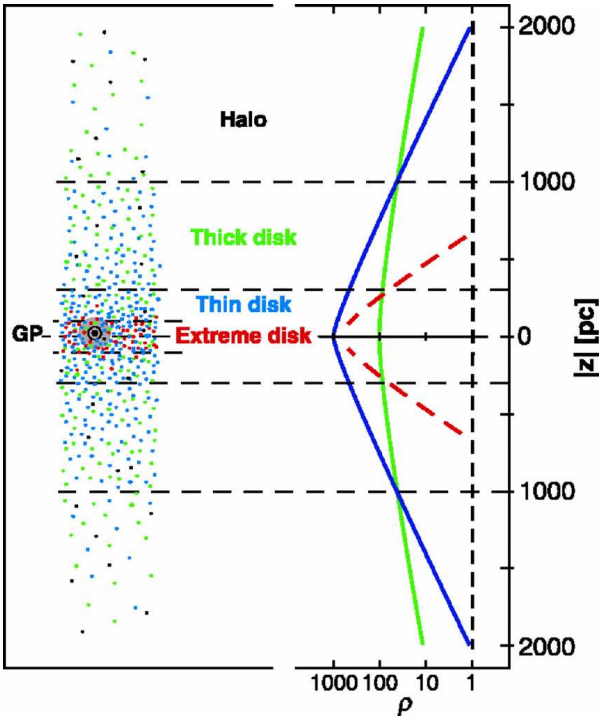

FIGURE 4.31.: Closeup view of the Galactic disk and halo structure perpendicular to the Galactic plane (Buser 2000). Note that the colours do not correspond to the code of the earlier Figures 4.27 - 4.30.

more or less circular orbits. In contrast to their rotation velocities, their z-velocities are very low (∼20 km s^{-1}, Buser (2000)), allowing only for small excursions above and below the central plane.
Due to their larger vertical velocity dispersion (∼ 40 km s^{-1}, Sparke & Gallagher (2000)), the thick-disk stars can leave the central plane by up to 1000 pc. Their rotational velocities lie around 180 km s^{-1} (Gilmore, Wyse & Kuijken 1989).
Finally, the halo stars are characterised by low rotational velocities (∼ 30 - 50 km s^{-1}, Chiba & Beers (2000)) but high vertical velocities, that bring them rapidly away from the disk on highly eccentric and strongly inclined orbits. Their vertical velocity dispersion lies at ∼ 100 km s^{-1} (Sparke & Gallagher 2000).
Figure 4.32 shows the kinematics of the restricted model Gaisphere' s stellar components: v_{ot} (right panel), v_z (right panel), respectively, as functions of z-distances in the upper two panels. The lower panel represents v_{rot} versus v_z.

Most thick− and thin disk−, and a few halo stars have rotational velocities of around 200 km s^{-1} (see Figure 4.32, upper left panel).
For thick and thin disk stars, this is in good agreement with the observationally deduced values of 180 km s^{-1} for thick disk− and ∼220 km s^{-1} for thin disk stars, respectively. A different behaviour is observed for those few halo stars that have such high rotational velocities that they seem to be members of the disk as well. The higher fraction of halo stars, which show lower rotational velocities (< 200 km s^{-1}), simulate the velocities of the Galactic halo stars in a much better way.
Looking at the vertical velocity distributions of the limited Gaiasample (Figure 4.32, upper right panel) it is striking that the vertical velocity distributions of all three stellar components, including some halo stars (with higher v_z, though), are centred at $v_z = 0.0$. Looking at both parameters, rotational velocity and vertical velocity, together, the lower plot of Figure 4.32 reveals that these few halo stars are either members of the bulge (perhaps captured), or are just traversing the bulge with only slightly inclined orbits.

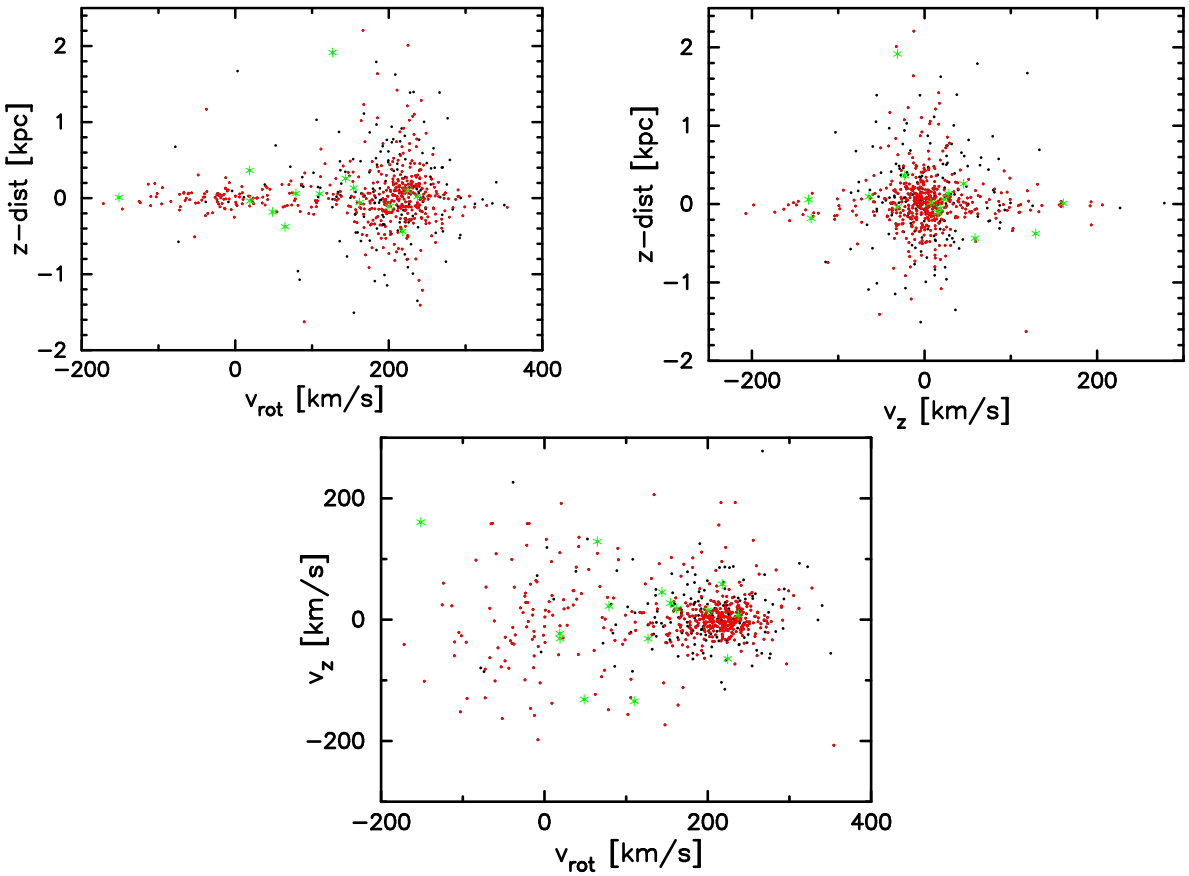

FIGURE 4.32.: Upper two panels: rotational velocities (left panel) and vertical velocities (right panel) as functions of vertical distances of the three stellar components, highlighted in different colours (thin disk stars: red dots, thick disk stars: black dots, and halo stars: green stars). Lower Panel: the radial velocities versus vertical velocities of all three components.

On the one hand their old ages and low metallicities argue for a membership of the halo, on the other hand their relatively high rotational velocities (the rotational velocity of the bulge is around 100 km s^{-1}) and low vertical velocities indicate membership of the bulge.

To solve this contradiction, we divide the halo stars into two subpopulations. Binney, Gerhard & Spergel (1997) defi ned the size of the Galactic barred bulge using an annulus that extends to $\sim$ 2.0 kpc on the minor axis and to $\sim$ 3.5 kpc on the major axis. We adopt their semi-major axis size of 1.8 kpc as the radius of a sphere (we named it "bulge-sphere"), within which all stars having radial distances $<$ 1.8 kpc belong to the bulge. We analyse the differences in positions in the v_{rot} - v_z plane of the halo stars within this bulge-sphere, and of the halo stars that are outside of it.

The two left plots of the Figure 4.33 show the positions of the stars from these two halo subsamples: in the upper panel the positions of the stars within the bulge-sphere, in the lower ones the ones outside of it. Most of the halo stars outside the sphere (except one) lie much closer to the central plane than the ones inside of it.
The two right plots show the different behaviour of the stars as functions of their rotational velocities: the stars within the radius of the bulge-sphere (upper right panel), have on average larger vertical velocities than the ones outside the sphere (lower right panel). The halo stars that are further away than 1.8 kpc have average vertical velocities of only $\pm$ 20 km s^{-1}. The rotational velocity dispersion of the bulge-sphere halo stars is much higher compared to the outer ones.

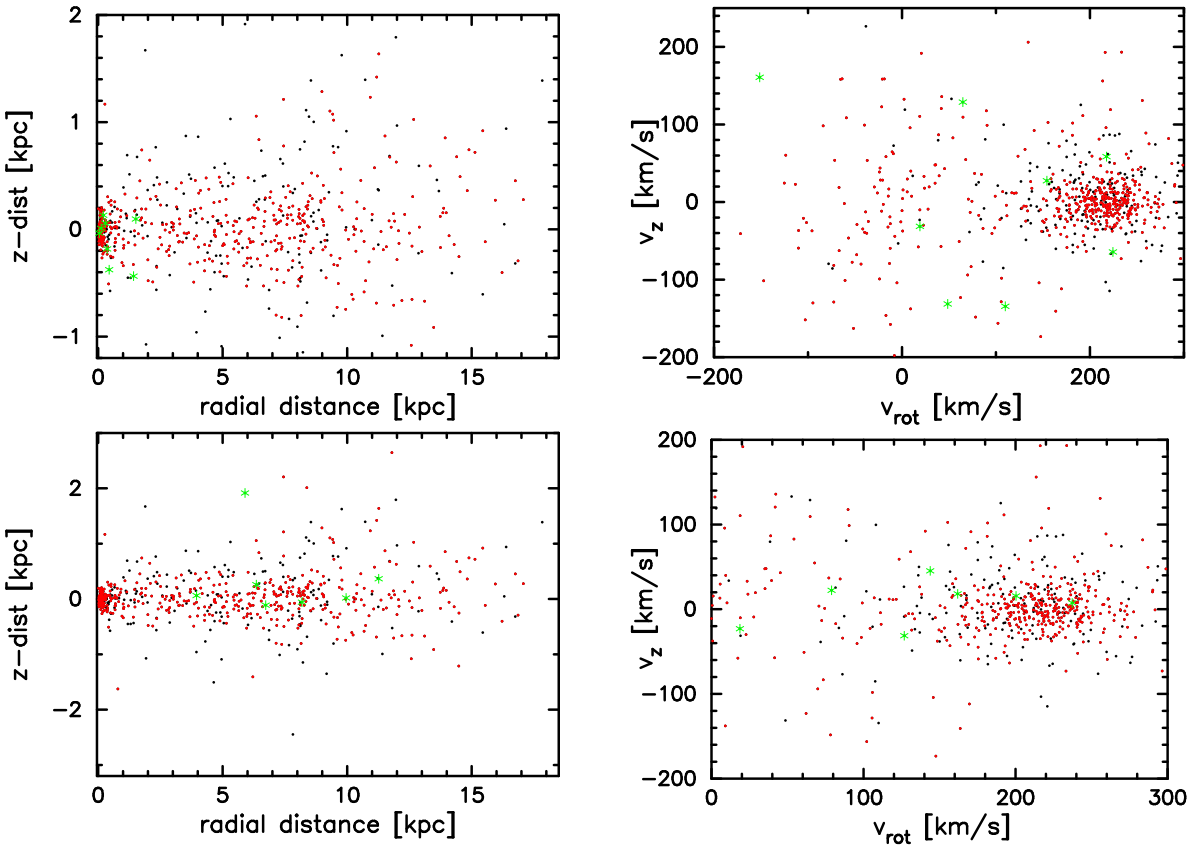

FIGURE 4.33.: Positions of the bulge-sphere halo stars (upper left panel) and the halo stars outside the sphere (lower left panel) in the z-distance - radial distance plane, marked in green. The two right panels show the positions of the bulge-sphere halo stars (upper panel) and the halo stars outside the sphere (lower panel) in the v_z - v_{rot} plane, marked in green.

From this, we conclude that the halo stars near to− or in the bulge do not belong to this central region of the model galaxy due to their relatively high v_z and relatively low v_{rot}. It seems that these are halo stars just traversing the inner-most region of the galaxy [5].
From this, we can justify our rough procedure of assigning stars to certain galactic components using only their metallicities.

[5]There is only one star with a relatively high rotational velocity of -111.8 km s^{-1} and a lower vertical velocity of 19.1 km s^{-1} that could be a member of the bulge. But taking metallicity as the major criterion to seperate the stars, this remains a halo star just showing bulge-like properties.

4.4. Theoretical stellar surveys

4.4.1. Galactic anticentre (SA94) and Galactic centre (SA107) fields

The Samland galactic model allows us to occupy the place of the sun in the model galaxy and simulate the observation of a field in a certain viewing direction and of a certain field size. The comparison of the stellar colour-magnitude diagrams in two out of all these available viewing directions reveals different turn-off point star distributions and main sequence widths.
The galactic anticentre (field SA94) population has a slightly (0.2 mag) brighter turn-off in the G band (Figure 4.34, top left panel) than the inner galaxy population (SA107, top right panel), indicating that stars in the anticentre direction are generally younger. Another hint of the lower stellar age can be found in the $U-G$ colour distributions (Figure 4.34, bottom panels). A larger fraction of high-mass stars are still alive, contributing particularly to the bluer-colour bins of the star count histograms ($U-G \leq 1.2$).

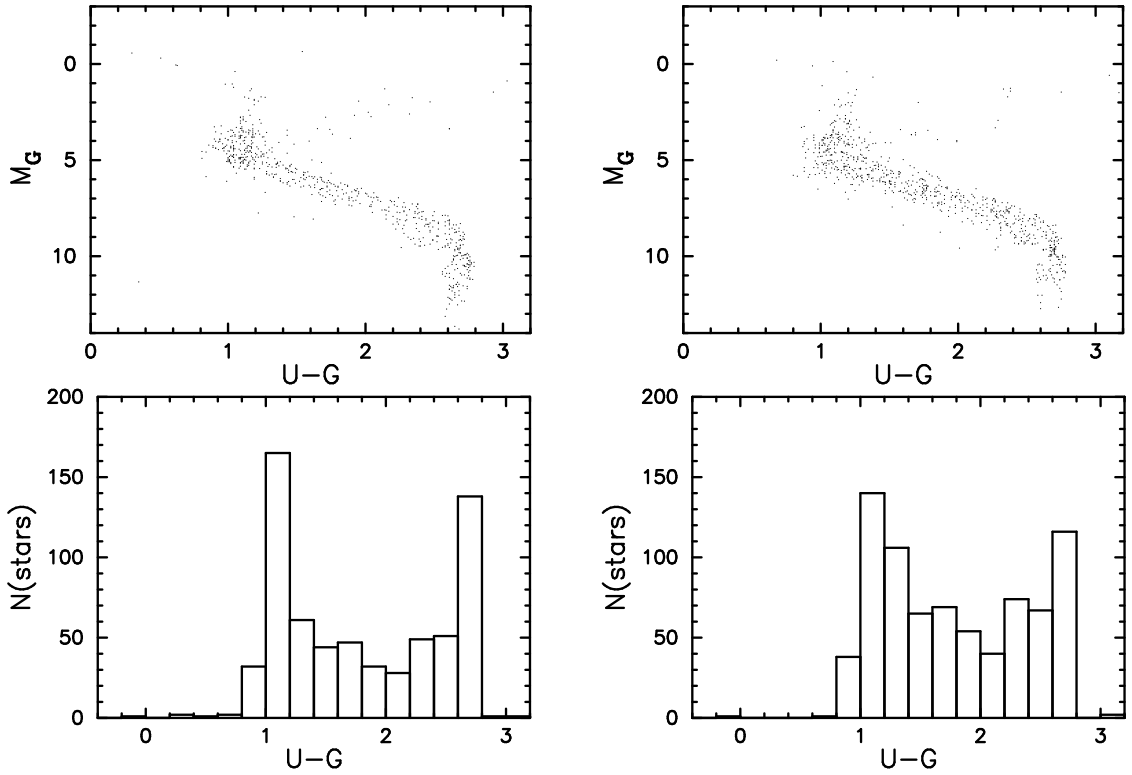

FIGURE 4.34.: H-R diagrams and the corresponding stellar distributions for two different viewing directions (left: SA94, right: SA107).

As mentioned in Subsection 3.2.1, the galaxy evolves from the inside out. Stars in the outer ranges of the galaxy are younger than in other parts. Apart from being younger, the stars in the anticentre are also more metal-rich, due to the outflow of already enriched gas. In the direction towards the Galactic centre, the stars have a higher diversity of metallicities than towards the anticentre. This is reflected in the broader width of the main sequence (Figure 4.34, top right panel).

4.4.2. Stellar distribution using appropriate isochrones

Theoretical isochrones are lines in the Hertzsprung-Russell– or colour-magnitude diagram, that represent the locus of all stars of the same age and metallicity, but different initial masses (meaning of *isochrone* from the Greek: *iso* = equal and *chronos* = time). For example, see the red line in Figure 4.35 and the coloured lines in Figure 4.37.

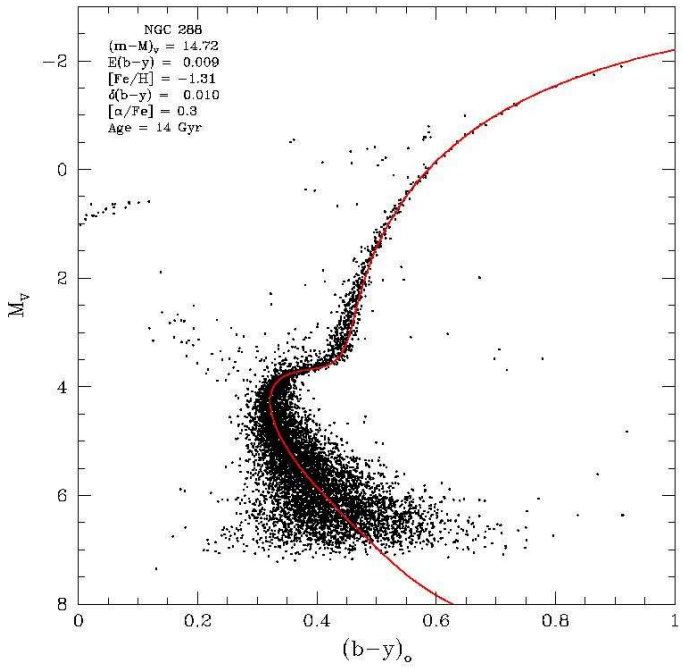

FIGURE 4.35.: Colour-magnitude diagram of the globular cluster NGC 288 (black dots) with a fitting theoretical isochrone (red line) produced by J. Clem.

Such isochrones - which correspond to the locations of single stellar populations (SSPs) in the H-R diagram or colour-magnitude diagram - allow the decomposition of the stellar distribution in a certain viewing direction of the Galaxy into several subpopulations of different ages and/or metallicities, and to use that information to verify different formation scenarios.
We investigate the method of ' isochrone fitting' illustrated using a composite theoretical stellar sample. Figure 4.36 shows in its left panel the distribution of all stars of the sample, a simulation of the Galactic halo field SA94 limited by an apparent magnitude of $m_v \leq 20.0$.
Recent observations and theoretical work suggest that the Galactic halo is built of several different stellar substructures. The distribution of RR Lyrae stars, for example, indicates that the halo has two principal components: Within the inner solar circle a somewhat flattened distribution of stars, and further out a spherical component (see Norris (1996)). This bimodality argues for the existence of both a dissipative (inner part) and an accreted (from low-mass dwarf galaxies) component (outer halo). The method of isochrone fitting could be used to separate the earlier formed and the later accreted populations as a key test of hierarchical galaxy formation models.
Beside this dual nature of the halo there is another fact that forbids us to treat the stellar sample like an SSP.

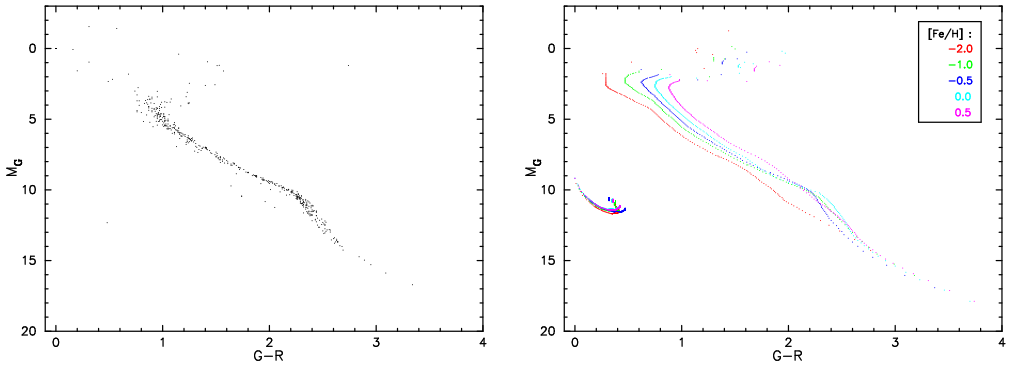

FIGURE 4.36.: Left panel: Colour-magnitude diagram of the stars in the halo field SA94. Right panel: Isochrones of single stellar populations of the same age (4.5 Gyr), but different metallicities.

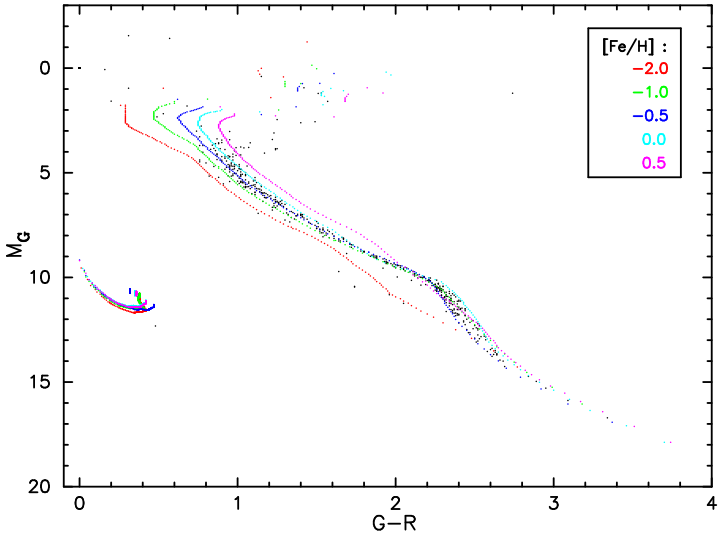

FIGURE 4.37.: Isochrones and the halo population in a colour-magnitude diagram.

Apart from the stars from the composed halo, our sample also comprises disk stars, the metallicities and ages of which differ strongly from the ones of the halo stars. Therefore, we need several SSPs to cover the metallicity and age parameter ranges of this stellar sample.
As a first (simplified) illustration of the isochrone fitting method, the isochrones of 5 SSPs, all of the *same* age (4.5 Gyr) but different metallicities ($[\mathrm{Fe/H}]$ = -2.0, -1.0, -0.5, 0.0 and +0.5), are displayed in the right panel of Figure 4.36. We overlay the theoretical stellar sample and the arbitrarily chosen isochrone set (Figure 4.37) to investigate, if it is possible to assign one of these isochrones, and hence a specific metallicity and age to each star (provided it is 4.5 Gyr old).

Unfortunately, certain couples of combinations of age and metallicity lead to isochrones that cross each other at certain points in the colour-magnitude diagram, which makes it impossible for some stars to unambiguously assign a single SSP to them. The overlap of the isochrones in the colour range $2.2 \leq G - R \leq 2.6$ is clearly visible in even this simplified (mono-age) case of Figure 4.37.
For further (and more realistic) illustration, we generate a larger random set of isochrones, this time by choosing different ages (0.5, 1.5, 4.5 and 6.5 Gyr), metallicities ($[\mathrm{Fe/H}]$ = -2.0, -1.0, -0.5, 0.0 and +0.5), all covering the initial mass range from 0.1 to 50.0 $M_{\odot}$. All twenty isochrones are plotted in Figure 4.38, from which it becomes obvious that a clear assignment of each star of this composite stellar sample to a certain SSP is impossible using only the isochrone fitting method (called the "isochrone degeneracy").

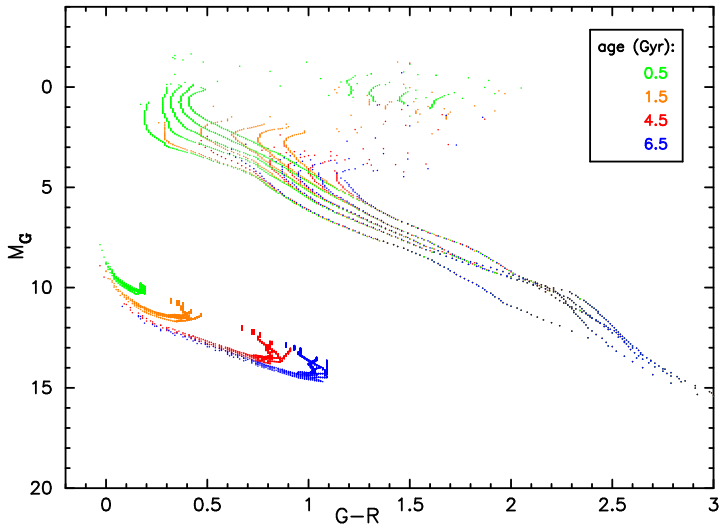

FIGURE 4.38.: Isochrones of 20 single stellar populations of different ages (0.5, 1.5, 4.5 and 6.5 Gyr) and metallicities ([Fe/H] = -2.0, -1.0, -0.5, 0.0 and +0.5).

A similar unfortunate phenomenon is the *age-metallicity degeneracy* (AMD), found in the integrated light of single stellar populations:
An increase in age leads to a redder colour, due to the decreasing number of hot blue stars. This can be counterbalanced by decreasing the metallicity, which results in bluer colours because of the lower opacity in the outer layers of the star (Wenger 2005).

Worthey (1999) illustrates the so called "3/2 age-metallicity degeneracy" on the integrated light of single age, single metallicity stellar populations: SSPs of 3 times the age or twice the metallicity of a certain base population have nearly identical spectra.
As an illustration, two almost identical spectra (particularly in the visible), but corresponding to different parameter combinations are plotted in the left panel of Figure 4.39 in red and orange. In black is shown the spectrum of the base population ($age = 4$ Gyr, $z = 0.004$) is shown, from which the populations corresponding to the red spectrum (three times the initial $age = 12$ Gyr) and the orange spectrum (twice the input metallicity $z = 0.008$), are derived.

Wenger (2005) investigated the age-metallicity degeneracy of the SSP spectra of the theoretical integrated spectral library (BLoIS (Wenger 2005)). As a first step, he compared all spectra with each other and found out that all single stellar populations have unique spectra [6].
From this, he concluded that no 100 % degeneracy between age and metallicity exists in the BLoIS spectra. On the negative side, he showed that certain combinations of age and metallicity can lead to very similar spectra.
As an illustrative example of an AMD in two BLoIS spectra, see Figure 4.39 (right panel), where the spectrum of a population with $Z = 0.05$ and $age = 0.004$ Gyr (in blue) is almost identical to the spectrum of a population with a metallicity around 50 % lower and an age of around 50 % higher (green spectrum).

For a closer look at such similar SSP spectra and therewith at the AMD, he compared the low resolution spectra of a test single population (with a metallicity of Z =0.008 and at the ages 0.14, 0.9 and 2.0 Gyr) with the spectra of 6 other populations that have the same IMF:

[6] They can have the same colours in some cases, for more details see Wenger (2005).

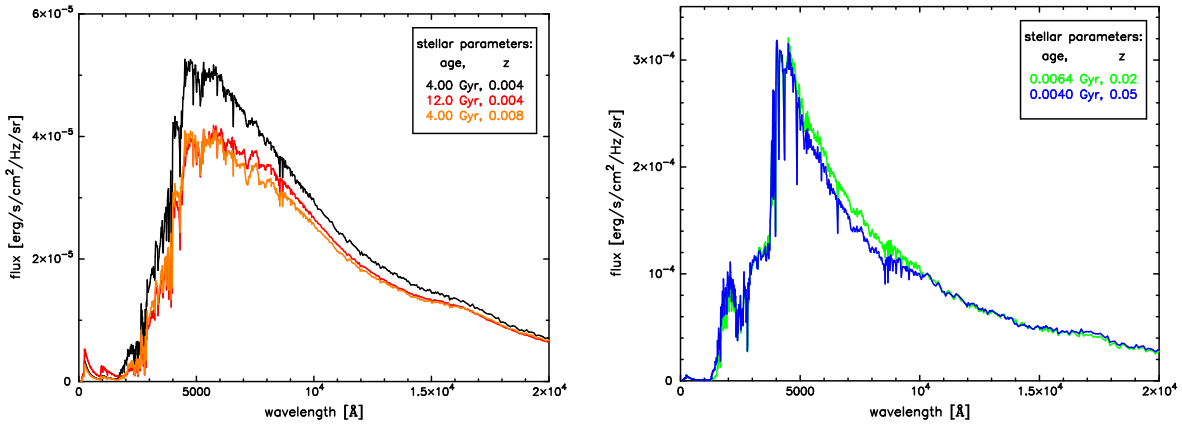

FIGURE 4.39.: Left panel: The age-metallicity degeneracy as visualised by Worthey (1999). Right panel: The age-metallicity degeneracy visualised by Wenger (2005).

$$\begin{pmatrix} \text{IMF slope} \\ \text{IMF mass range} \end{pmatrix} \quad : \quad \begin{pmatrix} 1.35 \\ 0.1 - 100.0 \end{pmatrix},$$

but different metallicities (Z =0.0001, 0.0004, 0.004, 0.02, 0.05 and 0.1) at different ages.
By determining a best fitting spectrum for each of the three ages of the test population and for each of the six metallicities, he ended up with 18 best-fitting ages.
From plotting the metallicities versus the ages of the best fitting SSPs, he concluded that, in the age-metallicity plane, populations with similar spectra are located at positions that can be approximated by a power law, written as follows in a double logarithmic scale:

$$log_{10}(z) = s \cdot log_{10}(t) + c. \tag{4.3}$$

Depending on the location in the age-metallicity plane, the slope of this power law can vary from -5 for young to -1 for old ages.
The slope of $\frac{d\,log(age)}{d\,log(Z)} = -\frac{3}{2}$ suggested by Worthey (1999) is confirmed by Wenger (2005) only at old ages. At younger ages the slope is much steeper.

Coming back to the problem of the 'isochrone fitting' method, it is necessary to apply other diagnostic methods to assign stellar parameters to stars in the colour-magnitude diagram (for further details see e.g., Hernandez, Valls-Gabaud & Gilmore (1999), Harris & Zaritsky (2001) and Frayn & Gilmore (2002, 2003)). The method of isochrone fitting is not adequate to resolve our test composite population into several SSPs. The test population lacks prominent features like a horizontal branch or ared giant branch, which could have been used for the separation. Furthermore, the main sequence turn off (MSTO) is so fuzzy that it can not be resolved into several distinct SSP-MSTOs.

In contrast to the "isochrone degeneracy", for composite spectra with a higher resolution, the degeneracy can be broken by using specific spectral indices that are almost exclusively sensitive either to age (like Hγ_{HR} introduced by Jones (1996)) or metallicity (certain metallic spectral indices, see Worthey (1999)) or show nonlinear behaviour with the temperature of the main sequence turnoff region (like near-UV-to red colours and Balmer line strengths, see Worthey (1999)).

4.4.3. Stellar distributions resulting from different IMFs

The initial Mass Function

The Initial Mass Function (IMF) defines the mass distribution of a stellar population created in one star formation event in a given volume of space of a galaxy. It describes, how many stars out of the total number of stars that formed at the birth of the population, are in each mass interval.
Since the mass of a star determines its lifetime, luminosity, and ability to enrich the interstellar medium with elements heavier than H and He after its death, the evolution of a galaxy is in many ways highly sensitive to the IMF. Together with the Star Formation Rate (SFR) and the star formation metallicity, the IMF dictates the evolution and fate of a galaxy (Kroupa 2002).
In our days, many different theoretical approaches to derive theoretical IMFs are being tried (see Figure 4.43). Here, we want to concentrate on two of the most important schools: the Salpeter- and the Kroupa-IMF. We refer to the model galaxy with a Salpeter-IMF as Salpeter-galaxy and with a Kroupa-IMF as Kroupa-galaxy.
Salpeter published the first IMF in 1955, in form of a single-slope power law (as already mentioned in Subsection 4.2.1). In Figure 4.40 the Abstract of his famous paper "Luminosity Function and Stellar Evolution" is shown, and in Figure 4.41 the Salpeter-IMF is shown.

THE LUMINOSITY FUNCTION AND STELLAR EVOLUTION

EDWIN E. SALPETER*
Australian National University, Canberra, and Cornell University
Received July 29, 1954

ABSTRACT

The evolutionary significance of the observed luminosity function for main-sequence stars in the solar neighborhood is discussed. The hypothesis is made that stars move off the main sequence after burning about 10 per cent of their hydrogen mass and that stars have been created at a uniform rate in the solar neighborhood for the last five billion years.

Using this hypothesis and the observed luminosity function, the rate of star creation as a function of stellar mass is calculated. The total number and mass of stars which have moved off the main sequence is found to be comparable with the total number of white dwarfs and with the total mass of all fainter main-sequence stars, respectively.

FIGURE 4.40.: The Abstract of Salpeter's famous paper "Luminosity Function and Stellar Evolution" (Salpeter 1955).

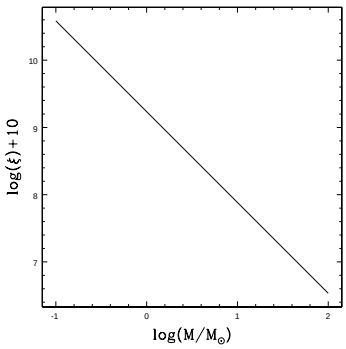

FIGURE 4.41.: The Salpeter-IMF, normalized to a total mass of 1 $M_{\odot}$.

His pioneering work (Salpeter 1955) was based on the analysis of the luminosity function of main-sequence stars in the solar neighbourhood [7] (see Figure 4.42), which he converted into a mass distribution using an adopted mass-luminosity relation. The first IMF was derived by supplementing this mass distribution with those stars which, due to their assumed lifetimes, must already have died during the disk evolution.

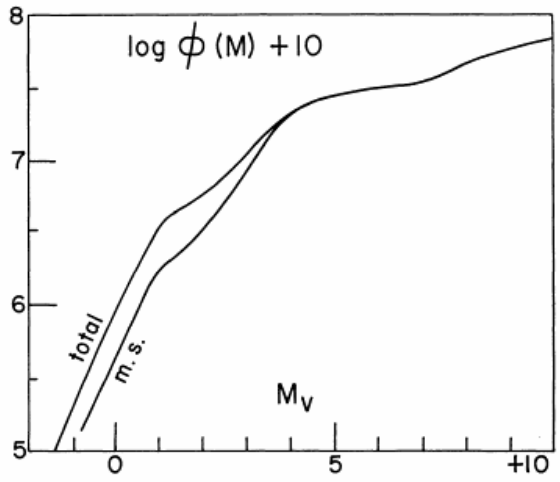

FIGURE 4.42.: The logarithm of the stellar luminosity function ϕ as a function of the visual magnitude, M_v (*total* = all stars, *m.s.* = main-sequence stars only) (Salpeter 1955)).

Miller & Scalo (1979) examined the (supposedly time-independent) IMF of the solar neighbourhood stars as well, but concluded that the IMF flattens significantly in the low-mass region (see Figure 4.43). Kroupa (2001) investigated a Galactic-field and confirmed Miller & Scalo's results. He pointed out that there is evidence for a change in the power law index at around 0.5 $M_\odot$ (resulting in his universal IMF), or even two changes, one at 0.5 $M_\odot$ and at 1.0 $M_\odot$ (called Kroupa present-day IMF, see Figure 4.44).
In his newer work, Chabrier (2002) showed that the IMF for Brown Dwarfs (BDs) is even shallower than for low-mass stars, so that very-low-mass stars and BDs contribute insignificantly to the local mass density.

The derivation of the IMF leads to various difficulties:
The IMF inferred from the local field stars suffers from significant uncertainties by depending on assumptions about stellar lifetimes and the evolutionary history of the Galactic disk.
The determination of the IMF from star clusters, which ideally represent single stellar populations, causes problems as well. The first difficulty comes from the account of faint stars. Some of the faint cluster members may be perceived as background Galactic field stars, and vice versa. Due to mass segregation and star-star encounters, clusters may have lost some single low-mass stars. Furthermore, systematical errors can also arise from unresolved binary stars since they are brighter than each of their individual component stars (e.g., Kroupa (2001)).

Another, still unsettled issue concerning the IMF is its universality, which was confirmed by several authors. While it seems plausible that the IMF varies with star forming conditions such as pressure, density, or metallicity of the forming cloud, Kroupa (2002) found little evidence for large systematic variations in the IMFs of different

[7] No exact radius defining "the solar neighbourhood" exists. We use the term for the region of the Milky Way close to the Sun - within about 25 pc (Kroupa 2002).

star forming galaxies, and therefore favours a universal and time-independent IMF.
Figure 4.43 shows the most frequently used IMFs in our days. For recent reviews see Elmegreen (2001), Kroupa (2002) and Chabrier (2003).

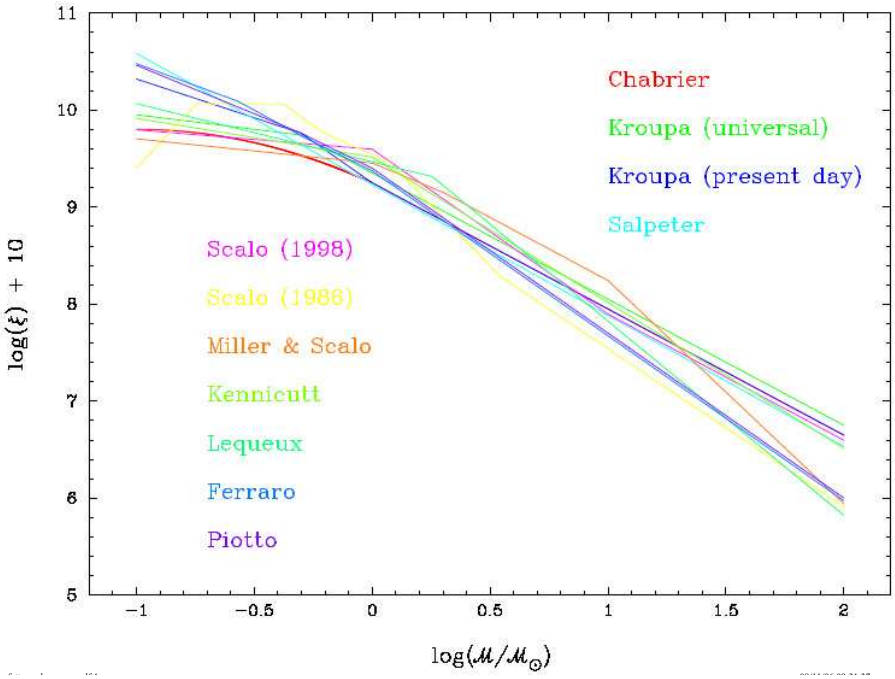

FIGURE 4.43.: Various IMFs, all normalized to a total mass of 1 $M_{\odot}$ (Wenger 2005).

Model galaxies with different IMFs

The IMF can be implemented as an input parameter in the chemo-dynamical models of Samland, Hensler & Theis (1997) and Samland & Gerhard (2003). We analyse the effects on the stellar distribution implementing two different IMFs in the model: the *Salpeter-IMF* (Salpeter 1955), which is a single power law IMF, and the *universal Kroupa-IMF* (Kroupa 2001), which flattens in the low-mass region.

Both IMFs are described by power laws:

$$log(\xi(\mathcal{M})) = log(c \cdot \mathcal{M}^{-x}) \tag{4.4}$$

where
$\xi(\mathcal{M})$: number of stars of mass $\mathcal{M}$
c : normalizing factor (total mass = 1.0 $M_{\odot}$)
$\mathcal{M}$: stellar mass (in $M_{\odot}$)
x : exponent (negative).

Tables 4.11 and 4.12 list the values of the mass range ($\mathcal{M}$), the slope (x) and the normalizing factor (c) of the Salpeter- and the Kroupa-IMF, respectively.

TABLE 4.11.: The Salpeter (1955) IMF

$\mathcal{M}$	0.10 – 100.00
x	1.35
c	1.7164E–01

TABLE 4.12.: The Kroupa (2001) Universal IMF

$\mathcal{M}$	0.10 – 0.50	0.50 – 100.00
x	0.30	1.30
c	4.4891E–01	2.2446E–01

Note: A positive value for x means a negative slope.
The constant c is used to normalise the total stellar mass to 1.0 $M_{\odot}$. To calculate the total mass ($\mathcal{M}_{tot}$), we integrate Equation 4.4 between a lower ($\mathcal{M}_l$) and an upper mass limit ($\mathcal{M}_u$) of a stellar population:

$$\mathcal{M}_{tot} = \int_{\mathcal{M}_l}^{\mathcal{M}_u} \cdot c \cdot \mathcal{M}^{-x} \cdot d(\mathcal{M}) = 1 M_{\odot} \tag{4.5}$$

Both mass limits are arbitrary, but suggested by the actual data used to derive the IMFs. For our project we adopt 0.1 $M_{\odot}$ for the lower mass limit and 50.0 $M_{\odot}$ for the upper mass limit.

Both IMFs have almost the same slope for higher mass stars ($\geq 0.5 M_{\odot}$) (Salpeter: $x = 1.35$, Kroupa: $x = 1.30$), but compared to the Salpeter-IMF, the Kroupa-IMF flattens at lower masses.
To evaluate the effects of this flattening on the evolution of a galaxy, we generate two model galaxies, one with a Salpeter-IMF (Salpeter-galaxy), and another one with a Kroupa-IMF (Kroupa-galaxy), and compare their star count histograms in different viewing directions.
The stellar U-G distributions of the simulated Basel survey field SA94 in Figure 4.45 reveal such a difference. Depending on their masses and ages, stars populate different regions in such a histogram. After an evolution of around 13.5 Gyr, stars with colours U-$G \leq 1.5$ are mainly high- and near solar-mass stars ($\geq$ 0.75 $M_{\odot}$), whereas lower-mass stars dominate the redder part (U-$G \geq 2.0$).
One indication that the Kroupa-IMF produces more high-mass stars is seen in the $1.0 \leq U$-$G \leq 1.2$ bin. Compared to the same bin in the right-hand panel, a galaxy with a Kroupa-IMF contains more near-solar-mass stars. In contrast, more low-mass stars are formed relative to the number of higher-mass stars in a galaxy with a Salpeter-IMF, which can be seen from the higher $2.6 \leq U$-$G \geq 2.8$-column to $1.0 \leq U$-$G \geq 1.2$-column ratio in the right panel.

Table 4.13 shows the absolute numbers of the ratios of low-mass stars ($\leq$ 0.6 $M_{\odot}$) to all stars in the upper part and the ratios of intermediate-mass stars (1.0 $M_{\odot} \leq M_{*} \leq\sim$ 4.0 $M_{\odot}$) to all stars in the lower part, as functions of IMF and viewing direction.
In whatever direction you look, in a galaxy with a Kroupa-IMF low-mass stars make up only for a percentage of approximately 18%, in one with a Salpeter-IMF for about 36%, respectively. 26% of the stars in the Kroupa-galaxy are equal to or more massive than 1.0 $M_{\odot}$, whereas in the Salpeter-galaxy only 17% belong to this mass range.

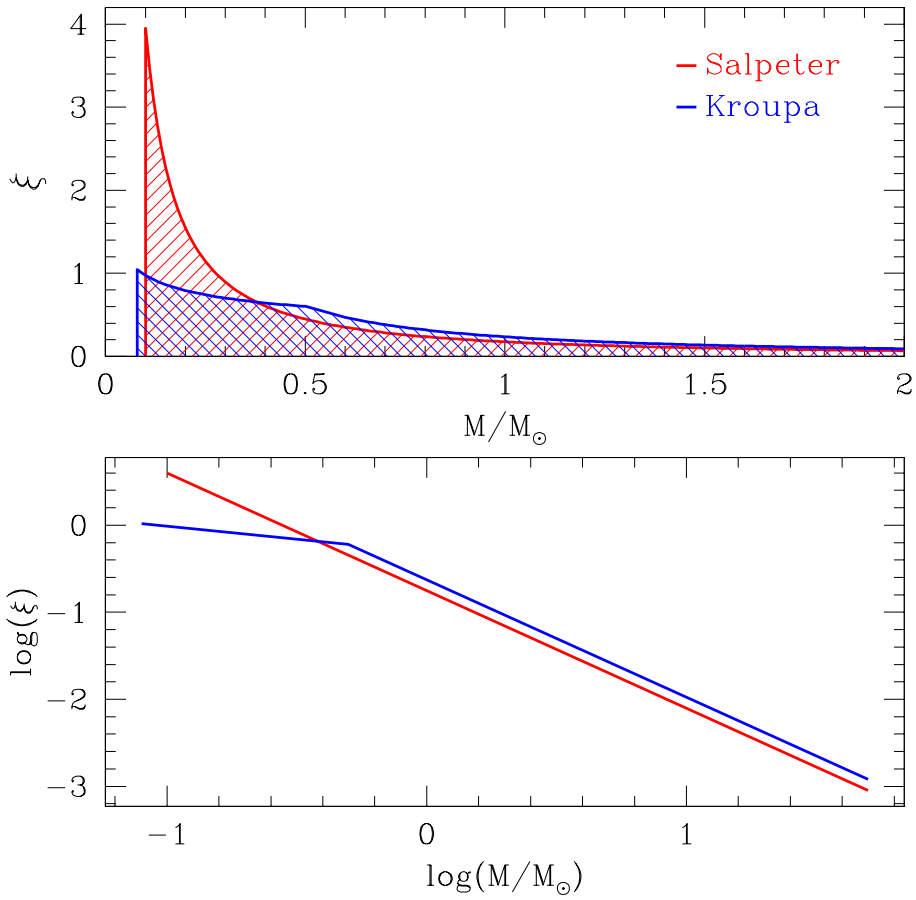

FIGURE 4.44.: The two stellar Initial Mass Functions used to generate the two different model galaxies: the Kroupa-IMF in blue and the Salpeter-IMF in red. In the upper panel the Initial Mass Functions (ξ) are plotted on a linear scale, whereas $\mathcal{M}_{tot} = \int_{\mathcal{M}_{0.1}}^{\mathcal{M}_{50.0}} \cdot c \cdot \mathcal{M}^{-x} \cdot d\mathcal{M} = 1 M_{\odot}$. In the lower panel both IMFs are shown on a logarithmic scale. Figure produced by P. Westera.

Of 10' 000 drawn stars, a small fraction drops out in form of *black holes*[8]. Table 4.14 lists the numbers of black holes in the three different directions, both for the Salpeter- and the Kroupa-galaxy. The relative number of black holes is much higher in a galaxy with a Kroupa-IMF, in which more high-mass– ($\geq 5.5\ M_{\odot}$) and therefore shorter-lived stars are formed.
The evolution of the theoretical galaxy from the inside outwards can not be deduced from the number of black holes. On the contrary, the generally younger field towards the Galactic anticentre (SA94) shows in both galaxy models a slightly higher fraction of black holes than the other fields, even though the stars of both fields (SA107 and M101) have had more time to evolve into black holes.

Since black holes are not important for practical observations, we turn our attention in the following part to observable stars:

[8]The stellar evolutionary tracks describe the evolution of all the stars until different ages, depending on their initial stellar masses. We define all the stars that are older than the last age step in the tracks as *black holes*, neglecting their real end-stage according to their masses (neutron stars, black dwarfs or black holes).

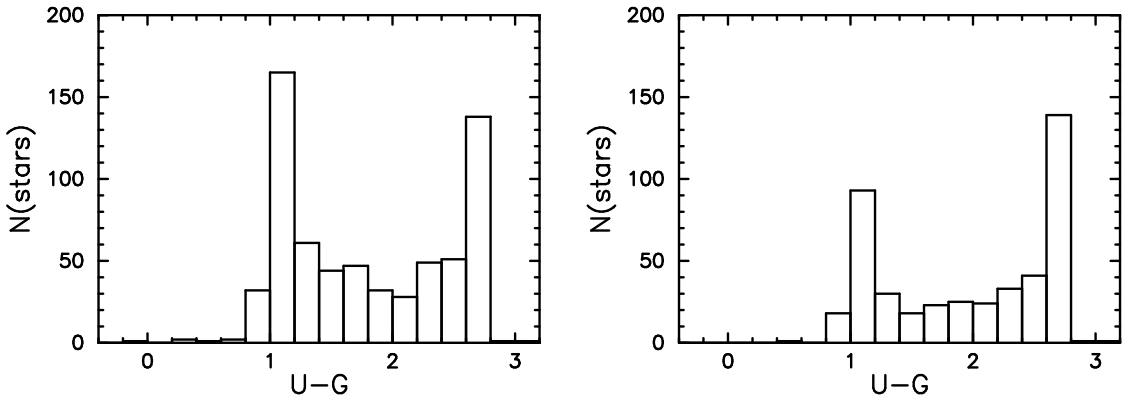

FIGURE 4.45.: Stellar U-G distributions (field SA94) of a galaxy with a Kroupa-IMF (left panel) and a Salpeter-IMF (right panel).

TABLE 4.13.: Mass ratios

Low-mass stars to all stars

Field	Kroupa-IMF	Salpeter-IMF
SA107	110/773	123/373
M101	126/664	145/419
SA94	130/655	169/447

Intermediate-mass stars to all stars

Field	Kroupa-IMF	Salpeter-IMF
SA107	181/773	47/373
M101	168/664	76/419
SA94	195/655	89/447

TABLE 4.14.: Stellar distributions towards the inner Galaxy (SA107), the outer Galaxy (M101) and the Galactic anticentre (SA94).

IMF	Field	Full sample	Black holes
Salpeter-IMF	SA107	10' 000	34
Kroupa-IMF	SA107	10' 000	95
Salpeter-IMF	M101	10' 000	40
Kroupa-IMF	M101	10' 000	86
Salpeter-IMF	SA94	10' 000	41
Kroupa-IMF	SA94	10' 000	103

TABLE 4.15.: Stellar distributions towards the inner Galaxy (SA107), the outer Galaxy (M101) and the Galactic anticentre (SA94).

IMF	Field	All stars with $M_v \leq 22.0$	Main sequence stars	Giants	White dwarfs
Salpeter-IMF	SA107	965	949	9	7
Kroupa-IMF	SA107	1769	1728	29	12
Salpeter-IMF	M101	1098	1069	15	14
Kroupa-IMF	M101	1541	1495	31	15
Salpeter-IMF	SA94	1136	1110	18	8
Kroupa-IMF	SA94	1421	1379	30	12

With the black holes omitted, we reduce all six stellar samples by applying a limiting apparent magnitude of $m_v \leq 22.0$ to the remaining stars to simulate real observations. Subdividing the now smaller stellar samples of the Kroupa- and the Salpeter-galaxy into different stellar types, Table 4.15 gives an overview of the relative numbers of **main sequence**–, giant–, and white dwarf stars in the three viewing directions; and Figures 4.46 and 4.47 show their positions in the Hertzsprung-Russell and the two-colour diagrams.

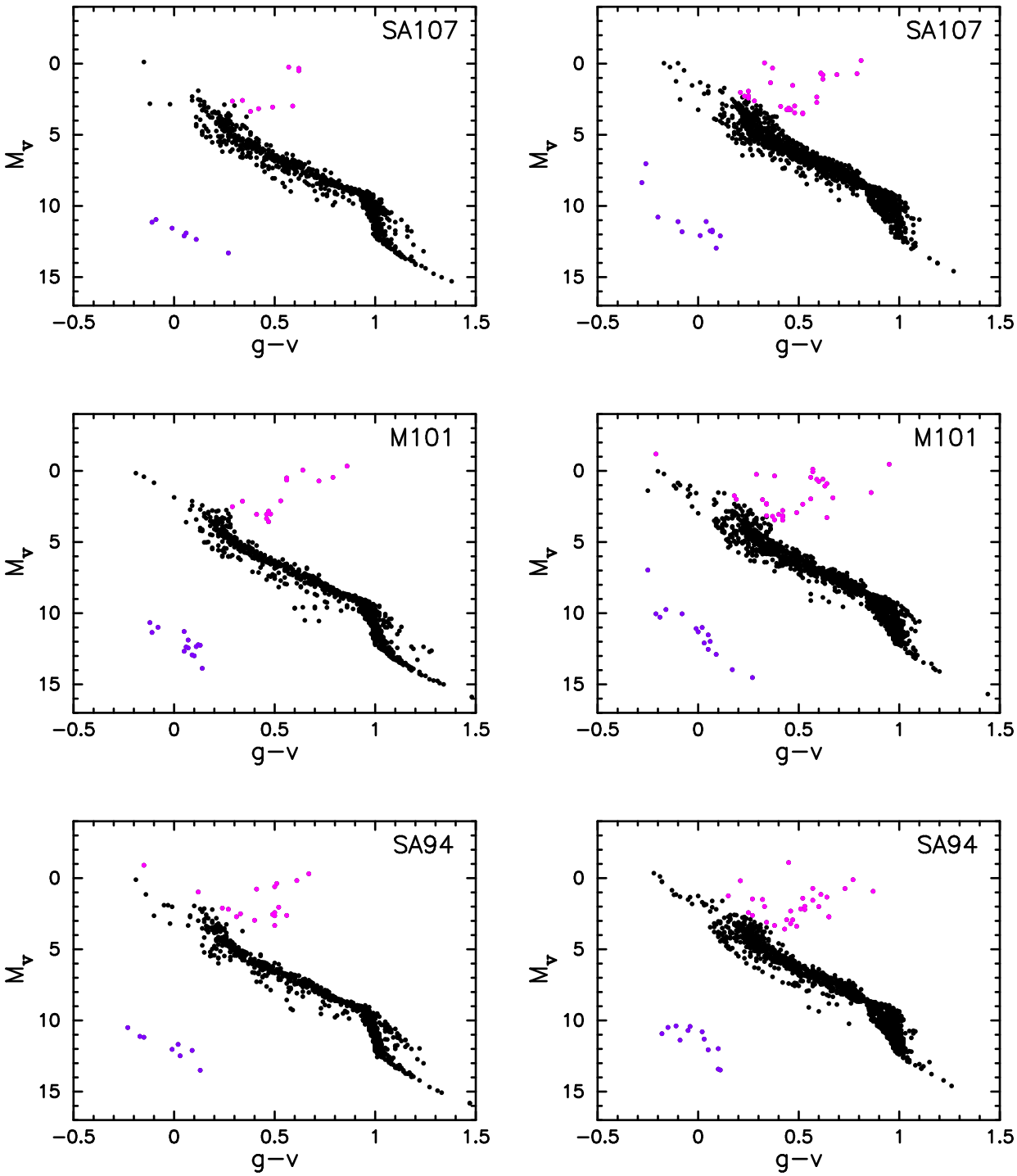

FIGURE 4.46.: The positions of **main sequence**–, giant–, and white dwarf stars in the Hertzsprung-Russell diagrams of the three viewing directions are plotted. In the left panels, the stellar distributions of the Salpeter-galaxy are shown and in the right panels those of the Kroupa-galaxy.

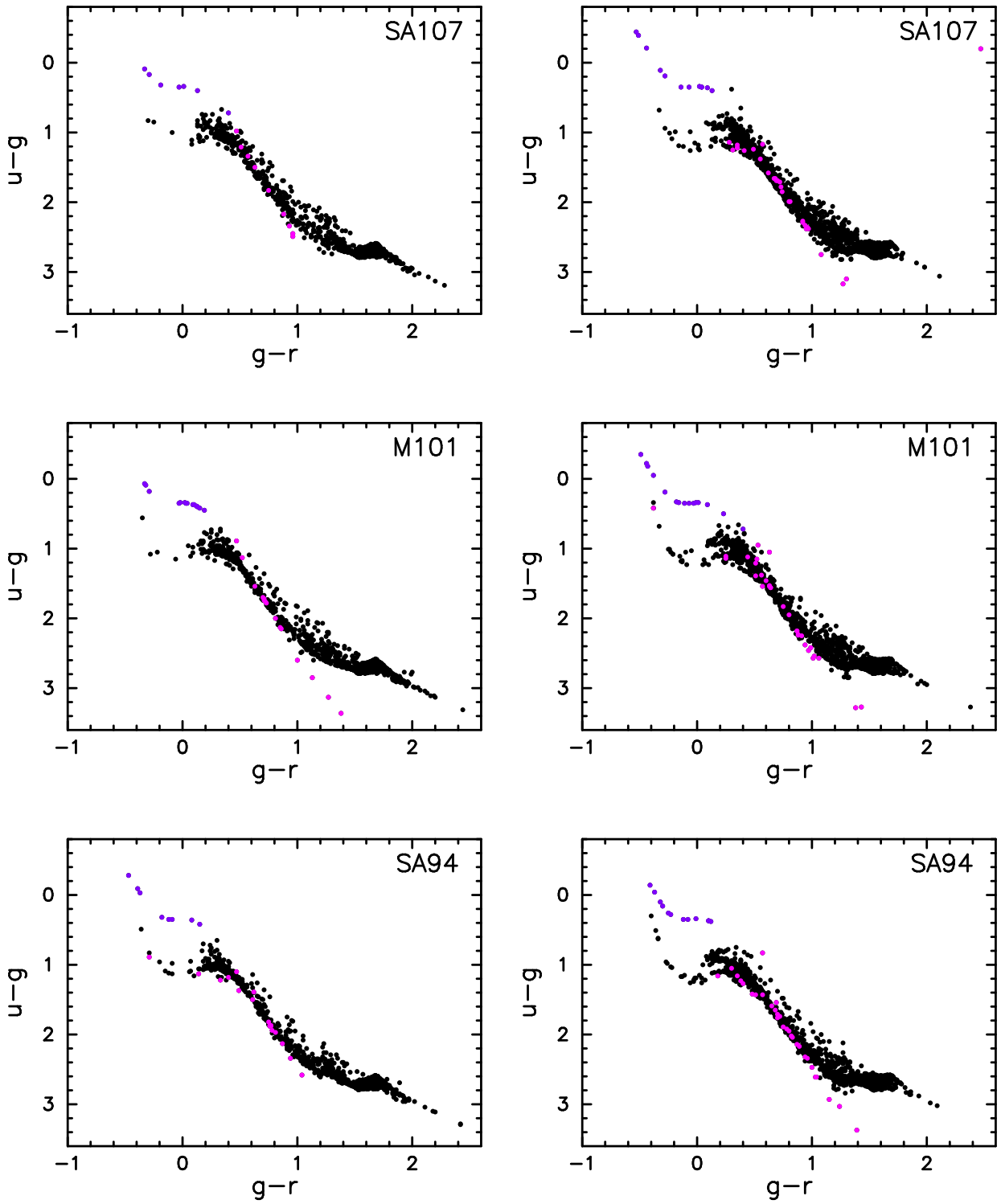

FIGURE 4.47.: The positions of **main sequence**–, giant–, and white dwarf stars in the two-colour diagrams of the three viewing directions are plotted. In the left panels, the stellar distributions of the Salpeter-galaxy are shown and in the right panels those of the Kroupa-galaxy.

Only around 1' 000 out of 10' 000 stars are detectable, that is brighter than 22nd magnitude in V, in the Salpeter-galaxy. Most stars in this galaxy are low-mass stars that drop out because of their low luminosities. The smaller sizes of these samples are clearly visible from the thinner main sequence in the left panels of Figures 4.46 and 4.47 (black dots represent main sequence stars).

Taking into account statistical fluctuations, both model galaxies contain almost identical numbers of giants or white dwarfs in all three viewing directions.
This is astonishing, since (as mentioned in Subsection 4.4.1) the slightly brighter main sequence turn-off of field SA94 towards the anticentre indicates a generally younger age of the stars in this direction. From this, one would expect less white dwarfs in SA94 compared to the more evolved fields SA107 and M101 and a brighter turn-off as well.

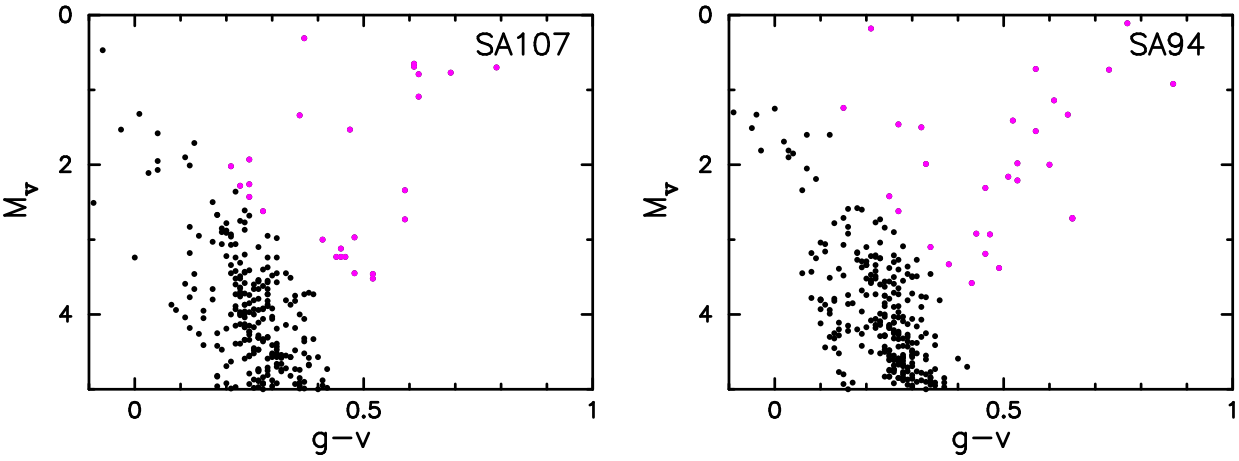

FIGURE 4.48.: Colour-magnitude diagrams of two different viewing directions in the Kroupa-galaxy.

The number of white dwarfs is more or less the same in every direction [9], but the turn-offs of the main sequences show differences in their absolute V-magnitudes (for a closer look in case of the Kroupa-galaxy, see Figure 4.48). A rough naked eye estimate shows different turn-off points: The turn-off of the inner Galactic field SA107 of the Kroupa-galaxy (Figure 4.48, left plot) lies in the range of $M_v \sim 2.75$ and the one of field SA94 (Figure 4.48, right plot) in the range of $M_v \sim 2.5$. The same is true for the Salpeter-galaxy, where the turn-off of the inner Galactic field SA107 lies in the range of $M_v \sim 2.90$ and the one of field SA94 in the range of $M_v \sim 2.75$. It seems that the age differences are too small to affect the number of white dwarfs significantly.

We conclude that the position of the turn-off point of the main sequence in a H-R diagram can be used as a reliable indicator for the relative mean age of a single or composed stellar population, whereas the number of detected white dwarfs is not necessarily correlated with the stellar mean age. The star formation rate is more important!

Short excursus: IMF-effects on the integrated colours of galaxies

In their study, Westera et al. (2006) analysed the effects of the IMF on the integrated magnitudes and colours especially of high-redshift galaxies, which cannot be resolved into individual stars.

[9] A reason for the uniform distribution of the white dwarfs could lie in the limitating apparent magnitude that smears out the age differences. However, looking at the whole (unlimited) samples gives the same result: There are only small differences in the numbers of white dwarfs in the different viewing directions.

Using the same chemo-dynamical models (Samland et al., 1997; Samland & Gerhard, 2003) as in our work, they also developed two model disk galaxies with the same boundary conditions, but different IMFs: a Salpeter-IMF and a Kroupa-IMF.
They found that the IMF affects the internal gas absorption of the model galaxies more than the direct light from the stellar content. These two effects (internal gas absorption and bluer– and brighter star-light) influence the integrated magnitudes and colours in opposite ways. The Kroupa-IMF produces more high-mass stars and thus leads to brighter and bluer direct star-light. But while the stellar light is brighter and bluer, the high-mass stars also produce more interstellar dust in the interstellar medium and thus more absorption occurs, making the integrated light fainter and redder again. They call this coincidence "IMF degeneracy".
As a consequence of this effect, the two different IMFs are not distinguishable from each other using only the integrated magnitudes and colours of unresolved disk galaxies. This is in strong contrast to our results for a "resolved" disk galaxy, where the two different mass distributions significantly influence the star count histograms.

5. Comparisons of theory and observations

5.1. Basel survey fields

After having investigated theoretical stellar populations in the last few Sections (4.2, 4.3 and 4.4), we present in this section the most important results of our comparisons between the theoretically predicted stellar data, obtained by applying our code as described in Section 3, and the stellar data of the Basel or SDSS survey catalogues observed in different viewing directions.
We make many comparisons with observations in this part. In all the following plots, the observed stellar data are drawn in black, while the model calculations are plotted in other colours.

5.1.1. The effects of extracting a certain number of stars

To investigate if the number of extracted stars changes anything in the applied IMF or colour distribution of the models, we run the code twice for the same Basel field (SA94), but with different numbers of drawn stars. The first sample consists of 100' 000– and the second of only 10' 000 stars.
In Subsection 4.1.1 we described the method for drawing the stars from the stellar particles. Here, we summarise it very briefly: The stellar particles that build up the Samland galaxy are distributed in the model galaxy in such a way as to reflect the star formation history.

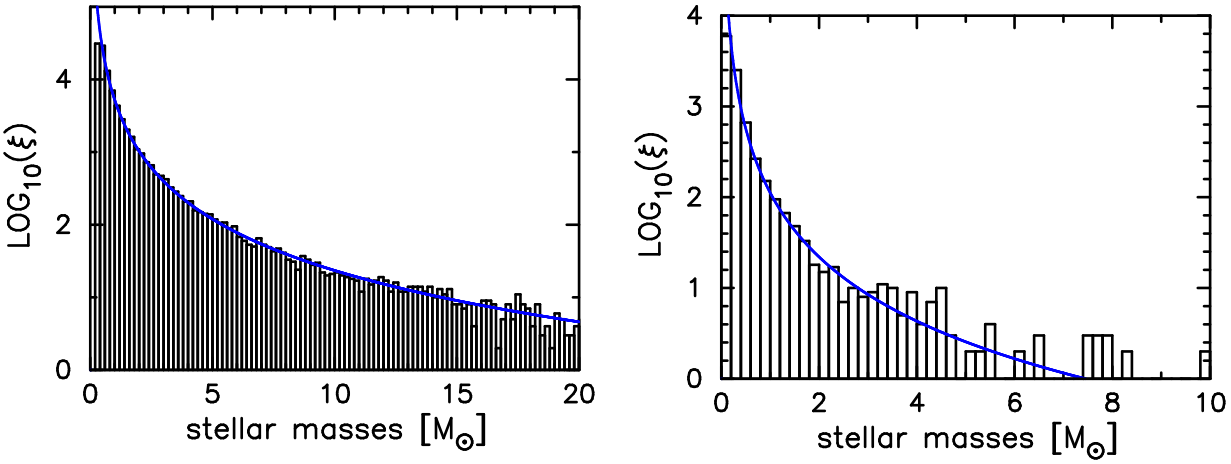

FIGURE 5.1.: The stellar initial mass distributions of the 100' 000 stars sample (left panel) and the 10' 000 stars sample (right panel), respectively. The blue curve marks the Salpeter(1955)-IMF.

To extract stars, we take into consideration only stellar particles that lie in the chosen viewing direction and field size. In this viewing cone, the stellar particles have slightly different masses. The more massive they are, the higher is the probability of being drawn. In a next step, stars are chosen from these selected stellar particles

with mass-dependent probabilities according to the applied IMF (here the Salpeter-IMF). The total number of stars extracted from them can be chosen freely.
We analyse the mass distributions of these two samples by comparing the initial masses of all stars with the IMF of Salpeter (1955). Figure 5.1 represents the mass distributions of both samples: in the left panel the sample consisting of 100' 000 stars is shown and in the right panel the one of the sample of 10' 000 stars. In blue, the Salpeter-IMF is added.

As expected (by design), both samples follow the Salpeter-IMF quite accurately, independent of the size of the stellar sample.

Exceptions can be found in the higher stellar mass range (right plot: stellar masses $\geq$ 5.0 $M_{\odot}$), where we are dealing with small number statistics.

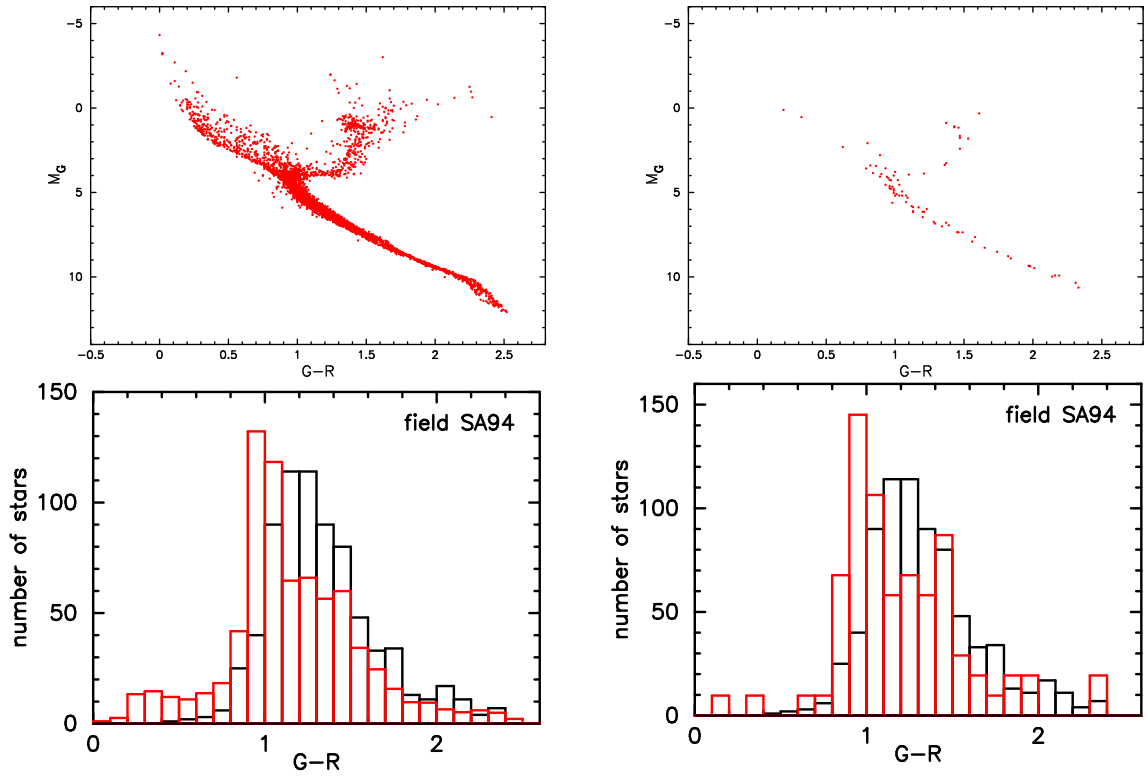

FIGURE 5.2.: HR-diagrams (upper panels) and $G-R$ colour distributions (lower panels) of two theoretical stellar samples towards the anticentre (SA94), both with applied limiting apparent $G-$ and $R-$ magnitude, plotted in red. The two left plots are produced with a sample of 100' 000 stars, whereas the right panels show the HR-diagram and star count of a sample of only 10' 000 stars in red (normalised to the total number of stars in the corresponding field of the survey). The observed $G-R$ colour distribution towards the Galactic anticentre is plotted in black in the lower two panels.

In a next step, we investigate the differences of these two stellar data sets regarding their distributions in the colour-magnitude diagram (CMD) and in $G-R$ star count.
The upper panels of Figure 5.2 show the colour-magnitude diagrams of these two stellar sets. In the upper left plot, the stars with apparent magnitudes $m_G \leq 17.4$ and $m_R \leq 15.8$ (the limiting apparent magnitudes of the Basel survey in the field SA94 towards the anticentre) of the bigger sample are plotted. The upper right plot shows the colour- magnitude distribution of all stars of the smaller sample, that have apparent magnitudes of

$m_G \leq 17.4$ and $m_R \leq 15.8$.
As can be seen, both stellar samples cover almost the same regions in the CMD.
After applying the limiting apparent magnitudes (defined in Section 2.4) the observed stellar sample is reduced by a factor of ~ 0.5, whereas the theoretical stellar data are reduced by much more. Out of 100' 000 stars only 4 % are left, and out of the smaller sample less than one hundred stars remain. All the others stars are too faint to be detectable.
Both theoretical distributions are scaled by a multiplication factor to the same number of stars as in the Basel survey. In order to examine the similarity – or not – of the shapes of the distributions (obs. versus theor.), not the absolute numbers.
Table 5.1 gives an overview of the different star counts of all three data sets and the applied multiplication factors: The first column lists the names of the three data sets, the second one the numbers of all stars, the third column shows the number of stars remaining after applying the limiting apparent magnitudes, and in the fourth column the scaling factors are given.

TABLE 5.1.: Star counts and applied factors

stellar set	all stars	residual stars	scaling factor
Basel survey set	1369	745	1.00
100'000 sample	84490	3456	0.22
10'000 sample	9962	77	9.68

Even though the two theoretical samples have different sizes and scaling factors, the resulting shapes of the $G-R$ colour distributions are almost the same, and both differ in the same way from the observed distribution. Note: A statistical fluctuation factor of amounting to the square root of the number of stars $\sqrt{\#\,\mathrm{stellar\ particles}}$ should also be taken into account. In the Samland code, every one million years 50 stellar particles are created in the regions of the galaxy, where the star formation takes place. In this way, the actual star formation rate is reflected in the age distribution of the stellar particles. In the direction towards the galactic anticentre (and halo too), the Samland model does not contain many stellar particles, since the star formation rate is low there. This leads to high statistical fluctuations in these regions compared to the more populated regions such as the Galactic thin disk.
The calculated samples give high star counts in the bins $0.9 \leq G-R \leq 1.1$. These bins are populated by stars with masses of $0.7\ M_\odot \leq M_* \leq 1.9\ M_\odot$. Both samples have too few stars in the colour bins of $1.1 \leq G-R \leq 1.5$, which correspond to stellar masses of $0.6\ M_\odot \leq M_* \leq 4.3\ M_\odot$. Most of the stars with masses lower than $0.5\ M_\odot$ are excluded from the theoretical samples by the limiting apparent magnitudes imposed on the survey selection. As seen in Section 4.4.3, the Salpeter- and Kroupa-IMF differ only for stellar masses $M_* \leq 0.5\ M_\odot$.

The stellar particles are created and distributed according to the star formation history. Perhaps this SFH does not truly represent the actual star formation history of our Galaxy [1]. ***Apart from the model, another problem could lie in the transformations of the theoretical parameter values (initial masses, current ages, metallicities) into observable ones (apparent magnitudes and colours). We do not know, if stellar evolution is fully understood and if our stellar spectral libraries reproduce the stellar energy distributions of all types of stars correctly. It is not possible to analyse these ingredients separately to date.***

[1] Unfortunately, we are not able anymore to produce other model galaxies with slightly different SFHs for further comparisons.

5.1.2. Comparison of only a small part of the $G-R$ colour distribution

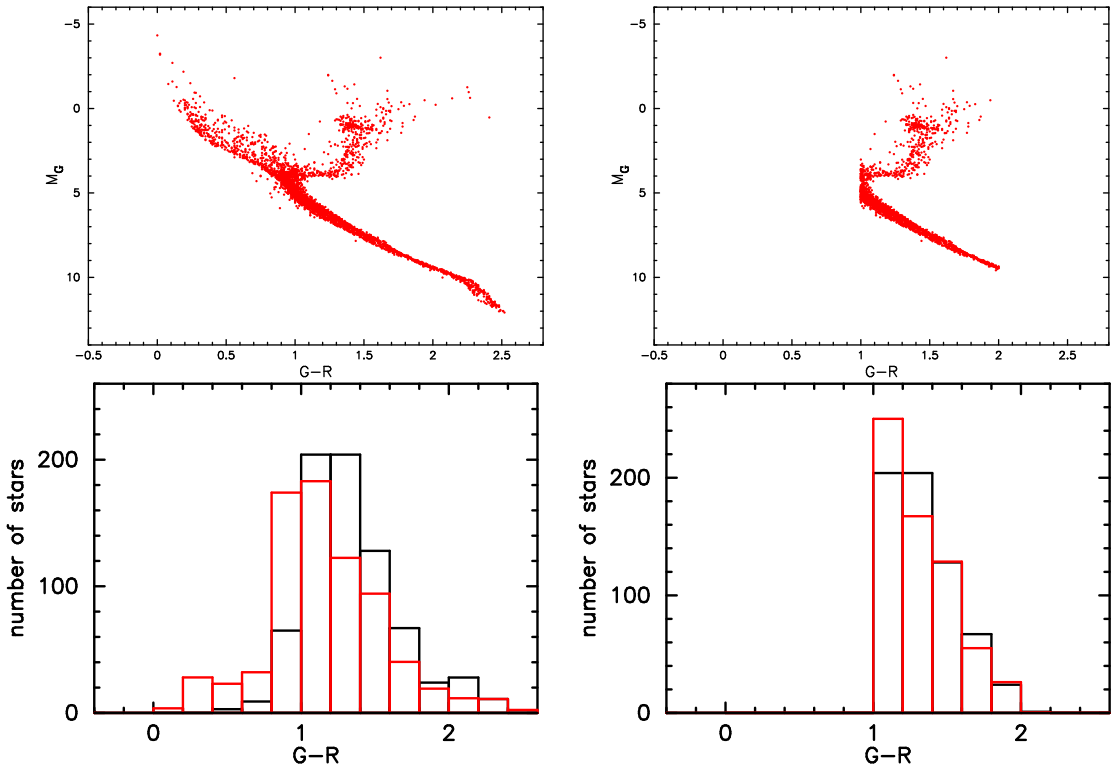

FIGURE 5.3.: CMDs (upper panels) and $G-R$ colour distributions (lower panels) of the same theoretical stellar sample towards the anticentre (SA94) plotted in red. In the left panels all 100' 000 theoretical stars are plotted, whereas in the right panels only theoretical stars in a certain colour range ($1.0 \leq G-R \leq 2.0$) are taken into account. The observed $G-R$ colour distribution towards the Galactic anticentre is plotted in black in the lower two panels.

Most of the stars observed in the Basel survey towards the Galactic anticentre (SA94) belong to the thick disk and the halo of our Galaxy. After studying thick disk globular clusters, Harris (1998) determined the mean age of the thick disk to be $\sim$ 11.4 $\pm$ 0.8 Gyr. For the age of the halo, VandenBerg (1999) determined the ages of globular clusters and fi eld stars in the halo on the basis of new stellar evolutionary models that treat the observed enhancements of α-elements explicitly. He attributes a mean age of $\sim$ 12.5 Gyr $\pm$ 2.0 Gyr to the Galactic halo.
In the distribution of the larger sample (consisting of 100' 000 stars) in the colour-magnitude diagram (Figure 5.3, upper left panel), the bright blue (and thus young) stars with absolute G-magnitudes of $M_G \leq 0.0$ and $G-R$ colours of $-0.2 \leq G-R \leq 0.5$ catch the eye.
It seems that these bright blue stars are artefacts of the Samland model. During the evolution of the galaxy, gas falls into the halo. If the gas density exceeds a certain threshold, the code generates new and thus bright stars, which may not exist in reality. We ignore this problem by eliminating all stars with $G-R$ colours bluer than 1.0 mag [2]. Of course, this procedure only illustrates the gravity of the problem, and has been applied here for illustration only.
Another uncertainty lies in all the low mass stars, where the stellar evolutionary tracks und spectra are not well calibrated. These relatively red stars are eliminated by applying a colour limit of $G-R = 2.0$.

[2] We fi x the limit at $G-R$ = 1.0 mag, due to the high discrepancy between the observed and the theoretical star numbers in the colour bin $0.8 \leq G-R \leq 1.0$ (see Figure 5.3, lower left panel).

From this selection procedure a new sample consisting only of stars with colours $1.0 \leq G-R \leq 2.0$ results. Its distribution in the colour-magnitude diagram can be seen in Figure 5.3, right panel. The two lower panels show the colour distributions of the whole sample (left) and plot of the dissected sample (right). Both samples are adjusted to the number of stars of the Basel survey (745 stars).
The $G-R$ star count of the dissected sample in the lower right panel shows good agreement with the observed stellar data.

On the basis of this knowledge, one could try to suppress the recent star formation rate in the outer part of the model galaxy halo. Furthermore, it seems to be necessary to avoid the redder stars.

In Appendix A.1, we show that most of the discrepances between the PHOENIX and the BaSeL 3.1 stellar spectral libraries can be found at lower temperatures and higher surface gravities. Due to our lack of a better understanding of these stellar types, we do not include them in the final analysis of the present work.

5.1.3. Comparison of two colours in the same viewing direction (SA94)

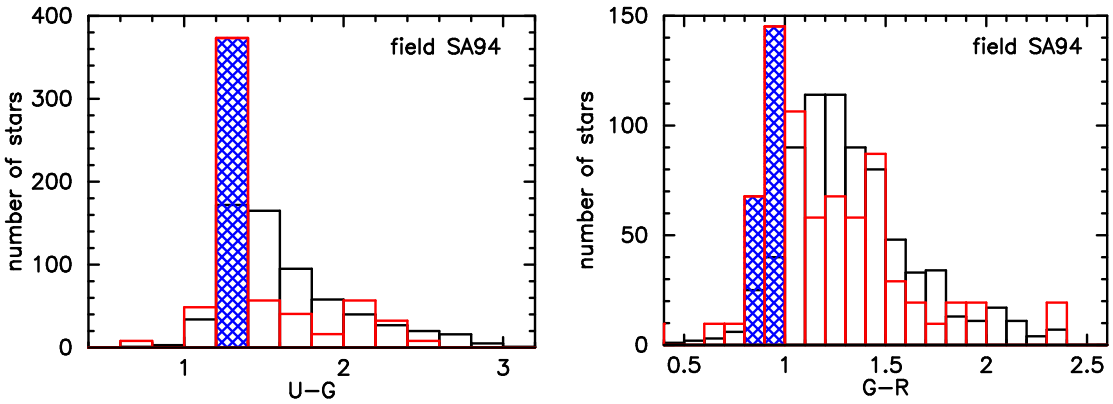

FIGURE 5.4.: $U-G$ (left panel) and $G-R$ (right panel) colour distributions towards the Galactic anticentre (field SA94). In black the colour distributions of the Basel survey data are shown and in red the ones of the model galaxy.

In the previous subsection, we investigated the $G-R$ colour distribution. Here, we want to analyse if the differences between theoretical− and observed stellar data are the same for all the other colours too.
Figure 5.4 shows the $U-G-$ (left panel) and $G-R$ (right panel) colour distributions of the Basel field SA94. In black, the binned star counts of the Basel survey are given, and in red those of the model (set of initially 10' 000 stars). Both theoretical colour distributions exhibit similar differences relative to their observed counterparts: too many stars in the bluer part and too few stars in the redder part of the histogram.

We point out that the differences between theoretical− and observed stellar data can be seen in all the other colours too.

5.1.4. Comparison of the $U-G$ colour distributions in different viewing directions

In order to see, if such differences between observed and theoretical star counts also occur in other viewing directions, we compare three fields (towards the Galactic anticentre (SA94, Figure 5.5), the inner Galaxy (SA107, upper panel of Figure 5.6) and the outer Galactic halo (M101, lower panel of Figure 5.6) of the Basel survey with the model data.

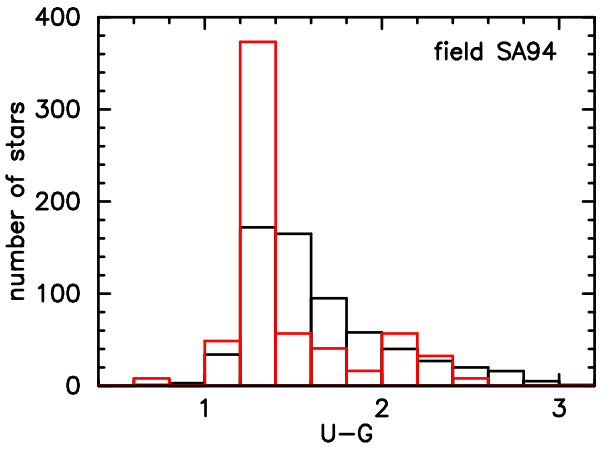

FIGURE 5.5.: Stellar $U-G$ colour distributions towards the Galactic anticentre (SA94). In black the colour star counts of the Basel survey data are shown, and in red the corresponding colour distributions of the model galaxy.

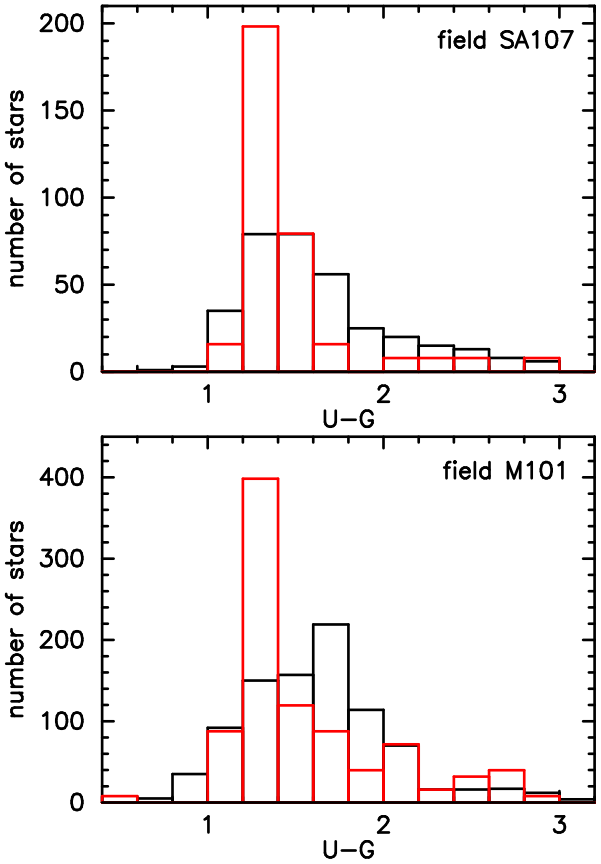

FIGURE 5.6.: As in Figure 5.5, but towards the inner Galaxy (SA107, upper panel) and the outer Galactic halo (M101, lower panel).

As it is clearly visible, regardless of the viewing direction, the $1.2 \leq U-G \leq 1.4$ bin is always overcrowded by model stars.

Towards the inner Galaxy (SA107), the star formation rate and, therefore, the stellar particle density are higher. But even with more stellar particles available in this direction and, thus, better statistics, the theoretical distribution does not agree better with the observed one (Figure 5.6, upper panel).

The comparison of these three fields of the Basel survey with the model data reveals that the discrepancies between observation and theory are independent of the viewing direction.

5.1.5. Comparison of the BaSeL 3.2– and the PHOENIX stellar spectral libraries

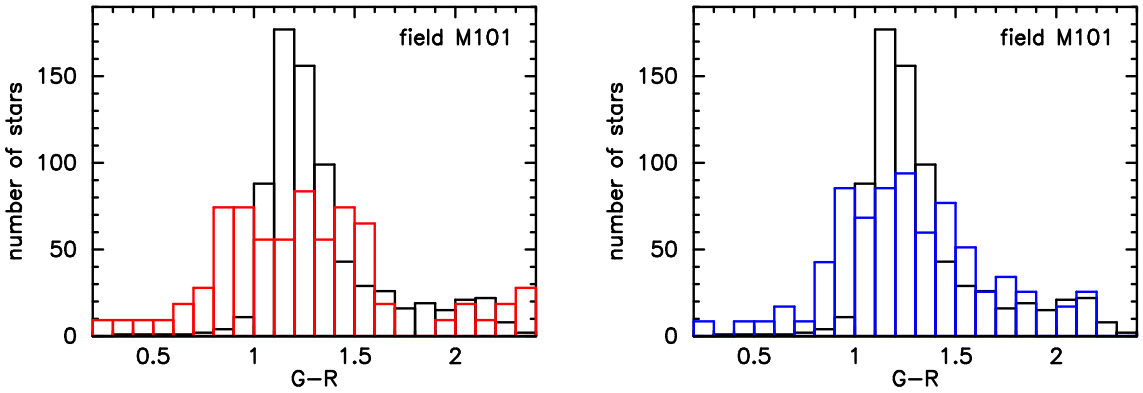

FIGURE 5.7.: Stellar $G-R$ colour distributions towards the outer Galactic halo (M101). The left panel shows the distribution obtained with the BaSeL 3.2 stellar spectral library (in red) and the right panel the one using the PHOENIX stellar spectral library (in blue), respectively. In black the colour star count of the Basel survey data is shown.

Apart from the enhanced BaSeL 3.2 stellar spectral library, we also used the PHOENIX stellar spectral library, as already mentioned in Section 3.4.5.
Figure 5.7 shows the $G-R$ colour distributions of the stellar set produced using the BaSeL 3.2 (in red) in the left, and the PHOENIX library (in blue) in the right panel. All in all, the two libraries produce the same overall shape in the $G-R$ colour histogram. Some small differences are visible at $G-R \geq 2.1$, but all within the statistical fluctuations of $\sqrt{\#\,\text{stellar particles}}$.

Because of the relatively bright limiting apparent magnitudes (which are taken from the Basel survey: $m_G \leq 18.1$ and $m_R \leq 15.9$), most of the lower mass stars drop out. Since the discrepancies between these two libraries are the largest in this low-mass region (see A.1), applying a relatively bright limiting apparent magnitude can eliminate the differences.

We conclude that, for our purpose, the two libraries are equivalent. But due to its larger parameter range, we will henceforth use the Basel 3.2 stellar spectral library.

5.2. SDSS survey fields

Comparison of the $u-g$ colour distributions towards the anticentre

In Section 5.1, we revealed the large differences between the Basel survey and the model data. In this section, we compare our calculated magnitudes and colours to the data of another survey, namely the Sloan Digital Sky Survey (SDSS).
The Third Data Release (DR3) of the SDSS (Abazajian et al. 2005) mapped the same three fi elds (SA94, SA107, M101) as the Basel survey. We take this opportunity to investigate, if the discrepancies between observation and theory diminish, when we use the SDSS data.
This survey detects faint stars down to a limiting apparent magnitude of $m_g = 22.2$, whereas the limiting apparent magnitude of the Basel survey lies at $m_G \sim 17.5$. To demonstrate the differences between these two surveys, we create two theoretical stellar subsets out of a single sample, by applying the appropriate limiting apparent magnitudes of the two surveys (SDSS: $m_g \leq 22.2$, $m_u \leq 22.0$; Basel survey: $m_G \leq 17.4$, $m_U \leq 18.5$).

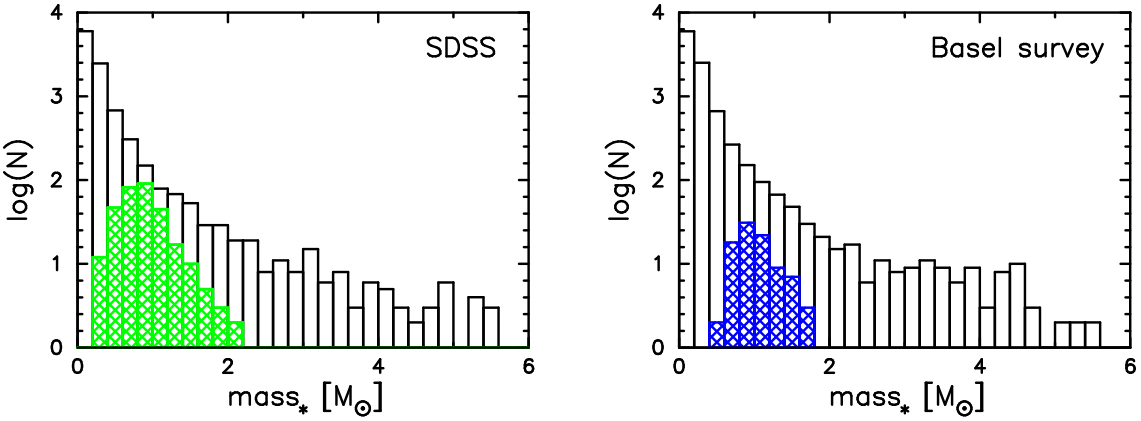

FIGURE 5.8.: Mass distributions of all stars of the theoretical data set (in black) towards SA94. Shown in colours are the distributions of the stars resulting from the cuts at the limiting apparent magnitudes (with the limiting magnitudes of the SDSS in the left– and of the Basel survey in the right panel).

The stellar mass distributions of both simulated surveys are plotted in Figure 5.8. In both panels, the full theoretical stellar sample towards the Galactic anticentre is shown in black. The distribution of the stars resulting from the application of the limiting apparent magnitudes are shown in green for the SDSS (left panel) and in blue for the Basel survey (right panel).
It is clearly visible, that the limited theoretical SDSS star sample consists of roughly 3.5 times more stars than the one from the theoretical Basel survey, solely because different apparent magnitude limits are applied.

We now analyse the relation between the theoretical star sample produced using the SDSS limiting magnitudes and the SDSS data towards the Galactic anticentre.
Figure 5.9 shows in red the theoretical $u-g$ colour distribution and in black the observed one. Both samples here are limited by the SDSS survey apparent magnitude limits of $m_g = 22.2$ and $m_u = 22.0$. Unfortunately, at fi rst glance, it seems that the differences between the observed SDSS data set and the calculated one are not smaller than the ones between the Basel survey and the model data.
In Subsection 4.2.1 we pointed out that the $u-g$ colours of a calculated theoretical thick disk peak between 0.8 and 1.2.
As one can see in Figure 5.9, the colour distribution of the theoretical star set (in red) has such peaks in this colour range too ($u-g$ colours highlighted in green: $0.8 \leq u-g < 1.0$ and in orange $1.0 \leq u-g < 1.2$). In contrast, the observed (mostly thick disk star-) (shown in black) peaks at colours shifted 0.2 mag to the red,

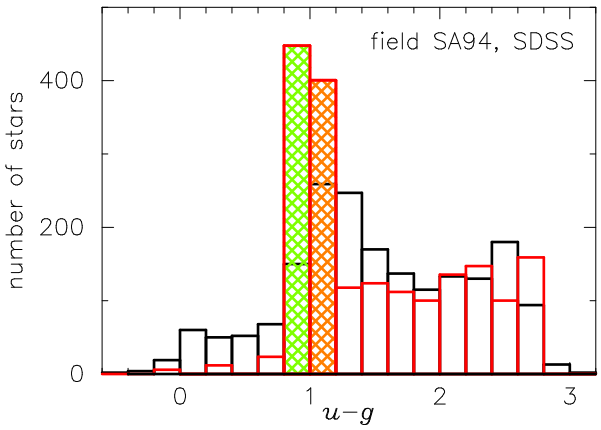

FIGURE 5.9.: $u-g$ colour distribution of the theoretical stellar sample towards the anticentre (SA94) in red, and of the observed SDSS data in black. Both after applying the limiting apparent $g-$ and $u-$ magnitudes. The hatched bins (in colour) are the two most populated colour bins.

$1.0 \leq u-g < 1.4$.
The displacement of the peak in the theoretical star count in relation to the observed one could provide an indication of an imprecise setting of the magnitudes' zeropoints. Incorrect zeropoints would affect all colour bins. Unfortunately, the good fit of the theoretical colour distribution in the redder part of the histogram ($1.6 \leq u-g < 2.8$) invalidates this simple explanation. To be able to get to the root of this inconsistency, we have to carry out further investigations.

To get an idea of the characteristics of the stars in these overpopulated bins, Figure 5.10 shows the distributions of the theoretical stellar sample in different diagrams: a) mass − metallicity-, b) mass − age-, c) mass − distance-, d) mass − surface gravity- and e) mass − effective temperature. The stars belonging to the overloaded bins are shown in colour (in green and orange). The remaining stars are shown as black dots.
Most of the stars in green and orange have masses of $M_* \geq 0.7$ $M_\odot$, and both bins are populated with stars that lie in almost the same mass range: stars of 0.69 $M_\odot \leq M_* \leq 2.03$ $M_\odot$ in the $0.8 \leq u-g \leq 1.0$ bin, and stars of 0.71 $M_\odot \leq M_* \leq 1.99$ $M_\odot$ in the $1.0 \leq u-g < 1.2$ bin.
Concerning their metallicities, the stars in the redder bin are metal-richer (Figure 5.10 plot a, orange dots), than the stars in the bluer bin. The stars in both bins cover almost the same age range (Figure 5.10, plot b). Plot c shows what was already expected: The low-mass stars of the bluer bin ($0.8 \leq u-g < 1.0$) are visible out to larger distances than even the high-mass stars of the redder bin. The distribution of surface gravities ($3.7 \leq \log g \leq 4.6$) indicates that all these stars are main sequence stars. Furthermore, one can see the clear separation in effective temperature. The bluer bin stars cover a smaller temperature range (5' 900K $\leq T_{\rm eff} \leq$ 7' 000K) than the redder one with effective temperatures of 5' 500K $\leq T_{\rm eff} \leq$ 8' 800K.
We try to find the reason for the overcrowding of these two bins, by looking at all the stellar parameters metallicity, age, surface gravity and effective temperature, and searching for common characteristics.
The first striking feature is the quite narrow mass range covered by the stars in these two bins: Most of them have masses of 1.0 ± 0.2 $M_\odot$. Due to the fact that the theoretical sample reproduces the Salpeter-IMF very well, one can not simply argue that the Samland code produces too many solar-like stars.
Another common characteristic is the low metallicity of all of these stars: more than 65 % of the stars with $u-g$ colours between 0.8 and 1.2 have metallicities of -0.7 $\leq$ [Fe/H] $\leq$ -0.2. The differences between the theoretical and the observed colour histogram can be explained by the fact that some of the ingredients of the transformation of the theoretical parameters into observables (like stellar evolutionary tracks, theoretical spectra, filter functions ect.) are not fully understood and may not be realistic for such lower-mass, lower-metallicity main sequence stars. Further analyses in the next part should bring to light, where the inconsistency lies.

After a first inspection of the $u-g$ colour distribution, we now take all colours in the same field (SA94) and

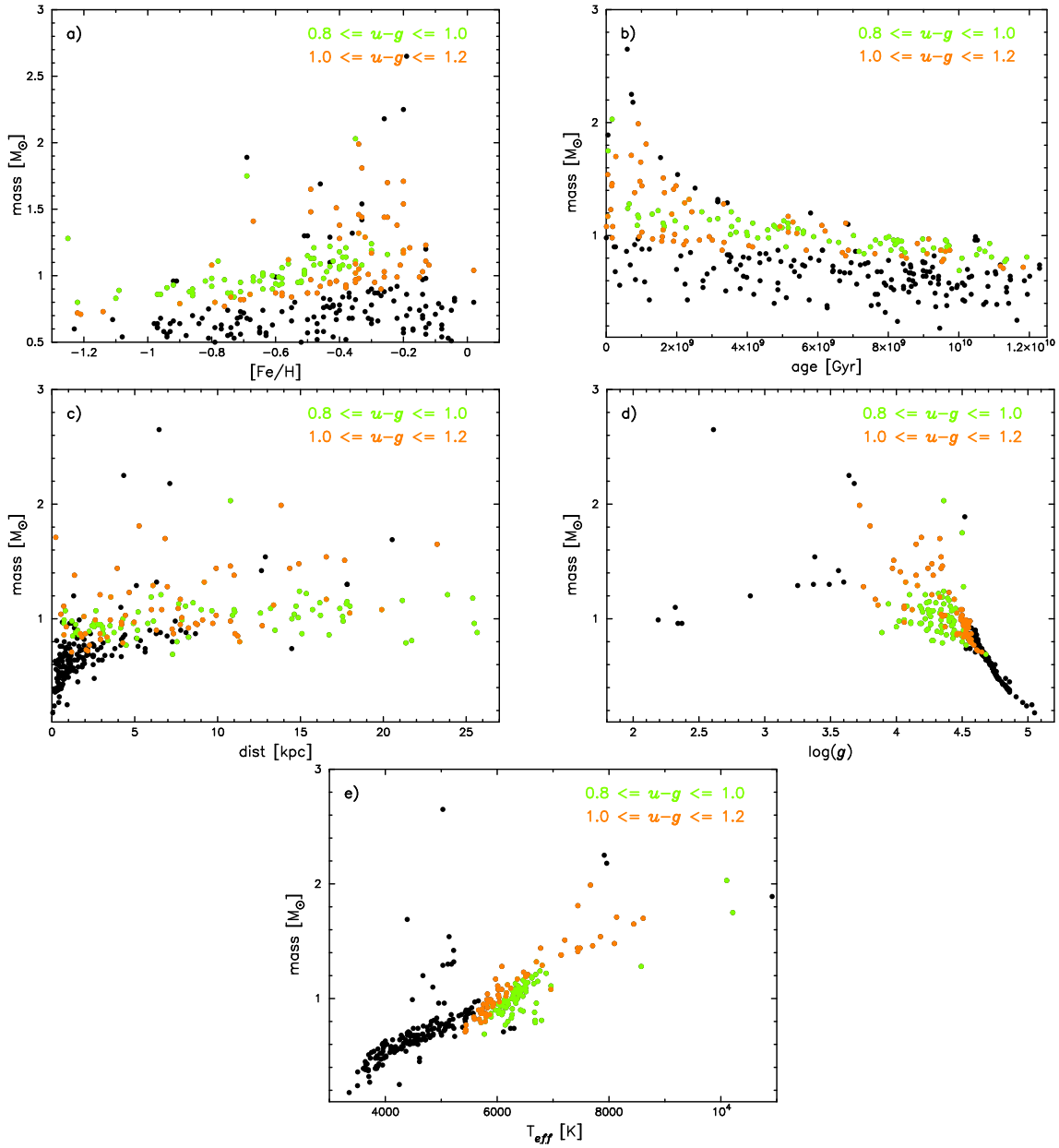

FIGURE 5.10.: Distribution of the theoretical stellar sample towards the Galactic anticentre in five different diagrams: a) mass – metallicity-, b) mass – age-, c) mass – distance-, d) mass – surface gravity - and e) mass – effective temperature. In green, all stars with $u-g$ colours between 0.8 and 1.0 are highlighted, and in orange, all stars with any colours between 1.0 and 1.2. The rest of the stars are shown as black dots.

their discrepancies compared with observations into account to provide a deeper insight into the suitability of our code.

Figure 5.11 shows the stellar distributions in four colours ($u-g$, $g-r$, $r-i$ and $i-z$, respectively) towards the Galactic anticentre. In each panel, the theoretical distribution is plotted in red and the observed SDSS stellar distribution in black.

As can be seen, the theoretical distributions differ in a certain range from the observed ones in all colours. These

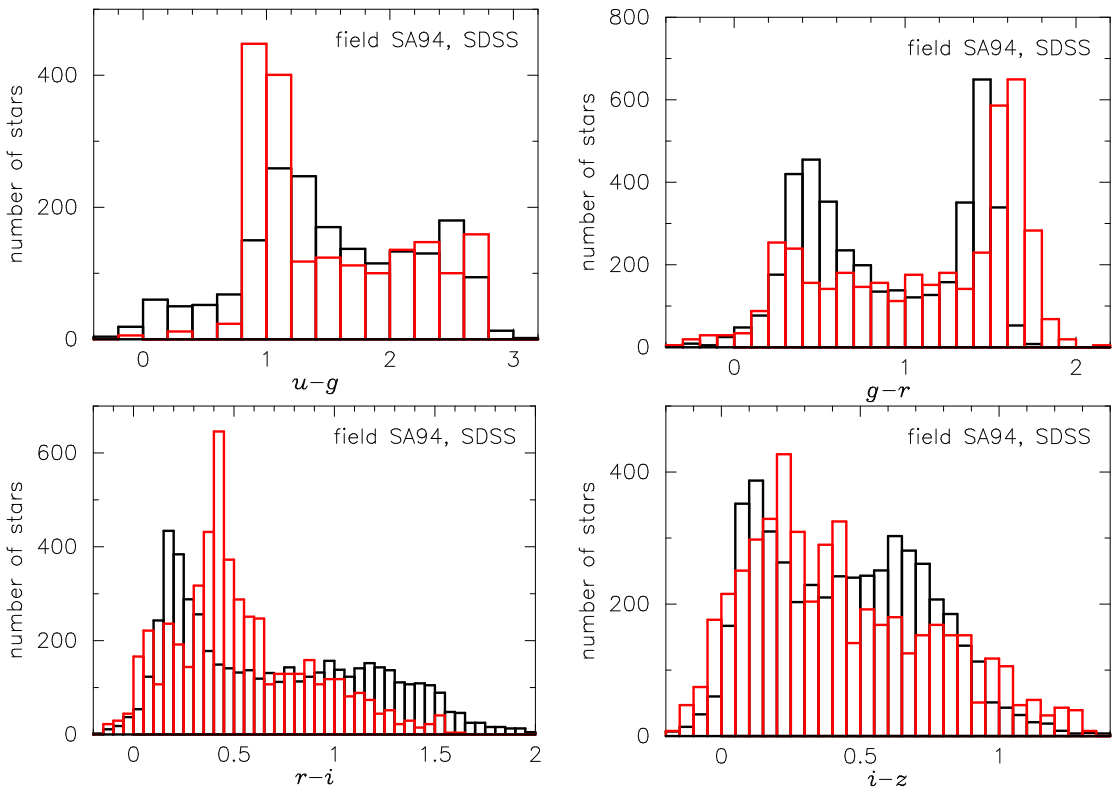

FIGURE 5.11.: Stellar colour distributions in all SDSS colours towards the Galactic anticentre. In each panel, the observed distribution is shown in black, and in red the theoretical one.

differences are not always in the same position in the different colours: The theoretical $u-g$ distribution has its most populous bins in the bluer part of the colour distribution, whereas the colours $r-i$ and $i-z$ feature such bins in the middle of the distribution, and the $g-r$ colour has its fullest bins in the redder part.
To see if these are the same stars, which populate the most overcrowded bins in all four colours (in each colour around 150 stars), we extract them and plot their temperatures versus $\log g$s in the left– and their $ages$ versus $stellar\ masses$ in the right panel of Figure 5.12.

The left panel of this Figure reveals that only a small number of stars are in the overcrowded bins of all four colours at the same time. In the temperature and surface gravity range of 3' 500 $\leq T_{\rm eff} \leq$ 4' 000 and 4.72 $\leq \log g \leq$ 5.0, a certain overlap is visible. But all in all, only a few stars, that populate overcrowded bins, really can be found in all four colours.
The same applies for the age-mass diagram: in the region of 0.2 $M_\odot \leq M_* \leq$ 0.6 $M_\odot$ and 4.6 Gyr $\leq age_* \leq$ 10.3 Gyr, only a few stars belong to the overcrowded bins in all colours.
This makes it impossible to defi ne the necessary adjustments to the Samland code. If the four colour distributions had more supernumerary stars in common, it would be easier to attribute those to either an inappropriate SFR (common stellar ages and metallicities) or IMF (common stellar masses).
Clearly visible in these two plots are the different properties of the stars belonging to the overpopulated bins in the $u-g$ colour. They have relatively low $\log g$s, high $T_{\rm eff}$s, and, compared to the masses of the other stars, much higher masses. Figure 5.13 provides an insight into the reason, why more high-mass stars are misplaced in the $u-g$ colour.

The application of certain apparent magnitude limits reduces the stellar sample in the $u-g$ colour (Figure 5.13, upper left panel, stars in blue) much more than in the other colours.

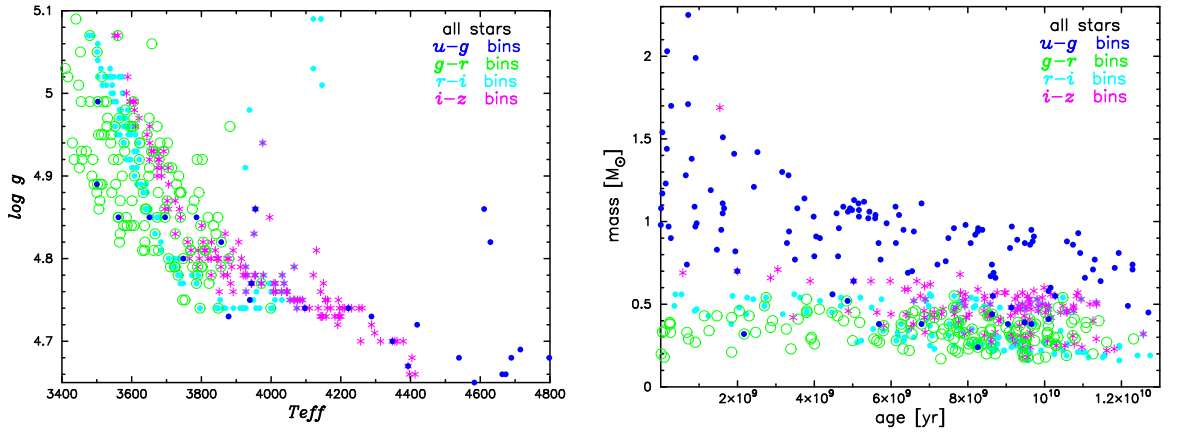

FIGURE 5.12.: Left panel: $T_{\rm eff}$ versus $\log g$ of all the stars that populate the most overcrowded bins in each colour. Right panel: $stellar\ mass$ versus age of the same stars as in the left panel.

Only higher-mass stars remain in the limited sample. No low-mass star exists that is bright enough in the blue range of the stellar spectrum (u-filter region) to survive the apparent magnitude cut. On this account, one should not take the stars of the most populous $u-g$ bins into consideration when looking for shared stellar properties. The limiting apparent u-magnitude constraints the stellar sample much more than the four others.

But even without the "$u-g$-stars", no recipe for adjustments can be read out of Figure 5.12.

For further investigation about the discrepancies between the theoretical and the observed star counts, we show a two-colour diagram (see Figure 5.14). Like in the colour histograms of Figure 5.11, the black dots represent the observed SDSS stars and the red ones the model stars, both distributed towards the Galactic anticentre and limited with the same apparent magnitudes.
Some of the observed stars lie in the colour regions of $-0.4 \leq \ g-r\ \leq 0.84$ and $-0.55 \leq \ u-g\ \leq 0.82$, where no model star appears.
To see if the model stars with such colours are excluded from the full sample due to the applied limiting apparent magnitudes, or if such colours simply can not be produced at all using the theoretical spectral library combined with the SDSS response filter functions, we also include (in orange) the colours of all the stars of the BaSeL 3.2 library. As can be seen in Figure 5.14, not even this overall stellar sample covers this particular colour region. (The model stars, being a subset of the theoretical spectral library, have to lie within the region covered by the BaSeL 3.2 library.)

From this, we conclude that our theoretical spectral library in conjunction with the SDSS response filter functions is not able to produce such colours. The question arises, what kind of objects populate this colour region.

In the Third Data Release of the SDSS (Abazajian et al. 2005), no distinction between stars and quasars is made. Therefore, our observed stellar samples consist of all such objects within the fields of the Basel survey.

Schneider et al. (2005) published the third edition of the Sloan Digital Sky Survey Quasar Catalog consisting of the 46' 420 objects in the SDSS Third Data Release that have luminosities higher than M_i = -22.0 mag, have at least one emission line with a Full-Width at Half-Maximum larger than 1000 km/s or are unambiguously broad absorption line quasars, are fainter than i = 15.0 mag, and have highly reliable redshifts.
We compare this Quasar Catalog with our stellar sample towards the Galactic anticentre and find 26 objects that match both of them. In Figure 5.15 the found quasars are plotted in green.

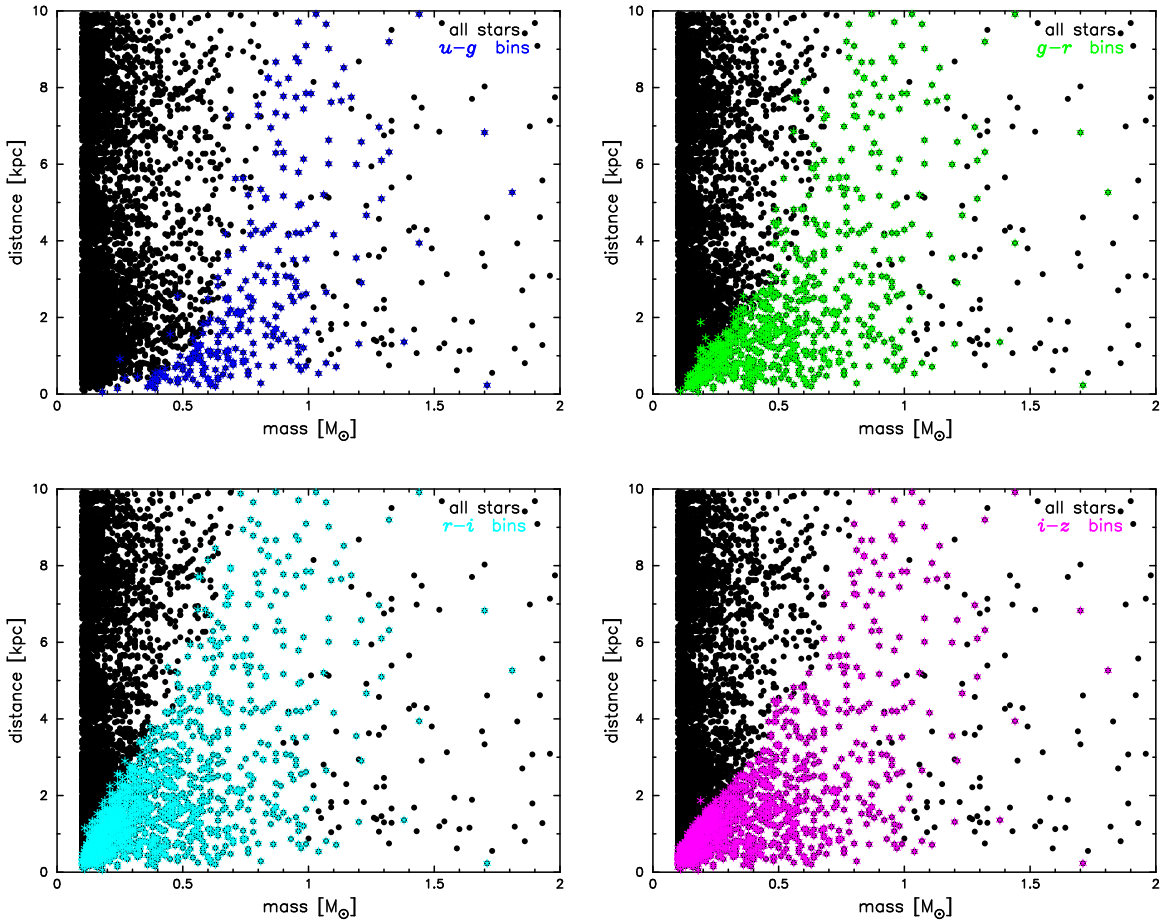

FIGURE 5.13.: Stellar mass - distance diagrams of the sample as limited in all four SDSS colours. The black dots show the full theoretical stellar sample towards the galactic anticentre (field SA94), the coloured stars the limited ones.

The quasar definiton of Schneider et al. (2005) only accounts for a few objects, and hence the majority of the objects that belong to this particular colour region still remain unidentified.

Another way of defining quasars is described in Richards et al. (2002). They designed an algorithm for selecting quasar candidates from multicolour imaging data in the Sloan Digital Sky Survey by matching unresolved sources to the FIRST radio catalogs (Becker, White & Helfand 1995). All objects are considered to be low redshift quasars that meet the following magnitude- and colour criteria:

m_g	$<=$	22.2 mag	and			
$u-g$	$>=$	-0.27	and	$u-g$	$<$	0.71
$g-r$	$>=$	-0.24	and	$g-r$	$<$	0.35
$r-i$	$>=$	-0.27	and	$r-i$	$<$	0.57
$i-z$	$>=$	-0.35	and	$i-z$	$<$	0.70.

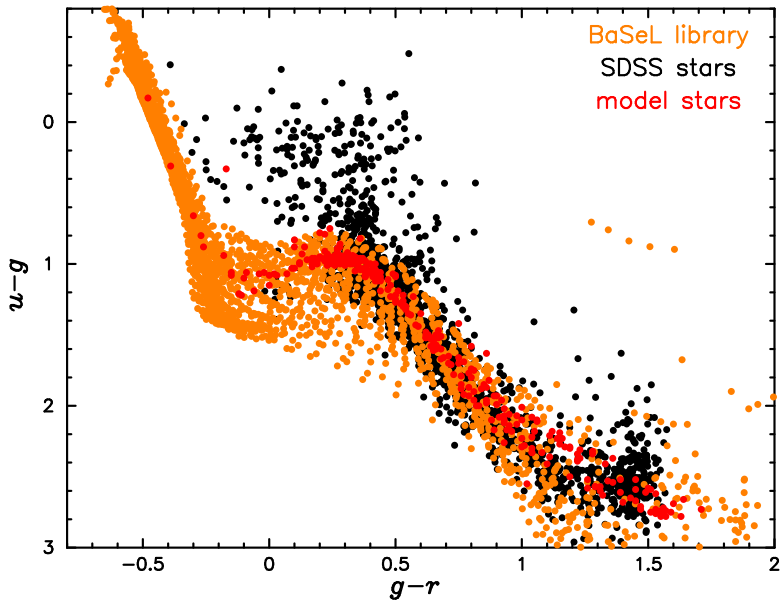

FIGURE 5.14.: A two-colour diagram ($g-r$ versus $u-g$) of the observed SDSS stars (plotted in black), of the limited theoretical model stars (red) towards the Galactic anticentre, and of all the stars that are included in the entire Basel 3.2 stellar spectral library (orange).

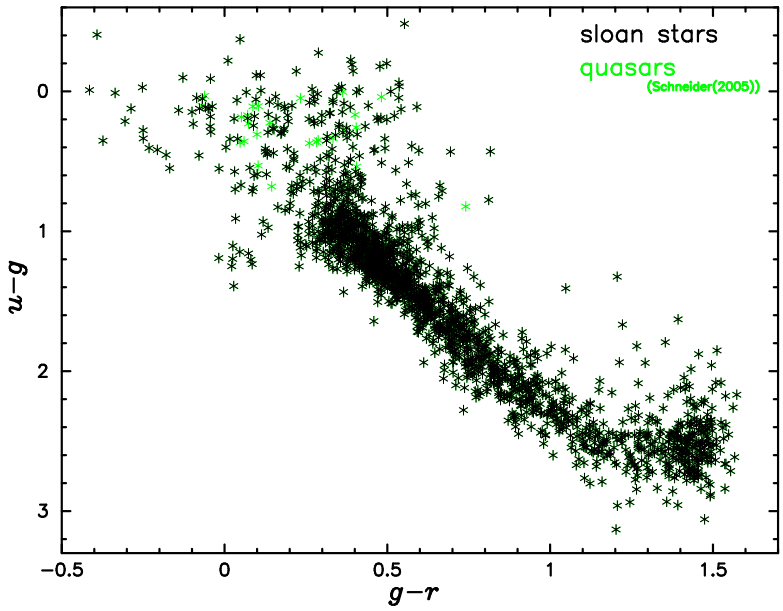

FIGURE 5.15.: A two-colour diagram ($g-r$ versus $u-g$) of the objects classified as quasars (in green) and the residual SDSS objects (in black) of the observed stellar sample towards the Galactic anticentre.

In Figure 5.16, the dots in magenta stand for the objects of our observed SDSS sample, that fulfil the constraints of Richards et al. (2002), and therefore can be regarded as quasars.
In blue the quasars (limited with the same apparent magnitudes as our sample) of the second edition of the Sloan Digital Sky Survey Quasar Catalog (Schneider et al. 2003) are shown. We show them just to get an idea of where

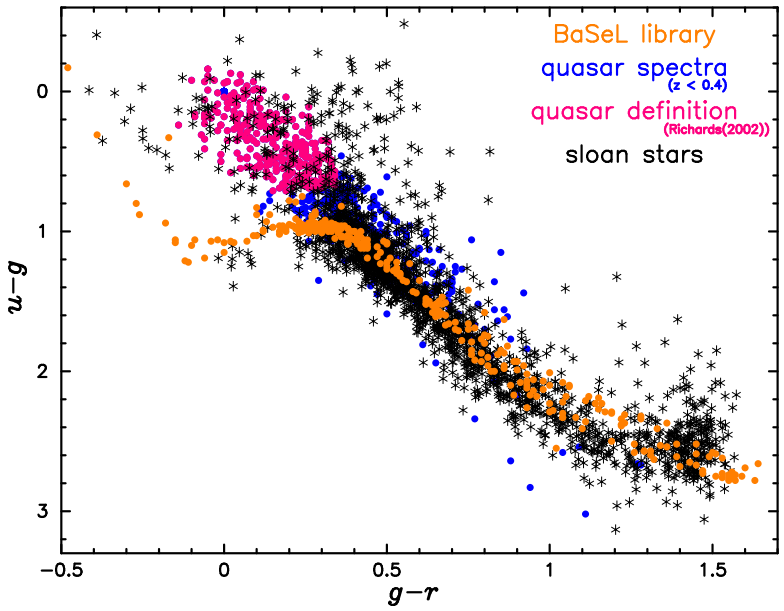

FIGURE 5.16.: Two-colour diagram of all SDSS objects towards the Galactic anticentre. The objects classified as quasars by Richards et al. (2002) are plotted in magenta. In orange the appropriately limited BaSeL 3.2 spectral library and in blue the quasars of the second edition of the Sloan Digital Sky Survey Quasar Catalog are plotted. In black the observed SDSS stars in the field SA94 are shown.

these quasi stellar objects appear in the $u-g$ – $g-r$ colour diagram [3].
As can be seen, the blue dots cover quite a large region, which in some parts overlaps the stellar main sequence. In the region of $0.2 \leq \ g-r \ \leq 1.3$ and $0.82 < \ u-g \ \leq 2.65$, a distinction between stars and quasars only on the basis of their colours seems not to be feasible.

The definition of Schneider et al. (2005) also does not filter out all the objects in the region $-0.4 \leq \ g-r \leq 0.84$ and $-0.55 \leq \ u-g \ \leq 0.82$, where there are no stars in the BaSeL 3.2 spectral library.
Due to the uncertainties concerning the nature of these objects, we exclude them from our sample in order to ensure that only reliable stars remain. Our exclusion criteria are the following:

$$\begin{aligned} u-g &\leq 0.82 \quad \text{and} \\ u-g &\leq 1.48 + 3.8 * \ (g-r). \end{aligned}$$

Figure 5.17 graphically illustrates our quasar definition in red.

The excluded objects (considered as quasars) are shown in the left panel of Figure 5.18 and in the right panel all objects considered as real stars are shown.

[3]The third edition of the Sloan Digital Sky Survey Quasar Catalog does not provide magnitudes in the u-band, that is the reason why we switch to the second edition which provides the magnitudes in all five filter bands. Both, the second and the third editions are obtained using the same selection procedure.

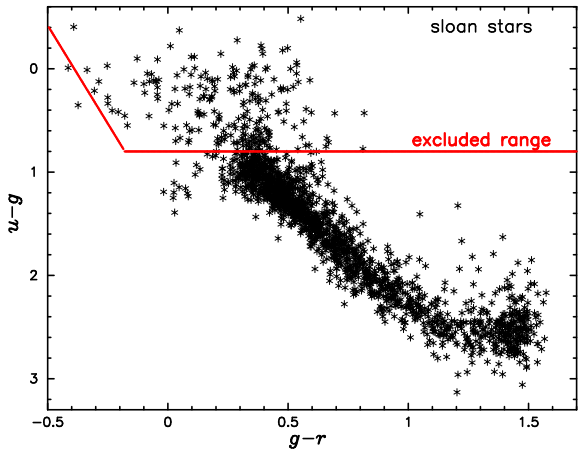

FIGURE 5.17.: The red lines highlight the region in the two-colour diagram within we defi ne all stars as quasars.

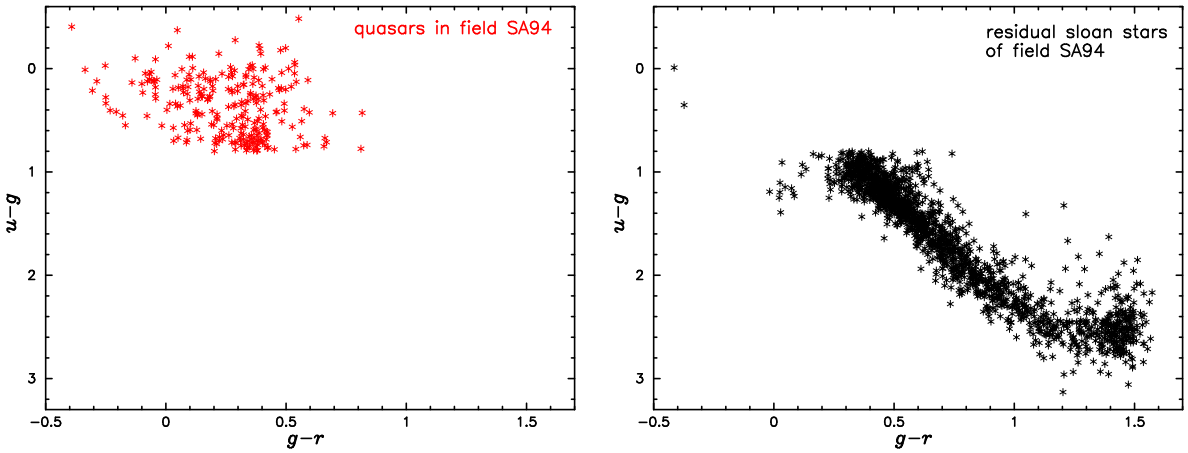

FIGURE 5.18.: In the left panel, the objects classifi ed by us as uncertain are shown. In the right panel, the reduced SDSS sample, that is the sample of all objects classifi ed as real stars, towards the Galactic anticentre is plotted.

Beside the quasars which we have to exclude from the SDSS data sets, we also have to consider the possible observational errors. Apart from the magnitudes and several data quality flags, the SDSS DR3 (Abazajian et al. 2005) includes magnitude errors as well (see Figure 5.19, below).

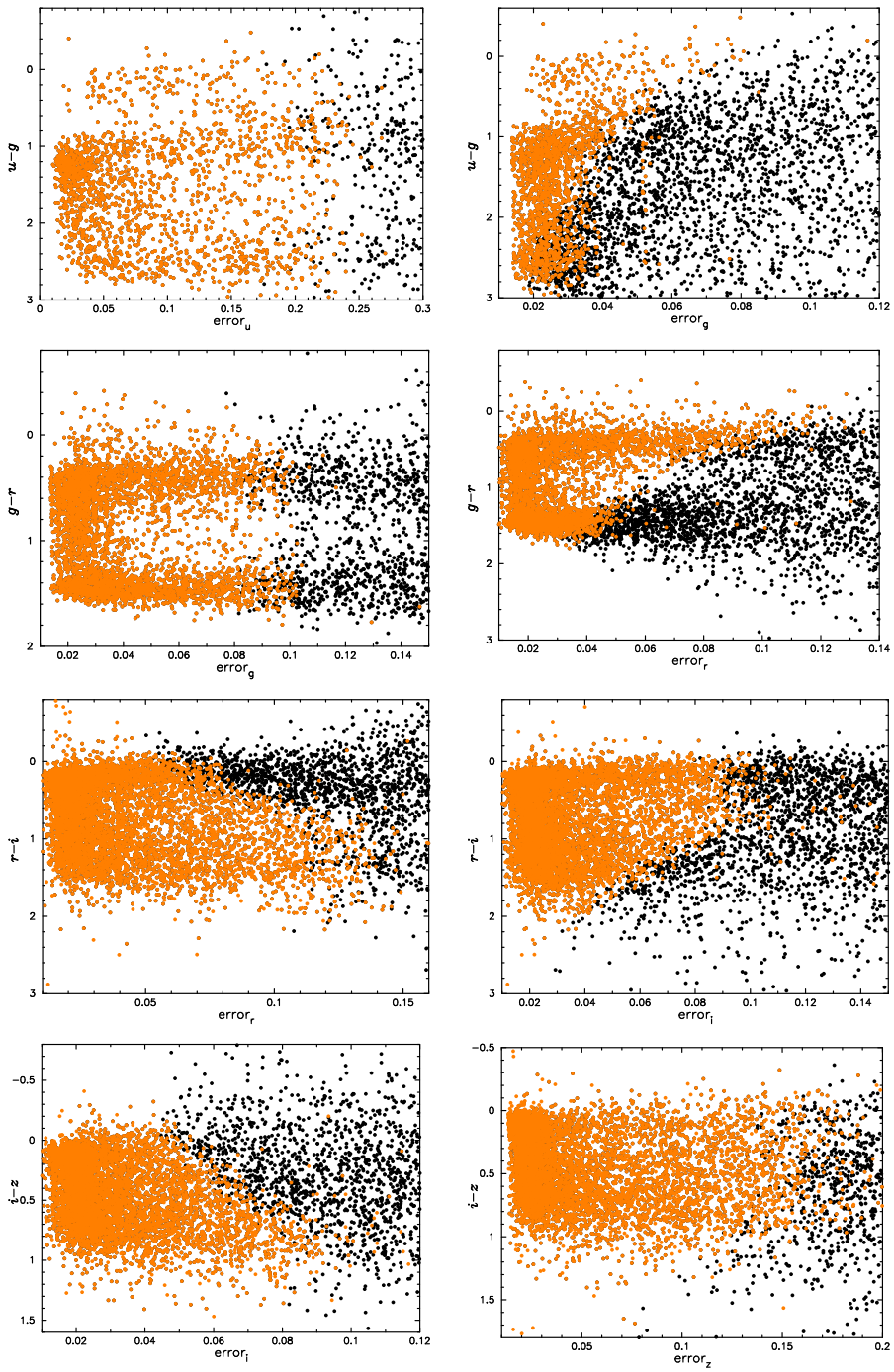

FIGURE 5.19.: Magnitude errors for all stars (in black) and for the ones with restricted magnitude limits (in orange).

We simulate the Gaussian normal distribution of the SDSS DR3 errors (Figure 5.19) by adding random noise using a Gaussian normal distribution along with the given observational errors.

After excluding possible quasars and adding observational errors to the theoretical stellar magnitudes, we

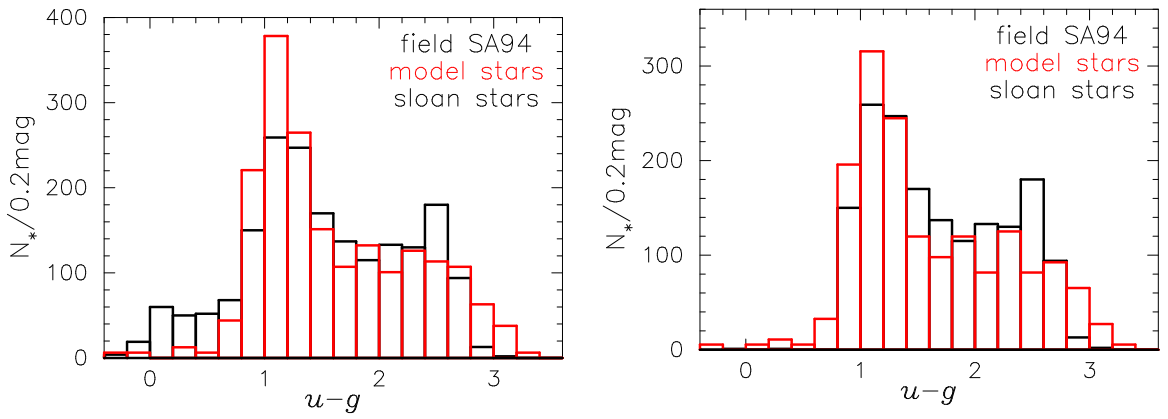

FIGURE 5.20.: Star counts in the $u-g$-colour towards the Galactic anticentre: the observed distribution is shown in black, and in red the theoretical one. In the left panel the "raw" theoretical distribution is shown, whereas in the right panel the one without the "assumed model quasars" and added observational errors is plotted.

end up with the stellar distribution shown in the right panel of Figure 5.20 in red. In contrast to the "raw" distribution (left panel, in red) the resulting histogram agrees much better with the observed distribution (shown in black). The deviations that are still visible in some parts of the histogram are not larger than the statistical fluctuations.

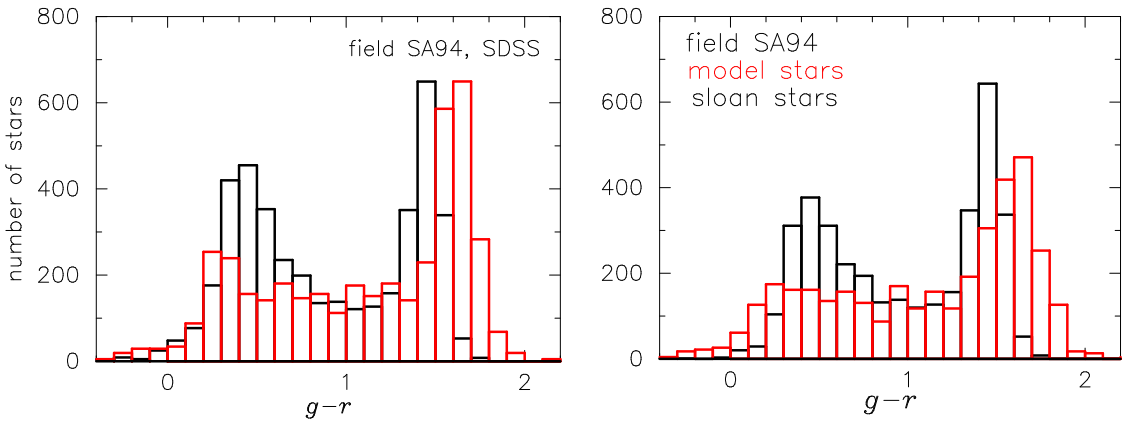

FIGURE 5.21.: Star counts in the $g-r$-colour towards the Galactic anticentre: the observed distribution is shown in black, and in red the theoretical star count. In the left panel the "raw" theoretical distribution is shown, whereas in the right panel the one without quasars and added observational errors is plotted.

Figure 5.21 shows the same colour distributions as Figure 5.20, but in $g-r$. Even after subtracting possible quasars and adding the observational errors (right panel), this theoretical colour distribution can not be brought into agreement with the observed one.
In the range of $1.5 \leq \ g-r \ \leq 1.7$, the theoretical distribution in the right panel agrees much better with the observed data than before, but in the bluer part of the histogram ($0.3 \leq \ g-r \ \leq 0.9$), there are still too many stars missing.
A look at the ($i-z$ versus $r-i$) diagram in Figure 5.22 reveals a huge deviation of the colour relations of the model stars (red dots) and the observed stars (black dots), which increases with redder colours.

To see if this divergence is due to the theoretical spectra in the BaSeL 3.2 library, we apply synthetic pho-

tometry in the Johnson-Cousins system (Johnson & Morgan 1953; Cousins 1976) to all spectra and transform these $UBVRI$-colours into SDSS $ugriz$-colours as described in Jordi, Grebel & Ammon (2005). The resulting $i-z-r-i$ colour relation can be seen in blue in Figure 5.23.

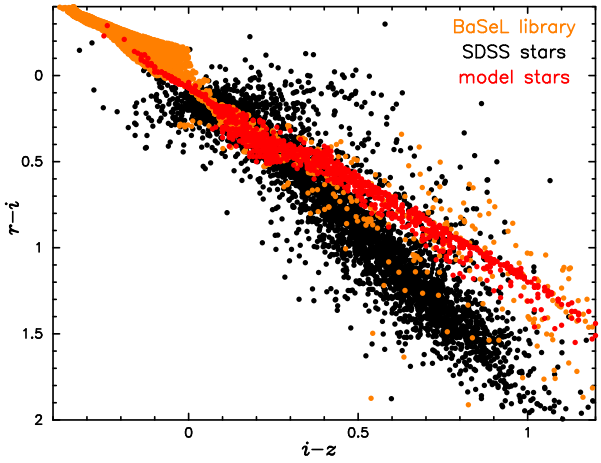

FIGURE 5.22.: A two-colour ($i-z$ versus $r-i$) diagram of the observed SDSS stars (in black) and the limited theoretical stellar sample (red) towards the Galactic anticentre, and of the entire Basel 3.2 stellar spectral library (orange).

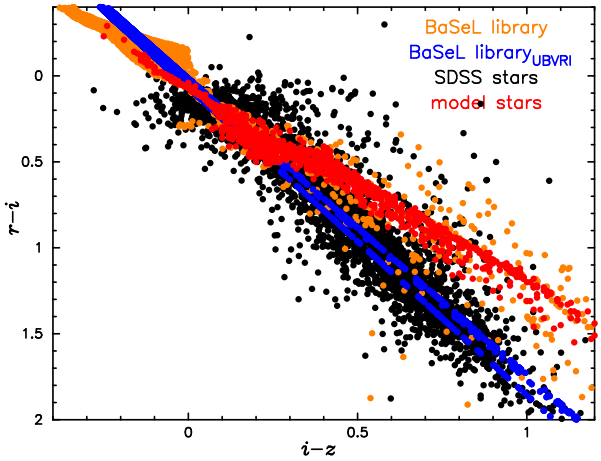

FIGURE 5.23.: As in Figure 5.22, but with the BaSeL 3.2 colours transformed from the Johnson-Cousins– to the SDSS system, added in blue.

Clearly visible, the transformed colours follow the same relation as the observed stars. The same good agreement between the observed colour relation and the transformed theoretical colours is seen in $g-r$ versus $u-g$ (Figure 5.24), where the ugr-colours were transformed from RGU-colours (Becker 1946, 1965; Buser 1978), again using the transformation relations calculated by Jordi, Grebel & Ammon (2005).

As a next step, we apply synthetic photometry in the Johnson-Cousins system (Johnson & Morgan 1953; Cousins 1976) to all stellar model spectra, transform these $UBVRI$-colours into SDSS $ugriz$-colours and end up with a new function (in green) in the two-colour ($i-z$ versus $r-i$) diagram (see Figure 5.25). Like the transformed library stars, the transformed model stars follow the colour relation of the observed stars quite nicely.

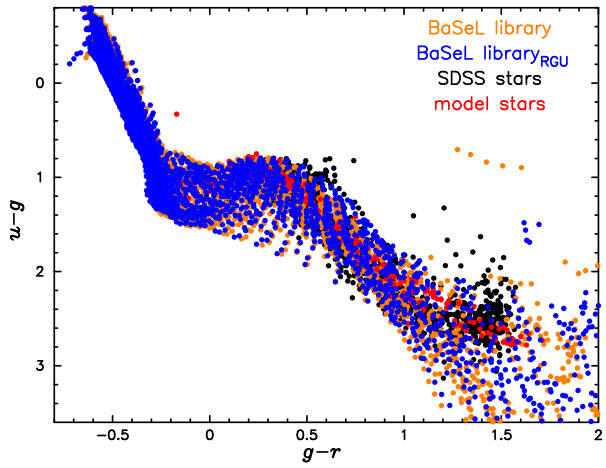

FIGURE 5.24.: As in Figure 5.23, but for the $g-r$ versus $u-g$.

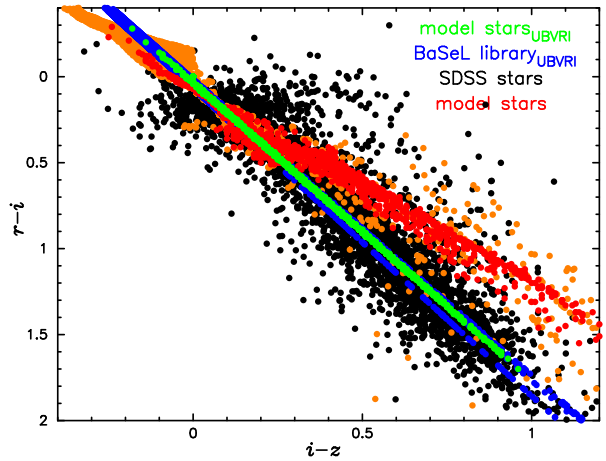

FIGURE 5.25.: As in Figure 5.23, the two-colour ($i-z$ versus $r-i$) diagram of the observed SDSS stars (in black) and the limited theoretical stellar sample (red) towards the Galactic anticentre, and two times of the entire Basel 3.2 stellar spectral library, once of the original one (orange) and once of the transformed one (blue). In green the transformed model stars are shown.

Due to the perfect fit of the transformed colours to the observed ones, it seems that we can exclude errors in the theoretical spectral energy distributions of the BaSeL 3.2 library as the reason for the misbehaviour of our colours.

For completeness, we add fiducial relations (black lines) in the two-colour ($i-z$ versus $r-i$) diagram (5.26). Overall, a perfect fit of the transformed colours to the observed mean colour values can be found again.

As a next possibility, we analyse the settings of the filter zeropoints. On the webpage of the DR3[4] a summary of the errors in the zeropoints is given. According to this summary, the u-band zeropoint is in error by 0.04 mag, in the sense that uAB = given u-magnitude - 0.04 mag, and that g, r, and i are close to the AB system (Oke & Gunn 1983), which the SDSS photometry is intended to be in (a magnitude 0 object should generate the same flux as a source of $F_{\nu} = 3631$ Jy). For the z-band zeropoint, there is mild evidence of an error of about 0.02

[4]http://www.sdss.org/dr3/algorithms/fluxcal.html

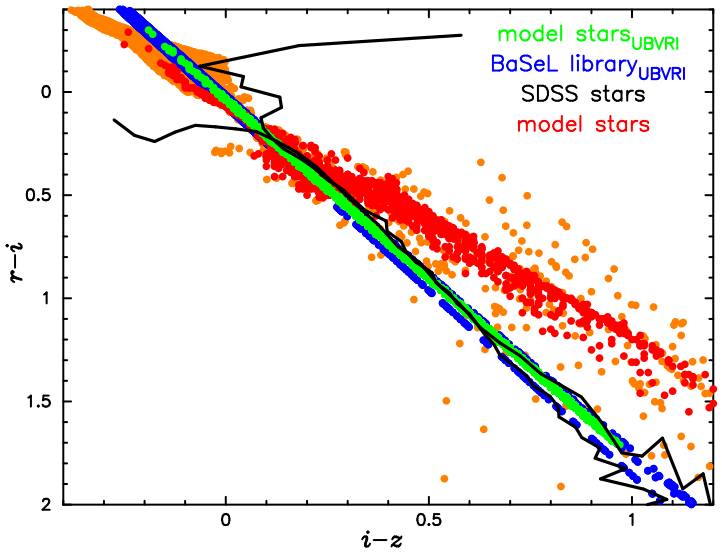

FIGURE 5.26.: As in Figure 5.25, but additionally fiducial relations (black lines) are added.

mag. The zeropoints of the synthetic $ugriz$ photometry are set to the colours of Vega ($T_{\rm eff}$ = 9400 K, $\log g$ = 3.9, [Fe/H] = 0.5 dex):

$$g-V\text{: } \text{-0.110}, \quad u-g\text{: } \text{1.020}, \quad g-r\text{: } \text{-0.250},$$
$$r-i\text{: } \text{-0.230}, \quad i-z\text{: } \text{-0.170}.$$

In Figure 5.27 all stars of the stellar spectral library BaSeL 3.2 are shown using three different $i-z$-zeropoints: the colour distribution after applying a zeropoint of $zp_{(i-z)}$ = 0.17 is shown in orange, one with a randomly chosen zeropoint of $zp_{(i-z)}$ = 0.07 is shown in green, and, finally, a colour distribution with a zeropoint of $zp_{(i-z)}$ = 0.27 is plotted in cyan.
A lower zeropoint shifts the stars towards redder $i-z$-colours (green sample), whereas a bigger zeropoint drives the stars towards bluer $i-z$-colours (blue sample). But the crucial point is, that the slope of the distributions always remains the same. With a change of the zeropoint's position, we are not able to reproduce the $i-z$ versus $r-i$ relation of the observed stars.

To prove if it is possible at all to reproduce the observed stellar distribution in the $i-z$ versus $r-i$ diagram with the transformed BaSeL 3.2 library, we show Figure 5.25 again, this time with the boundaries corresponding to the largest possible errors included in cyan (Figure 5.28). As can be seen, several different colour ranges can not be covered by library stars, even with the largest errors applied.

Assuming, that the theoretical spectra of the BaSeL 3.2 library simulate the observed stellar spectral energy distributions correctly and that the zeropoints of all $ugriz$-colours are accurately set, the only possible reason for the deviation left over, are errors of the shapes of some of the five SDSS $ugriz$ passbands' filter curves used in the synthetic photometry.

Two filter functions that can be considered correct are the u- and the g-filter functions: the model -, the transformed library -, and the observed stars agree well enough in the $g-r$ versus $u-g$- plot (Figure 5.24), and the comparison between theoretical and observed colour distributions (Figure 5.20) as well, so that these two filter curves can not be the uncertain ones. (The comparison between the theoretical and observed $g-r$ distributions

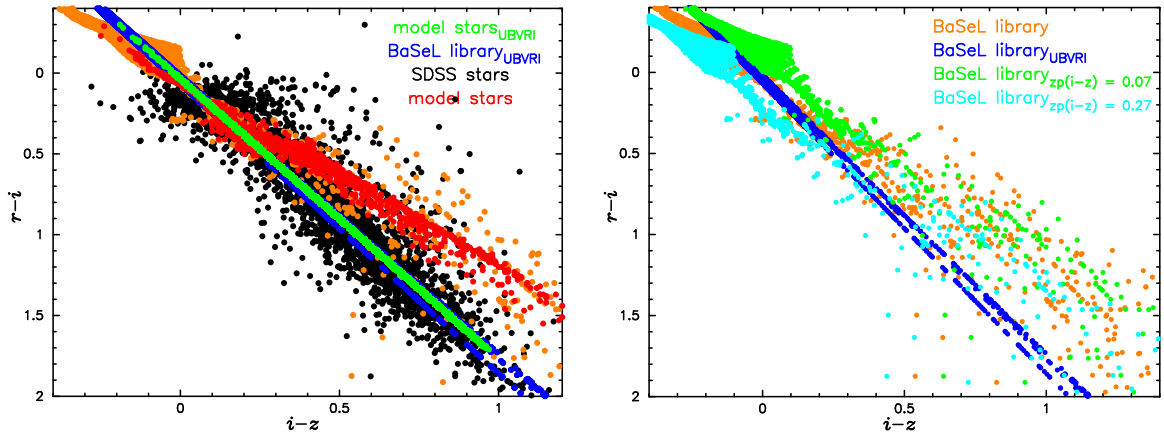

FIGURE 5.27.: Left panel: As in Figure 5.25. Right panel: The transformed BaSeL 3.2 colours (in blue) together with the synthetic photometry of the entire BaSeL 3.2 library using three different zeropoints: $zp_{(i-z)}$ = 0.17 (orange), $zp_{(i-z)}$ = 0.07 (green) and $zp_{(i-z)}$ = 0.27 (cyan).

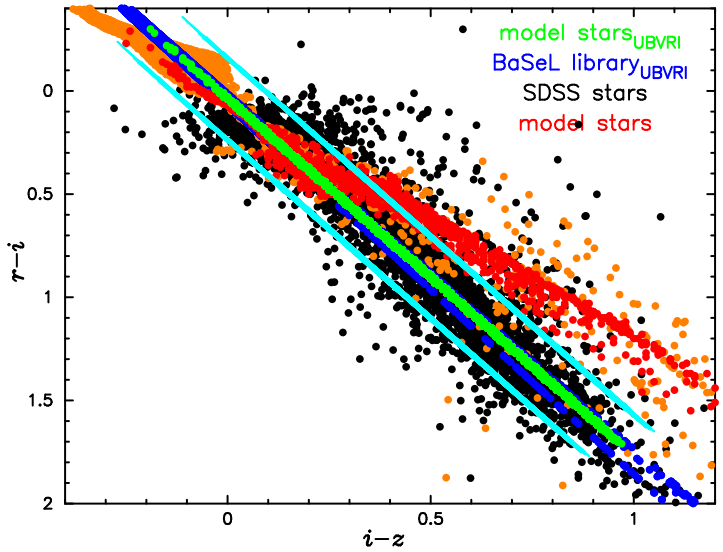

FIGURE 5.28.: As in Figure 5.25, but additionally the outer limits of the error ranges (cyan) are drawn in.

revealed so many differences, so that the r-filter function can not be considered correct.)
After this exclusion of u and g, only three filter functions remain (r, i and z) that could be responsible for the differences in the slope between the two-colour relations of the observed– and the model stars.

6. Summary and Conclusions

The last chapter is dedicated to the compilation of the results and the discussion about the success of – but also about the problems that have arisen during and – in part also survived – this work.
The main goal of this thesis was first to convert the stellar parameters given by galaxy models into observables, and then to compare these theoretical stellar distributions in different viewing directions with real observational data to check, if it is possible to find a best-fitting galaxy model for our Milky Way.

To do so, we transformed the physical parameters, i. e. the stellar mass, current age and constant chemical abundance of each star in a certain viewing direction and field size, given by ten different, detailed galaxy models that were computed with the **3D chemo-dynamical code** of Samland, Hensler & Theis (1997) and Samland & Gerhard (2003) into observable absolute and apparent magnitudes and colours.
For each star, we used its stellar mass, age and chemical abundance to select the corresponding evolutionary track from the **stellar evolutionary track library**, **Padova 1994**, computed by Bressan et al. (1993), Fagotto et al. (1994a, 1994b, 1994c) and Girardi et al. (1996), to derive the appropriate stellar atmospheric parameters (i.e., $\log g$ and $T_{\rm eff}$).
Using stellar metallicity, effective temperature and surface gravity, we interpolate an appropriate spectral energy distribution provided by **synthetic stellar spectral libraries**, **BaSeL 3.2** or **PHOENIX**, and in connection with the response filter functions of various photometric filter systems (e. g., RGU and $ugriz$) for observable magnitudes and colours for each star.
By means of the spectrophotometric data we compile synthetic colour-magnitude diagrams, and age– and metallicity distributions for a number of viewing directions and field sizes. These theoretical data are then compared with the photometric field star observations from both the **Basel** and the **Sloan Digital Sky Surveys**.

Our intention is to first compare the differences between our suite of models and observations, so as to identify the correlations between the observed data and the input parameters of our models. In a next step we want to fine-tune the model parameters to fit the Basel and/or SDSS survey data and thereby to find the best-fitting galaxy model for our Milky Way.

Unfortunately, the fine-tuning of the model galaxy parameters has not been possible[1] – which forced us to limit our analysis to only 10 different models without any further adjustments.

6.1. Success

Befor starting our comparison of theoretical wih observational data, we complete the BaSeL 3.1 (Westera 2001; Westera et al. 2002)- and the PHOENIX (Hauschildt & Baron 1999, 2004) stellar spectral libraries by implementing a grid of theoretical white dwarf stellar spectra covering high surface gravities ($\log g > 5.0$) and high effective temperatures (50' 000 K $\leq T_{\rm eff} \leq$ 100' 000 K) calculated by Koester (2004). Similarly, we also include

[1] Markus Samland, the very creator of these model galaxies, had to resign his research position at the institute – owing to the lack of funds and the imminent closure of the institute – and to assume a position in the private industry sector.

hot central star spectra of planetary nebulae computed by Rauch (2003) that cover a temperature range of 100' 000 $\leq T_{\rm eff} \leq$ 1' 000' 000 K and surface gravities of 5.0 $\leq \log g \leq$ 9.0.
Finally, we end up with a useful tool for reproducing stellar data of various stellar types on different photometric systems, such as RGU and SDSS. By means of these theoretical spectral libraries the interpretation of any stellar data (e.g., SDSS SEGUE proprietary data) in terms of physical stellar parameters is highly warranted.

As mentioned above, for our comparison we only have ten model galaxies available. Out of these ten, we find the best-fitting model galaxy to be the spiral model galaxy *S10*, described in detail in Subsection 3.2.2.

During our work of comparison we gain deeper insights into all the different fields of work that are involved in the conversion of the model data into observables. The major ingredients of this study are highlighted in blue in the previous paragraph:

stellar evolutionary models, stellar atmosphere models,
photometric system parameters, and last, but not least:
the chemo-dynamical galaxy models themselves .

Beside the fact, that gathering and comprehending the actual knowledge of all of them is a great challenge, the coin also has another side: each field of work still has some unknown or untested parts and therefore brings its own, sometimes inestimable, uncertainties with it.
We track down several inconsistences in the above-mentioned ingredients and discuss them in due detail in the present work.

In future work, we suggest that appropriate corrections need to be applied, before making further *and* unbiased comparisons. In the next Sections, we enlist the major inconsistencies between the surveys, spectral libraries and between synthetic and observed SDSS colours and propose possible future scientific projects.

6.2. Problems and uncertainties

6.2.1. Chemo-dynamical galaxy model

Westera et al. (2002) showed that the bulge colours derived from disk galaxy formation models of Samland & Gerhard (2003) agree very well with Hubble Deep Field North bulge colours. In our case, where we are immersed in a galaxy model and compare its spatial stellar distributions und luminosity functions with the much more detailed substructures of our own Galaxy, no such good agreement can be found.
The validity of any galactic model is always questionable, as it describes a smooth and in the case of the Samland models an axially symmetric galaxy, while in our days we know through observations that inhomogeneities exist even in the disk or in the halo.
Thanks to the increasing computational power, we are able to simulate the formation and evolution of a disk galaxy in three-dimensional numerical models, including the most important physical processes. But even in our days, the computational power has its limits. Therefore, it is not possible to account for all the processes acting from atomic to galactic scale.
In the Samland code, the stellar particles are created and distributed according to the star formation. The restriction to the fundamental processes, which determine the galactic evolution, may affect the detailed shape of the star formation history. Too many important details influence the formation and evolution of a model star that affect the stellar radiative properties and spatial distributions in a crucial way which exceeds by far the error bars of the empirical calibrations of the local luminosity functions.
Beside these general problems of simulating complex interactions, the Samland code revealed additional artefacts as we have seen for example in Subsection 5.1.2. Unfortunately, the easily implementable adjustments to the code are not possible anymore, as mentioned above.

6.2.2. Stellar evolutionary tracks and synthetic photometry

Stellar evolutionary tracks

Even though the stellar evolutionary models are increasingly sophisticated, with improved physics, various uncertainties still lie in the description of the details in the shape of stellar evolutionary tracks, and the evolutionary lifetimes. Here we just mention some of them: Core convection, mass loss, mixing length, rotation, diffusion, meridional circulation, and nuclear reactions.
Additionally, the complete set of evolutionary tracks of the Padova94 library does not include the TP-AGB nor the post-AGB phase. On account of this we adopted the enhancements of Bruzual & Charlot (2003) that consist only of *simplified* descriptions of these phases.

Spectral libraries

In addition, we have shown that the two theoretical stellar spectral libraries, BaSeL 3.2 and PHOENIX, do not provide matching synthetic colours throughout the full parameter ranges. The largest differences between the two stellar spectral libraries show up in almost all colours at lower effective temperatures (3' 500 $\geq T_{\rm eff}$) and higher surface gravities (2.5 $\leq \log g$) (see A.1).
Due to the bright limiting apparent magnitudes that we apply to produce model colours under the same conditions as the observed colours, these uncertainties do not affect our work that much. Still, the (small) contribution of such stars that are not yet sufficiently tested is difficult to estimate and their impacts on the stellar radiative properties not yet definitely determined.

Filter functions

The comparison of the SDSS survey- with the model star counts reveals a satisfying agreement in the $u-g$-colour. Unfortunately, other colours do not show the same result, and therefore lead us to analyse the SDSS colours more deeply.
The comparison of theoretical and observed stellar distributions in the $i-z$ versus $r-i$- plane (see 5.2) demonstrates impressively, that the observed two-colour distribution can not be reproduced by synthetic colours of any theoretical stars. Only synthetic colours transformed from the Johnson-Cousins system (Jordi, Grebel & Ammon 2005) follow the $i-z$ versus $r-i$ colour relation of the observed stars correctly.
By contrast, the model -, the transformed synthetic -, and the observed stars in the $g-r$ versus $u-g$- plane fit well. The conclusion appears inevitable that three published SDSS filter functions (r, i and z) do not match the observational system, and are therefore responsible for this deviation.

6.2.3. Observational data

The comparison of the Basel survey with our model galaxies reveals large inadjustable inconsistencies in star counts in all the avaliable viewing directions. We therefore include checks on SDSS data and compare the apparent magnitude histograms of stars in common fields.
A comparison of the Basel- with the Sloan Digital Sky Survey uncovers unexpected large systematic deviations between the apparent magnitude histograms in the magnitude range that is common to both surveys.
The higher resolution of the SDSS CCD photometry compared with the one of the Basel survey can only partly explain the differences of these two surveys. By comparing three fields that both surveys have in common, Jordi, Grebel & Ammon (2005) discovered uncertainties concerning the identification of some of the observed objects: Some objects recognised by the Sloan Digital Sky Survey as galaxies are treated as stars in the Basel survey. In other cases, the SDSS detector simply did not observe a star, whereas the Basel survey detected one. Occasionally the SDSS detected a fainter object within a radius of 1" to 3" of the dominant star, whereas Basel detected only one single source. Around 10 % of the Basel stars are not identified in the SDSS catalogue as single stars. In our work we compare (assumed) observed single stars with single model stars. If a survey classifies galaxies

or the like as single stars, the whole stellar spatial distribution gets affected.
Furhermore, the SDSS survey has a saturation cutoff at the apparent magnitude of $r \sim 14.0$, which means that the images of all stars brighter than this magnitude contain saturated pixels and that their photometry is questionable. Another uncertainty of the SDSS DR3 are quasars which have not yet been separated. And, as we showed in Subsection 5.2, a satisfactory algorithm to unambiguously identify and exclude all quasars from a mixed stellar sample does not exist. But all that is not a final explanation, why these two surveys end up with different star numbers.
Of course, such mismatches between the two surveys do not allow a definite validation of the model.

Because of all these still considerable inconsistencies and uncertainties accompaning the use of the major ingredients (stellar evolutionary models of Padova, stellar atmosphere models of the BaSeL 3.2 and the PHOENIX library, photometric system parameters, such as the SDSS filter functions, and last but not least: the chemodynamical model galaxies) mentioned above, we are unable – unfortunately – to draw final conclusions about the validity of the Samland models, or to find a unique best-fitting solution for the Milky Way.

6.3. Future work

As we demonstrated, the galaxy models of Samland & Gerhard (2003) can not reproduce the complex internal structure of a galaxy like our own Milky Way – due to many insufficiently understood and reproducible details, but are able to simulate images of entire galaxies very well. Even though the available models are restricted in number and no longer modifiable, these magnificent models should be further used to achieve deeper insights into the formation and evolution of other galaxy types on the base of their integrated light.
Another way of doing the models justice lies in their application to visualise some of the main processes that shape galaxies. These galactic evolutionary models represent a perfect tool to reveal the processes behind the convoluted transmutations of energy and matter, from stellar to galactic scale. (Some applications are described in the Subsections 4.2, 4.3 and 4.4.)

Concering the mismatches in star numbers of the Basel and SDSS surveys, we propose to investigate further the different definitions of single stellar objects by the two surveys, and thus to verify the cause of these striking differences.

Especially for further comparisons between our model and SDSS observations in the $g-r$, $r-i$ and $i-z$ colours, systematic investigations of the passbands in connection with spectral energy distributions for stars of various spectral types and luminosity classes will be necessary. The synthetic photometry algorithm – employing theoretical (e.g., BaSeL 3.2 and PHOENIX) and/or observational stellar spectral libraries (e.g., STELIB (Le Borgne et al. 2003)) – could be used to track down (see, e.g., Buser (1978) and Lejeune (1997)), in which way the filter functions have to be modified in order to be able to reproduce the observed SDSS-colours. Only after precise adjustments of the filter functions further evaluations of the discrepancies between theory and practice can be regarded as significant.

All the newly gathered observational photometric and spectroscopic data of stars (Hipparcos, Sloan) should be used for a verification of the synthetic spectral libraries, BaSeL 3.2 and PHOENIX, particularly in the low-temperature – high surface gravity ranges where we still find discrepancies (e.g., Westera (2001)).

6.4. Final thoughts

Without astronomy, no world view...

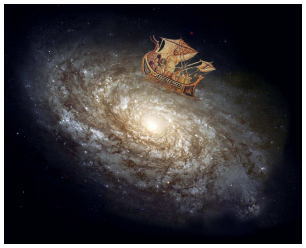

This study in hand has made considerable – although not as much as originally hoped for – progress: we uncover several, to date unknown inconsistencies in different astronomical fields of work that now can be taken as challenging scientific starting points for further and more detailed investigations – towards a final elimination of all these weak points.

If the Milky Way should be reproducible by a *unique model* at all, we first have to be in possession of an adequately profound knowledge about all the various physical and chemical components and interaction processes that govern the complex formation and evolution of our Galaxy.

Bibliography

Abazajian, K., Adelman-McCarthy, J. K., Ageros, M. A., Allam, S. S., & Anderson, K. S. J., et al. 2005, AJ, 129, 1755

Allard, F., & Hauschildt, P. H. 1995, ApJ, 445, 433

Angelov, T. 1996, BOBeo, 153, 19

Bahcall, J. N., & Soneira, R. M. 1980, ApJS, 44, 73

Bahcall, J. N., & Soneira, R. M. 1984, ApJS, 55, 67

Bahcall, J. N., Ratnatunga, K. U., Buser, R., Fenkart, R. P., et al. 1985, ApJ, 299, 616

Barman, T. S., Hauschildt, P. H., & Allard, F. 2000, A&AS, 197, 1110

Barry, D. C. 1988, ApJ, 334, 446

Bastian, U. 2006, private communications

Becker, W. 1946, Veröffentl. der Universitätssternwarte zu Göttingen, 5, 195

Becker, W. 1965, Zeitschrift für Astrophysics, 62, 54

Becker, W. 1972, Q. J. R. Astron. Soc., 13, 226

Becker, W. 1980, A&A, 87, 80

Becker, W., & Steppe, H. 1977, A&AS, 28, 377

Becker, R. H., White, R. L., & Helfand, D. J. 1995, ApJ, 450, 559

di Benedetto, G. P. 1998, A&A, 339, 858

Bessell, M. S. 1983, PASP, 95, 480

Bessell, M. S., & Brett, J. M. 1988, PASP, 100, 1134

Bessell, M. S., Brett, J. M., Wood, P. R., & Scholz, M. 1989, A&AS, 77, 1

Bessell, M. S., Brett, J. M., Scholz, M., & Wood, P. R. 1991, A&AS, 89, 335

Binney, J., Gerhard, O., & Spergel, D. 1997, MNRAS, 288, 365

von Braun, K., Chiboucas, K., Minske, J. C., Salgado, J. F., & Worthey, G. 1998, PASP, 110, 810

Le Borgne, J.-F., Bruzual, G., Pell, R., Lanon, A., Rocca-Volmerange, B., et al. 2003, A&A, 402, 433

Bressan, A., Fagotto, F., Bertelli, G., & Chiosi, C. 1993, A&A, 100, 647

Brott, I., & Hauschildt, P. H. 2005, tdug.conf., 565

Bruzual, G., & Charlot, S. 2003, MNRAS, 344, 1000

Bullock, J. S., Dekel, A., Kolatt, T. S., Kravtsov, A. V., Klypin, A. A., et al. 2001, ApJ, 555, 240

Buser, R. 1978, A&A, 62, 411

Buser, R. 2000, Science, 287, 5450

Buser, R., & Chui, L.-T., G. 1981, MitAG, 52, 40

Buser, R., & Kaeser, U. 1985, A&A, 62, 411

Buser, R., & Fenkart, R. 1990, A&A, 239, 243

Buser, R., & Kurucz, R. L. 1992, A&A, 264, 557 (BK)

Buser, R., & Rong, J. 1995, BaltA, 4, 1

Buser, R., Rong, J., & Karaali, S. 1998, A&A, 331, 934

Buser, R., Rong, J., & Karaali, S. 1999, A&A, 348, 98

Carney, B. W., Wright, J. S., Sneden, C., Laird, J. B., Aguilar, L. A., et al. 1997, AJ, 114, 363

Chabrier, G. 2001, ApJ, 554, 1274

Chabrier, G. 2002, ApJ, 567, 304

Chabrier, G. 2003, PASP, 115, 763

Chiba, M., & Beers, T. C. 2000, AJ, 119, 2843

Cignoni, M., Prada Moroni, P. G., & Degl' Innocenti, S. 2004, MmSAI, 75, 85

Cousins, A. W. J. 1976, MNSSA, 35, 70

Curty, D. 2005, Corrélations de paramètres stellaires - un outil didactique, Travail de diplôme, Univ. Basel, 34pp.

Eggen, O.J. 1987, in The Galaxy, eds. G. Gilmore & B. Carswell, p. 211

Elmegreen, B. G. 2001, ASPC, 243, 255

Fagotto, F., Bressan, A., Bertelli, G., & Chiosi, C. 1994a, A&A, 104, 365

Fagotto, F., Bressan, A., Bertelli, G., & Chiosi, C. 1994b, A&A, 105, 29

Fagotto, F., Bressan, A., Bertelli, G., & Chiosi, C. 1994c, A&A, 105, 39

Fenkart, R. 1977, A&A, 56, 91

Fenkart, R. 1980, A&AS, 91, 352

Fenkart, R. 1989, A&AS, 78, 217

Fenkart, R. 1989, A&AS, 79, 51

Fenkart, R. 1989, A&AS, 80, 89

Fenkart, R. 1989, A&AS, 81, 187

Fenkart, R. & Esin-Yilmaz, F. 1983, A&AS, 54, 423

Fenkart, R. & Esin-Yilmaz, F. 1984, A&AS, 58, 357

Fenkart, R. & Esin-Yilmaz, F. 1985, A&AS, 62, 39

Fenkart, R. P., & Karaali, S. 1984, A&AS, 57, 419

Fenkart, R., Topaktas, L., Boydag, S., & Kandemir, G. 1986, A&AS, 63, 49

Fenkart, R., Topaktas, L., Boydag, S., & Kandemir, G. 1987, A&AS, 67, 245

Finley, D. S., Koester, D., & Basri, G. 1997, ApJ, 488, 375

Fluks, M. A., Plez, B., The, P. S., de Winter, D., Westerlund, B. E., & Steenman, H. C. 1994, A&AS, 105, 311

Frayn, C. M., & Gilmore, G. F. 2002, MNRAS, 337, 445

Frayn, C. M., & Gilmore, G. F. 2003, MNRAS, 339, 887

Fukugita, M., Ichikawa, T., Gunn, J. E., Doi, M., Shimasaku, K., & Schneider, D. P. 1996, AJ, 111, 1748

Gilmore, G., & Reid, N. 1983, MNRAS, 202, 1025

Gilmore, G. 1984, MNRAS, 207, 223

Gilmore, G., & Wyse, R. F. G 1985, AJ, 90, 2015

Gilmore, G., Wyse, R. F. G., & Kuijken, K. 1989, Ann. Rev. Astr. Ap., 27, 555

Girardi, L., Bressan, A., Chiosi, C., Bertelli, G., & Nasi E. 1996, A&A, 117, 113

Gray, D., F. 1992, Cambridge Astrophysics Series, 20

Gunn, J. E., Carr, M., Rockosi, C., Sekiguchi, M., & Berry, K., et al. 1998, AJ, 116, 3040

Harris, W. E. 1998, in Star Clusters, Labhardt, L., & Binggeli, B., Eds. 1998, Saas-Fee Advanced Course Lecture Notes 28

Harris, J., & Zaritsky, D. 2001, ApJ, 136, 25

Hauschildt, P. H. 2006, in preparation

Hauschildt, P. H., & Baron, E. 1999, J. of Comp. and Appl. Math., 102, 41

Hauschildt, P. H., & Baron, E. 2004, A&A, 427, 987

Hauschildt, P. H., Allard, F., & Baron, E. 1999, ApJ, 512, 377

Hauschildt, P. H., Lowenthal, D. K., & Baron, E. 2001, ApJs, 134, 323

Hernandez, X., Valls-Gabaud D., & Gilmore G. F. 1999, MNRAS, 304, 705

Homeier, D., Koester, D., Hagen, H.-J., Jordan, S., Heber, U., Engels, D., Reimers, D., & Dreizler, S. 1998, A&A, 338, 563

Hu, W., & Dodelson, S. 2002, ARAA, 40, 171

Ibata R.A., Gilmore, G., & Irwin, M.J. 1994, Nature 370, 194.

Iglesias, C. A., Rogers, F. J., & Wilson, B. G. 1992, ApJ, 397, 717

Immeli, A. 2003, Ph.D. Thesis, University of Basel

Irwin, M.J. et al. 1996, in Formation of the Galactic Halo... Inside and Out, eds. H. Morrison & A. Sarajedini, p. 84.

Johnson, H. L.; Morgan, W. W.1953, ApJ, 117, 313

Jones, L. A. 1996, ASPC, 86, 1996

Jordi, K., Grebel, E. K., & Ammon, K. 2005, Astron. Nachr., 326, 657

Kawaler, S. D., & Winget, D. E. 1987, Sky and Telescope, 74, 132

Kennicutt, R. C., Jr. 1998, ApJ, 498, 541

King, J. R. 1997, AJ, 113, 2302

Kleinman, S. J., Harris, H. C., Eisenstein, D. J., Liebert, J., Nitta, A., et al. 2004, ApJ, 607, 426

Koester, D. 2004, private communication

Koester, D., & Wolff, B. 2000, A&A, 357, 587

Kroupa, P. 2001, MNRAS, 322, 231

Kroupa, P. 2002, Sci, 295, 82

Kucinskas, A., Hauschildt, P. H., Ludwig, H.-G., Brott, I., Vansevicius, V.et al. 2005, A&A, 442, 281K

Kurucz, R. L. 1995 (private communication to R. Buser)

Lambert, D. L. 1989, AIPC, 183, 168

Lejeune, T. 1997, Ph.D. Thesis, University of Basel

Lejeune, T., Cuisinier, F., & Buser, R. 1997, A&A, 125, 229

Lejeune, T., Cuisinier, F., & Buser, R. 1998, A&A, 130, 65

Miller, G. E., & Scalo, J. M. 1979, ApJ S. S., 41, 513

Navarro, J. F., Frenk, C. S., & White, S. D. M. 1995, MNRAS, 275, 56

Navarro, J. F., & Steinmetz, M. 2000, ApJ, 538, 477

Nissen, P. E.; Schuster, W. J. 1997, A&A, 326, 751

Noh, H.-R., & Scalo, J. 1990, ApJ, 352, 605

Norris, J.E. 1996, in Formation of the Galactic Halo... Inside and Out, eds. H. Morrison & A. Sarajedini, p. 14.

Oke, J. B.,& Gunn, J. E. 1983, ApJ, 266, 713

Petz, A.. 2005, Ph.D. Thesis, University of Hamburg

Penzias, A. A., & Wilson, R. W 1965, ApJ, 142, 419

Rauch, T. 2003, A&A, 403, 709

Richards, G. T., Fan, X., Newberg, H. J., & Strauss, M. A., et al. 2002, AJ, 123, 2945

Ridgway, S. T., Joyce, R. R., White, N. M., & Wing, R. F. 1980, ApJ, 235, 126

Rong, J., Buser, R., & Karaali, S. 2001, A&A, 365, 439

Rubin, V. C., & Ford, W. K., Jr 1970, IAUS, 38, 61

Salpeter, E. E. 1955, ApJ, 121, 161

Samland, M., Hensler, G., & Theis, Ch. 1997, ApJ, 476, 544

Samland, M. 2004, PASA, 21, 175

Samland, M., & Gerhard, O. E. 2003, A&A, 399, 961

Samland, M. 2004, PASA, 21, 175

Schlegel, D. J., Finkbeiner, D. P., & Davis, M. 1998, ApJ, 500, 525

Schneider D. P., Fan X., Hall P. B., Jester S., & Richards G.T., et al. 2003, AJ, 126, 2579

Schneider, D. P., Hall, P. B., Richards, G. T., Vanden Berk, D. E., & Anderson, S. F., et al. 2005, AJ, 130, 367

Schmidt, M., 1959, ApJ, 129, 243

Smith, L., L., & Steinlin, U. 1964, Z. Astrophys., 58, 253

Scholz, M. 1997 (private communication to R. Buser)

Sekiguchi, M., & Fukugita, M. 2000, AJ, 120, 1072

Sparke, L., S., & Gallagher, J., S. 2000, Galaxies in the Universe: An introduction, Cambridge University Press, Cambridge

Stoughton, C., Lupton, R. H., Bernardi, M., Blanton, M. R., Burles, S., et al. 2002, AJ, 123, 485

Trefzger, C. F. 1981, A&A, 95, 184

Twarog, B. A. 1980, ApJ, 242, 242

Unsöld, A., & Baschek, B. 2002, Der neue Kosmos: Eine Einführung in die Astronomie und Astrophysik. Springer Verlag Berlin Heidelberg New York

Vallee, J. P. 1994, ApJ, 437, 179

VandenBerg, D. A. 1999, ASPC, 165, 46

Weidemann, V. 1971, in White Dwarfs, Proceedings from IAU Symposium no. 42, eds. W. J. Luyten, p.81

Wenger, E. 2005, Ph.D. Thesis, University of Basel

Westera, P. 2001, Ph.D. Thesis, University of Basel

Westera, P., Lejeune, T., Buser, R., Cuisinier, F., & Bruzual, G. 2002, A&A, 381, 524

Westera, P., Samland, M., Buser, R., & Gerhard, O. E. 2002, A&A, 389, 778

Westera, P., Samland, M., Kautsch, S. J., Buser, R., & Ammon, K. 2006, in preparation

Wildt, R. 1939, ApJ, 90, 611

Worthey, G. 1999, ASPC, 192, 283

York, D. G., Adelman, J., Anderson, J. E., Jr., Anderson, S. F., & Annis, J., et al. 2000, AJ, 120, 1579

Acknowledgements -
Danksagung, Remerciements

Zum Schluss ist es mir noch ein grosses Anliegen, all denjenigen Menschen zu danken, die mich während meiner Doktorarbeit tatkräftig unterstützt haben.

Zuallererst möchte ich mich herzlichst bei meinem Doktorvater, Herrn Professor Dr. Roland Buser, dafür bedanken, dass er mir ermöglicht hat, mich in ein mir bis dahin noch weitgehend unbekanntes, doch sehr anziehendes Gebiet, die Astronomie, einzuarbeiten. Ich bin mir voll und ganz im Klaren darüber, was für ein grosses Privileg ich dadurch erfahren durfte! Herzlichen Dank!
Unbezahlbar waren mir seine immer für Erklärungen bereite Haltung und die unendliche Geduld, mit der er mir komplizierte Sachverhalte - beschämenderweise zum Teil mehrmals - verbal und graphisch verständlich nahe brachte. Denkblockaden oder geistige Durststrecken, die während meiner ganzen Dissertationszeit immer wieder sporadisch auftraten, konnte er gezielt mit seinen auf Weitsicht beruhenden Ratschlägen und vor allem auch mit seinem unbesiegbaren Optimismus in Luft auflösen.
Neben den Gesprächen mit dem erfahrenen Astronomen, Roland Buser, haben mir auch die vielen Diskussionen zu anderen Themen, in die sich dann meist auch der Philosoph, Roland Buser, einschaltete, die Grenzen und Ungereimtheiten meines Weltbildes vor Augen geführt und mich oftmals dazu angespornt, nochmals gründlich über die Sachverhalte nachzudenken und weiter zu lernen.

Je remercie Prof. Dr. François Cuisinier pour l' intérêt particulier qu' il a toujours porté a mon travail. Ses conseils et son sense critique m' ont été toujours très profi tables! Surtout, je suis très heureuse qu' il a accepté de prendre la place de mon corapporteur. Merci beaucoup, François!

Ganz herzlich möchte ich mich auch bei Dr. Markus Samland bedanken, der mich mit seinem fundierten Wissen und seinem wissenschaftlichen Drang stets vorwärts trieb. Auch nach seiner Zeit hier am Institut hatte er immer ein offenes Ohr für meine Anliegen und Zeit, mir seine fantastischen Galaxienmodelle zu erläutern und mich an seinem enormen Fachwissen teilhaben zu lassen. Ohne seine fachliche und moralische Unterstützung wäre ich wohl nie an diesem Ziel angelangt!

Tatkräftige Unterstützung erhielt ich auch von Pieter Westera, mit dem ich für eine gewisse Zeit das Büro teilen durfte. Sei es auf mentaler Ebene, da er mich mit seiner positiven Art immer wieder auf den Boden der Tatsachen zurückholen konnte oder aber auch auf der physischen, korrigierte er doch tapfer meine ganze in nicht immer ganz gutem Englisch verfasste Dissertation! Und all unsere Gespräche über Astronomie und sonstiges möchte ich nicht missen!

I would also like to thank Niranjan Sambhus who helped me daffi ng several uncertainties aside by patiently explaining complex physical and/or computational theories in a very comprehensive manner. I even liked his way of teasing me and I know, I will miss it very much in the future :-)!
Un grand merci aussi à Daniel Cerrito pour sa serviabilité chaleureuse et surtout pour son travail si précieux lors de realiser beaucoup de différentes fi gures qui complètent cette thése de magnifi que manière.

Futhermore, I would like to express my gratitude to Gustavo Bruzual, Detlef Koester, Thomas Rauch, Peter Hauschildt and Ines Brott, who in one way or the other gave me a hand to gather all the ingredients needed for the present code.

Ein grosses Dankeschön richtet sich auch an alle anderen Mitglieder des Astronomischen Instituts, die mich alle auf die eine oder andere Art und Weise unterstützt haben. Unsere gemeinsamen Kaffeerunden und Diskussionen über Gott und die Welt am Küchentisch waren immer eine willkommene Abwechslung! Andrea Kayser, Andreas Koch, Wolfgang Löffler, Thorsten Lisker, Katharina Glatt, Katrin Jordi and Marco Longhitano. Und vor allem möchte ich mich bei Caroline Girard für ihre tolle und motivierende Unterstützung während meiner ganzen Disszeit und für unsere spannenden philosophischen Gesprächsrunden bei Kaffee und meist irgendwas Süssem :-) bedanken!

Deine liebevolle chaotische Art, dein Charme und Humor haben mich die Sorgen um die Diss beim Ankommen in unserem gemütlichen Zuhause immer schnell vergessen lassen. Danke dir vielmals, Hase!

Au bi mine liebe Eltere und mim allerbeschte Schwösti Reni mit samt Familie moecht i mi gaaaanz härzlech bedanke für die tolli Unterstützig und Wärmi, wo si mer immer entgäge bringe!

Öli, du weisst, ohne dich gehts nicht.

Pascal Saint-Hilaire, Barbara Bächli and Margrit Oser, thanks for your patience and close friendships!

Schlussendlich möchte ich mich noch beim Schweizerischen Nationalfonds für meine Anstellung als wissenschaftliche Assistentin bedanken.

Declaration

I declare, that I have written the thesis

"From theoretical stellar spectra to realistic models of the Milky Way: a never ending Odyssey"

only with the use of the resources mentioned therein, and that I haven' t handed it in at any other faculty.

Karin Ammon

Curriculum vitae

Personalien

Name	Ammon
Vornamen	Karin
Geburtsdatum	13. Juni 1973
Geburtsort	Brüssel, Belgien

Ausbildung

1990 - 1994	Gymnasium Typus D, Wettingen
1994 - 2001	Studium **Geographie** und **Germanistik** (Hauptfach), Studium Biologie und Chemie (Nebenfach), Universität Basel
2000 - 2001	Lizentiatsarbeit in **Physiogeographie** Titel: "Die Nitrat- und Phosphatdynamik in Vorfluter und Drainage eines Einzugsgebietes im Schweizer Tafeljura (Länenbachtal, Kanton Baselland)." Betreuer: Prof. Dr. rer. nat. Dr. h.c. Hartmut Leser Abschluss als **Liz. Phil. Geo.**
2002 - 2007	Doktorarbeit in **Astronomie**, Universität Basel Betreuer: Prof. Dr. Roland Buser Weitere Professoren: Prof. Dr. Bruno Binggeli, Prof. Dr. Ortwin Gerhard, Prof. Dr. Eva K. Grebel, Prof. Dr. Andreas G. Tammann Abschluss als **Dr. Phil. Nat.**

Arbeitserfahrung

1999 - 2001	Hilfsassistentin am **Geographischen Institut** der Universität Basel
Aufgaben	- Durchführung von Wasserprobenanalysen im institutseigenen Labor: Nitrat, Phosphat, Ammonium, pH-Wert, Leitfähigkeit, TOC. - Verarbeitung der Daten und Herleitung der Dateninterpretationen.
2001 - 2002	Wissenschaftliche Mitarbeiterin an der **ETH Zürich**
Aufgaben	- Mitarbeit im Projekt "Carbon pools and fluxes in Swiss Forests", Abschätzung der vorhandenen Kohlenstoffvorräte in Schweizer Wäldern und deren Böden und die zukünftige Speicherfähigkeit in Bezug auf die Ratifizierung des Kyotoprotokolls. - Erarbeitung und Lektorat des Berichts "Bestandesaufnahme zum Thema Senken in der Schweiz" im Auftrag des BUWAL.
2002 - 2003	Lehrerin an der **Kant. Schule für Berufsbildung**, Aarau
Aufgaben	Unterrichten von SchülerInnen im Fach Deutsch

2004 - 2005	Dozentin am **Institut für Lehrerinnen - und Lehrerbildung**, Bern
Aufgaben	Unterrichten von angehenden SekI-LehrerInnen im Fach Geographie
Nov. 2006	Dozentin an der **IBZ**, Aarau und Bern
Aufgaben	ABU-Unterrichten von angehenden InformatikerInnen
2002 - 2007	Assistenzstelle am **Astronomischen Institut**, Universität Basel
Aufgaben	Öffentlichkeitsarbeit, Führungen

A. Appendix: Comparisons

A.1. Comparison: BaSeL 3.2 - PHOENIX

In this Section, we give a rough picture of the colour differences of the two spectral libraries we use in our code. We calculate the differences of 8 BaSeL 3.2 and PHOENIX synthetic $UBVRIJHK$ (di Benedetto 1998; Bessell 1983; Buser 1978) colours in the $T_{\rm eff} - logg$ plane, plot them and analyse them by eye.
In the future, it will be necessary to make more profound investigations by comparing the synthetic colours of both libraries with observational data in the whole parameter range, in order to evaluate, which library reproduces the empirical colours more accurately.

The BaSeL 3.2 and the PHOENIX spectral library differ in several distinctive features listed in Table A.1.

TABLE A.1.: Comparison of the main characteristics of the two synthetic libraries

Distinctive feature	BaSeL 3.2	PHOENIX
way of construction:	semi-empirical	fully computed
parameter range coverage:		
$T_{\rm eff}$	2'000 $\leq T_{\rm eff} \leq$ 50'000 K	2'700 $\leq T_{\rm eff} \leq$ 10'000 K
$logg$	$-1.02 \leq$ log g $\leq$ 5.5	$-0.5 \leq \log g \leq 5.5$
[Fe/H]	-2.0 $\leq$ [Fe/H] $\leq$ +0.5	$-3.5 \leq$ [Fe/H] $\leq$ +0.5
resolution:	1'221 wavelength points	$\sim$ 50'000 wavelength points

For our examination we take into account only the colours of those stars that have solar metallicity and of which the effective temperature and surface gravity lie in the $T_{\rm eff}-$ and $logg$-parameter range that both libraries have in common:

- 2' 700 $\leq T_{\rm eff} \leq$ 10' 000 K
- $-0.5 \leq$ log g $\leq$ 5.5

The biggest discrepancies in almost all colours (except $B-V$) are found in the parameter range of $T_{\rm eff} \leq$ 3' 500 K and 2.5 $\leq$ log g $\leq$ 5.0, as can be seen in Figures A.1 to A.5.
In the atmospheres of cool stars, millions of atomic and molecular lines have a signifi cant opacity. Even in our days, existing line data from laboratory measurements and theoretical calculations are generally not accurate

enough to reproduce any observed spectrum with an even moderate S/N ratio.

Good agreement can be found in the $R-I$ colour (Figure A.4, right panel) and also in the $J-H$ colour (Figure A.5, right panel). In the $R-I$ filter region, there is no dominant stellar feature present that could be treated in a different way by one of the two libraries. The same can be said for the $J-H$ filter pair. These filters too lie in a spectral region where the continuum is not disturbed by any special stellar feature.

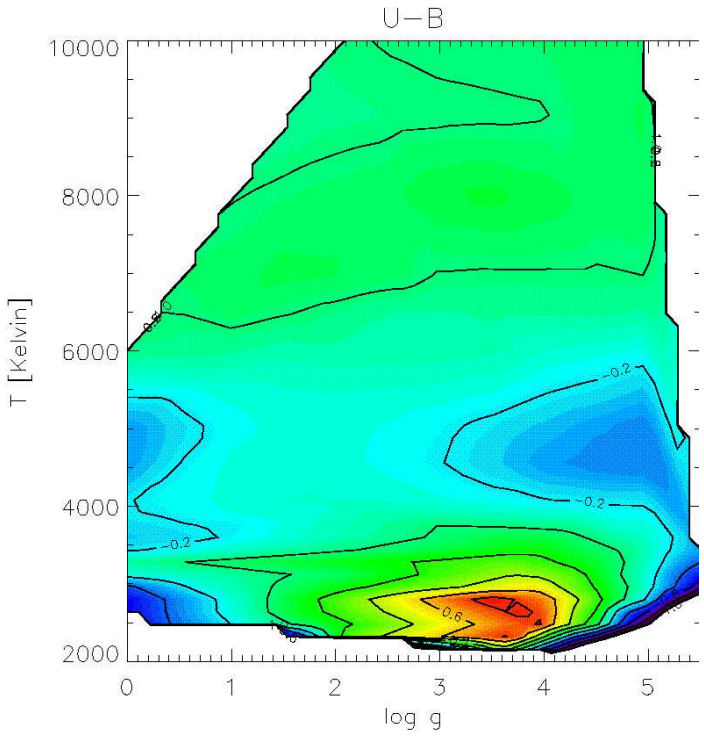

FIGURE A.1.: Comparison of BaSeL 3.2– and PHOENIX $U-B$ colours in the $T_{\rm eff}-logg$ plane. The colour code of the differences works as follows: red = 1.0 mag, orange = 0.6 mag, green = 0.2 mag, and blue = -0.2 mag difference.

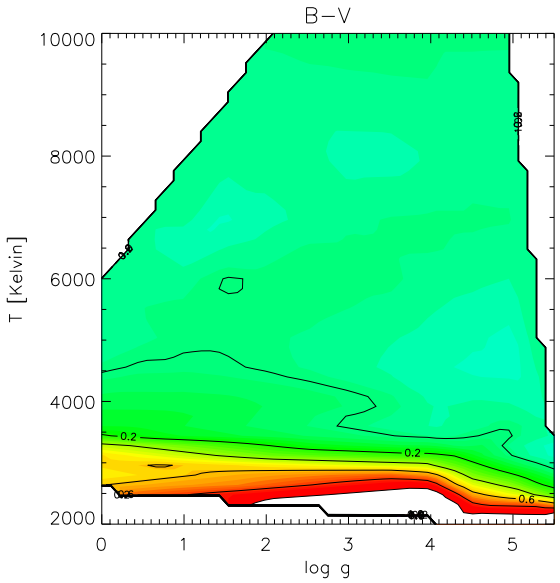

FIGURE A.2.: Comparison of BaSeL 3.2– and PHOENIX $B-V$ colours in the $T_{\rm eff} - logg$ plane.

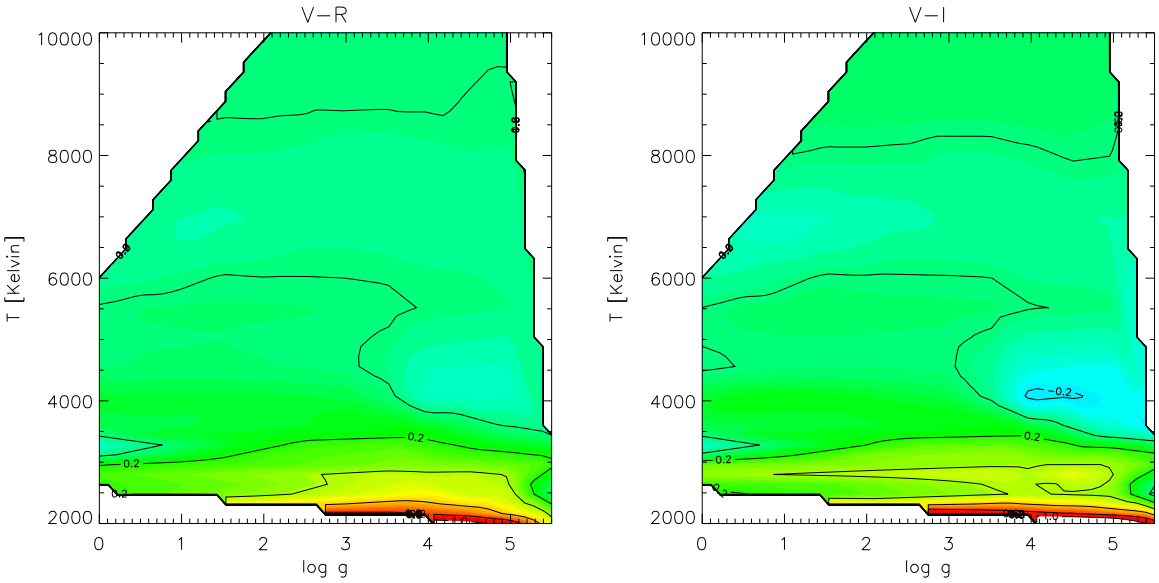

FIGURE A.3.: Comparison of BaSeL 3.2– and PHOENIX $V-R$ colours (left panel) and $V-I$ colours (right panel), respectively, in the $T_{\rm eff} - logg$ plane.

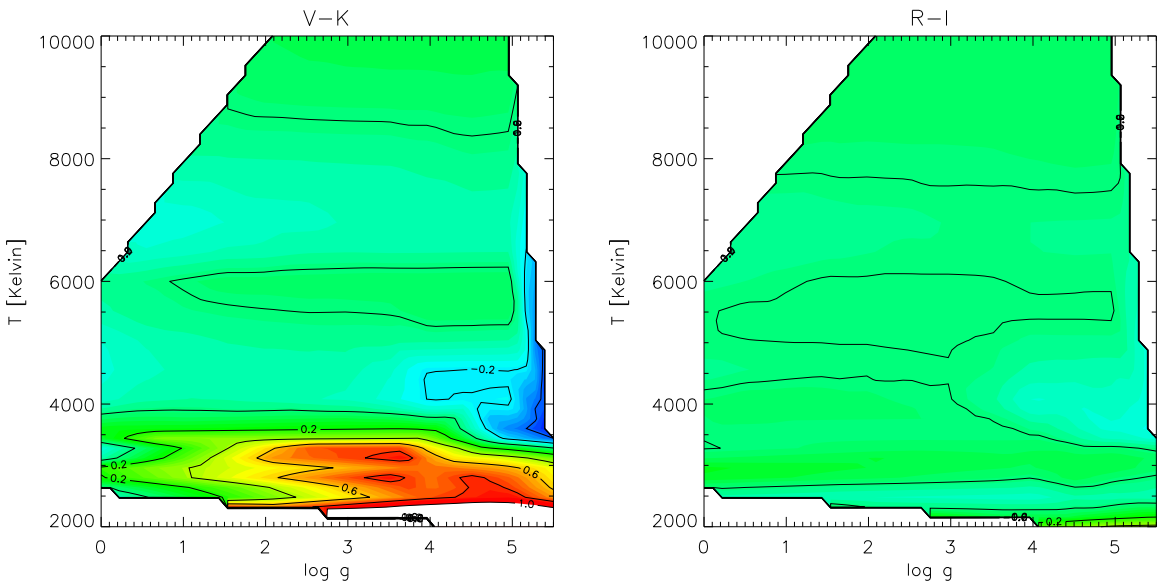

FIGURE A.4.: Comparison of BaSeL 3.2– and PHOENIX $V-K$ colours (left panel) and $R-I$ colours (right panel), respectively, in the $T_{\rm eff} - logg$ plane.

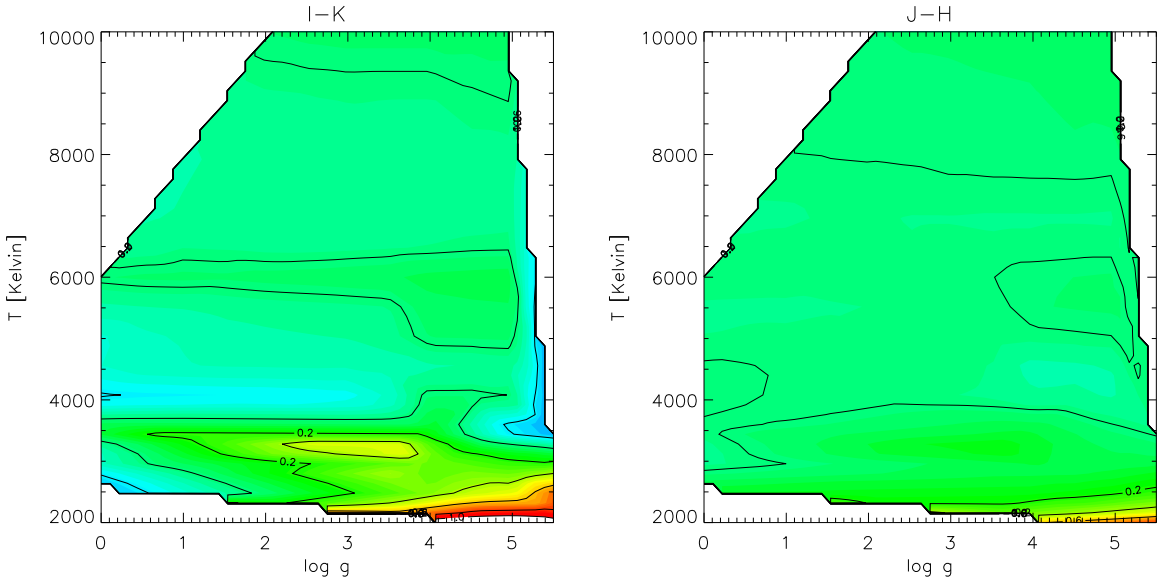

FIGURE A.5.: Comparison of BaSeL 3.2– and PHOENIX $I-K$ colours (left panel) and $J-H$ colours (right panel), respectively, in the $T_{\rm eff} - logg$ plane.

A.2. Comparison: NLTE and LTE structure of PHOENIX

Although the PHOENIX code is able to generate spectra under the assumption of NLTE (= "Non Local Thermodynamic Equilibrium"), all the Gaia grid spectra are calculated based on LTE (= "Local Thermodynamic Equilibrium") for the ionization/dissociation equilibria and the level populations.

Figures A.6 and A.7 display the differences between NLTE and LTE structure of PHOENIX solar NLTE models produced by Hauschildt, Allard & Baron (1999) and of PHOENIX Vega NLTE models, respectively.

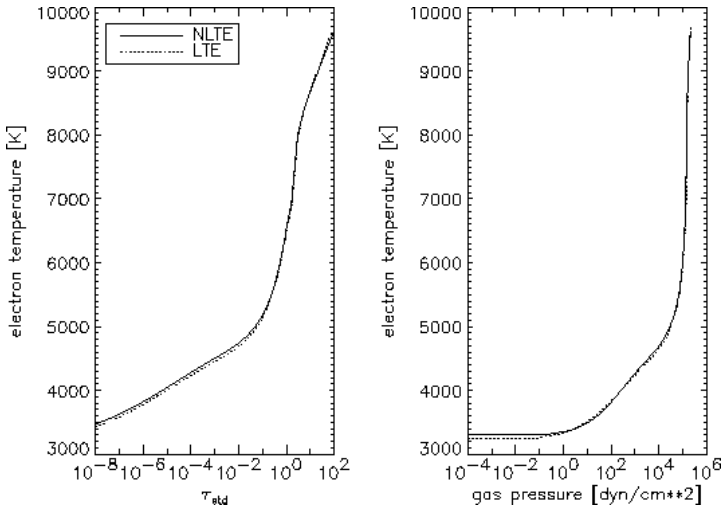

FIGURE A.6.: Comparison between NLTE and LTE structure of PHOENIX solar NLTE models. τ_{std} is the optical depth in the continuum at 1.2 μ.

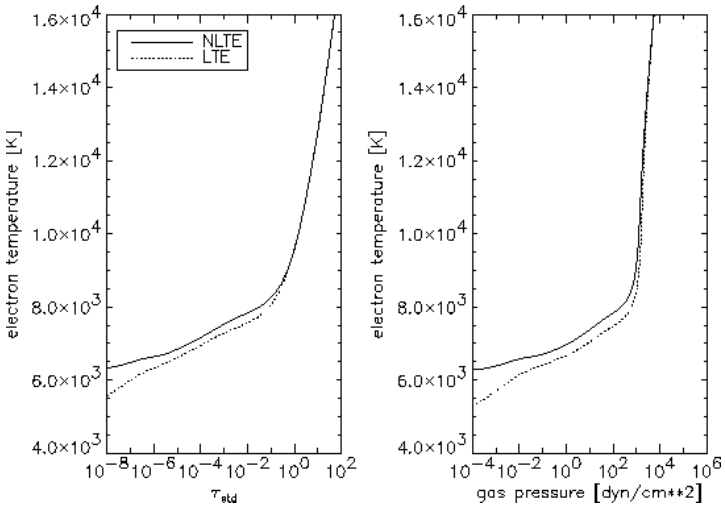

FIGURE A.7.: Comparison between NLTE and LTE structure of PHOENIX Vega NLTE models. τ_{std} is the optical depth in the continuum at 1.2 μ.

For the solar type model (Figure A.6), Hauschildt, Allard & Baron (1999) used $T_{\rm eff}$ = 5770 K, $\log g$ = 4.44 with solar abundances, and for the Vega model (Figure A.7) $T_{\rm eff}$ = 9550 K, $\log g$ = 3.95 with the "Vega abund-

ances".
As one can see, the assumption of LTE is a useful approximation for stars with solar effective temperatures. For a solar type star the differences between LTE and NLTE are very small: The NLTE effects on the photospheric structure and the line-forming regions are negligible.
By contrast, the Vega spectrum shows that NLTE changes the shape of the energy distributions of stars with higher temperatures quite strongly. Hauschildt, Allard & Baron (1999) conclude that their LTE models for stars with effective temperatures of 4500 K $\leq T_{\rm eff} \leq 10'000$ K agree reasonably well with the NLTE spectra. For higher temperatures, NLTE effects become relevant, equally for cooler models, where NLTE effects are important for individual atomic lines. Therefore detailed NLTE models for these two temperature ranges are required.

Note: A large NLTE model grid is currently under construction and will later replace the now available LTE model grid (Hauschildt 2006).

B. Appendix: Publications

B.1. Public outreach

The Astronomical Institute of Basel provides different outreach offers for a broad audience. Particularly, guided tours for schools, and other groups including demonstrations with the telescope in the dome cause high public interest. Last year circa 80 guided tours visited by roughly 2000 persons had taken place.

In order to build up a permanent exhibition in the room under the dome, the Astronomical society Basel asked to create posters to different astronomical themes. In June 2004, two posters were provided by our research group and can be eyed on the following two pages.

OBJEKTE UND STOFFZYKLUS DER MILCHSTRASSE

DER STOFF DER MILCHSTRASSE DURCHLÄUFT EINEN GROSSEN ZYKLUS VON MANNIGFALTIGEN PROZESSEN, DIE IHN AUS EINER URSPRÜNGLICHEN, UNFÖRMIGEN WOLKE VON WASSERSTOFFGAS IN EIN WOHLGESTALTES SYSTEM VON HIMMELSKÖRPERN MIT EINEM SCHIER UNERSCHÖPFLICHEN FORMEN- UND FARBENREICHTUM VERWANDELN.
DIE MILCHSTRASSE IST DIE HEIMAT UNSERER SONNE. MIT IHR GEHÖREN HUNDERT MILLIARDEN STERNE, GRÖSSERE UND KLEINERE, HELLERE UND SCHWÄCHERE DAZU, ABER AUCH STERNHAUFEN UND NEBEL UND GAS UND STAUB ERFÜLLEN SIE. DIE MILCHSTRASSE IST DIE GROSSE FAMILIE ALL DIESER OBJEKTE UND ZUGLEICH DEREN GEBURTS-, LEBENS- UND STERBESTÄTTE.

Die Milchstrasse am Himmel: Anblick von blossem Auge.

Die Schwarze Wolke B68, eine nahe Globule

STERNBILDUNG
Elefantenrüssel sind dichte, kühle Massen aus einem Gemisch von Gas und Staub, die vom heisseren, umgebenden Gas zusammengedrängt und abgeschnürt werden, so dass sich schliesslich kugelige **Globulen** bilden. Unter dem allseitigen Druck des heissen Gases werden die Globulen weiter zusammen gepresst, bis sie unter ihrem eigenen Gewicht kollabieren, sich dadurch aufheizen und in ihrem Inneren Kernreaktionen zu zünden vermögen. So beginnen sie als **neugeborene Sterne** zu strahlen.

Im Zentrum dieser Milchstrassengegend, die von dichten und heftig bewegten **Gas- und Staubwolken** verhängt ist, hat sich vor ca. 2 Millionen Jahren ein Sternhaufen gebildet, dessen hellsten und auch massereichsten Sterne ihre Umgebung in ein kurzwelliges blaues Licht tauchen. An den Spitzen der dunklen Staubfinger (siehe auch Grossaufnahme links), die aus dem kühleren Wolkenmaterial heraus in das heissere Haufengebiet hineinragen, bilden sich gerade neue Sterne - eine auch für unsere Milchstrasse typische stoffliche Metamorphose.

Adlernebel M16 im südlichen Sternbild der Schlange

Rosettennebel NGC 2237 im Einhorn

Die heissen Sterne des jungen Haufens im Zentrum heizen die Wasserstoffwolke auf und regen sie zum Leuchten an. Die heissen Gase dehnen sich explosionsartig in die kühleren Staubgebiete hinein aus und schnüren Teile von diesen in langen ‚Elefantenrüsseln' ab, die schliesslich in kleinere Globulen zerfallen.

Eine leuchtende Wolke von heissem, ionisiertem Wasserstoffgas in bewegter Auseinandersetzung mit den sie durchdringenden kühlen, dunklen Staubmassen. Aus den kollabierenden Gas- und Staubmassen einer solchen, HII-Region entsteht ein *offener Sternhaufen* mit zwischen wenigen Hundert und mehreren Tausend Mitgliedsternen.

Trifidnebel M20 im Schützen

Ein Supernova-Überrest:

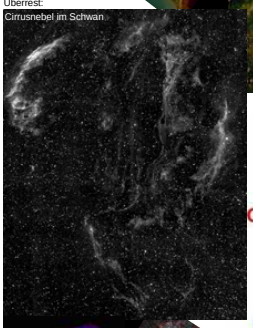

Cirrusnebel im Schwan

Krabbennebel M1 - der Überrest der Supernova aus dem Jahre 1054 n.Chr. im Licht der (von links oben) Radio-, optischen, UV- und Röntgen-Strahlung mit dem **Pulsar** im Zentrum.

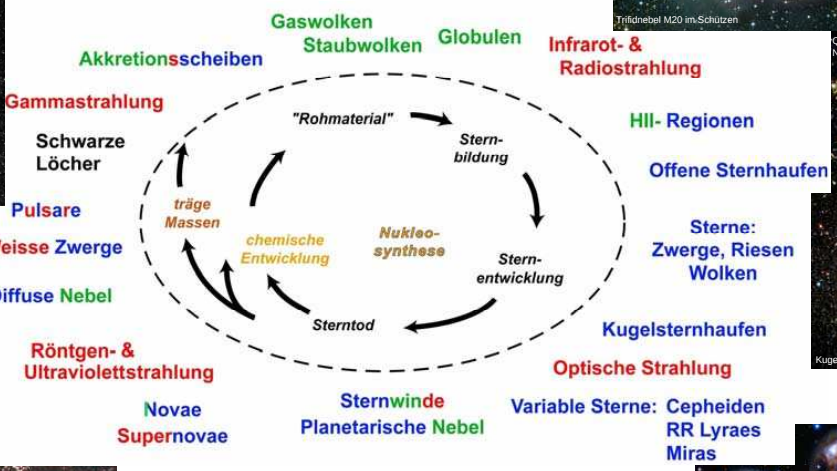

Quintuplet, Offener Sternhaufen in der Nähe des Zentrums der Milchstrasse.

Kugelhaufen M80 im Skorpion

Variabler Stern V838 im Einhorn:

Die von einem plötzlichen Ausbruch herrührende Lichtfront beleuchtet die staubige Umgebung des alten Sternes in immer grösseren Distanzen.

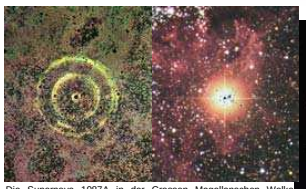

Die Supernova 1987A in der Grossen Magellanschen Wolke (GMW) kurz nach Erreichen der maximalen Helligkeit (rechts) und die heute (2004) sichtbaren Reflexionen (Lichtechos) an den sich ausbreitenden Gasfronten (links). Die GMW ist eine kleine Begleitgalaxie unserer Milchstrasse in einer Distanz von nur 150'000 Lj.

Helix

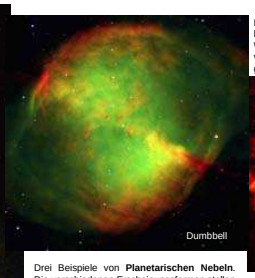

Dumbbell

Der massereiche und sehr leuchtkräftige Wolf-Rayet Stern WR124 im Schützen verliert viel Masse in Form eines heftigen Sternwindes.

STERNENTWICKLUNG
Die Sterne leuchten, indem sie die Energie abstrahlen, die in ihrem Innern erzeugt wird durch Verschmelzung (Fusion) von Wasserstoff zu Helium und später zu schwereren chemischen Elementen ("Metallen") wie Kohlenstoff und Eisen. Diese Erzeugung von schwereren aus leichteren Atomkernen nennt man **Nukleosynthese**. *Das Fortschreiten und Erschöpfen dieser Prozesse führt mit dem Alter zur Veränderung von Struktur* (z.B. Entwicklung vom Zwerg- zum Riesenstern und/oder zu einem Veränderlichen – z.B. durch Einsetzen einer periodischen Pulsation der Oberfläche etc.) *und chemischer Zusammensetzung* (Anreicherung mit Metallen) *der Sterne*. In solchen besonders hellen und/oder fortgeschrittenen Lebensphasen geben die Sterne nicht nur Strahlung, sondern auch Masse an die Umgebung zurück (Massenverlust), z.B. in der Form von kontinuierlichen Gas- und Staubpartikelströmen (Sternwinde) oder durch Abstossen ganzer Hüllen (Planetarische Nebel).

In der Fülle der Lichtquellen und ihrem Farbenreichtum in diesem kleinen Feldausschnitt aus dem Sternbild des Schützen manifestiert sich die enorme Vielfalt der Sterngesellschaft unserer Milchstrasse zwischen hell und schwach, heiss und kalt, gross und klein, schwer und leicht, jung und alt, arm und reich an Metallen.

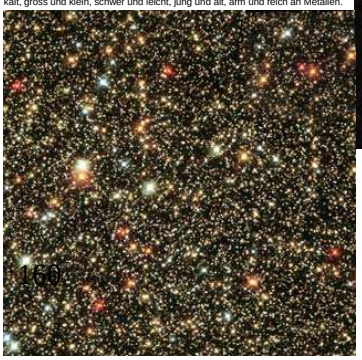

Drei Beispiele von **Planetarischen Nebeln**. Die verschiedenen Erscheinungsformen stellen verschiedene Stadien bzw. Geometrien des Massenverlusts dar: Dumbbell - Frühstadium mit noch nahezu kompakter Hülle; Helix - Spätstadium mit bereits stark expandierter und entsprechend "verdünnter" Hülle; MyCn 18 - Gasausfluss vor allem über die Pole des Sterns und daher zwiefach. In jedem Falle befindet sich jeweils im Zentrum ein so genannter Weisser Zwerg, ein kompakter und heisser, aber nur noch schwach leuchtender Stern, dessen Vorrat an verwertbarem Brennstoff erschöpft ist und der deshalb keine Kernenergie mehr erzeugen kann. Er strahlt nur noch seine innere Wärme ab und kühlt dadurch allmählich aus.

MyCn18

STERNHAUFEN
Sternhaufen vereinfachen das Studium der Sternentwicklung, weil ihre Mitgliedsterne von Geburt alle ungefähr *dasselbe Alter, dieselbe Metallizität und dieselbe Entfernung* haben, jedoch auch *alle möglichen Werte von Geburtsmassen* repräsentieren - von welcher Masse die *Art und Dauer des Lebenslaufs eines Sterns* in erster Linie bestimmt wird.

Scutum-Wolke: In dieser tiefen Aufnahme gegen das galaktische Zentrum zu löst sich der diffuse, helle Schleier des Milchstrassenbandes in unzählige Einzelsterne auf.

NUKLEOSYNTHESE UND CHEMISCHE ENTWICKLUNG
Bei massereichen Sternen erfolgt der Übergang vom Alter ins Endstadium mit einem explosiven Massenverlust. Der Stern stürzt infolge der plötzlich versiegenden Kernenergieerzeugung in sich zusammen. Die dadurch freigesetzte Gravitationsenergie zerreisst den Stern zwar, vermag aber gleichzeitig auch schwere chemische Elemente (Eisen, Kobalt, Nickel etc.) zu fusionieren, die sie bis auf einen kompakten Sternrest (Neutronenstern oder Schwarzes Loch) in den interstellaren Raum wegschleudert. Der ganze Vorgang manifestiert sich in einem gewaltigen Helligkeitsausbruch - dem Kennzeichen einer so genannten **Supernova**. Die während des Sternenlebens oder zuletzt während der Explosion neu synthetisierten Metalle gelangen durch die Auswürfe der Supernova in Form von Gasnebeln zurück in das interstellare Medium, wo sie sich mit den schon vorhandenen Gas- und Staubmassen vermischen. Jede daraus entstehende neue Sterngeneration erhält also eine durch ihre Vorläufer-Generation *mit Metallen angereicherte* chemische Zusammensetzung und wird auf dieser Grundlage durch Fortsetzung der **Nukleosynthese** und Supernova-Produktion selbst zur **chemischen Entwicklung** der Galaxie, der sie angehört, beitragen.

AUFBAU UND ENTWICKLUNG DER MILCHSTRASSE

DIE MILCHSTRASSE IST DAS GROSSE SYSTEM DER STERNE UND STERNHAUFEN, DER GASNEBEL UND STAUBWOLKEN – ODER EINFACH: UNSER STERNSYSTEM, ZUM DEM WIR SELBST MIT UNSEREM PLANETEN ERDE UND UNSERER SONNE GEHÖREN. WELCHEN PLATZ NIMMT DIE SONNE IN DIESER RIESIGEN GALAXIE EIN? WIE IST DIE MILCHSTRASSE AUFGEBAUT, WIE IST SIE ENTSTANDEN UND WIE HAT SIE SICH ENTWICKELT?

Steckbrief unserer Milchstrasse			
Galaxientyp	Sb	Durchmesser	~ 100'000 Lj
Anzahl Sterne	~ 100 Milliarden	Distanz Sonne - Zentrum	~ 27'000 Lj
Alter	12 - 14 Milliarden Jahre	Umlaufszeit Sonne	230 Millionen J
Scheibendicke	~ 20'000 Lichtjahre (Lj)	Geschwindigkeit Sonne	250 km/s

Die Scheibengalaxie NGC 4565 vom Hubble-Typ Sb bietet einem weit entfernten äusseren Betrachter einen offensichtlich sehr ähnlichen optischen Anblick wie unsere Milchstrasse einem inneren Beobachter in der Nähe ihres Randes.

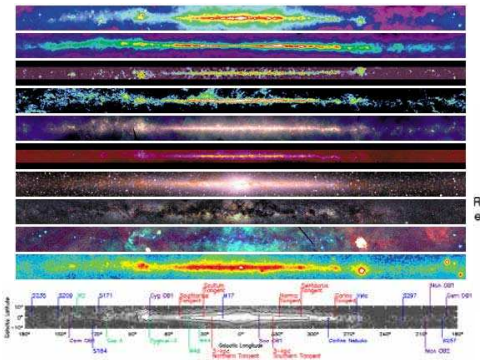

Findekarte mit wichtigen strukturellen Bestandteilen der Milchstrasse (rot), optisch sichtbaren HII-Regionen (ionisierte Wasserstoff-Wolken, blau), Radio-Quellen (grün) und OB-Assoziationen (violett). Die Koordinaten bezeichnen galaktische Länge und Breite.

Die Karten links stellen zehn Anblicke unserer Milchstrasse dar im Lichte der verschiedensten Wellenlängen von der Radio- über die Infrarot- bis zur Gammastrahlung.

Seitenansicht des räumlichen Aufbaus des Milchstrassensystems aus seinen hauptsächlichen Komponenten: Querschnitt durch Sonne und galaktisches Zentrum und senkrecht zur Rotationsebene.

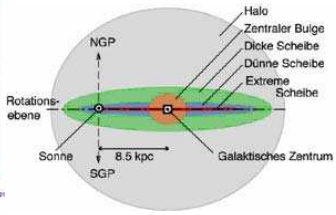

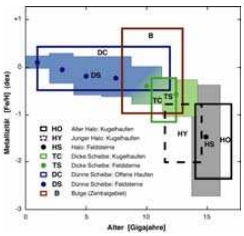

Die beobachtete AMR – **Relation** zwischen **Alter** und **Metallizität** (Verhältnis der relativen Häufigkeiten von Eisen und Wasserstoff, [Fe/H]) für Sterne und Sternhaufen der Milchstrasse. In der AMR zeigt sich nicht nur die **chemische Entwicklung** des galaktischen Systems, sondern auch die **Geschichte seiner Entstehung** aus verschiedenen Komponenten.

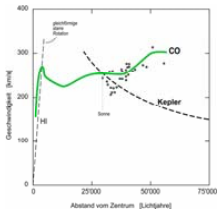

Die beobachtete Rotationskurve der Milchstrasse (grün). Steiler, geradliniger Anstieg im Zentralbereich: starre Rotation des Balkens. Wellenförmiger, flacher Anstieg bis in grösste Zentrumsabstände: differentielle Rotation der Scheibe; die Abweichung vom Kepler-Gesetz wird durch die Gravitationswirkung unsichtbarer Materie erklärt, die mit entsprechender Masse und räumlicher Verteilung als so genannter **dunkler Halo** identifiziert wird, der die sichtbare Milchstrasse weiträumig umfasst (unten).

Relative Sterndichten der Hauptkomponenten in der Sonnenumgebung und Dichteprofile in Richtung zu den galaktischen Polen.

In der Sonnenumgebung kommen auf 1000 Mitgliedsterne der dünnen Scheibe etwa 100 Sterne der dicken Scheibe und nur etwa ein einziger Halostern.

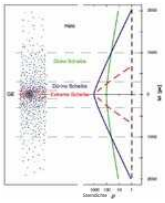

In der Höhe |z|=1000 pc = ungefähr 3000 Lj hingegen halten sich die Mitgliedszahlen pro Volumeneinheit der dünnen und der dicken Scheiben praktisch die Waage. Bei noch grösseren Distanzen von der Ebene und bis weit in den Halo hinein dominieren dann die Sterne der dicken Scheibe.

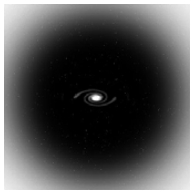

DAS RÄTSEL DER DUNKLEN MATERIE
Obschon die Natur und Beschaffenheit der dunklen Materie noch völlig unbekannt ist, ist ihre Existenz und Gravitationswirkung absolut unerlässlich, um die Entstehung massereicher, leuchtender Galaxien aus den ursprünglich kleinen Dichtefluktuationen zu erklären.

Die räumlichen Gestalten der drei Hauptkomponenten unserer Milchstrasse kommen durch die unterschiedlichen BAHNEIGENSCHAFTEN UND BEWEGUNGEN ihrer Objekte zustande:

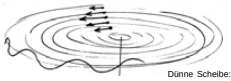

Dünne Scheibe: schnelle Rotation (~220 km/s) auf nahezu kreisförmigen und koplanaren Bahnen um das galaktische Zentrum.

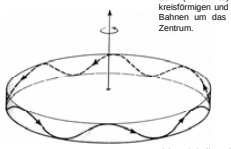

Dicke Scheibe: langsamere Rotation (~170 km/s) plus stärkere Pendelbewegung mit grösserer Amplitude senkrecht zur Rotationsebene.

Halo: Umlauf auf lang gestreckten Ellipsenbahnen (mit beliebigen Exzentrizitäten und räumlichen Orientierungen) um einen gemeinsamen, im galaktischen Zentrum liegenden Brennpunkt.

BASLER KOLLAPS- (KM) UND AKKRETIONS-MODELLE (AM) DER ENTSTEHUNG UND CHEMO-DYNAMISCHEN ENTWICKLUNG VON SCHEIBENGALAXIEN

Zeitliche Rate der Sternbildung durch schnellen Kollaps einer ursprünglichen Gaswolke (KM, links) oder durch allmähliche Gasaufsammlung/Akkretion aus einem Reservoir in der näheren Umgebung (AM, rechts).

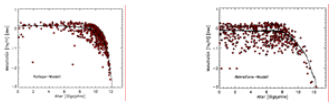

Resultierende AMR: langsamere Umwandlung des Gases in Sterne führt im AM (rechts) auch zu etwas langsamerer Anreicherung des Stoffes mit Metallen und ergibt auch zu jeder Zeit eine grössere Streuung der Metallizitäten als im KM (links) - was mit der beobachteten AMR in der Milchstrasse (siehe oben) auch besser übereinstimmt.

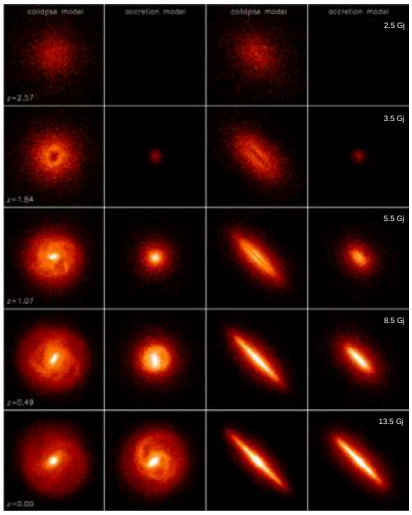

Zeitliche Entwicklung der im infraroten K-Band (bei 2.2 µm) beobachtbaren räumlichen Strukturen der Modellgalaxien in Front- (linke Spalten) bzw. Seitenansicht (rechte Spalten). Bildsequenzen von oben nach unten: Entwicklung zwischen 2.5 und 13.5 Milliarden Jahren (Gj = Gigajahre) nach Entstehung der Galaxien (die eingefügten Zahlen am linken Rand stellen entsprechende Rotverschiebungen z dar). Unterste Bildzeile: gegenwärtiger Anblick - man beachte die grosse Ähnlichkeit mit Aufnahmen realer Galaxien! Die Sequenzen der einzelnen Spalten lassen eine schnellere (KM) bzw. langsamere (AM) Bildung einer **Scheibe** mit **Spiralstruktur** sowie eines **Zentralgebietes** klar erkennen. Der aus leuchtender Materie bestehende **stellare Halo** ist relativ massearm und bleibt deshalb auch ziemlich lichtschwach.

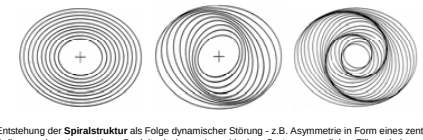

Entstehung der **Spiralstruktur** als Folge dynamischer Störung - z.B. Asymmetrie in Form eines zentralen Balkens oder einer nahen Begleitgalaxie - eines idealen Systems paralleler Ellipsenbahnen. Die **systematische** Verdrehung der grossen Bahnhalbachsen gegeneinander führt zu starr rotierendem Spiralmuster von erhöhter Bahn- und Materiedichte und damit auch zu kontinuierlicher Neubildung von kurzlebigen, massereichen Sternen hoher Leuchtkraft. Spiralarme sind also die prominentesten Gebiete junger, heller Objekte!

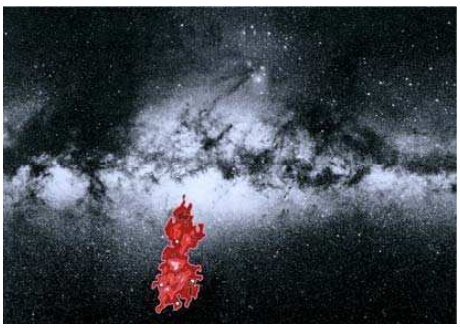

Die **Sagittarius-Zwerggalaxie** - hier rot eingefärbt - befindet sich lediglich etwa 75'000 Lichtjahre vom galaktischen Zentrum entfernt und ist im Begriffe, durch die starken Gezeitenkräfte auseinander gerissen und der Milchstrasse einverleibt zu werden. Sagittarius stellt ein spätes Beispiel jenes Prozesses der Aufsammlung/Akkretion und Verschmelzung kleiner Protogalaxien oder protogalaktischer Fragmente aus Sternen und/oder Gas dar, der vermutlich schon bei der Entstehung und frühen Entwicklung der Milchstrasse eine wesentliche Rolle gespielt hat.

In Basel vermessene Lage der jüngsten offenen Sternhaufen und hellen Wasserstoff-Wolken im Umkreis der Sonne. Die beobachtete Verteilung dieser Objekte zeichnet die lokale Spiralstruktur der Milchstrassenscheibe nach.

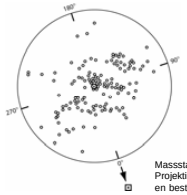

Massstabsgetreue Projektion der (oben bestimmten) Verteilung der galaktischen Sternhaufen und HII-Regionen auf die externe Galaxie NGC 1232.

Unsere Milchstrasse dürfte im Ganzen gesehen dieser Spiralgalaxie (NGC 1232) im Sternbild des Eridanus sehr ähnlich sein.

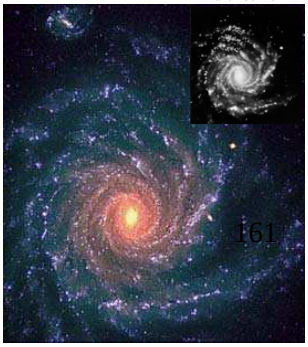

B.2. Scientific publications

Astronomy & Astrophysics manuscript no. 6082
December 8, 2006

Empirical Color Transformations Between SDSS Photometry and Other Photometric Systems

K. Jordi*, E. K. Grebel, and K. Ammon

Astronomical Institute of the University of Basel, Department of Physics and Astronomy, Venusstrasse 7, CH-4102 Binningen, Switzerland
e-mail: jordi@astro.unibas.ch, grebel@astro.unibas.ch, ammon@astro.unibas.ch

Received August 14, 2006; accepted August 28, 2006

ABSTRACT

Aims. We present *empirical* color transformations between the Sloan Digital Sky Survey (SDSS) *ugriz* photometry and Johnson-Cousins *UBVRI* system and Becker's *RGU* system, respectively. Owing to the magnitude of data that is becoming available in the SDSS photometric system it is particularly important to be able to convert between this new system and traditional photometric systems. Unlike earlier published transformations we based our calculations on stars actually measured by the SDSS with the SDSS 2.5-m telescope. The photometric database of the SDSS provides in a sense a single-epoch set of 'tertiary standards' covering more than one quarter of the sky. Our transformations should facilitate their use to easily and reliably derive the corresponding approximate Johnson-Cousins or *RGU* magnitudes.

Methods. The SDSS survey covers a number of areas that were previously established as standard fields in the Johnson-Cousins system, in particular, fields established by Landolt and by Stetson. We used these overlapping fields to create well-photometered star samples on which our calculated transformations are based. For the *RGU* photometry we used fields observed in the framework of the new Basel high-latitude field star survey.

Results. We calculated *empirical* color transformations between SDSS photometry and Johnson-Cousins *UBVRI* and Becker's *RGU* system. For all transformations we found linear relations to be sufficient. Furthermore we showed that the transformations between the Johnson-Cousins and the SDSS system have a slight dependence on metallicity.

Key words. Surveys – Catalogs – Techniques: photometric

1. Introduction

The Sloan Digital Sky Survey (SDSS) is the largest photometric and spectroscopic survey in the optical wavelength range. The SDSS is mapping one quarter of the entire sky and is measuring positions and magnitudes for over 100 million celestial objects (York et al. 2000; Grebel 2001). The SDSS photometric system was specifically designed for the survey (Fukugita et al. 1996; Smith et al. 2002), but many observatories worldwide have since purchased SDSS filters as well. The five SDSS *ugriz* filters are a modified Thuan-Gunn system (Thuan & Gunn 1976). Their most prominent feature are the wide passbands, which cover an effective wavelength range of ~ 380 nm to ~ 920 nm, and the lack of overlap between neighboring passbands. These properties ensure a high efficiency for faint object measurements, independent spectral information in each band, and coverage of essentially the entire optical wavelength range accessible from the ground.

The SDSS provides a photometric catalog of unprecedented depth, homogeneity, and quality. Owing to the magnitude of the data that are becoming publicly available in this new photometric system (Stoughton et al. 2002; Abazajian et al. 2003, 2004, 2005; Adelman-McCarthy et al. 2006), it is important to have well-calibrated transformation relations between this system and traditional photometric systems such as the Johnson-Cousins system (Johnson & Morgan 1953; Cousins 1976). It is easy to imagine situations where one wishes to know, e.g., the V-band magnitude of a star of interest that happens to be in the SDSS database and for which no other photometry is available. Moreover, the large area coverage of the SDSS and the high quality of its drift-scan photometry make it also suitable as a source of 'tertiary standards', although there is no information on variability for the majority of the SDSS objects. This disadvantage is compensated by the large number of photometered sources even within a small patch of the sky. Thus a few variable objects will merely appear as outliers and will not have a major effect on a photometric transformation. Also, if observations in a traditional photometric system are being obtained during a non-photometric night, existing transformable SDSS photometry of the same field will prove very use-

* Guest User, Canadian Astronomy Data Centre, which is operated by the Dominion Astrophysical Observatory for the National Research Council of Canada's Herzberg Institute of Astrophysics.

ful for at least an approximate photometric calibration (Koch et al. 2004a,b). Other large-area photometric survey catalogs are already being used in this manner; for instance, Udalski et al. (1998, 2000, 2002); Epchtein et al. (1999); Zaritsky et al. (2002, 2004); Skrutskie et al. (2006).

Prior to the start of SDSS observations, Fukugita et al. (1996) derived theoretical transformation relations between the Johnson-Cousins system and the SDSS $u'g'r'i'z'$ system. The primes refer to the filter-detector combination envisioned to be used at the 20″ photometric monitoring telescope at Apache Point Observatory. This auxiliary telescope observes SDSS photometric standards while the science observations are done in drift-scan mode with the actual SDSS survey telescope, a dedicated 2.5-m telescope at the same site (see, e.g., York et al. (2000); Stoughton et al. (2002); Gunn et al. (2006)). Fukugita et al. (1996) calculated synthetic magnitudes using the planned filter-detector combinations and spectral energy distributions of stars from the Gunn & Stryker (1983) spectrophotometric atlas. These synthetic magnitudes were then used to determine photometric transformations.

Smith et al. (2002) calculated transformations between the SDSS $u'g'r'i'z'$ system and the Johnson–Cousins photometric system based on actual observations in $u'g'r'i'z'$ filters. In this context the primes refer to the SDSS filter-detector combination used at the 1.0-m telescope at the US Naval Observatory (USNO), Flagstaff Station. These observations were used to set up a system of 158 bright standard stars that define the $u'g'r'i'z'$ system and to derive the above mentioned transformation equations. Smith et al. (2002) point out that there are "small but significant" differences between the USNO SDSS filters and the SDSS filters used at the 2.2-m telescope at Apache Point Observatory, leading to expected systematic differences between the USNO magnitudes and the final SDSS magnitudes.

Similarly, Karaali et al. (2005) used observations obtained in $u'g'r'$ filters at the Isaac Newton Telescope (INT) at La Palma, Spain. These filters were designed to reproduce the SDSS system. These data were complemented by Landolt (1992) *UBV* standard star photometry and used to calculate transformations between the INT SDSS $u'g'r'$ filter-detector combination and standard Johnson–Cousins photometry. Karaali et al. (2005) presented for the first time transformation equations depending on two colors. Since the INT filters and detector differ from the actual filter-detector combinations used by the SDSS, again systematic deviations are to be expected.

Direct empirical transformations between SDSS point-source photometry from the "early data release" (EDR; Stoughton et al. (2002)) and certain Johnson-Cousins filters were calculated by Odenkirchen et al. (2001) and by Rave et al. (2003). Rave et al. (2003) based their transformations on resolved stellar photometry of the Draco dwarf spheroidal galaxy obtained with the SDSS as well as with various other telescopes in different variants of the Johnson-Cousins system. The SDSS EDR photometry was then superseded by later SDSS data releases (Abazajian et al. 2003, 2004, 2005; Adelman-McCarthy et al. 2006).

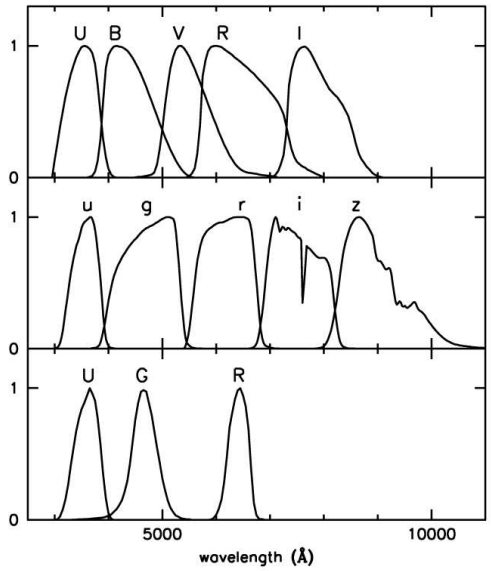

Fig. 1. Comparison of the (normalized) filter curves of the Johnson-Cousins *UBVRI* passbands (upper panel, the SDSS *ugriz* passbands (middle panel), and Becker's *RGU* photometry in the lower panel.

A recent *theoretical* transformation was carried out by Girardi et al. (2004). These authors used the actual SDSS passbands and CCD sensitivity curves of the SDSS camera (Gunn et al. 1998) employed at the 2.5-m SDSS telescope at Apache Point Observatory to transform theoretical stellar isochrones into the SDSS *ugriz* system.

The third photometric system that we are considering here is the *RGU* system by Becker (Becker 1946), a broad-band photometric system that was initially introduced with the goal of measuring stellar parameters and Galactic structure. No earlier transformations between SDSS photometry and *RGU* photometry have been published. For transformation relations between *RGU* and *UBV* see Steinlin (1968a,b); Bell (1972); Buser (1978a,b). While *RGU* photometry is not widely used, it plays a continuing role due to the existence of the "new Basel high-latitude field star survey" (Buser & K¨aser 1985; Buser et al. 1998). The goal of this single-epoch photographic survey is to map the Galactic density structure and the metallicity distribution in the various components of the Milky Way. For this purpose, 14 intermediate and high-latitude fields were observed, in which three-color *RGU* photometry of over 18 000 stars was measured. The limiting magnitude of this Galactic survey is approximately $G \sim 19$ or $V \sim 18$. This survey may seem to be obsolescent by modern standards due to its small number of stars, the shallow exposures, the limited photographic resolution, and the availability of much deeper, more homogeneous, and much larger CCD surveys. On the other hand, this photographic survey has played an important role in uncovering the structure of our Galaxy (e.g., Buser et al.

(1999)). Transformation relations between SDSS and *RGU* photometry help to evaluate the earlier findings with respect to modern explorations of the structure of the Milky Way (e.g., Chen et al. (2001); Juric et al. (2005)). The Basel survey provides star counts (or space densities) also for distances relatively close to the Sun, whereas there is a gap at these distances in studies carried out using SDSS data due to the saturation limit at $r \sim 14$. Space densities for stars with brighter apparent magnitudes can be combined with Hipparchos parallaxes, thus providing reliable Galactic model parameters. Moreover, the metallicity sensitivity of the *RGU* system (e.g., Buser & Fenkart (1990)) adds continuing value to the Basel high-latitude field star survey. Finally, this survey comprises a number of important Galactic sight lines that are not included in the currently available wide-field CCD surveys, and the analysis of these sight lines is continuing.

Here we present *empirical* color transformations between the SDSS *ugriz* photometric system using point-source photometry obtained with the SDSS 2.5-m telescope at Apache Point Observatory, and the Johnson-Cousins *UBVRI* system as well as the *RGU* system, respectively. These empirical colors have the advantage of not having to rely on synthetic colors or on passband-detector combinations of other telescopes. Hence, they provide the most direct transformations possible. In Sect. 2 we present the sources of our star samples and the criteria applied to choose the stars. Section 3 contains our calculations and the resulting transformation equations. In Sect. 4 we discuss our results and some possible future developments.

Table 1. The 23 Stetson fields that overlap with the SDSS DR4 sky coverage, and the number of matched stars.

Fields	Stetson Stars	Matches[a]
L92	214	138
L95	427	250
NGC 2419	1 188	520
NGC 2420	188	54
NGC 2683	27	7
PG 0918	122	53
L101	118	67
Leo I	1 840	508
PG 1047	67	36
NGC 5194	39	3
NGC 5272	432	111
NGC 5466	29	3
L106_550	16	5
Pal 5	65	48
L107	729	490
Pal 14	163	116
Draco	529	256
L112	74	26
NGC 7078	967	114
NGC 7089	377	26
L113	484	320
PG 2213	36	16
Pegasus	38	28
Total	**8 169**	**3 195**

[a] with *clean* photometry

2. Data

Our goal is to derive empirical transformations between the SDSS photometry as defined by the public SDSS data and the two other aforementioned photometric systems while minimizing the dependence on specific filter-detector combinations that deviate from the generic ones. The data used for our transformations were taken from the four different sources described below.

The SDSS data release 4 (SDSS DR4; Adelman-McCarthy et al. (2006)) comprises stellar point-source magnitudes provided by the SDSS photometry pipelines (Lupton et al. 2001; Stoughton et al. 2002). This point-source photometry is not expected to change anymore between DR4 and later releases (e.g., Adelman-McCarthy et al. (2006)).

2.1. Johnson-Cousins photometry

For Johnson-Cousins photometry the most generic standard star database available that lends itself to a comparison is the system of standard stars set up by A. Landolt, in particular the catalog published by Landolt (1992). This catalog contains an extensive set of mainly equatorial fields observed repeatedly with photoelectric aperture photometry. A number of the Landolt fields overlap with the area scanned by the SDSS. The Landolt photometry is widely used to transform and calibrate imaging data. The Landolt stars cover a *V*-magnitude range of approximately 11.5 to 16.0. With respect to SDSS photometry, the Landolt standard stars have one drawback: Many of them are brighter than the saturation cutoff in the SDSS system ($r \approx 14$). Nonetheless, the Landolt stars are valuable particularly for the transformation of the *U*-band photometry as we will see later.

The problem of the reduced number of stars in common between the Landolt catalog and the SDSS due to saturation is alleviated by the extension of Landolt's standard stars to fainter magnitudes by Stetson (2000). Stetson used a large set of multi-epoch CCD observations centered on Landolt fields and other regions in the sky and reduced them in a homogeneous manner tied to the Landolt *UBVRI* system. The larger area coverage and greater sensitivity of the CCD observations as compared to the earlier photomultiplier observations permitted Stetson to include stars down to $V \approx 19$ or 20. Since 2000, Stetson has been publishing a gradually growing list of suitable faint stars (Stetson 2000) with repeat observations at the website of the Canadian Astronomy Data Center[1]. The Stetson catalog contains only stars that were observed at least five times under photometric conditions and the standard error of the mean magnitude is less than 0.02 mag in at least two of the four filters. Stetson's data base also contains fields not covered by Landolt, e.g., fields in globular clusters and in nearby resolved dwarf galaxies. While Landolt's original fields contained mainly Population I stars, Stetson's new fields also include a sizable fraction of Population II stars.

[1] http://cadcwww.dao.nrc.ca/standards/

For our work the Stetson fields published as of January 2005 were used. As most of the SDSS DR4 sky coverage is in the northern part of the sky, it was straightforward to select those fields from the Stetson catalog that overlap with the SDSS DR4: 30 fields were identified and all stars available from the SDSS DR4 database within these fields were downloaded. For the subsequent matching and calculation of transformation relations only SDSS stars with *clean* photometry were used. The combination of flags describing the *clean* photometry can be found on the SDSS DR4 webpage[2]. This flag combination excludes stars whose photometry may be questionable for a number of reasons, e.g., due to saturation, overlaps with other objects (blends), location at the edge of a frame, large errors in fitting a point spread function, etc.

We then matched the Stetson stars and the SDSS stars by their coordinates. The coordinates of the stars in DR4 are measured with an accuracy of less than 0.1″ rms per coordinate (Adelman-McCarthy et al. 2006). In the Stetson catalog the coordinates are published with an accuracy of 0.15″ for the right ascension and 0.1″ for the declination. Two stars – one from each sample – are considered equal if their angular separation is smaller than 0.5″: $\sqrt{(\alpha_1-\alpha_2)^2 cos(\delta_1)^2+(\delta_1-\delta_2)^2} \leq 0.5''$, where α and δ stand for the right ascension and declination of the stars in arcsec.

Although the matching radius was chosen generously we do not find a matching SDSS star for each Stetson star (see Table 1). The *clean* photometry rule removes between 30 and 40 percent of our initial star sample. Furthermore, the SDSS photometric pipeline only detects a reduced number of stars in crowded fields. This affects in particular fields in globular clusters such as NGC 2419, NGC 5272, NGC 5466, NGC 7078, and NGC 7089, and fields with luminous extended galaxies such as NGC 2683. For fields with a very high degree of crowding, no SDSS data are available since these fields were intentionally omitted during the pipeline reduction process. Owing to these limitations, our original number of 30 common fields is actually reduced to 23 fields in which common stars in Stetson's and the SDSS catalogs could be identified. Fields without *any* common stellar objects with clean photometry include regions centered on the galaxies M81, NGC 4526, and NGC 4736, on the globular clusters M5 and M13, and on fields with stars that are all saturated in the SDSS like L114-750. In Table 1 the number of matches for each of the remaining 23 fields is listed. In Fig. 2 we plot the *R* magnitude of Stetson stars against their photometric error and the *r* magnitude of SDSS stars against their photometric error in order to illustrate how many stars we lose in the matching process. The Stetson stars are all brighter than 20^{th} magnitude, but at the same time the brightest SDSS stars with *clean* photometry are of 14^{th} magnitude. Possible matches between stars in the Stetson and in the SDSS database will therefore lie within this magnitude interval (see dashed vertical lines in Fig. 2).

Since Stetson's fields do not include *U*-band photometry in the fields that overlap with the SDSS, we complemented the Stetson data by standard stars from Landolt (Landolt 1992), our third data source. Only 54 stars from the Landolt catalog overlap with the DR4 sky coverage and have *clean* photometry in the SDSS, hence transformations involving *U* are necessarily based on a small subsample of stars.

[2] http://cas.sdss.org/astrodr4/en/help/docs/sql_help.asp#clean

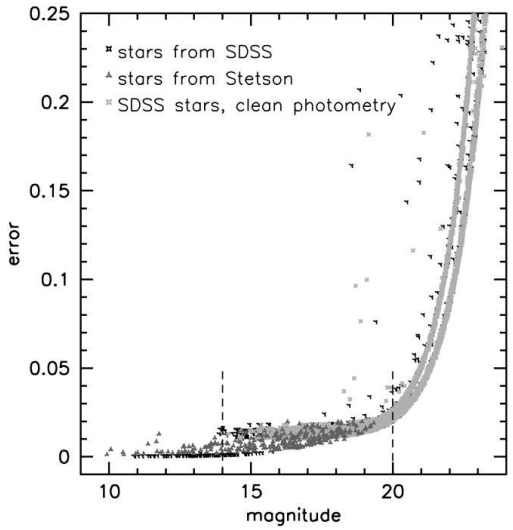

Fig. 2. For field L95 we plot the *R* magnitude of Stetson's standard stars (dark gray triangles) and the *r* magnitude of the SDSS stars (black crosses) against their photometric errors. The light gray crosses are those SDSS stars with *clean* photometry. The vertical dashed lines indicate the magnitude intervall in which possible matches in field L95 will lie.

2.2. *Becker's* RGU *system*

Our fourth source of data is the "new Basel high-latitude field star survey" (Buser & K¨aser 1985; Buser et al. 1998). The fourteen fields of the Basel high-latitude field star survey are all specified by a pair of galactic coordinates (Buser et al. 1998). These coordinates are not consistently defined and do not necessarily mark the center of the field. In most of the fields, they mark one of the corners. Three fields completely overlap with the SDSS DR4 sky coverage and six others have a partial overlap. The other five fields do not lie in the region of the sky that the SDSS DR4 has scanned. For deriving transformations, those two of the completely overlapping fields were used that had the best photometric quality. Table 2 lists the two fields and the number of found matches. The sample for the second set of transformations contained a total of 775 stars.

The Basel survey does not list coordinates of the stars in its fields, so they were matched visually using the Basel finding charts. In these prints of the photographic plates each measured star is marked with its catalog number, making the identification of stars in common with the SDSS a rather tedious enterprise. Not for all Basel stars a matching partner was found. The SDSS CCD photometry has higher resolution than the photographic plates of the Basel survey. In some cases, the SDSS recognized an object as a galaxy, whereas in the Basel survey

Table 2. The two fields from the new Basel Catalog that overlap with the SDSS DR4 sky coverage, and the number of matched stars.

Fields	Stars in Basel	Matches[a]
SA94	1 239	545
SA107	532	230
Total	**1 771**	**775**

[a] with *clean* photometry

it was treated as a star. In other cases, there was simply no star in the SDSS where Basel detected one. Occasionally the SDSS detected a fainter object within a radius of 1″ to 3″ of the dominant star, whereas in the Basel catalog only one source was detected. In all those cases these stars were deleted from our sample in order to ensure that only reliable photographic photometry was included. Moreover, we only used SDSS sources with *clean* photometry.

3. Results

3.1. Transformations between SDSS and Johnson–Cousins Photometry

The transformation between the Johnson–Cousins *UBVRI* photometry system and the SDSS *ugriz* system was carried out using the following eight general equations:

$$g - V = a_1 (B - V) + b_1 \quad (1)$$
$$r - i = a_2 (R - I) + b_2 \quad (2)$$
$$r - z = a_3 (R - I) + b_3 \quad (3)$$
$$r - R = a_4 (V - R) + b_4 \quad (4)$$
$$u - g = a_5 (U - B) + b_5 (B - V) + c_5 \quad (5)$$
$$g - B = a_6 (B - V) + b_6 \quad (6)$$
$$g - r = a_7 (V - R) + b_7 \quad (7)$$
$$i - I = a_8 (R - I) + b_8 \quad (8)$$

Not for all of the standard stars in Stetson's catalog measurements in all four bands (*BVRI*) are available, hence the number of stars used differed somewhat depending on the filters used in the transformation equation. We calculate in all but one case transformations depending on one color only. For the $u-g$ equation two colors are used since the SDSS g passband overlaps with the Johnson B and V passband, so a dependence on $(B - V)$ can be expected, and more importantly, the variation in position of the stellar locus owing to temperature, surface gravity, and metallicity is particularly large in this wavelength range (e.g., Grebel & Roberts (1995); Lenz et al. (1998)).

3.1.1. 'Global' transformations between *UBVRI* and *ugriz*

In Fig. 3 the colors specified on the left-hand side and on the right-hand side of our transformation equations are plotted against each other for all the stars used in each of the transformations. The resulting linear relations are plotted as solid lines. With the exception of the $(r - R)$,$(V - R)$ transformation (equation 4), which exhibits a pronounced slope change (see also Fukugita et al. (1996)), the relations are linear to first order. In Table 3 the resulting coefficients for the 'global' transformations are listed.

Here 'global' means that the entire star sample described above was used for the calculation without differentiating between potential Population I and Population II stars. The coefficients were calculated using least-squares minimization. The individual stars are weighted according to their formal photometric error. In Fig. 4 the deviations between the measured and the calculated magnitudes and colors are shown. The deviations get bigger for fainter magnitudes.

3.1.2. Metallicity-dependent transformations between *BVRI* and *griz*

The influence of metallicity on the transformation was investigated to the extent possible with the available standard star fields. One of the Stetson fields covers part of the Draco dwarf spheroidal galaxy. The majority of the stars from this Milky Way companion has a very low metallicity: Draco's mean metallicity is [Fe/H] ~ -2.0 dex (Grebel et al. 2003). Moreover, Stetson and the SDSS provide photometry for the surroundings of the similarly metal-poor globular clusters NGC 2419 (−2.12 dex according to Harris (1996)) and NGC 7078 (−2.26 dex; Harris (1996)). Probable member stars of these three objects were selected based on their color-magnitude diagrams. This provides us with a metal-poor sample of ancient Population II stars. We may assume that the ages of the three old objects are comparable within the measurement accuracy (see also Grebel & Gallagher (2004)).

In contrast, the metallicity of the stars in Landolt's equatorial fields is not known. We may assume that many of them belong to the Galactic disk, that Population I stars dominate, and that they have a range of metallicities. Presumably the metallicity of these stars is comparatively high and may reach values up to solar. Our old, metal-poor Population II subsample and our more metal-rich Population I subsample allow us to empirically assess a possible impact of metallicity on photometric transformations. Here our calculations involve only *BVRI* (equations 1 to 4 and 6 to 8). For equation 5, a distinction between metal-poor and metal-rich stars was not possible because of the lack of U-band photometry. This is unfortunate since colors including U or u are particularly sensitive to stellar parameters including metallicity (see, e.g., Grebel & Roberts (1995); Lenz et al. (1998); Helmi et al. (2003)).

In Table 4 the resulting equations are listed. The resulting linear relations are plotted in Fig. 5. While the metal-rich stars are distributed fairly evenly across a wide range of colors, the metal-poor stars are concentrated within a fairly small range of colors corresponding mainly to the locus of the red giant branch. There are no metal-poor stars in our Population II sample with colors redder than $(V - R) = 0.93$. In the diagrams including $(R - I)$ the locus of the Population I stars is shifted towards somewhat bluer $(r - i)$ and $(r - z)$ colors as compared to the Population II stars. The coefficients of the linear transform-

Table 3. Coefficients of the 'global' transformations between *UBVRI* and *ugriz* (equations 1–8)

Color	Color Term	Zeropoint	Range
$g - V$	$(0.630 \pm 0.002)(B - V)$	$-(0.124 \pm 0.002)$	
$r - i$	$(1.007 \pm 0.005)(R - I)$	$-(0.236 \pm 0.003)$	
$r - z$	$(1.584 \pm 0.008)(R - I)$	$-(0.386 \pm 0.005)$	
$r - R$	$(0.267 \pm 0.005)(V - R)$	$+(0.088 \pm 0.003)$	$V - R \leq 0.93$
$r - R$	$(0.77 \pm 0.04)(V - R)$	$-(0.37 \pm 0.04)$	$V - R > 0.93$
$u - g$	$(0.750 \pm 0.050)(U - B) + (0.770 \pm 0.070)(B - V)$	$+(0.720 \pm 0.040)$	
$g - B$	$-(0.370 \pm 0.002)(B - V)$	$-(0.124 \pm 0.002)$	
$g - r$	$(1.646 \pm 0.008)(V - R)$	$-(0.139 \pm 0.004)$	
$i - I$	$(0.247 \pm 0.003)(R - I)$	$+(0.329 \pm 0.002)$	

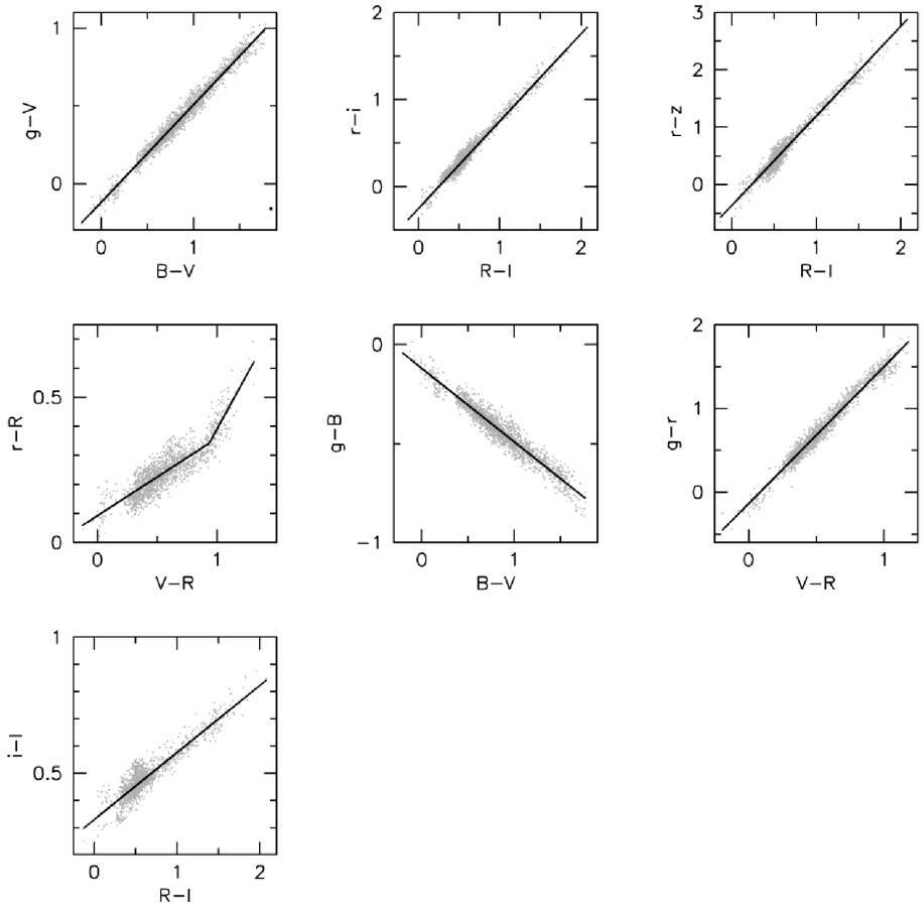

Fig. 3. The 'global' transformations between *UBVRI* and *ugriz*. The solid black line is the best-fi t relation. Its coefficients are listed in Table 3.

ation relations (solid lines in Fig. 5) result in slightly different slopes for metal-rich and metal-poor stars. At the main stellar locus, these deviations are less than the observed scatter in the colors of the stars in the two samples. Owing to the large scatter in the $(r - R)$,$(V - R)$ and $(i - I)$,$(R - I)$ diagrams, little can be said about possible trends here.

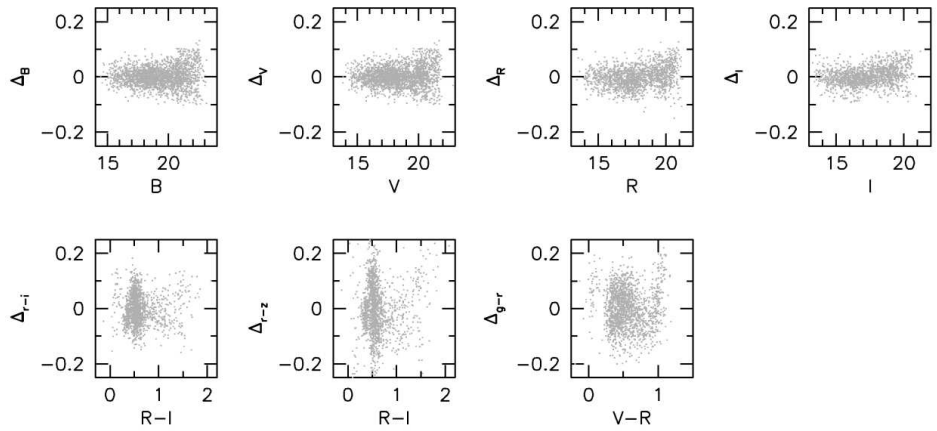

Fig. 4. The deviations of the measured magnitude and color values from the calculated values is shown, using the notation $\Delta_{\rm magnitude}$ = (magnitude)$_{measured}$ − (magnitude)$_{calculated}$. For the magnitudes B, V, and R the deviations are smaller than for the three colors $(r-i)$, $(r-z)$, and $(g-r)$.

Table 4. Metallicity-dependent transformations between *BVRI* and *griz* for metal-poor Population II and more metal-rich Population I stars.

Color	Color Term	Zeropoint	Validity
$g-V$	$(0.634 \pm 0.002)\,(B-V)$	$-(0.127 \pm 0.002)$	Population I
$g-V$	$(0.596 \pm 0.009)\,(B-V)$	$-(0.148 \pm 0.007)$	metal-poor Population II
$r-i$	$(0.988 \pm 0.006)\,(R-I)$	$-(0.221 \pm 0.004)$	Population I
$r-i$	$(1.06 \pm 0.02)\,(R-I)$	$-(0.30 \pm 0.01)$	metal-poor Population II
$r-z$	$(1.568 \pm 0.009)\,(R-I)$	$-(0.370 \pm 0.006)$	Population I
$r-z$	$(1.60 \pm 0.06)\,(R-I)$	$-(0.46 \pm 0.03)$	metal-poor Population II
$r-R$	$(0.275 \pm 0.006)\,(V-R)$	$+(0.086 \pm 0.004)$	$V-R \leq 0.93$; Population I
$r-R$	$(0.71 \pm 0.05)\,(V-R)$	$-(0.31 \pm 0.05)$	$V-R > 0.93$; Population I
$r-R$	$(0.34 \pm 0.02)\,(V-R)$	$+(0.015 \pm 0.008)$	$V-R \leq 0.93$; metal-poor Population II
$g-B$	$-(0.366 \pm 0.002)\,(B-V)$	$-(0.126 \pm 0.002)$	Population I
$g-B$	$-(0.401 \pm 0.009)\,(B-V)$	$-(0.145 \pm 0.006)$	metal-poor Population II
$g-r$	$(1.599 \pm 0.009)\,(V-R)$	$-(0.106 \pm 0.006)$	Population I
$g-r$	$(1.72 \pm 0.02)\,(V-R)$	$-(0.198 \pm 0.007)$	metal-poor Population II
$i-I$	$(0.251 \pm 0.003)\,(R-I)$	$+(0.325 \pm 0.002)$	Population I
$i-I$	$(0.21 \pm 0.02)\,(R-I)$	$+(0.34 \pm 0.01)$	metal-poor Population II

3.1.3. Comparison between our transformations and earlier work

We compared our 'global' transformations with transformations published by Fukugita et al. (1996), Smith et al. (2002) and Karaali et al. (2005). Fukugita et al. (1996) used synthetic magnitudes from the spectrophotometric atlases of Gunn & Stryker (1983) and of Oke (1990) for their transformations. Smith et al. (2002) presented transformations based on actually measured magnitudes of 158 SDSS standard stars. Their measurements were not done with the 2.5-m SDSS telescope, but with the 1.0-m telescope at the US Naval Observatory, Flagstaff Station. Karaali et al. (2005) were the first to do transformations depending on two colors. For their transformations they used 251 stars of Landolt (1992) for the *UBV* data and data from the CASU INT Wide Field Survey measured in filters close to the SDSS *ugr* passbands. In Fig. 6 the color-color plots show our transformation relations, which are based directly on the 2.5-m SDSS data, in comparison with the previously published transformations listed above.

As Fig. 6 demonstrates, for the $(B-V)$ transformation (upper left panel and equation 1) the *earlier* transformations lie below our star distribution and have a slightly different slope. For the $(R-I)$ transformation in equation 2 (upper right panel) our data do not support a change of slope for red colors as suggested in the previous studies. The distribution gets broader for $R-I > 1.15$, and the Fukugita et al. (1996) and Smith et al. (2002) transformations represent the upper half of the distribution whereas our fit reproduces the average of the stellar locus. For equation 3 (lower left panel) the earlier studies and our work show close agreement. Transformations for $(u-g)$ (equation 5) were calculated by Smith et al. (2002), Karaali et al.

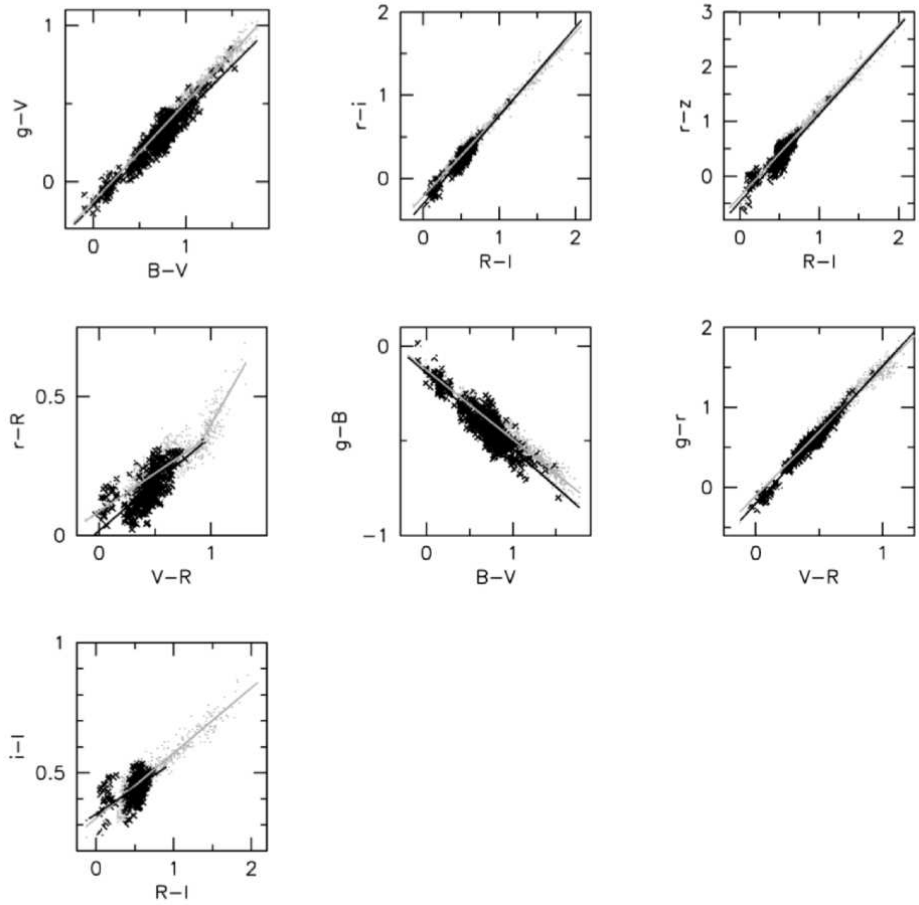

Fig. 5. The metallicity-dependent transformations. The solid black line is the fit for metal-poor Population II stars (black dots). The solid gray line is fit for the Population I stars (gray dots). The coefficients of the best-fit curves are given in Table 4.

(2005), and by us. Smith et al.'s equation differs from the others because it only depends on one color. The lower right diagram in Fig. 6 shows the deviation between the measured $(u-g)$ color and the calculated $(u-g)$ color. The one-color transformations by Smith et al. do not reproduce the colors of the combined Landolt and Stetson samples very well. The transformation by Karaali et al. resembles our result in spite of the somewhat different filter–telescope combinations.

3.2. Transformations between SDSS and RGU Photometry

For the transformation between the *RGU* system and the SDSS *ugriz* system we defined the following three equations:

$$U - G = a_1\,(u-g) + b_1 \quad (9)$$

$$G - R = a_2\,(g-r) + b_2 \quad (10)$$

$$G = a_3\,g + b_3 \quad (11)$$

The stars of our SDSS–*RGU* sample show a relatively large scatter in the color planes. One of the reasons for the scatter is the lower photometric accuracy of the photographic data as compared to modern CCD data, namely typical internal uncertainties of $\sigma_G = 0.05$, $\sigma_{G-R} = 0.07$, and $\sigma_{U-G} = 0.08$ (Buser et al. 1998). Some of our 775 common stars lie far off the broad, mean stellar loci. Since the resolution of the photographic data is relatively low, these deviant points are most likely false matches or blends in the photographic photometry. We thus removed them from our sample before we calculated the transformation relations. For this set of transformations we used the same procedure as before. The coefficients are listed in Table 5.

In Fig. 7 in the upper three panels the distribution of the stars in the color planes is shown, and the calculated transform-

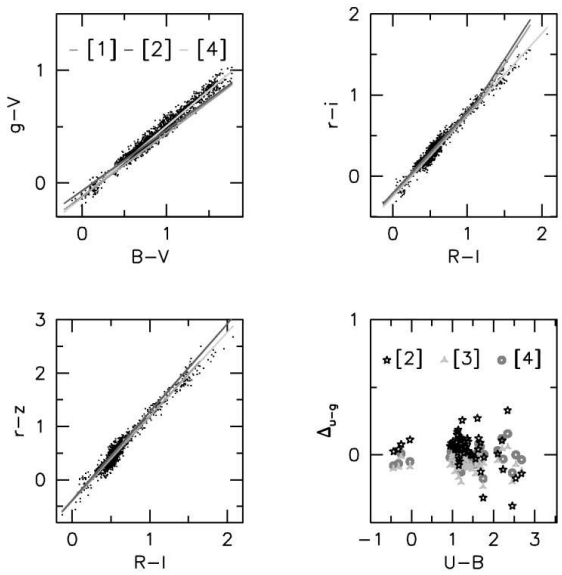

Fig. 6. Comparison of our transformations [4] with the transformations by Fukugita et al. (1996) [1], Smith et al. (2002) [2], and Karaali et al. (2005) [3]. The black dots in the first three panels represent the entire star sample described in Section 3.1.1. The fourth panel shows the deviations between the measured and the calculated $(u - g)$ color.

Table 5. Coefficients of the transformations between *ugriz* and *RGU* (equations 9–11)

Color	Color Term	Zeropoint
$U - G$	$(0.95 \pm 0.01)(u - g)$	$+0.16 \pm 0.02$
$G - R$	$(1.07 \pm 0.02)(g - r)$	$+0.64 \pm 0.02$
G	$(0.989 \pm 0.005)g$	00.37 ± 0.08

ations are plotted as straight lines. Given the larger scatter, it is not surprising that the uncertainties of the coefficients are now larger than for the *UBVRI* transformations. Moreover, the stellar data exhibit some wiggles, which we attribute to a nonlinear response of the photographic plates used in the Basel survey. Especially for the $(u - g)$ transformation the nonlinearity appears to be a problem. We investigated whether we could improve the transformation relations by making them dependent on two color terms instead of one, but this yielded no noticeable improvement.

4. Discussion

We presented empirical color transformations for the conversion of the SDSS *ugriz* photometric system into the Johnson-Cousins *UBVRI* system and into Becker's *RGU* system, respectively. These are the first transformations between the SDSS and the Becker system, whereas several earlier transformations between variants of the SDSS and of the Johnson-Cousins system have been published. For the Johnson-Cousins conversions, the novelty of our approach lies in the use of actual SDSS data obtained with the 2.5-m SDSS telescope at Apache Point Observatory and the use of well-defined Johnson-Cousins standard stars taken from the lists of Landolt (1992) and Stetson (2000). For all transformations linear relations were found to be sufficient, with a slope change in transformations involving $(V - R)$.

A comparison with previously published transformations shows that they qualitatively reproduce our transformations, but that they show systematic differences that may amount to $\sim$ 0.1 mag. This is due to the fact that the earlier transformations were either done with data that used other filter–detector–telescope combinations than that of the actual 2.5-m SDSS telescope and therefore differ intrinsically from the actual SDSS data, or that the data are based on early versions of the SDSS photometry catalogs before the SDSS photometry was in its final form, or that non-standard Johnson-Cousins data were used.

For conversions between the SDSS and the Johnson-Cousins systems, we tested the transformations for a possible metallicity dependence. Some of the Stetson standard stars lie in a field centered on the Draco dwarf spheroidal galaxy or on metal-poor (~ -2.0 dex) globular clusters. Most of the stars

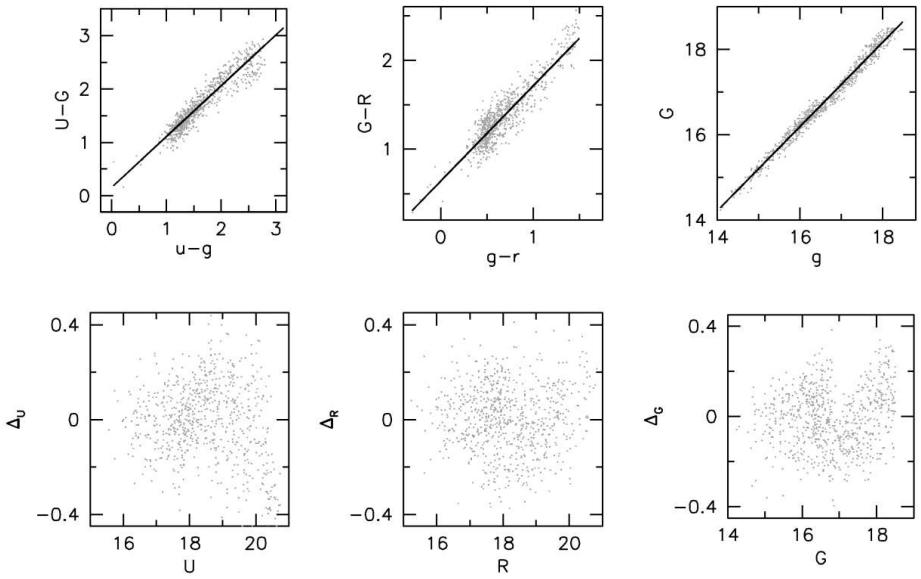

Fig. 7. The transformations between SDSS *ugr* and Becker's *RGU* system in the upper row. In the lower three panels the deviations of the measured magnitude values from the calculated values is shown.

in these fi elds are Population II stars and have much lower metallicities than the majority of the stars in Landolt's equatorial standard fi elds, where Population I stars dominate. The latter sample necessarily comprises stars with a range of ages and abundances, while our Population II sample is essentially limited to very old and very metal-poor stars. The calculated coefficients for the metal-poor stars result in slightly different slopes as compared to the more metal-rich stars, which affect very blue and very red stars most. Although our metallicity differentiation is quite crude, there does seem to be a slight dependence of the transformations on the metallicity. A more accurate separation into metal-rich and metal-poor stars – ideally aided by spectroscopically measured stellar abundances – is needed to fully evaluate the magnitude of this trend.

Acknowledgements. We acknowledge support by the Swiss National Science Foundation through grant 200020-105260 and 200020-105535.

Funding for the SDSS and SDSS-II has been provided by the Alfred P. Sloan Foundation, the Participating Institutions, the National Science Foundation, the U.S. Department of Energy, the National Aeronautics and Space Administration, the Japanese Monbukagakusho, the Max Planck Society, and the Higher Education Funding Council for England. The SDSS Web Site is http://www.sdss.org/.

The SDSS is managed by the Astrophysical Research Consortium for the Participating Institutions. The Participating Institutions are the American Museum of Natural History, Astrophysical Institute Potsdam, University of Basel, Cambridge University, Case Western Reserve University, University of Chicago, Drexel University, Fermilab, the Institute for Advanced Study, the Japan Participation Group, Johns Hopkins University, the Joint Institute for Nuclear Astrophysics, the Kavli Institute for Particle Astrophysics and Cosmology, the Korean Scientist Group, the Chinese Academy of Sciences (LAMOST), Los Alamos National Laboratory, the Max-Planck-Institute for Astronomy (MPIA), the Max-Planck-Institute for Astrophysics (MPA), New Mexico State University, Ohio State University, University of Pittsburgh, University of Portsmouth, Princeton University, the United States Naval Observatory, and the University of Washington.

This research has made use of NASA's Astrophysics Data System Bibliographic Services.

References

Abazajian, K., et al. 2003, AJ, 126, 2081
Abazajian, K., et al. 2004, AJ, 128, 502
Abazajian, K., et al. 2005, AJ, 129, 1755
Adelman-McCarthy, J. K., et al. 2006, ApJS, 162, 38
Becker, W. 1946, Ver¨offentlichungen der Universit¨ats-Sternwarte zu G¨ottingen, 5, 159
Bell, R. A. 1972, MNRAS, 159, 349
Buser, R. 1978a, A&A, 62, 411
Buser, R. 1978b, A&A, 62, 425
Buser, R. & K¨aser, U. 1985, A&A, 145, 1
Buser, R., & Fenkart, R. P. 1990, A&A, 239, 243
Buser, R., Rong, J., & Karaali, S. 1998, A&A, 331, 934
Buser, R., Rong, J., & Karaali, S. 1999, A&A, 348, 98
Chen, B., et al. 2001, ApJ, 553, 184
Cousins, A. W. J. 1976, MNASSA, 35, 70
Epchtein, N., et al. 1999, A&A, 349, 236
Fukugita, M., Ichikawa, T., Gunn, J. E., et al. 1996, AJ, 111, 1748

Girardi, L., Grebel, E. K., Odenkirchen, M. & Chiosi, C. 2004, A&A, 422, 205
Grebel, E. K. 2001, Reviews of Modern Astronomy, 14, 223
Grebel, E. K., & Roberts, W. J. 1995, A&AS, 109, 293
Grebel, E. K., & Gallagher, J. S., III 2004, ApJ, 610, L89
Grebel, E. K., Gallagher, J. S., III, & Harbeck, D. 2003, AJ, 125, 1926
Gunn, J. E. & Stryker, L. L. 1983, ApJS, 52, 121
Gunn, J. E., et al. 1998, AJ, 116, 3040
Gunn, J. E., et al. 2006, AJ, 131, 2332
Harris, W. E. 1996, AJ, 112, 1487
Helmi, A., et al. 2003, ApJ, 586, 195
Johnson, H. L. & Morgan, W. W. 1953, ApJ, 117, 313
Juric, M., et al. 2005, submitted (astro-ph/0510520)
Karaali, S., Bilir, S., & Tunç el, S. 2005, PASA, 22, 24
Koch, A., Odenkirchen, M., Grebel, E. K., & Caldwell, J. A. R. 2004a, AN, 325, 299
Koch, A., Grebel, E. K., Odenkirchen, M., Mart´ınez-Delgado, D., & Caldwell, J. A. R. 2004b, AJ, 128, 2274
Landolt, A. U. 1992, AJ, 104, 340
Lenz, D. D., Newberg, J., Rosner, R., Richards, G. T., & Stoughton, C. 1998, ApJS, 119, 121
Lupton, R., Gunn, J. E., Ivezi´c, Z., Knapp, G. R., Kent, S., & Yasuda, N. 2001, in ASP Conf. Ser. 238, Astronomical Data Analysis Software and Systems X, eds. F. R. Harnden, Jr., F. A. Primini, and H. E. Payne (San Francisco: ASP), 269
Odenkirchen, M., et al. 2001, AJ, 122, 2538
Oke, J. B. 1990, AJ, 99, 1621
Rave, H. A., Zhao, C., Newberg, H. J., Yanny, B., Schneider, D. P., Brinkman, J., & Lamb, D. Q. 2003, ApJS, 145, 245
Skrutskie, M. F., et al. 2006, AJ, 131, 1163
Smith, J. A., Tucker, D. L., Kent, S., et al. 2002, AJ, 123, 2121
Stoughton, C., et al. 2002, AJ, 123, 485
Steinlin, U. W. 1968a, in IAU Symp 50: Spectral Classifi cation and Multicolour Photometry
Steinlin, U. W. 1968b, Z. Astrophys. 69, 276
Stetson, P. B. 2000, PASP, 112, 925
Thuan, T. X. & Gunn, J. E. 1976, PASP, 88, 543
Udalski, A., Szymanski, M., Kubiak, M., Pietrzynski, G., Wozniak, P., & Zebrun, K. 1998, AcA, 48, 147
Udalski, A., Szymanski, M., Kubiak, M., Pietrzynski, G., Soszynski, I., Wozniak, P., & Zebrun, K. 2000, AcA, 50, 307
Udalski, A., Szymanski, M., Kubiak, M., Pietrzynski, G., Soszynski, I., Wozniak, P., Zebrun, K., Szewczyk, O., & Wyrzykowski, L. 2002, AcA, 52, 217
York, D. G., Adelman, J., Anderson, J. E., et al. 2000, AJ, 120, 1579
Zaritsky, D., Harris, J., Thompson, I. B., Grebel, E. K., & Massey, P. 2002, AJ, 123, 855
Zaritsky, D., Harris, J., Thompson, I. B., & Grebel, E. K. 2004, AJ, 128, 1606

Astronomy & Astrophysics manuscript no. Westera
December 8, 2006

IMF Effects on the Colour Evolution of Disk Galaxies

P. Westera[1], M. Samland[1], S. J. Kautsch[1], R. Buser[1], and K. Ammon[1]

Astronomical Institute. Department of Physics and Astronomy, University of Basel, Venusstr. 7, CH-4102 Binningen, Switzerland e-mail: westera@astro.unibas.ch, buser@astro.unibas.ch

Received; Accepted

ABSTRACT

Aims. In this work, we want to find out if the IMF can be determined from colour images, integrated colours, or mass-to-light ratios, especially at high redshift, where galaxies cannot be resolved into individual stars, which would enable us to investigate dependencies of the IMF on cosmological epoch.
Methods. We use chemo-dynamical models to investigate the influence of the Initial Mass Function (IMF) on the evolution of a Milky Way-type disk galaxy, in particular of its colours.
Results. We find that the effect of the IMF on the internal gas absorption is larger than its effect on the light from the stellar content. However, the two effects work in the opposite sense: An IMF with more high mass stars leads to brighter and bluer star-light, but also to more interstellar dust and thus to more absorption, causing a kind of "IMF degeneracy". The most likely wavelength region in which to detect IMF effects is the infrared (i. e., *JHK*). We also provide photometric absorption and inclination corrections in the SDSS *ugriz* and the HST WFPC2 and NICMOS systems.

Key words. Stars: luminosity function, mass function – Galaxies: evolution – Galaxies: stellar content – Galaxies: ISM – dust, extinction – Galaxies: photometry

1. Introduction

The determination of the Initial Mass Function (IMF) of stellar populations and the detection of its possible variations are long lasting questions in astronomy. The first IMF, a single-slope power law, was published by Salpeter (1955) based on stars in the solar neighbourhood, and is still occasionally used in stellar population studies. However, it has been known since Miller & Scalo's (1979) milestone paper on the subject that the IMF flattens at low masses. In the meantime, this finding has been confirmed in numerous works (Scalo (1986), Kroupa et al. (1993), Gould et al. (1997), Reid & Gizis (1997), Gould et al. (1998), Chabrier (2001), Piotto & Zoccali (1999), Zoccali (2000), and others). Recently, Chabrier (2002) also found indications of a turn-over in the brown dwarfs regime. For recent reviews see Kroupa (2002), Chabrier (2003).
An indication of the importance of the subject is the number of IMFs produced over the years: Salpeter (1955), Miller & Scalo (1979), Lequeux (1979), Kennicutt (1983), Scalo (1986), Ferraro et al. (1997), Piotto et al. (1997), Scalo (1998), Carigi et al. (1999), Kroupa (2001) (universal and present day IMFs), Chabrier (2001), and others.
Another important issue are variations of the IMF with the star forming conditions (pressure, density, metallicity of the forming cloud, etc.). Although such variations are predicted, only little evidence of them has been found so far (Kroupa (2001)). We expect especially at high redshift to see differences from the present-day IMF, as the lower metallicity of the star-forming clouds is expected to cause higher temperatures and thereby higher average stellar masses (Larson (1998)). Unfortunately, high redshift galaxies are too faint to be resolved into individual stars, which makes it difficult, if not impossible, to determine their IMFs. Therefore, it would be interesting to know if other, more global observables, such as integrated spectra or colours, can also yield some information about the stellar IMF. The IMF influences the light of a galaxy not only directly through the contributions of the stars of different (birth) masses, but also indirectly by affecting the entire evolution. The fraction of high mass stars determines the gas- and "dust"-yield of the partial populations and, hence, the star formation history (SFH) from the second stellar generation on, as well as the gas absorption. For these reasons, we hope to be able to see signatures of the IMF even in the integrated light of galaxies.
For this purpose, Portinari et al. (2004) studied the influence of the IMF on the (*I* band) mass-to-light (M/L) ratio of galactic disks (Sbc/Sc) using chemo-photometric models and adopting 6 different IMFs, including the Salpeter (1955) and Kroupa (1998) IMFs, which is interesting in connection with this work, because in the present work, we also compare models us-

Send offprint requests to: P. Westera

ing the Salpeter IMF and a more recent IMF by Kroupa. For each IMF, they calculate chemical evolution models with infall, metallicity gradients, and SFHs representative of late-type spiral disks (but not varying with the IMF). They find that so-called "bottom-light" IMFs (i. e., with less low-mass stars than Salpeter) yield low M/L ratios ($\sim 0.7 - 1$), in agreement with various dynamical arguments and cosmological simulations. However, they calculate only stellar M/L ratios without taking into account gas absorption.

In this work, we use fully consistent 3-dimensional chemo-dynamical models by M. Samland to calculate the evolution of two galaxies, with the same boundary conditions (cosmology, gas infall history, etc.), but adopting different IMFs: the Salpeter and the Kroupa (2001) "universal" IMFs. Although these are not the most state-of-the-art IMFs available, they were chosen because of their clear differences in their low-to-high-mass stars ratios, so any IMF-induced differences should appear clearly. The spectra and (Hubble Space Telescope (HST), SLOAN Digital Sky Survey (SDSS) and Washington) colour images and integrated colours were then calculated using the same method as in Westera et al. (2002). An important advantage of our programme is that we can disentangle different effects on the spectral properties of a model galaxy, such as of internal absorption, by artificially blinding these contributions out, and then recalculating the spectral properties.

The outline of this paper is as follows: Section 2 describes the physics and properties of the two chemo-dynamical models, and in Section 3, it is explained how the spectral properties of these models were calculated. Section 5 contains the results, and a comparison of the model colours with SDSS data, which were extracted in the way described in Section 4. In Section 6, we draw some conclusions and give a brief summary.

2. The chemo-dynamical models

The models simulate the formation of a $8 \cdot 10^{11} M_\odot$ galaxy leaving all parameters, except for the IMF, the same for both models. The models are for a Milky Way-type galaxy, but we expect our results (IMF effects) to be similar for other disk galaxies, as the properties, which are important for the colour evolution (star formation history, gas feedback and enrichment, etc.) probably depend in a similar way on the IMF for different types of disk galaxies.

The two models have different IMFs implemented, a Salpeter (1955) IMF, which is a one-segment potential law with an exponent $\alpha = 2.35$ in the mass range from 0.1 to 50 $M_\odot$, and a Kroupa "universal" (also called "standard" or "canonical") IMF (Eq. 2 of Kroupa (2001)), a two-segment law with $\alpha = 1.3$ from 0.08 to 0.5 $M_\odot$ and $\alpha = 2.3$ from 0.5 to 50 $M_\odot$, respectively, in order to investigate the influence of the IMF shape on the formation processes of a disk galaxy. The main difference between the two IMFs lies in the high-to-low mass stars ratio, in the sense that a population with a Kroupa IMF has more high-mass stars than a population of the same mass, but with a Salpeter IMF.

The 3-dimensional chemo-dynamical models are of the same type as those described in Samland & Gerhard (2003); so here, we only summarise very briefly the main properties, but take a more detailed look at the few quantities that will become interesting for the interpretation in Subsection 5: the (stellar) mass surface density, the stellar particle ages, the stellar metallicities, and the gas density and metallicity.

The models take into account initial cosmological and environmental conditions, but also internal feedback processes, such as heating by supernovae, dissipation, radiative cooling,

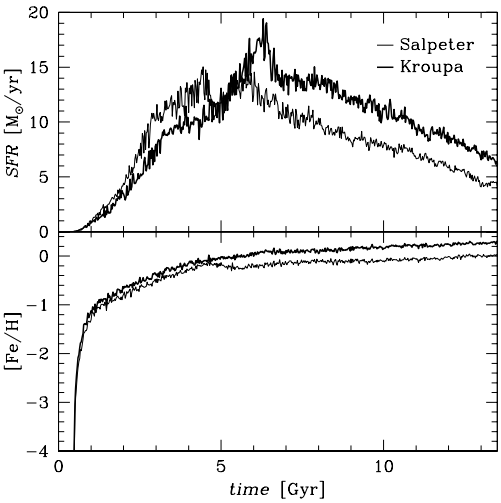

Fig. 1. Star formation histories of the Salpeter (thin) and Kroupa (thick) models. Top panel: star formation rates, bottom panel: average star formation metallicities.

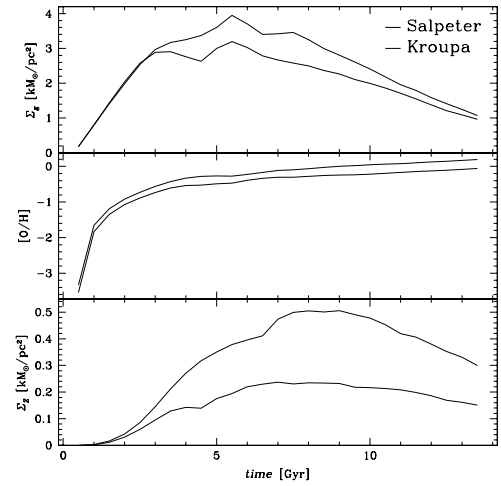

Fig. 2. Average gas column densities (top panel), gas metallicities (middle panel), and "dust" gas column densities, that is $Z_g * \Sigma_g$, of the Salpeter (thin) and Kroupa (thick) models.

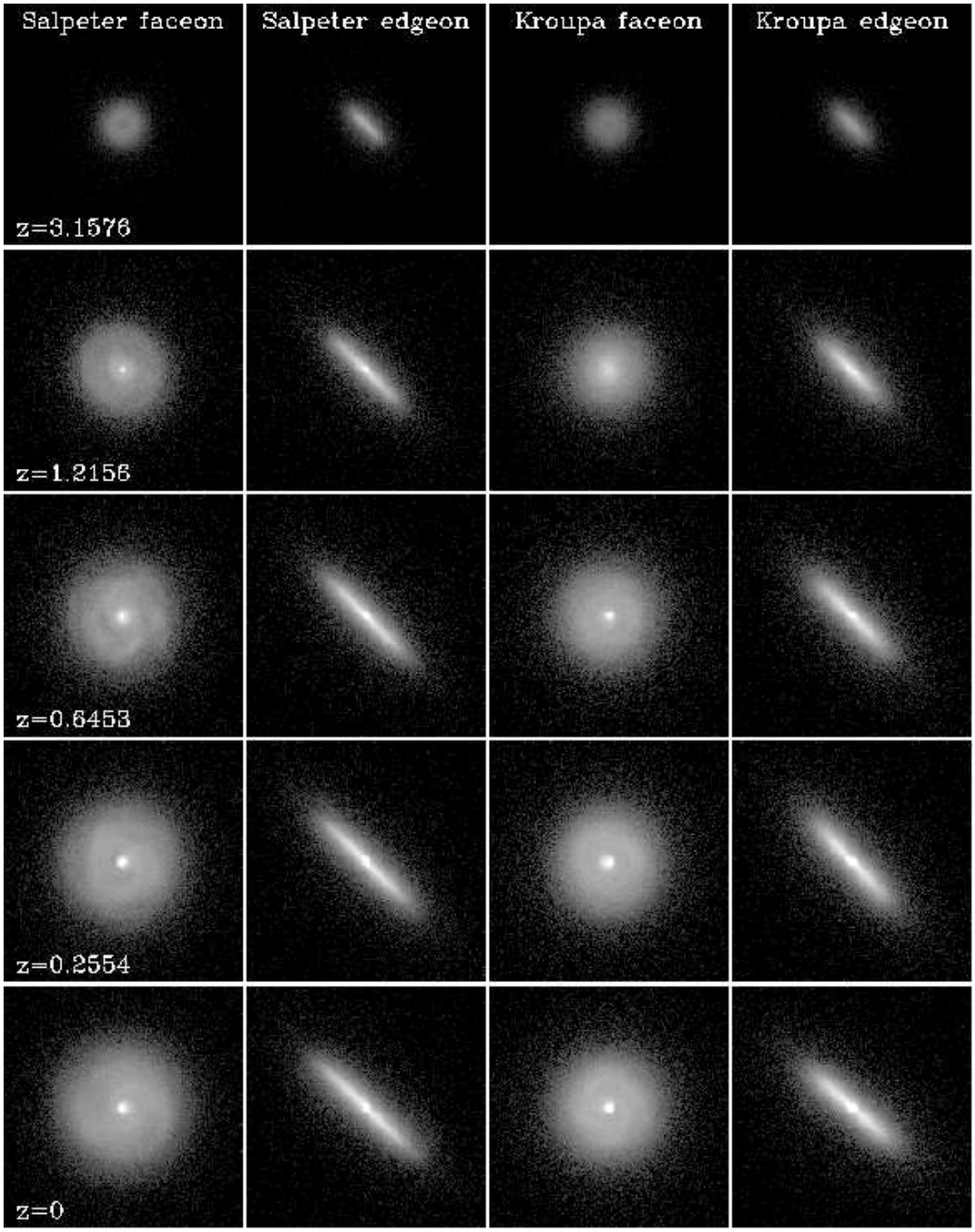

Fig. 3. Stellar mass distributions of the Salpeter and Kroupa models at different redshifts/ages (the redshifts correspond to ages of 2, 5, 7.5, 10.5, and 13.5 Gyr) seen face-on and edge-on. The colour scale is logarithmic and covers four orders of magnitudes. The images show an area of 40x40 kpc.

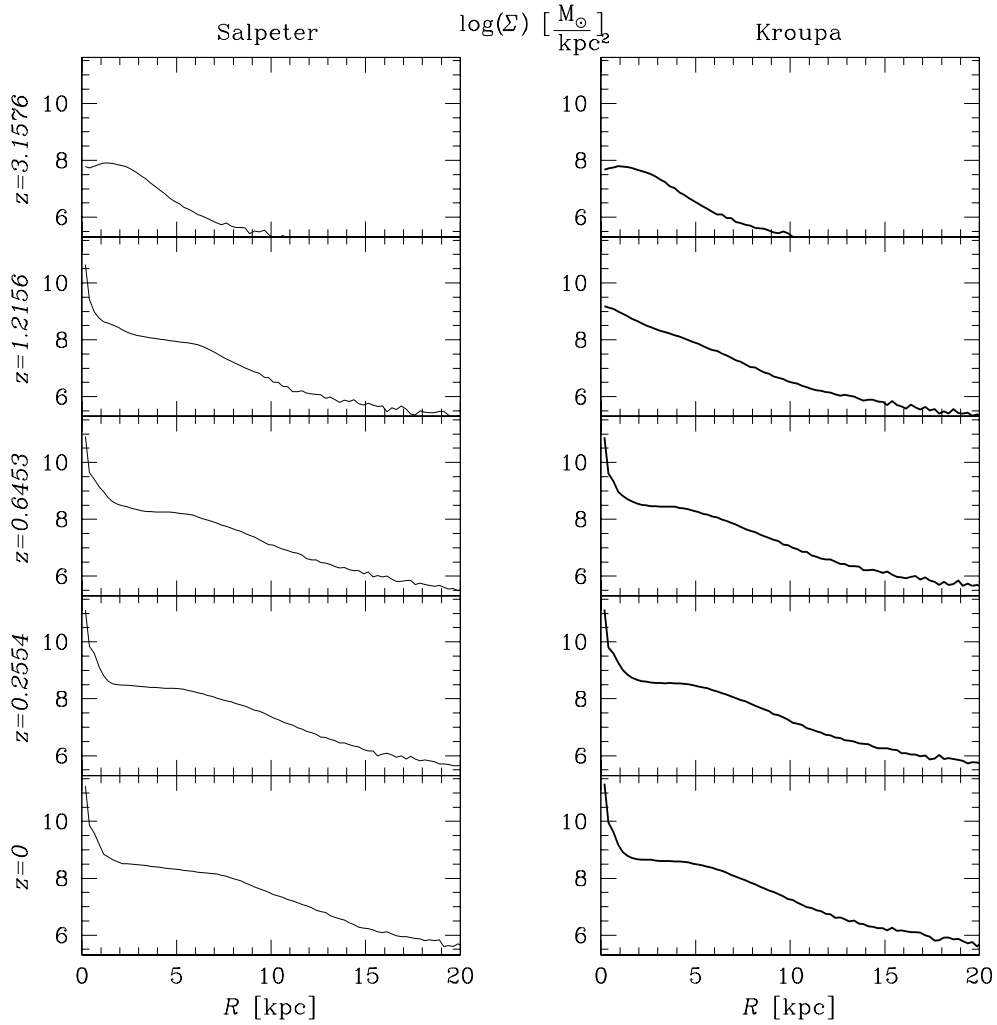

Fig. 4. Stellar (face-on) mass profiles of the Salpeter and Kroupa models at different redshifts/ages. The profiles correspond to the first and third columns of Fig 3.

nucleosynthesis, and in- and outflows. Since they are fully self-consistent models, they include dark matter, stars and the different phases of the interstellar medium (ISM), as well as the processes ("chemistry") which connect the ISM and the stars. More quantitatively, the models assume a flat Universe with the following cosmological parameters: $H_0 = 70\frac{km}{s \cdot Mpc}$, $\Omega_0 = 0.3$, $\Omega_\Lambda = 0.7$, and $\frac{M_{Bary}}{M_{Dark}} = \frac{1}{8}$. The total spin parameter of the model galaxies was chosen to be $\lambda = 0.05$ (Barnes & Efstathiou (1987)), and the angular momentum distribution was calculated according to Bullock et al. (2001) using $\mu = 10$. We follow the evolution from $z = 9.5$ (corresponding in this cosmology to an age of the Universe of 0.5 Gyr) until $z = 0$ (13.5 Gyr).
The models are characterised by a slowly growing dark halo and a continuous gas infall following the universal mass accretion histories found by van den Bosch (2002) and Wechsler et al. (2002) using a formation redshift $z_{Formation}$ of 4.0 and a total mass M of $8 \cdot 10^{11} M_\odot$. As the gas infall continues until the present day, we expect for both models a mixture of stellar populations of many different ages.

However, the two models do not show the same SFH. As the Kroupa IMF features more high mass stars, star formation will result in a stronger heating by stellar radiation, more stellar

wind, more feedback from supernovae I and II and thus a higher mass return and metal yield. As a result, the Kroupa model has a lower SFR than the Salpeter model for the first ∼ 5 Gyr, due to the heating from the stellar winds from the first generations. Afterwards, that is after ∼ 5.5 Gyr, the Kroupa model has a higher SFR due to the larger available amount of gas (as seen in Fig. 2, top panel). After around 7.5 Gyr, this higher SFR has compensated for the lower SFR in the beginning, so from that point on the total stellar mass is higher in the Kroupa model galaxy. In the end (at 13.5 Gyr or redshift 0), the total stellar mass amounts to $1.07 \cdot 10^{11} M_{\odot}$ in the Salpeter model and to $1.25 \cdot 10^{11} M_{\odot}$ in the Kroupa model. The two SFRs can be studied in detail in Fig. 1 (top panel), from which can also be seen that the SFR remains significant until the present epoch, as expected from the gas infall history. The bottom panel shows the average star formation metallicity.

The average gas metallicities [O/H] of the models (shown in Fig. 2, middle panel) increase most steeply during the phases of maximum star formation. They start at [O/H] $\simeq -4$, and reach their present values of ~ -0.1 dex or $\sim +0.2$ dex at $z \simeq 1$. This higher gas metallicity of the Kroupa model, combined with the higher gas density (top panel of Fig. 2), causes the Kroupa model galaxy to contain about twice as much metals in the interstellar matter (ISM), or "dust", as the Salpeter galaxy, which can be seen in the bottom panel of Fig. 2.

The output quantities of interest (which are the input quantities for the programme which calculates the spectral properties) are the following, at each time step: a number of stellar particles, each with its spatial position, initial mass, age, and metallicity, as well as the gas density and metallicity on a 3-dimensional grid covering the galaxy out to where the gas density is negligible (100 kpc), as a function of time.

Fig. 3 shows the stellar mass distributions of the two models projected face-on and edge-on. Both models result in disk galaxies with weak spiral arms, whereas the Salpeter model produces a bulge 2 Gyrs sooner (at ∼ 4 Gyr) than the Kroupa model, which can be seen in the second row of Fig. 3 (z = 1.2156, which corresponds to 5 Gyr). In the Kroupa model (right two panels), the bulge is not yet present at this epoch, but in the Salpeter model (left two panels), it is. This can also be seen in the profiles (Fig. 4, second row). This delay in bulge formation in the Kroupa model is probably also due to stellar winds. As soon as the bulge appears in either model, we also see a plateau in the mass profiles at around 2 to 5 kpc. This is due to stellar winds from the bulge, which push out the gas from the inner disk (at 2 kpc) to a distance of 4 kpc, where Star Formation then takes place. It is not bar-induced as in the more massive galaxy studied by Samland & Gerhard (2003). The fact, that, in Fig. 3, the Kroupa model galaxy seems to have a thicker disk than the Salpeter one, is just a by-eye impression. We calculated the thick and thin disk scaleheights for both models as functions of time, but found no significant differences between the models.

3. From theoretical quantities to colours and spectra

To derive 2-dimensional colour images (HST (WFPC2 and NICMOS), SDSS *ugriz*, Washington $CNT1T2$, and other photometric systems) from the star and gas distributions of the galaxy models, we proceeded in the following way:

First, two libraries of simple stellar population (SSP) spectra were produced: one with a Salpeter IMF from 0.1 to 50 $M_{\odot}$, and one with a Kroupa IMF from 0.08 to 50 $M_{\odot}$, in accordance with the galaxy models. With the Bruzual and Charlot 2000 Galaxy Isochrone Spectral Synthesis Evolution Library (GISSEL) code (Charlot & Bruzual (1991), Bruzual & Charlot (1993), Bruzual & Charlot (2003)), integrated spectra (ISEDs) of populations were calculated for a grid of population parameters consisting of 7 metallicities ([Fe/H] = −2.252, −1.65, −0.65, −0.35, 0.09, 0.447, and 0.748) and 221 SSP ages ranging from 0 to 20 Gyr. As input, we used Padova 1994 isochrones (Fagotto et al. (1994), Girardi et al. (1996)). There exist more recent versions of the Padova isochrones, Padova 2000 (Girardi et al. (2000)), but there is some doubt as to whether these newer tracks produce better agreement with observed galaxy colours than the Padova 1994 models (Bruzual & Charlot (2003)). Furthermore, the Padova 1994 isochrones cover a wider range of metallicities. The spectral library used was the BaSeL 3.1 "WLBC 99" (Westera (2001), Westera et al. (2002)) stellar library. The spectra of this ISED library contain fluxes at 1221 wavelengths from 9.1 nm to 160 μm, comfortably covering the entire range where galaxy radiation from stars is significant. The GISSEL software also has a higher resolution stellar library implemented, STELIB, which has a resolution high enough to study spectral (absorption) lines (1Å in the relevant wavelength range), but, with 6900 flux points per spectrum, these spectra proved too large in terms of memory and CPU time to be included in our programme.

After choosing (through three angles) the viewing direction with respect to the galaxy principal plane, and the size (up to 320 × 320 pixels) and resolution for the "virtual CCD camera", the stellar particles are grouped into pixels. For each stellar particle, the spectrum is (geometrically, flux point by flux point) interpolated from the ISED library. For metallicities lower than the range covered by the library, the spectra for the lowest metallicity ([Fe/H] = −2.252) were used. This should not pose any problems, as trends of spectral properties with metallicity are expected to become weak below [Fe/H] = −2.0, and these lowest-metallicity stellar particles become negligible in number very soon. For SSPs of 50 Myr and younger, we added nebular emission to the spectra in the same way as described in Leitherer et al. (1999), and accordingly removed the flux below 912 Å. On the other hand, the emission of HII regions is not implemented. The inclusion of HII regions, as well as planetary nebulae and supernovae, will be one of the next steps in improving the programme.

Then, the spectra were reddened as follows, using the gas density and metallicity in the model to trace the three-dimensional distribution of dust: For each stellar particle, the metallicity-weighted gas density was integrated along the line of sight to

derive the absorption coefficient A_V according to Quillen & Yukita (2001):

$$A_V = \frac{1}{50\frac{M_\odot}{pc^2}} \int_{LOS} \rho_g(r) \left(\frac{Z(r)}{Z_\odot}\right) dr \ . \quad (1)$$

The spectrum of the stellar particle was then reddened using the extinction law of Fluks et al. (1994).

All the spectra of stellar particles from the same pixel were added up to give the integrated absolute spectrum of the pixel, which was then redshifted and dimmed using the redshift z from the models, and calculating the distance modulus $m - M$ according to Carroll et al. (1992):

$$m - M(z) = 5 \log\left(\frac{c}{H_0}(1+z) \int_0^z [(1+z')^2(1+\Omega_M z') - z'(2+z')\Omega_\Lambda]^{-1/2} dz'\right) + 25 \ . \quad (2)$$

We then corrected the spectra for Lyman line blanketing and Lyman continuum absorption by absorption systems at cosmological distances using the formulae given by Madau (1995) for QSO absorption systems. Finally, apparent HST (WFPC2 and NICMOS), SDSS *ugriz*, Washington $CNT1T2$ colours and magnitudes were calculated for each pixel through synthetic photometry. Other photometric systems, i. e. Johnson-Cousins *UBVRIJHKLM*, Strömgren *ubvy*, Kron *RI*, are also implemented in the programme, but we limited our study to the above-mentioned systems for memory - and CPU time reasons. Including more systems is unlikely to yield further discoveries, since the filter bands of those systems lie in the same wavelength range as the ones of the systems we used, and will thus most probably show the same behaviour with IMF (and other) variations. Furthermore, the HST and SDSS systems seemed most likely to allow extensive comparison with observational data.

At the same time, the absolute (rest frame) spectra and the apparent spectra of all the pixels were added up to derive the absolute and apparent integrated spectra of the galaxy. Examples of such integrated (intrinsic, that is unredshifted and all with the same distance modulus) spectra are shown in Fig. 5. The metallicity-dependent distribution of the stars and the spatially resolved treatment of the gas absorption are the most important for the spectra and colours.

On these integrated spectra, synthetic photometry was performed, too. For computer memory reasons, the spectra of individual pixels or stellar particles were not stored, so the final output quantities of the programme are:

1. a 2-dimensional colour image of the model galaxy, including the effect of internal absorption in intrinsic magnitudes of up to 320×320 pixels, as seen from a freely chosen angle,
2. the same image in apparent (redshifted and corrected for the distance modulus and Lyman line blanketing) magnitudes,
3. the integrated intrinsic spectrum of the entire galaxy plus integrated intrinsic colours and absolute magnitudes,
4. the integrated apparent spectrum of the entire galaxy plus integrated redshifted colours and apparent magnitudes.

Our programme also includes the possibility to account for Galactic foreground reddening. But since this option only makes sense for specific applications, where the foreground reddening is known, it was not used in this work.

These quantities were calculated for both the Salpeter IMF and the Kroupa IMF models, at ages from 0.5 Gyr (corresponding to $z = 9.5$, or 0.3 Gyr after the beginning of the simulation) to 13.5 Gyr (the present day) in steps of 0.5 Gyr, and from three different directions: face-on, inclined by 60°, henceforth called the diagonal view, and edge-on. The size of a pixel was chosen to be 0.25 kpc. Higher resolution would make no sense, as the galaxy model has a precision of only 0.37 kpc. The entire "camera" was chosen 320×320 pixels wide, thus representing a field of view of 80×80 kpc.

To identify absorption effects, the same photometric properties were calculated for both models without internal absorption. Thus, the differences between the regular models and these ones should reflect absorption effects, or the error in models that do not include internal absorption. These models will be called the absorptionless models, and will be used in Section 5.

4. Data Extraction

In order to test our models, we compare them to galaxy data from the Sloan Digital Sky Survey (SDSS) (York et al. (2000)), which offers a large sample of galaxies. The current volume of the SDSS is the Data Release 4 (DR4) which covers in the imaging mode about 180 million unique objects in an area of 6670 square degrees and 849,920 spectra within 4783 square degrees (Adelman-McCarthy et al. (2005)). We use the SDSS Batch Query Services[1] on the DR4 Galaxy Table View and SpecObj Table View. This web interface allows to perform queries on the available SDSS archives using the Structured Query Language (SQL). The Galaxy Table View contains optical parameters of all galaxies at the time of the data release. The spectral properties of the galaxies are given in the SpecObj Table View. We remove all objects which are flagged with one or more of the PhotoFlags as given in the Galaxy Table View: blended (object had multiple peaks detected within it); edge (object is too close to edge of frame of the survey); saturated (object contains saturated pixels); ellipfaint (not measured isophotal properties and incomplete profiles). These flags allow us to reject all objects near the survey borders and blended with spikes of nearby stars. As our model colours differ for the face-on and edge-on view (see Section 5), we extract two samples, one for either viewing direction.

For the edge-on sample, we adopt the query used by Kautsch et al. (2006) to collect a catalog of edge-on galaxies, wherein the axial ratio a/b is chosen to be > 3, a and b being the major and minor angular isophotal axes in the g band; the major axis a is chosen larger than 15 pixels (which corresponds to 5.94 arcsec) and colours in the ranges $-0.3 < g - r < 3$ mag and $-0.3 < r - i < 3$ mag, in order to exclude spurious objects and other artefacts. We limit the sample to a Petrosian magnitude[2]

[1] http://casjobs.sdss.org/CasJobs/default.aspx

[2] the Petrosian magnitudes are derived from the Petrosian flux using a circular aperture centered on every object. The advantage of

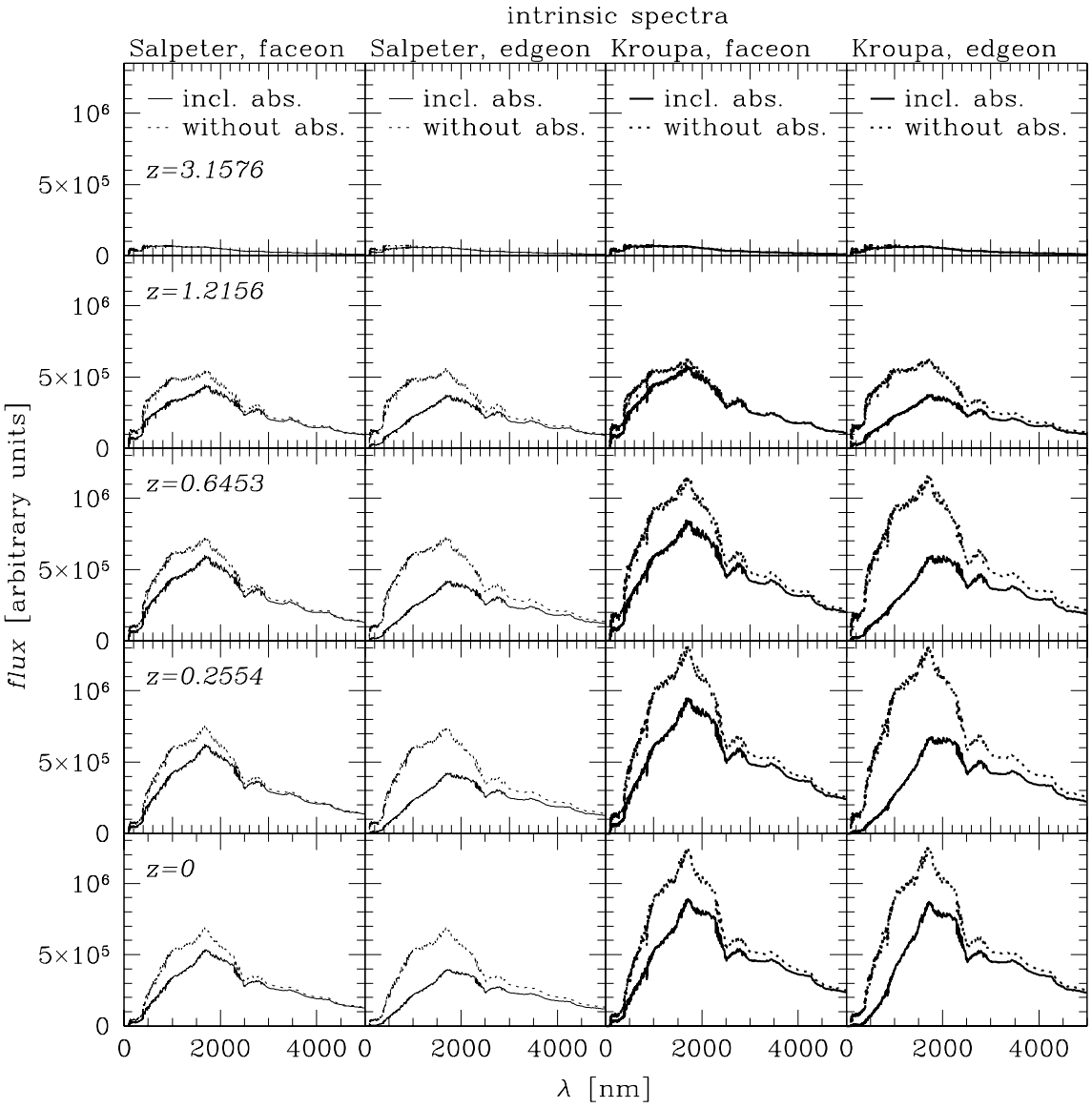

Fig. 5. Intrinsic spectra of the Salpeter (left two columns) - and Kroupa (right two columns) models at five different epochs (different rows), both face-on (columns 1 and 3) and edge-on (columns 2 and 4), and both without (dotted) and including (solid) absorption.

this method is that this allows an unbiased measurement of a constant fraction of the total galaxy light using the technique based on that of Petrosian (1976). For a detailed description of the Petrosian parameters used in the SDSS we refer to Blanton et al. (2001) and Yasuda et al. (2001).

in the g band of 20.

For the face-on sample, a/b is chosen to be smaller than 1.5, the isophotal major axis a is also > 15 pixels, and the colours again lie in the ranges $-0.3 < g-r < 3$ mag and $-0.3 < r-i < 3$ mag. Here the Petrosian g band magnitude is limited to 19 mag, since galaxies seen face-on appear brighter than the same ones

seen edge-on (see Section 5). Using these limiting magnitudes, the two samples contain a similar number of galaxies.

The following biases affect our selection: "Shredded galaxies," i. e., these galaxies are detected as two or more independent objects (this is found in particular for extended objects with substructure and diameters $\geqslant 1'$); galaxies with unusual colours caused by an AGN and/or dust. Due to these effects we lose less than 1% of the targets from the SDSS database as estimated from a by-eye-inspection of randomly selected subsamples.

Wrong classification can be the result of various causes: (i) "Inverse shredding", where objects arranged in chains are detected as a single object; (ii) bars or spiral arms in faint disks being classified as edge-on galaxies. However, we estimate that these effects affect about 2% of the targets only.

5. Results

In Fig. 6, we see the calculated intrinsic *urz* band images of the Salpeter and Kroupa model galaxies, both in the same magnitude scaling. The images confirm that the bulge forms later in the Kroupa model (at around 6 Gyr) than in the Salpeter model (∼4 Gyr), as mentioned in Section 2. Apart from that, the images of the models look extremely similar. In this section, we will explain why.

5.1. Intrinsic magnitudes and mass-to-light ratios

In Tables A.1 to A.4 are listed the intrinsic bolometric, *V* Johnson, SDSS *ugriz*, and HST (WFPC2 and NICMOS) magnitudes of the two models integrated over the full galaxies in the diagonal view. We calculated the Washington magnitudes as well, and they can also be calculated for other colour systems, such as Johnson-Cousins *UBVRIJHKLM*, Strömgren *ubvy*, and Kron *RI*. The evolution of the magnitudes show some oscillations around their mean tendencies, which are the result of shadowing of the bulge by dense streams of infalling molecular gas. They only show up in the diagonal view when absorption is included. One should keep in mind that this can be an additional source of scatter when looking at observed magnitudes and colours of galaxies.

In the following, most figures concerning magnitudes will show the SDSS *u* band and the HST NICMOS *K*222 band, and most figures concerning colours will show $u - g$ and $J110 - K222$, which are the bluest and reddest calculated magnitudes and colours, respectively, and therefore are the most illustrative of the range of possible effects on colours and magnitudes. For other passbands and colours, the trends will usually lie between the trends of the ones shown in the figures.

Tables B.1 to B.4 give the stellar mass-to-light ratios (M/L) of the two models both including and omitting absorption, in bolometric light, Johnson Vj, the SDSS *ugriz* system, and the HST NICMOS *JHK* system. They are shown in Fig. 7 in *u*, *r*, *i*, and *K*222 as a function of time since the Big Bang. We see that, from around 6 Gyrs on, the Kroupa model has M/Ls about one third lower than the Salpeter model. It is ∼ 0.5 mags brighter, due to its higher SFR (see Fig. 1). Unfortunately, when absorption is included, this effect is partly canceled out by the higher gas content of the Kroupa model to a level varying between 0 (*K*222) and 0.4 mags (*u*), which is probably undetectable. The effect in colour bands bluewards of *i* is, that the two models become indistinguishable, an unfortunate coincidence we call "IMF degeneracy". It is weakest in the *K*222 band, where the absorption is smaller and the difference between the Salpeter - and Kroupa models remains around ∼ 0.5 mags, leaving the difference in M/L unaltered, but even this will be difficult to measure.

The above-mentioned absorption effects vary with the viewing angle, as is illustrated for the Kroupa model in Fig. 8 (for the Salpeter model they look similar). It shows the *u* - and *K*222 evolution of the model in all angles, as well as the absorptionless model (which has the same intrinsic magnitudes viewed from any angle). The lower panels show the absorption effects on these magnitudes (that is the differences between the models with different viewing angles and their absorptionless counterparts). These differences translate into differences in magnitudes between the different inclinations. They amount to 1.5 mags in *u*, and still 0.5 mag in *K*222, which is more than the IMF effects. Nevertheless, it will be difficult to say something about the orientation of an unresolved galaxy by its intrinsic magnitude alone, since too many things can affect the total magnitude of a real distant galaxy, besides inclination.

5.2. Intrinsic colours

If IMF effects on magnitudes or Mass-to-light ratios are insignificant, suffering from a degeneracy, does the IMF manifest itself more strongly in the colours? In Fig. 9, top panel, we see the time evolution of $(u - g)_0$ and $(J110 - K222)_0$ of both the Salpeter (thick) - and the Kroupa (thin) models, including absorption (solid) and without (dashed). The bottom panel shows the differences in these colours between the two models, both including absorption (solid) and without (dashed). The thin dotted line shows zero level.

For the $(u - g)_0$ colour, we see the same conspiracy between SFR and absorption as before. The colour difference in unabsorbed starlight between the two models (bottom left panel dashed line), which was already very small from the beginning (below 0.1 mag), is even diminished by the absorption. In $(J110 - K222)_0$, on the other hand, the differences between the Salpeter - and the Kroupa models increase when absorption is taken into account, but they remain too small to be measured (only up to 0.2 mags). In colours made up of two magnitudes from widely separated wavelength regions, such as $(u - K222)_0$, they even reach 0.5 mags, but in relation to the larger variation of these colours, these differences are less expressive than the 0.2 mags in $(J - K)_0$.

In Fig. 10, we see the effect of reddening on the bluest and the reddest colours of our study, $(u - g)_0$ and $(J110 - K222)_0$, respectively. The top panels show the time evolution of these two colours for the Kroupa model in all three viewing angles, as well as the absorptionless case, which is the same for all viewing angles. The bottom panel shows the differences between the absorbed and the unabsorbed models in all three inclinations. Clearly, the absorption effects on the bluest colours are

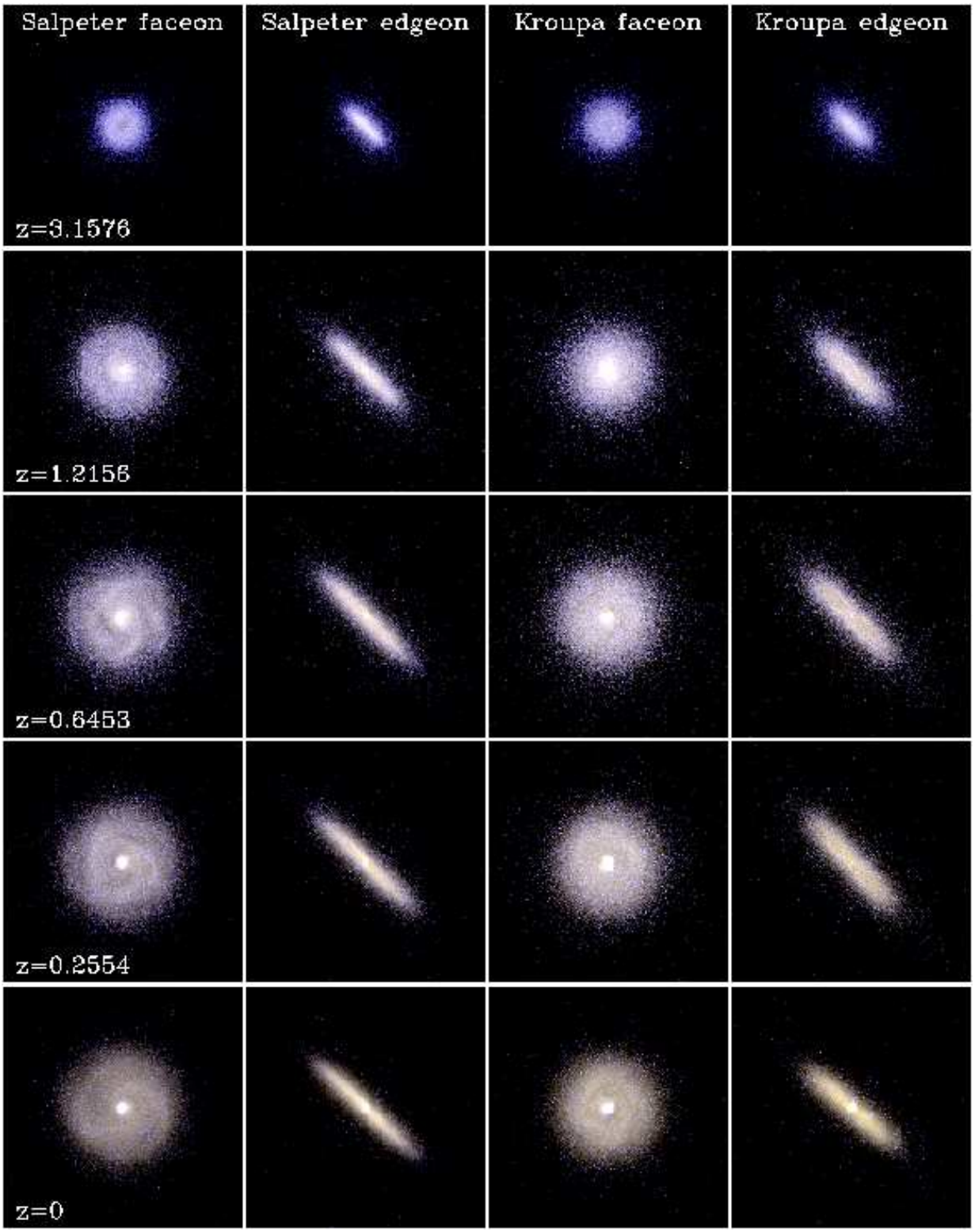

Fig. 6. Calculated intrinsic *urz* images of the Salpeter and Kroupa models, face-on and edge-on, both in the same magnitude scaling, where the calculated *u* distribution makes up for the blue portion of the composite image, the *r* distribution for the yellow portion, and the *z* distribution for the red portion. The images correspond to the images in Fig 3.

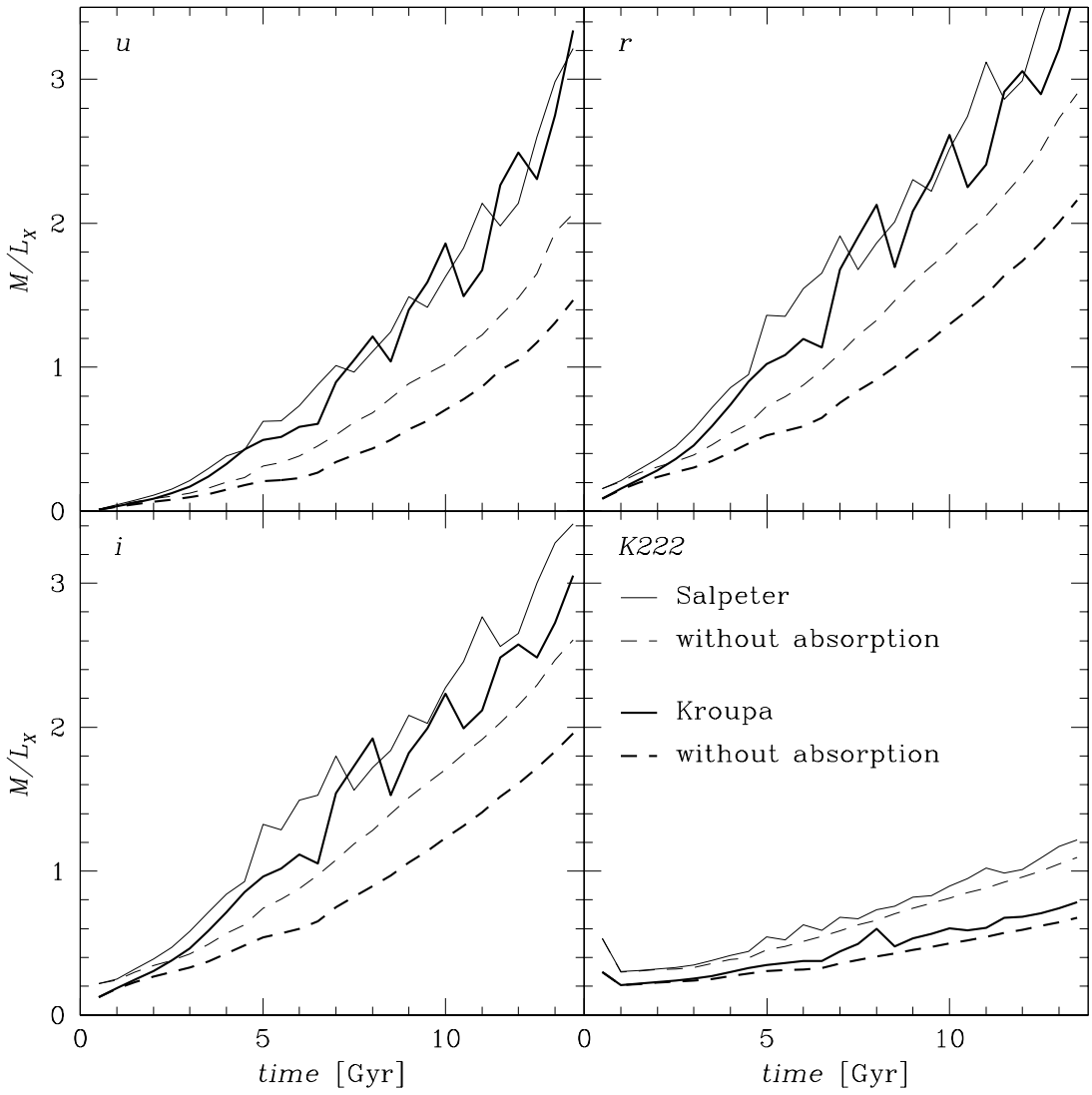

Fig. 7. Stellar mass-to-light ratio evolution in *u*, *r*, *i*, and *K*222 of the Salpeter (thin) and the Kroupa (thick) models, both including (solid) and omitting (dashed) gas absorption.

small, only up to $\sim$ 0.2 mags in $(u-g)_0$. In $(J110-K222)_0$, on the other hand, they reach up to 0.8 mags (edge-on), so this colour might be suitable to detect orientation effects. It may seem counter-intuitive, that inclination-induced reddening on the bluest colour is much smaller than in the near infrared. This must be because the differential extinction in *J*110 vs. *K*222 is much larger than in *u* vs. *g*.

Having calculated galactic models both omitting dust effects and, as a novelty, self-consistently including them, gives us the unique occasion to test the usual assumption that the combined absorption and reddening effects do not signifi cantly

alter colour-M/L relations (Bell & de Jong (2001)). Fig. 11 shows four such relations, combining colours and M/L ratios from the reddest and the bluest wavelength regions of our calculations. For the relations involving the $(u-g)_0$ colour (left panels), the assumption works reasonably well. The dust effects move the colours and the M/L ratios along the main relations, thereby keeping them in place. For the relations involving $J110-K222$ (right panels), on the other hand, the colour-M/L relations are shifted by around 0.2 mags to the red, when absorption is included (The dust affects this colour much more than the M/L ratios). It seems difficult to keep these relations intact by altering the colour and the M/L ratios at the same time, since they are not linear in the first place. A systematic investigation shows, that the assumption can be used for colours involving passbands bluewards of the SDSS *i* band.

5.3. Apparent magnitudes

In practice, apparent magnitudes (redshifted and corrected for distance) are more relevant than intrinsic magnitudes, as they are the quantities that are actually observed. They are given in Tables A.5 to A.8 for the same bands as in Tables A.1 to A.4. Due to the very low fluxes at the highest redshift (9.5116, corresponding to a Universe age of 0.5 Gyr), the calculation of the magnitudes at this age suffers too much from precision errors, so these values should be taken with a grain of salt, especially in the bluer passbands. In the bluest bands (u, g, $U336$, and $B439$), the errors might even affect the second time step (redshift 5.6177) as well, especially when combining the magnitudes to calculate colours, on which small differences have a much more dramatic effect than on magnitudes.

For the u and $K222$ bands, the redshift evolution is shown in the top panels of Fig. 13, again for both models in the diagonal view, and both including - and not including absorption, like in the first and fourth panels of Fig. 7. In the bottom panels, we see the differences between the Kroupa and the Salpeter models. These differences between the two models show the same tendencies as for the intrinsic magnitudes (~ 0.5 in the absorptionless case, reduced when absorption is included), and are probably even harder to detect than they would be in the intrinsic magnitudes, since they are dominated by distance modulus effects. Again, the $K222$ band is slightly better for detecting the differences (they remain around 0.5 mag even after including absorption) than the SLOAN filters, but still not good enough.

The absorption effects on the Kroupa model, that is the magnitude differences between the absorptionless and the absorbed model, are given in all calculated passbands in Tables C.1 and C.2 for the diagonal view. Together with the inclination corrections given in Tables C.3 to C.6, they can be calculated for all three viewing angles. By subtracting the inclination or absorption corrections for two magnitudes, the inclination or absorption (reddening) corrections for the corresponding colour can be derived. This can be useful to make absorption corrections to galactic models. We only give these corrections for the Kroupa model, because this model is more realistic, and the corrections are very similar for the Salpeter model. As expected, the absorption is the strongest in the edge-on view and the weakest face-on, but the latter does not differ much from the diagonal case. So even for face-on galaxies, it will be impossible to infer the IMF from an integrated magnitude, whereas for edge-on galaxies, the situation is even worse.

If the apparent magnitudes calculated from the models cannot be used to discriminate between the two different IMFs, do they at least reproduce the empirical data? In order to compare our model magnitudes with those from Section 4 that represent similar galaxies as in our models, we reduced both data sets (edge-on and face-on) to those galaxies with similar sizes (Petrosian radii) and structure (concentration indices) as the model galaxies. Ideally, one should compare the models to galaxies with the same mass and morphological type, but since these quantities are not given in the SDSS, we resort to size and concentration parameters. More precisely, we determined $\mathrm{petroR90}_r$ and C_r as a function of redshift z for both the Salpeter and the Kroupa models, face-on and edge-on, and then reduced the data sets to those galaxies that fulfilled the following criterion:

$$0.5 \cdot \mathrm{petroR90}_{r,mod}(z) < \mathrm{petroR90}_{r,emp}(z)$$

$$< 2.0 \cdot \mathrm{petroR90}_{r,mod}(z) \wedge$$

$$0.98 \cdot \mathrm{C}_{r,mod}(z) < \mathrm{C}_{r,emp}(z) < 1.02 \cdot \mathrm{C}_{r,mod}(z) \quad (3)$$

where $\mathrm{petroR90}_{r,mod}(z)$ and $\mathrm{C}_{r,mod}(z)$ are the Petrosian radius and concentration index calculated from the models and $\mathrm{petroR90}_{r,emp}(z)$ and $\mathrm{C}_{r,emp}(z)$ are the values taken from the SDSS data base, as well as the redshift z. The calculated Petrosian radii (both in kpc and in arcsec) and concentration indices are given for the Kroupa model in Tables D.1 to D.3, as they could be useful to identify Milky Way-type galaxies or progenitors at high redshift. At the first time step (0.5 Gyr, redshift 9.5116), however, these values still suffer from the initial border conditions of the model, and cannot be used. The concentration indices could only be calculated from redshift 1.5915 on.

The apparent u band magnitudes including their error bars of the subsamples are plotted as a function of redshift in Fig. 14. The thick dashed and dotted lines show the evolution of the corresponding models (dashed: face-on, dotted: edge-on). The thin lines show the respective other views for the same models (thus the thick lines in the upper panels correspond to the thin lines in the lower panels, and vice-versa), to show the differences in brightness between the two viewing angles. The models are only shown until the second-last time step at redshift 0.0369, as the magnitudes at redshift 0 depend on the actual distance, which is unknown. The distance modulus $m-M$ of 25 used in Tables A.5 to A.8 is only a convention, whereas in reality the distance modulus at zero redshift depends upon the actual distance and equation 2 is not valid.

As can be seen from Fig. 14, the models represent the u magnitudes of the empirical samples well, and they even reproduce the brightness differences between the face-on and the edge-on views.

Fig. 15 shows the same galaxies and models as Fig. 14, but in the r band. Here too, the agreement is good, although one

could argue that the magnitudes of the Salpeter model are a bit too faint.

5.4. Apparent colours

Let us move on to apparent colours. Fig. 16 shows the redshift evolution of apparent $u-g$ and $J110-K222$, the different line types and widths having the same meaning as in Fig. 13. The figure is only shown out to redshift 5.9, due to the above-mentioned imprecisions at redshift 9.5116. In $u-g$, they might even affect the data point at redshift 5.6177. In $u-g$, we again see our "IMF degeneracy", the fact that the higher absorption in the Kroupa model compensates the bluer colour caused by the higher SFR. This leaves the $u-g$ differences between the two models at a level of at most 0.05 mags, which is undetectable given the much larger variations this colour shows during the evolution. At best, the differences could be seen in $J110-K222$, where they amount to $\sim$ 0.2 mags (edge-on up to 0.4 mags), which is a significant fraction of the variation of this colour after 2.5 Gyr. ($\sim$ 0.7 mags). Let us see how the models compare to the empirical data. In Figs. 17 to 19, we see the $u-g$, $r-i$, and $r-z$ colours of the two models, face-on and edge-on, as a function of redshift in the same coding as in Fig. 14. Overplotted are the colours including error bars of the four subsamples of galaxies selected using equation 3, so the models are only compared to data from galaxies of the same types (angular sizes, concentration parameters, and viewing angles).

Obviously, the model colours are too blue by about 0.3 to 0.4 mags in $u-g$, by about 0.1 mags in $r-i$, and more or less in the right colour range for $r-z$. Also, the trends with redshift are not always well reproduced in the latter two colours. This could be an indication, that hierarchical-based accretion histories may induce a delayed galaxy formation, resulting in too blue colours especially at high redshift. It looks like SDSS galaxies on average have an earlier Hubble type star formation history than the Milky Way type model galaxy. This argument is also supported by the fact, that the monolithic collapse model in Westera et al. (2002) produces colours in better agreement with the data. In spite of these systematic deviations, the models do seem to reproduce relative properties, i. e. the effect of galaxy orientation on integrated colours, as can be seen from the fact, that they nicely reproduce the shift between face-on - and edge-on colours, thereby underlining the usefulness of the corrections given in Tables C.1 to C.6. This is why we believe that the results we found comparing the models with different IMFs are also realistic. We thus conclude that it is difficult to make statements about the stellar IMF from integrated colours or magnitudes of galaxies. Our best bet for this purpose are infrared colours, i. e. $J110-K222$.

6. Summary and Conclusions

In this work, we use chemo-dynamical models to investigate the influence of the Initial Mass Function (IMF) on the evolution of a Milky Way-type disk galaxy, in particular of its colours.

For this purpose, we developed two chemodynamical models of such a galaxy with the same boundary conditions, but using different IMFs: Salpeter and Kroupa, which differ in their low-to-high mass stars ratios. The Kroupa model, having a higher fraction of high mass stars, begins with a lower SFR than the Salpeter model, but from 5 Gyr on, this reverses. The Kroupa model also has a higher gas density and metallicity than the Salpeter model at all ages.

With these two models, we performed a spectral analysis, evaluated with a state of the art evolutionary code and spectral library. The programme transforming the models into spectral properties takes into account the three-dimensional distribution of the stars and the interstellar matter. It includes internal gas absorption and re-emission and is also able to include foreground reddening. We obtain two-dimensional HST (WFPC2 and NICMOS), and SDSS *ugriz* images of the model galaxies, giving intrinsic and apparent magnitudes and colours in up to 320×320 pixels. We also obtain intrinsic and apparent integrated spectra and colours of the model galaxies. All of these quantities were calculated with a time resolution of 0.5 Gyr. The programme is able to view the model galaxies from different angles (diagonally, face-on, and edge-on), which allows to analyse orientation effects on the spectral properties. Furthermore, by recalculating the models artificially omitting the gas absorption, we could disentangle absorption effects from other effects. We provide photometric absorption and inclination corrections in the SDSS *ugriz* and the HST WFPC2 and NICMOS systems (Tables C.1 to C.6).

We find, that the effect of the IMF on the internal gas absorption is larger than its effect on the light from the stellar content. However, the two effects work in the opposite sense (An IMF with more high mass stars leads to brighter and bluer stellar light, but also to more interstellar dust and thus to more absorption), causing a kind of "IMF degeneracy". The most likely wavelength region, in which to detect IMF effects is the infrared (i. e. *JHK*). Here, the differences between the two models amount to $\sim$ 0.5 mags in $K222$, and to $\sim$ 0.2 mags in $J110-K222$.

The effects of inclination on a galaxy's magnitudes and colours, on the other hand, are larger than the ones due to the IMF. Seeing a galaxy edge-on instead of face-on or diagonally can make it appear up to 1.5 mags fainter in u, or 1 mag in z, or 0.6 mags redder in $J110-K222$.

A comparison of the calculated integrated model magnitudes and colours with SDSS data partly shows good agreement, especially in the u and g magnitudes, and the *riz* colours. There are some systematic deviations in the UV colours, indicating that SDSS galaxies might have on average an earlier Hubble type star formation history than the model galaxy, which is more like the Milky Way. On the other hand, the relative tendencies in these colours are well reproduced (i. e. the shift between face-on and edge-on colours of galaxies of the same type). We conclude from this, that the theoretical results presented in the two previous paragraphs should hold true in practice as well.

As a side study, we verify the assumption by Bell & de Jong (2001), that the combined absorption and reddening effects of dust do not significantly alter the colour-M/L relations for galaxy models, and find this assumption only to be true

for colours involving passbands in the bluer wavelength ranges (bluewards of the *I* band).

Acknowledgements. This work was supported by the Swiss National Science Foundation.

References

Adelman-McCarthy, J. K., et al. 2005, ApJS, 162, 38
Barnes, J., & Efstathiou, G. 1987, ApJ, 319, 575
Bell, E. F., & de Jong, R. S. 2001, ApJ, 550, 212
Blanton, M. R., et al. 2001, AJ, 121, 2358
Bruzual A., G., & Charlot, S. 1993, ApJ, 405, 538
Bruzual A., G., & Charlot, S. 2003, MNRAS 344, 1000
Bullock, J. S., Dekel, A., Kolatt, T. S., et al. 2001, ApJ, 555, 240
Carigi, L., Col´ın, P., & Peimbert, M. 1999, ApJ, 514, 787
Carroll, S. M., Press, W. H., & Turner, E. L. 1992, Annual Review of Astronomy and Astrophysics, 30, 499
Chabrier, G. 2001, ApJ, 554, 1274
Chabrier, G. 2002, ApJ, 567, 304
Chabrier, G. 2003, PASP, 115, 763
Charlot, S., & Bruzual A., G. 1991, ApJ, 367, 126
Eggen, O. J., Lynden-Bell, D., & Sandage, A. R. 1962, ApJ, 136, 748
Fagotto F., Bressan A., Bertelli G., & Chiosi C. 1994, A&AS 105, 39
Ferraro, F. R., Carretta, E., Bragaglia, A., Renzini, A., & Ortolani, S. 1997, MNRAS, 286, 1012
Fluks, M. A., Plez, B., The, P. S., de Winter, D., Westerlund, B. E., & Steenman, H. C. 1994, A&AS, 105, 311
Girardi L., Bressan A., Chiosi C., Bertelli G., & Nasi E. 1996, A&AS 117, 113
Girardi, L., Bressan, A., Bertelli, G., & Chiosi, C. 2000, A&AS, 141, 371 ("Padova 2000" isochrones)
Gould, A., Bahcall, J. N.., & Flynn, C. 1997, ApJ, 482, 913
Gould, A., Flynn, C.., & Bahcall, J. N. 1998, ApJ, 503, 798
Kautsch, S. J., Grebel, E. K., Barazza, F. D., & Gallagher, J. S., III 2006, A&A, 445, 765
Kennicutt, R. C. 1983, ApJ, 272, 54
Kroupa, P. 1998, The Stellar Mass Function (invited review) in Brown Dwarfs and Extrasolar Planets , ASP Conf. Ser., 134 ed. R. Rebolo, L. Eduardo Martin, & M. R. Zapatero Osorio (San Francisco: ASP), 483
Kroupa, P. 2001, MNRAS, 322, 231
Kroupa, P. 2002, Sci, 295, 82
Kroupa, P., Tout, C. A., & Gilmore, G. 1993, MNRAS, 262, 545
Larson, R. B. 1998, MNRAS, 301, 569
Leitherer, C., Schaerer, D., Goldader, J. D., et al. 1999, ApJS, 123, 3
Lequeux, J. 1979, A&AS, 80, 35
Lerner, M. S., Sundin, M., & Thomasson, M. 1999, A&A, 344, 483
Madau, P. 1995, ApJ, 441, 18
Miller, G. E., & Scalo, J. M. 1979, ApJ S. S., 41, 513
Petrosian, V. 1976, ApJ, 209, L1
Piotto, G., Cool, A. M., & King, I. R. 1997, AJ, 113, 1345
Piotto, G., & Zoccali, M. 1999, A&A, 345, 485
Portinari, L., Sommer-Larsen, J., & Tantalo, R. 2004, MNRAS, 347, 691
Quillen, A. C., Yukita, M. 2001, AJ, 121, 2095
Reid, I. N., & Gizis, J. E. 1997, AJ, 113, 2246
Salpeter, E. E. 1955, ApJ, 121, 161
Samland, M., & Gerhard, O. E. 2003, A&A, 399, 961
Scalo, J. M. 1986, The initial mass function of massive stars in galaxies Empirical evidence, in Luminous Stars and Associations in Galaxies, IAU Symp., 116, 451
Scalo, J. M. 1998, The IMF Revisited: A Case for Variations, in The Stellar Initial Mass Function (38th Herstmonceux Conference), ASP Conf. Ser., 142 ed. G. Gilmore & D. Howell (San Francisco: ASP), 201
Stephens, A. W., et al. 2000, AJ, 119, 419
van den Bosch, F. C. 2002, MNRAS, 331, 98
Wechsler, R. H., Bullock, J. S., Primack, J. R., Kravtsov, A. V., & Dekel, A. 2002, ApJ, 568, 52
Westera, P. 2001, The BaSeL 3.1 models: Metallicity calibration of a theoretical stellar spectral library and its application to chemo-dynamical galaxy models, PhD thesis, Univ. of Basel, 378 pp.
Westera, P., Lejeune, T., Buser, R., Cuisinier, F., & Bruzual A., G. 2002, A&A, 381, 524
Westera, P., Samland, M., Buser, R., & Gerhard, O. E. 2002, A&A, 389, 761
Wilkinson, M. I., & Evans, M. W. 1999, MNRAS, 310, 645
Yasuda, N., et al. 2001, AJ, 122, 1104
York, D. G., et al. 2000, AJ, 120, 1579
Zoccali, M. 2000, ApJ, 530, 418

C. Appendix: My life at the Astronomical Institute of Basel

FIGURE C.1.: All members of the Astronomical Institute in front of the Dome in March 2006.

FIGURE C.2.: The Buser group (from the left to the right): Erich Wenger, Thibault Lejeune, Roland Buser, Pieter Westera and my humble self.

FIGURE C.3.: Being astronomer, a job for women (included here are our two secretaries).

FIGURE C.4.: Excursion by institute members to the Papiliorama in Kerzers in June 2006 (only few are visible here).

FIGURE C.5.: Demonstrations against the closing of the Institute in March 2004.

FIGURE C.6.: Old Emma, the 20 cm refractor telesope of the Astronomical Institute of Basel.